Shock interaction phenomena

Shock interaction phenomena

Dissertation

for the purpose of obtaining the degree of doctor
at Delft University of Technology,
by the authority of the Rector Magnificus Prof. dr. ir. T.H.J.J. van der Hagen,
chair of the Board of Doctorates,
to be defended publicly
Friday 24 May 2024 at 12:30

by

Luis LAGUARDA SANCHEZ

Master of Science in Aerospace Engineering,
University of Applied Sciences Wiener Neustadt, Austria,
born in Barcelona, Catalonia.

This dissertation has been approved by the promotors and copromotor.

Composition of the doctoral committee:

Rector Magnificus	chairperson
Prof. Dr.-Ing. habil. S. Hickel	Delft University of Technology, promotor
Dr. ir. B.W. van Oudheusden	Delft University of Technology, promotor
Dr. ir. F.F.J. Schrijer	Delft University of Technology, copromotor

Independent members:

Prof. Dr. R. Pecnik	Delft University of Technology
Dr. M.P. Martin Aguirre	University of Maryland
Dr. I. Bermejo-Moreno	University of Southern California
Dr. M. Bernardini	University of Rome La Sapienza
Prof. Dr. F. Scarano	Delft University of Technology, reserve member

Part of the research presented in this thesis was made possible by the computational resources awarded by PRACE (Partnership for Advanced Computing in Europe) on the HAWK supercomputer at the High Performance Computing Center in Stuttgart, Germany (No. 2020225421).

Keywords: compressible flow, shock-shock interaction, shock-turbulence interaction, turbulent boundary layer, flow separation, aeroelasticity, large-eddy simulation

ISBN 978-94-6366-874-3

Printed by Uitgeverij U2pi, the Netherlands

An electronic version of this dissertation is available at
http://repository.tudelft.nl/.

A la meva família

Contents

Summary

This thesis, divided into two parts, explores shock interaction phenomena occurring in high-speed platforms. PART ONE focuses on shock-shock interactions (SSIs), which manifest as a bi-stable system with either the regular interaction (RI) or the Mach interaction (MI) as outcomes. Through numerical simulations, both interaction types are examined in the presence of perturbations to provide insights into their stability characteristics and the RI⇄MI transition process, which exhibits hysteresis effects. Subsequently, attempts are made to replicate these hysteresis effects in the transonic–supersonic blow-down wind tunnel (TST-27) at TU Delft by continuously varying the free-stream Mach number during a run. The evolving shock system is continually tracked using a systematic post-processing methodology that integrates schlieren visualizations, synchronous pressure readings, and insights gained from a variable focal plane study conducted with a focusing schlieren system.

In PART TWO of the thesis, wall-resolved and long-integrated large-eddy simulations (LES) are employed to explore the physics of strong shock-wave/turbulent boundary-layer interactions (STBLIs). A significant contribution of this work is the comprehensive assessment of Reynolds number effects in the flow dynamics and organization. This assessment is facilitated by a new database of Mach 2.0 interactions at multiple friction Reynolds numbers up to $Re_\tau = 5118$, significantly broadening the parameter range covered with high-fidelity simulations. Another key contribution involves exploring the dynamic coupling between a moderate-Reynolds STBLI flow and a compliant skin panel. This scenario, with potentially catastrophic implications during vehicle operation, is investigated with coupled fluid-structure interaction simulations involving wall-resolved LES. To distinguish the distinct effects of mean and dynamic panel displacements on the flow, the resulting mean panel deflection is then employed as a rigid-wall geometry in a separate simulation.

Nomenclature

Roman symbols

a	speed of sound or panel length
$\boldsymbol{a}$	Cholesky decomposition of Reynolds stress tensor
A	area
$\boldsymbol{A}$	linear mapping
b	test section width or filter coefficient
$\boldsymbol{b}$	vector of body forces
$c_{k,r,l}$	interpolation coefficient
c_p	specific heat at constant pressure
c_v	specific heat at constant volume
C	intercept value (law of the wall) or shock wave identifier
$\boldsymbol{C}$	convective flux
$\boldsymbol{d}$	displacement vector
D	flexural rigidity
$\boldsymbol{D}$	diffusive flux
e	specific internal energy
E	specific total energy or energy spectra or Young's modulus
$\boldsymbol{E}$	Green-Lagrange strain tensor
f	frequency
f_s	shock sensor
$\boldsymbol{f}$	force vector
F	flatness
F_c	compressible transformation function
$\boldsymbol{F}$	deformation gradient tensor
g	distance above the wall
h	panel thickness or wedge hypotenuse or grid spacing

H	shape factor or height
$\boldsymbol{H}$	pressure flux
i	incident shock polar
I	light intensity or target length scale
J	Jacobian
$\boldsymbol{k}$	turbulence kinetic energy
$\boldsymbol{K}$	stiffness matrix
l	viscous length scale
L	length
M	Mach number
M_τ	friction Mach number
$\boldsymbol{M}$	mass matrix
$\boldsymbol{n}$	normal vector
N	integer number
p	pressure
$\boldsymbol{p}$	Piola traction
Pr	molecular Prandtl number
Pr_t	turbulent Prandtl number
$\boldsymbol{P}$	first Piola-Kirchhoff stress tensor
$\boldsymbol{q}$	heat flux vector
r	recovery factor or transmitted shock polar
R	correlation coefficient
R^2	coefficient of determination
R_t	correlation function in transversal direction
Re	Reynolds number
Re_{δ_0}	δ_0-based Reynolds number
Re_θ	momentum-thickness Reynolds number
Re_τ	friction Reynolds number
$\boldsymbol{R}$	dissipation matrix
s	entropy or slipline or streamline
S	surface or velocity transformation or skewness
S_t	Strouhal number
$\boldsymbol{S}$	second Piola-Kirchhoff stress tensor

t	time
T	temperature
$\boldsymbol{T}$	Cauchy stress tensor
u	first velocity component (streamwise)
u_τ	wall-friction velocity
$\boldsymbol{U}$	state vector
v	second velocity component (wall-normal)
V	volume
$V_{i,j,k}$	cell volume
w	third velocity component (spanwise) or wedge hypotenuse
W	strain energy function
x	first spatial coordinate (streamwise)
x_{sw}	separation-shock location
$\boldsymbol{x}$	instantaneous snapshot
$\boldsymbol{X}$	snapshot matrix
y	second spatial coordinate (wall-normal)
z	third spatial coordinate (spanwise)

Greek symbols

α	modal amplitude or weight of reconstruction polynomial in ALDM
α_3	skewness coefficient
$\alpha_{i,j,k}$	fluid volume fraction
β	smoothness measure of ALDM or growth rate
γ	specific heat ratio
Γ	conjoined interface
$\Gamma_{i,j,k}$	moving surface
δ	boundary-layer thickness
δ_0	velocity-based boundary-layer thickness
$\Delta\mathrm{p}$	square of momentum defect
Δt	time step
Δx	grid spacing in first direction (streamwise)
Δx_{ui}	upstream influence parameter

Δy	grid spacing in second direction (wall-normal)
Δz	grid spacing in third direction (spanwise)
ϵ	dissipation term
θ	compressible momentum thickness or phase
ϑ	flow deflection
κ	thermal conductivity or wavenumber or von Kármán constant
λ	wavelength or second viscosity coefficient or second Lamé parameter
λ_{ci}	swirling strength
λ_{dp}	dynamic pressure parameter
μ	dynamic viscosity or first Lamé parameter or DMD eigenvalue
ν	Poisson ratio
Ξ	diagnostic function
Π	pressure-strain correlation term or wake parameter
ρ	density
σ	standard deviation or model parameter of ALDM
$\boldsymbol{\sigma}$	stress tensor or interface traction
τ	shear stress or Reynolds stress or time lag
ϕ	shock angle or scalar quantity
$\boldsymbol{\phi}$	eigenvector
Φ	pressure-gradient/velocity correlation term
χ	probability of reverse flow
$\chi_{i,j,k}$	interface exchange term
ω	angular frequency
Ω	fluid/solid domain or eigenvalue
$\Omega_{i,j,k}$	cell of Cartesian computational mesh

Other symbols

$\bar{\cdot}$	Reynolds average
$\tilde{\cdot}$	Favre average
$\breve{\cdot}$	approximate solution
$\langle\cdot\rangle$	time and spanwise average
$\cdot'$	fluctuation from a Reynolds-averaged quantity

$.''$	fluctuation from a Favre-averaged quantity
$\mathcal{B}$	STBLI case
$\mathcal{D}$	transport term or domain configuration
$\mathcal{F}$	power spectral density
$\boldsymbol{\mathcal{F}}$	total flux
$\mathcal{G}$	slice of space-time correlated random numbers or grid resolution
$\mathcal{M}$	turbulent mass flux term
$\mathcal{P}$	production term
$\mathcal{R}$	specific gas constant
$\mathcal{S}$	slice of uncorrelated random numbers
$\mathcal{T}$	TBL case

Subscripts

0	reference or stagnation property
$+$	maximum value
$-$	minimum value
∞	free-stream property
aw	adiabatic wall
ele	property of interface element
ext	external
F	fluid property
imp	inviscid shock-impingement point
in	value at the inflow plane
inc	equivalent incompressible value
int	internal
ms	Mach stem property
n	nominal value
ref	reference value
sep	topology parameter of recirculation region
S	solid property
t	total-stress-based–transformed
tip	value at the wedge tip

tri	property of interface triangle
ui	upstream influence
vD	van Driest-transformed
w	property at the wall

Superscripts

$+$	inner-scaled quantity
$*$	semi-locally scaled quantity
b	baseline value
d	value following detachment condition
e	quantity related to finite elements
m	value in the Mach interaction domain
n	value following von Neumann criterion or value at a given time step
r	value in the regular interaction domain
Γ	interface value

Frequently used abbreviations

ALDM	adaptive local deconvolution method
AROM	adaptive reduced-order model
DF	digital filter
DMD	dynamic mode decomposition
DNS	direct numerical simulation
DR	STBLI case over a deformed-rigid panel
DSD	dual-solution domain
FC	STBLI case over a flexible panel
FE	finite element
FEM	finite-element method
FSI	fluid-structure interaction
FTT	flow-through times
IBM	immersed boundary method
LES	large-eddy simulation

MI	Mach interaction
MTA	modal truncation augmentation
PDF	probability density function
PME	Prandtl-Meyer expansion
POD	proper-orthogonal decomposition
PSD	power spectral density
RANS	Reynolds-averaged Navier–Stokes
RI	regular interaction
RMS	root mean square
SGS	sub-grid scale
SPDMD	sparsity-promoting dynamic mode decomposition
SRA	strong Reynolds analogy
SSI	shock-shock interaction
STBLI	shock-wave/turbulent boundary layer interaction
TBL	turbulent boundary layer
TKE	turbulence kinetic energy
TNTI	turbulent/non-turbulent interface
UMZ	uniform momentum zone
UR	STBLI case over a flat-rigid panel
UZ	uniform zone

Prologue

1

Introduction

In the present work, we shall be concerned with dynamic flow phenomena involving *shock waves*. A shock wave is a strong disturbance in a medium over which the properties of the medium undergo an abrupt and irreversible change. Such occurrence is not rare in nature and in fact is present in many flows of practical interest. Examples include supernova explosions, which are powerful and luminous explosions of stars that expel a fraction of the star's mass and generate expanding shock waves through the interstellar medium [1]. Solar wind gusts can also lead to the formation of shock waves [2], when a fast-moving pulse plows into a slow-moving one, and these events can be strong enough to disrupt Earth's magnetic field and trigger geomagnetic storms. Another phenomenon associated with shock waves is atmospheric reentry of spacecraft, where detached shocks around blunt capsules, the so-called bow shocks, are key in the deceleration process and the diversion of heat [3]. The aerodynamic environment around high-speed aircraft is also dominated by shock waves [4, 5]. Flow devices such as air intakes, control surfaces and propulsion systems operate in the presence of shock waves, and the consequent challenges these devices face is in fact what motivates the present study.

But before going into further detail, it is instructive to consider how shock waves appear in high-speed vehicles and how they impact vehicle design. As a body moves through a fluid (like air), its frontal surface is constantly exerting a force on the fluid that accelerates and compresses it. Essentially, the body is pushing fluid molecules away. But while this push is only applied to the molecules directly in contact with the body, its effect extends much further outwards into the fluid. This is a consequence of inter-molecular collisions, which grant fluids the capacity of transmitting pressure and therefore of progressively adapting to the motion of an object. The speed at which pressure disturbances propagate in fluids, as a result of inter-molecular collisions, is called the speed of sound, and for air at standard sea level conditions is $a \approx 1230$ km/h.

The fact that the speed of sound is finite immediately prompts the question of what happens when a vehicle flies faster than the speed of sound. In this supersonic flight regime, it is no longer possible for fluid molecules to feel the presence of an approaching body, since pressure disturbances cannot 'outrun' the body itself. As a result, the fluid upstream simply remains unaltered until colliding with the body,

and only then it experiences a sudden acceleration and compression. The boundary over which fluid properties undergo the abrupt change, which is also an interface between fluid particles at rest and those disturbed by the vehicle motion, is what constitutes a shock wave.

The ratio of the flow velocity to the local speed of sound, that is, the Mach number, is thus a fundamental parameter in the analysis and description of compressible flow phenomena. A cruise Mach number below unity, for instance, indicates that the cruise speed is below the speed of sound (i.e., subsonic) and that the upstream propagation of pressure disturbances in the free-stream is physically possible. This is the case of general and commercial aviation aircraft like the Cessna 172, the Airbus A320 and the Boeing 747, which operate at subsonic speeds[1]. A cruise Mach number above 1, on the other hand, is synonym for operation in the presence of shock waves, since the flight speed is greater than the local speed of sound. Examples of aircraft that cruise at supersonic velocities include the Lockheed SR-71 Blackbird, the Franco-British Concorde and the X-59 Low Boom Flight Demonstrator [6]. If the flight speed surpasses about five times the speed of sound, i.e., the cruise Mach number is above 5, the vehicle is then said to operate in the hypersonic regime. This distinction is made because chemical effects (like the ionization and dissociation of gas molecules) as well as the heating of vehicle surfaces due to air friction can become important design concerns at such high speeds. Examples of hypersonic vehicles include rocket-powered airplanes like the experimental X-15, operated in the early 1960s, and space vehicles like the retired Space Shuttle and the super heavy-lift Starship, currently under development by SpaceX.

While a comprehensive description of high-speed vehicle design approaches is beyond the scope of this introduction, a few general design traits may be mentioned for the sake of illustration. For instance, high-speed vehicles are characterized by a sharp pointed nose[2] followed by a long slender fuselage. This particular cross-section distribution is employed to minimize the wave drag[3] induced by the nose-generated shock wave while preventing the formation of additional shocks [7]. Figure 1.1 illustrates the benefits of this design strategy on the flow around a test model of the Concorde. As observed, only the nose-generated shock wave[4] is present in the first segment of the vehicle, while any other shock is only formed once the flow reaches the wings.

Figure 1.1 also emphasizes the importance of the relative location of the wings with respect to the nose of the aircraft. In a poorly designed aircraft, an unfavorable interaction between the nose-induced shock wave and the flow over the wings can

[1] Even though passenger airliners cruise at speeds below the speed of sound, air can still reach supersonic conditions in some parts of the aircraft (e.g., over the wings). When this happens, the flight regime is said to be transonic.

[2] In the hypersonic regime, the pointed nose has to be blunted to ensure the formation of a detached shock wave for heat dissipation purposes (the limit case being the blunt shape of a reentry capsule mentioned earlier).

[3] The additional drag force due to the high-pressure fluid that appears behind shock waves, which essentially acts against the motion of the vehicle.

[4] The nose-generated shock wave is actually a conical discontinuity that emerges at the nose and extends around the entire vehicle. Only the flow inside has been accelerated and compressed, while the flow outside of it is not yet disturbed.

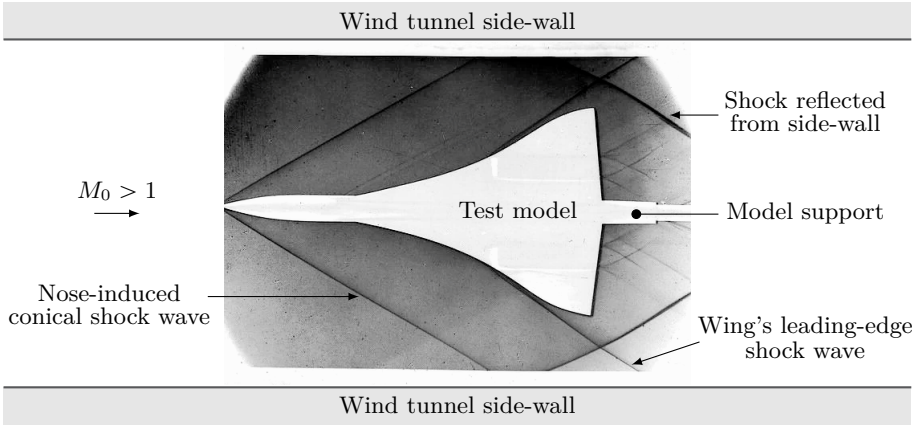

Figure 1.1: Experimental schlieren visualization of a test model of the Concorde at cruise conditions. Credit: the Royal Aeronautical Society (National Aerospace Library)/Mary Evans Picture Library.

result in decreased aerodynamic efficiency and a significant increase in drag. This has to be avoided for obvious reasons, and one effective solution involves positioning the wings towards the rear end of the aircraft, as illustrated in figure 1.1, along with high sweep angles. These design principles form the basis of delta wing planforms in high-speed aircraft (i.e., wings with triangular shape), which effectively prevent undesired shock interactions while maximizing wing area, and consequently, lifting capacity compared to conventional swept-back configurations. The iconic Concorde in figure 1.1 exemplifies this design strategy with its delta-wing configuration featuring varying sweep angles.

Another important characteristic of high-speed aircraft are supersonic inlets of air-breathing jet engines. These inlets, which are essentially ducts, generate a set of shock waves that efficiently decelerate and compress the incoming supersonic airflow prior to combustion [8]. In ramjet and scramjet[5] engines, which operate at supersonic and hypersonic velocities, the shock compression at the inlet is harnessed to the point where a mechanical compressor is no longer needed, thus reducing the complexity of the propulsion system and the corresponding weight requirements.

Since supersonic inlets are particularly helpful in establishing the motivation of the present thesis, we shall consider them in a bit more detail. A schematic view of a generic supersonic mixed-compression inlet[6] is shown in figure 1.2. The nominal shock pattern comprises external oblique shocks, internal shock reflections and a terminal normal shock wave beyond which the flow is subsonic. Such shock system is desirable for cruise Mach numbers M_0 between $\sim$ 2 and 5 because it enables a higher compression efficiency, i.e., total pressure recovery, than only one or few external shock waves leading to the same terminal Mach number [11]. The SR-71

[5] Supersonic combustion ramjet

[6] Mixed-compression because the inlet comprises both external oblique shocks and internal shock reflections. If only one or the other type are present, it is simply called internal or external compression inlet. If only a normal shock appears, it is then called normal or Pitot inlet [10].

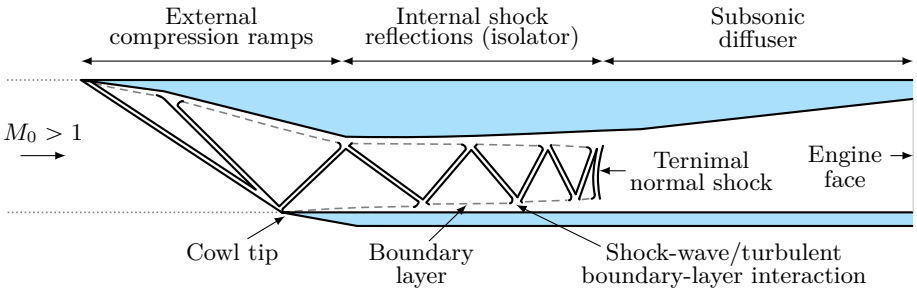

Figure 1.2: Schematics of a mixed-compression inlet. Adapted from Das and Prasad [9].

Blackbird, which cruised at over $M_0 \geqslant 3.2$, employed mixed-compression inlets on each engine unit [12]. The corresponding inlet geometry is schematically depicted in figure 1.3 where the relative position between the internal contour of the cowl and the outer surface of the translating axisymmetric spike determines the area contraction. The translation of the spike was scheduled with flight Mach number and vehicle altitude to maximize engine performance [13].

The benefits of allowing for internal shock reflections inside the inlet, however, come at the expense of significant losses as a result of the interaction between shock waves and the boundary layer at the walls. The boundary layer corresponds to the thin layer of fluid in the immediate vicinity of the wall, where viscous effects cause the flow to decelerate from the free-stream velocity to zero velocity right at the surface. If a boundary layer is subject to a sudden compression, like the one imposed by a shock wave, it can be disrupted to a point where the flow direction is reversed near the wall. And this event, referred to as flow separation or flow detachment, constitutes one of the key operational challenges that inlet systems and other components of high-speed vehicles face.

1.1. Motivation

The pursuit for supersonic commercial aviation and recoverable space launch vehicles has brought renewed attention to the operational challenges[7] of high-speed platforms [15, 16]. Some of these challenges include reducing the supersonic boom signature, which is of paramount importance to enable supersonic flight over land [17], minimizing stability and control development risk to ensure controllability at high speeds [18], and developing efficient propulsion systems (with a broad operating range) that meet emerging environmental goals [19, 20].

One of the major steps towards more fuel-efficient vehicles is to reduce the impact of shock-wave/turbulent boundary-layer interactions (STBLIs). These interactions develop when a turbulent boundary layer (TBL) encounters a shock wave, which

[7] Addressing these challenges is a complex interdisciplinary endeavor that will require advances in aerodynamic research, heat management, material science, fuel efficiency, multidisciplinary system design optimization, laboratory testing capabilities and high-fidelity computational simulations among others areas [14].

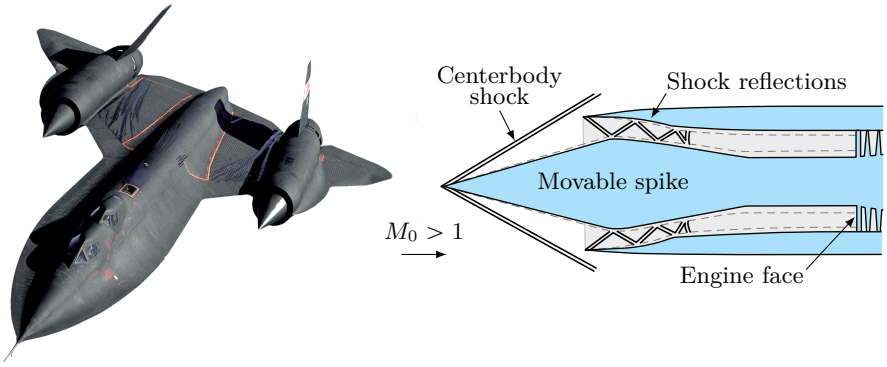

Figure 1.3: The SR-71 and its mixed-compression inlet geometry.

occurs in internal flow applications such as supersonic inlets and rocket nozzles as well as external flow applications including primary flight control surfaces. STBLIs are most concerning when the adverse pressure-gradient imposed by the shock is large enough to cause substantial boundary-layer separation. Flow separation is common in supersonic inlets and accounts for an important fraction of their operational losses [10, 21]. The reasons for that will become clear upon examination of the instantaneous configuration of STBLI, which is illustrated in figure 1.4.

As a primary characteristic, a bubble of reverse-flow is formed around the point where the impinging shock and the TBL meet, and the bubble extends in both the downstream direction but more considerably upstream. The latter seems to contradict the previous discussion on pressure disturbance propagation in supersonic flows, but it actually does not. Recalling the definition of a boundary layer, it is the region where the flow progressively decelerates from free-stream conditions to zero velocity right at the surface. If the free-stream is supersonic, the flow then reaches sonic conditions (Mach 1) at some point within the boundary layer, and at any point closer to the wall it is subsonic. A subsonic region means that pressure can propagate upstream, thus allowing the reverse-flow region in figure 1.4 to start ahead of the point where the impinging shock and the TBL meet. This effect is called the upstream influence.

The outer supersonic stream, in turn, is deflected away from the wall by the detached shear layer, which is now a free shear layer enclosing the reverse-flow region. And since pressure disturbances cannot propagate upstream in the outer region, a second shock forms at the leading edge of the interaction to adjust the outer flow direction and pressure level. This shock wave is called the separation shock, and it intersects the impinging shock typically before the latter reaches the TBL, see figure 1.4. An intersection of this sort, between two distinct shock waves far away from any surface, corresponds to another prevalent phenomenon in high-speed flows: inviscid shock-shock interactions [22]. A section of this thesis is devoted to this phenomenon, but this shall be appropriately introduced after the current discussion on STBLIs.

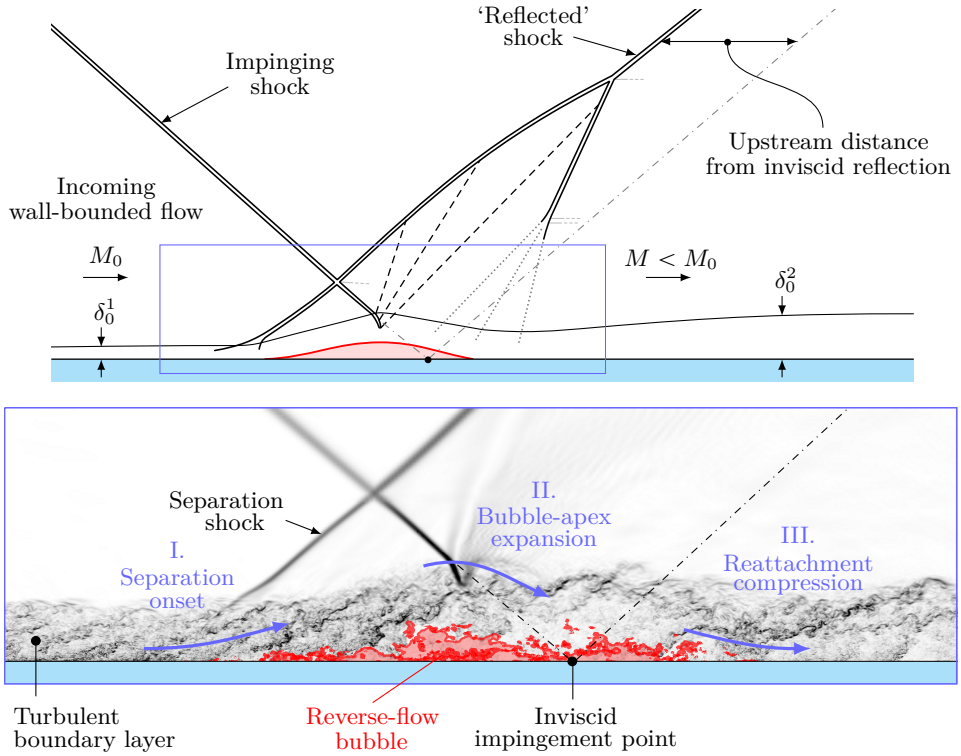

Figure 1.4: Schematics and instantaneous flow configuration (numerical schlieren visualization) of an impinging shock-wave/turbulent boundary-layer interaction.

Referring back to the instantaneous STBLI visualization in figure 1.4, the separation shock foot is thus formed around the separation location (labeled as I in the figure). Beyond this point, the free shear layer moves away from the wall until it intersects the impinging shock at a certain height above the wall. This intersection results in a progressive curvature of the impinging shock tip (as it penetrates into the free shear layer, see II in figure 1.4) and a subsequent convex turning of the shear layer towards the surface. The apex of the re-circulation region is thus established with a local expansion (i.e., acceleration) of the flow. The shear layer then meets the surface again downstream of the inviscid impingement point[8], where the flow is further compressed and the reattachment process takes place (see III in figure 1.4). This leads to the formation of the post-interaction TBL, which is substantially thicker than in the upstream region. The thickness of the boundary layer before and after the interaction region in figure 1.4 is respectively indicated with δ_0^1 and δ_0^2 for ease of comparison.

The flow distortion due to STBLI shown in figure 1.4 differs significantly from an inviscid reflection, which is also indicated with dash-dotted lines in the figure. The inviscid reflection would represent the ideal operating conditions for a supersonic

[8]The point where the impinging shock would bounce off the surface in the absence of the TBL

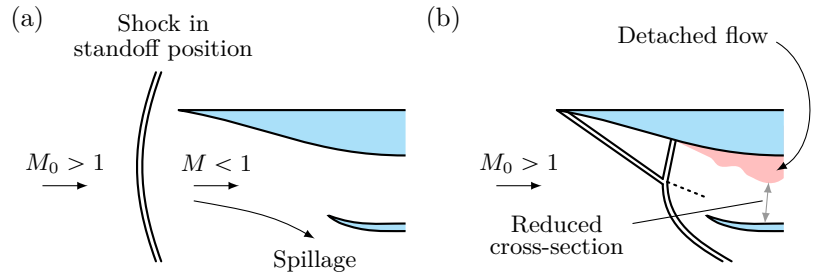

Figure 1.5: Schematics of (a) the unstart phenomenon, and (b) possible occurrence of the buzz instability.

inlet, where no TBLs would develop, and hence, no energy would be dissipated due to friction. So the mere presence of the TBL already incurs losses, but the consequent STBLI-induced separation leads to the formation of the separation shock upstream of the inviscid impingement point. Together with the reattachment compression (which in some instances can also coalesce into a shock wave, see e.g., References [23] and [24]), the separation shock leads to the 'reflected' shock wave that propagates away from the surface. In the framework of a supersonic inlet, it is this outgoing wave that produces the next shock reflection on the opposite wall, see figure 1.2. So the larger the recirculation region, the further upstream the reflected shock will move. In an uncontrolled event, this can completely distort the internal shock structure of a supersonic inlet. The implication of a major shock disruption can be severe as it not only degrades the compression performance of the inlet (due to an off-design flow pattern), but it can also make the inlet more susceptible to two critical operation modes. These are catastrophic inlet unstart and the so-called buzz phenomenon, both depicted in figure 1.5.

Figure 1.5(a) shows the unstart phenomenon, which corresponds to the terminal normal shock being abruptly expelled outside of the inlet[9]. This results in a sudden loss of engine thrust and an increase in drag due to the standoff distance between the normal shock and the inlet. One of the pilots of the SR-71 allegedly cracked his helmet when his head impacted the cockpit canopy after both engines suddenly experienced unstart [21]. All supersonic inlets with an internal throat are susceptible to the unstart instability, which has motivated the development of supersonic flow-through engines like the scramjet where the normal shock is eliminated during nominal operation [11]. The buzz instability is depicted in figure 1.5(b) and in this case, the normal shock is still pushed outside of the inlet duct but does not reach a standoff position. Instead, it remains oscillating over the external ramps, causing substantial flow separation as well as high-amplitude variations of the inlet mass-flow and static pressure. The mechanism sustaining these oscillations, the so-called big buzz, is attributed to the detached shear layer partially blocking the inlet duct [25]. Besides being detrimental for the engine operation, these shock oscillations can also significantly jeopardize the structural integrity of the outer inlet ramps. So

[9]Since the flow at the entrance of the inlet is now subsonic, shocks can no longer form inside.

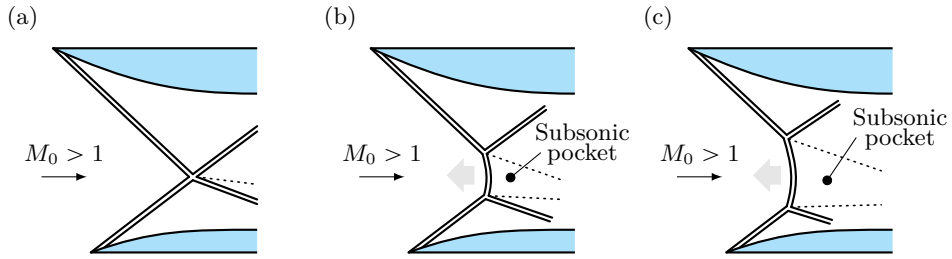

Figure 1.6: Transition from regular interaction to Mach interaction in a supersonic inlet.

much so that the buzz phenomenon experienced during an early test flight of the Concorde led to the collapse of a movable inlet ramp in front of its third engine [26].

The interactions between shock waves that occur within the inlet duct can also significantly affect the operation of the inlet. It is well known that, for a range of flow conditions, these shock interactions form a bi-stable system for which either the regular interaction (RI) or the Mach interaction (MI) can materialize [22]. The former is depicted in figure 1.6(a) and involves two incident shock waves, two reflected shock waves and a slipline (the latter indicated with a dotted line in the figure). This is the intuitive shock pattern resulting from two intersecting shock waves. The MI, in turn, is more complex and involves an additional quasi-normal shock segment beyond which the flow is subsonic, see figure 1.6(b). This subsonic region is enclosed by sliplines emanating from each triple shock-intersection point, and a necessary stability requirement is that these sliplines form a virtual convergent duct to allow the subsonic flow to accelerate. Another stability conditions for the MI is the presence of at least one external expansion fan that establishes a throat and a divergent segment on this virtual slipline duct so that the enclosed flow can actually reach supersonic conditions. If this condition is not met, the MI is unstable, in contrast to the RI. In such cases, the quasi-normal shock can move upstream and grow unrestricted, as illustrated in figure 1.6(c), which is highly undesirable because of the severe loss of stagnation pressure, flow distortion and the high risk of engine unstart. So in order to guarantee the nominal operation of supersonic inlets throughout the complete flight profile, an in-depth understanding of the causes leading to the transition between the RI and the MI is thus needed.

The irregular modes of inlet operation described above can thus be triggered by uncontrolled STBLIs, which highlights the criticality of this occurrence. But even during regular operation, the performance of supersonic inlets with internal compression can be significantly degraded in the presence of substantial flow separation. And this is not only due to the formation of a recirculation region and the upstream motion of the reflected shock, both apparent in figure 1.4 as already discussed, but also other effects such as the amplification of turbulence near the mean separation and reattachment points, where the flow is abruptly compressed. This increases the amount of energy dissipated by viscous effects [27, 28] and the corresponding viscous heating may become severe at hypersonic velocities, to the point where structural components may require additional insulation measures.

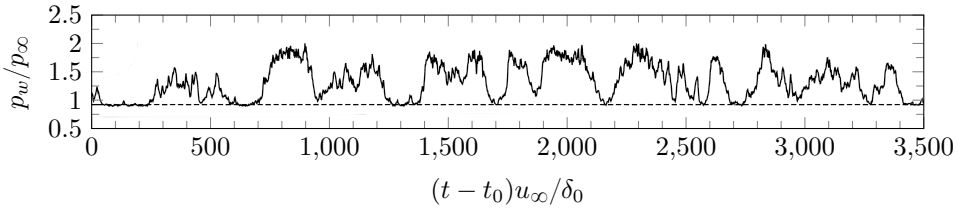

Figure 1.7: Experimental wall-pressure signal underneath the separation shock foot in a Mach 3.0 STBLI flow. Data from Daub *et al.* [29].

Furthermore, linked with the flow separation in STBLIs is the phenomenon of low-frequency and large-scale unsteadiness [30]. While the extent of the reverse-flow region may be in some instant like the one in figure 1.4, it can fluctuate substantially in size. This breathing motion of the reverse-flow bubble, where it continuously expands and contracts from both ends, is another salient feature of STBLI that has severe implications on the design of supersonic inlets and other components of high-speed platforms. Since the motion of the bubble is correlated with longitudinal excursion of the separation shock, which can be several δ_0 long, the low-frequency unsteadiness of STBLI leads to an intermittent and high-amplitude thermomechanical load on the surface. This is illustrated in figure 1.7, which shows the corresponding surface pressure underneath the separation shock foot in a Mach 3.0 STBLI [29]. As observed, the pressure alternates between the pre-shock value (denoted with p_∞) to the post-shock pressure level almost instantaneously, and the latter is a factor 2 larger than the former in this case. These characteristic pressure jumps are clearly aperiodic and not tonal, resulting in a broadband low-frequency content. The frequency around which the broadband activity is centered depends on the extent of the reverse-flow region and the free-stream flow velocity, but it typically falls below 1000 Hz. While this frequency may still seem rather high, it is two to three orders of magnitude lower than the typical frequency of small-scale turbulent fluctuations within the TBL, produced by the passage of turbulent eddies [31]. So with respect to the convective scales in the flow, the large-scale pulsation of STBLI occurs at low frequencies.

Oscillating loads of this kind, with large amplitude variations at relatively low frequencies, are of particular concern for the integrity of structural components, which may resonate[10] with the unsteady loading and potentially collapse by high-cycle fatigue [32]. The natural frequency of oscillation of structural skin panels and other components is also typically found below 1000 Hz so the dynamic coupling between STBLI and structure vibrations is not only possible but is in fact a common occurrence during operation [33]. Despite the attention that STBLIs have received in the past, however, there is still no consensus on the physical mechanisms driving

[10] Exhibit large amplitude and self-sustained oscillations due to the coupling among aerodynamic, elastic and inertial forces, which have a reinforcing effect at particular frequencies. A textbook example of dynamic aeroelastic phenomena is the wind-induced, large-scale structural oscillation (and later collapse) of the Tacoma Narrows Bridge near the city of Tacoma (U.S.) in November 7, 1940.

their characteristic low-frequency unsteadiness [30]. The lack of a definitive explanation on this front, which highlights the complexity of the phenomenon, hinders the development of flow control techniques that can efficiently mitigate the adverse effects of STBLI without incurring excessive performance or weight penalties.

While several theories have been proposed in the literature to explain the low-frequency unsteadiness of STBLIs, see Clemens and Narayanaswamy [30] for a comprehensive review, none have been conclusively supported by evidence. Proposed theories are broadly categorized into so-called upstream and downstream mechanisms. The upstream theories assume that the low-frequency dynamics arise from the passage of very large coherent structures present in the incoming TBL. These structures must be two to three orders of magnitude longer than boundary layer thickness to be compatible with observations for the shock-motion timescales. It has been debated, however, whether such elongated structures really exist at low Reynolds number or observations just show spurious artifacts formed upstream in wind tunnel facilities, or similar artifacts introduced through inflow in numerical simulations [34]. High-fidelity simulation results confirm that the low-frequency dynamics persists for boundary layers without large-scale structures [23, 35, 36], but the most convincing experimental data is for higher Reynolds numbers than the simulations and for nearly attached/incipient separations [37, 38]. For massively separated STBLI flows, on the other hand, theories of the second category are far more compelling as they regard the low-frequency unsteadiness as an intrinsic property of the reverse-flow bubble or the shock-bubble system [39]. Several models have been derived based on this idea, and some of the widely acknowledged include the possibility of an acoustic resonance mechanism in the recirculation region [40], a hydrodynamic instability in the free shear layer similar to the wake-mode in cavity flows [41], a depleting/recharge process based on fluid entrainment by the free shear layer [42] and the presence of centrifugal instabilities at separation and/or reattachment that continuously force the interaction [43]. Whether only one or several of these mechanisms are responsible for the low-frequency unsteadiness, which may also be modulated by upstream coherent structures depending on the shock strength and Reynolds number, remains an open question and requires further research.

It is also important to bear in mind that the impinging configuration discussed so far is only one type of STBLI present in high-speed vehicles; there are other relevant interaction configurations that exhibit very similar features [30, 44]. These include the fin-generated interaction and the compression ramp interaction, both schematically depicted in figure 1.8. The former is typically formed at body junctions, e.g., where the vertical or the horizontal stabilizers meet the fuselage, and the bow shock induced by the fin is what causes the incoming TBL to separate in this case. Another characteristic of the fin-generated STBLI is the fact that the inviscid shock-shock interaction between the separation shock and the bow shock leads to the formation of an additional shock that impinges on the fin, see figure 1.8. This shock impingement is very detrimental for the integrity of the fin since it is now exposed to similar fluctuating loads as those experienced underneath the separation-shock foot. The compression ramp case, on the other hand, involves a sharp surface deflection towards the flow as shown in figure 1.8. If this deflection is large enough, the re-

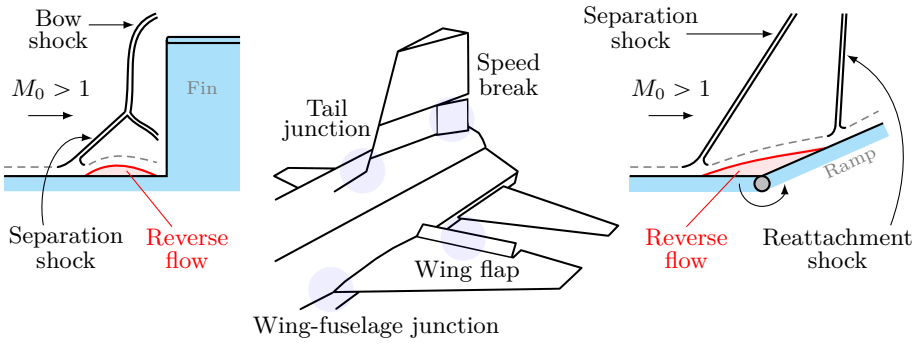

Figure 1.8: Schematics of (center) the rear section of the rocket-powered X-15, (left) fin-induced STBLI, and (right) compression ramp STBLI.

sulting adverse pressure gradient causes the incoming TBL to separate ahead of the corner, thus leading to an unsteady STBLI. Compression-ramp interactions appear wherever any surface is deployed, like in the case of primary control surfaces and speed-breaks, and can lead to a substantial loss of control authority if the resulting re-circulation region grows uncontrolled.

Despite the differences in flow organization, both the fin-generated interaction and the compression ramp interaction exhibit essentially the same features and energetic low-frequency dynamics as the impinging shock interaction over a flat wall. This means that various outer mold-line vehicle panels are also at risk of high-cycle fatigue due to STBLI, specially considering the minimum-weight requirements of these components and the potentially severe thermal loading they may experience at hypersonic velocities [45], which further degrades their mechanical properties.

At this point in the chapter, the reader has hopefully gained an overall, introductory picture of STBLIs. The main characteristics of these interactions are perhaps clear by now, as well as their impact on flow devices and the need for trade-offs between efficacy of damage mitigation measures and associated performance and weight penalties. This is the price to pay for operating in the presence of shock waves. But hopefully, there is still much room for improvement. And this improvement can be realized by studying STBLIs further, at high Reynolds number, off-design conditions and in the presence of flexible components, so that the underlying physics can be fully understood as well as their role in relevant aeroelastic interactions. It is only by doing so that we can fully optimize the aerodynamic and structural design of high-speed platforms, and this thesis represents a step towards this realization.

1.2. Contribution of this work

Most of the oblique shocks formed in supersonic inlets and other internal flows are affected by STBLIs. This means that they exhibit a characteristic unsteady motion that is constantly perturbing the SSIs taking place away from the walls. Recent

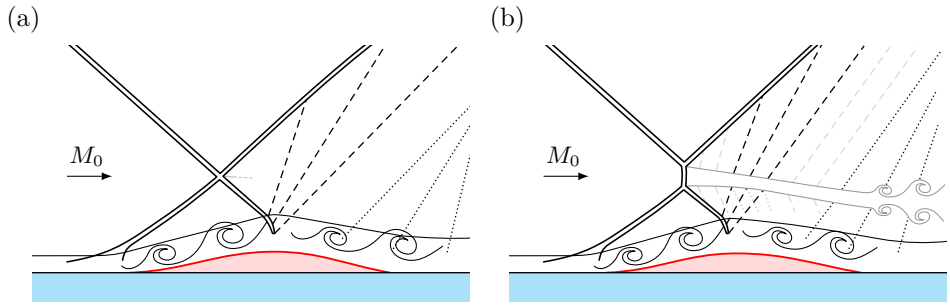

Figure 1.9: (a) Regular interaction, and (b) Mach interaction in STBLI with substantial flow separation.

numerical simulations performed by Matheis and Hickel [46] actually demonstrate that such shock unsteadiness can cause premature RI → MI transition and sustain the MI pattern for mean flow conditions beyond its steady-state stability boundary, see figure 1.9. This occurrence highlights the unpredictability of SSIs in presence of continuous perturbations and the need to better understand the transition process under such conditions. Perturbed shock interactions have been studied in the past [22]; however, fundamental research is still limited to the effect of impulsive disturbances on symmetric shock systems[11], mainly either in the form of incoming velocity perturbations [47], shocks, expansion waves and contact discontinuities in the free stream [48], laser pulses [49], dense particles [50], water vapour [51] or impulsive wedge rotation [52–54]. The practically relevant case of an asymmetric shock structure being continuously perturbed, on the other hand, remains to date unexplored.

So the first objective of this thesis is thus to investigate the dynamics of unsteady asymmetric shock interactions affected by a continuous excitation. A set of two-dimensional simulations are performed for the purpose, where two wedges are used to asymmetrically deflect the free stream flow and introduce oblique shock waves and expansion fans in the computational domain. After a steady state is reached, the shock system is excited according to three different excitation mechanisms: 1) pitching of the lower wedge across the region where both the RI and MI coexist, the so-called dual-solution domain (DSD); 2) a periodic (sinusoidal) oscillation of the lower wedge deflection around a mean value both within and outside of the DSD, and 3) a periodic (sinusoidal) streamwise oscillation of the lower wedge without pitch. These excitation modes, specially the latter two, are aimed at emulating the effect of the STBLI unsteadiness on the lower incident shock. The response of the shock interaction system to such perturbations is then carefully analyzed with a strong focus on the bi-directional RI⇄MI transition process and the underlying mechanism by which the MI is found to be more robust than the RI under such conditions.

Thanks to the variable free-stream Mach number functionality of wind tunnel facilities at TU Delft, we could also experimentally investigate the evolution and

[11] SSIs where the upper shock wave angle is the same as the lower one.

RI⇄MI transition process of various shock interaction systems subject to a quasi-steady variation of the inflow Mach number. Providing accurate measurements of this phenomenon is useful for the validation of analytical models and lower-fidelity simulations, specially considering that only one experimental investigation of this kind was previously available in literature [55]. Schlieren visualizations and synchronous pressure readings are employed as the main flow-diagnostics tools in our experiments, and the data processing is supported by a variable focal plane study conducted with a focusing schlieren system. The latter provides insights into three-dimensional side-wall effects and other features contaminating the regular schlieren visualizations, which allows for a more accurate identification of the shock system from the corresponding schlieren images. Since all parameters are quantified from the observed state of the flow rather than the nominal one, our results are thus free from manufacturing and mounting uncertainties as well as effects related to the boundary layer growth on the wedge surface and potential deformations due to aerodynamic loading. We demonstrate that this is in fact necessary to recover the agreement with theoretical predictions based on steady gas dynamics theory.

The second part of this thesis is focused on improving the physical understanding of STBLIs with substantial flow separation. In particular, we concentrate on two different aspects. The first one is the effect of the Reynolds number on the STBLI dynamics and topology. This knowledge is of paramount importance for the extrapolation of laboratory data to full-scale flight conditions. Past experimental investigations of compression ramp and impinging-shock configurations have been conducted for a wide variety of flow conditions [56] and have established a foundation on the effect of this parameter along with Mach number and shock strength. The knowledge base has been enriched in recent years with high-fidelity simulation results, which overcome inherent experimental limitations and potentially offer better insights into the interaction dynamics. However, despite the variety of configurations already investigated numerically [44], computational studies on STBLI are still mainly available at lower Reynolds numbers than complementary experiments [57].

As previous research has shown, only turbulence-resolving strategies, that is, direct numerical simulations (DNS) and large-eddy simulations (LES), are capable of capturing all relevant STBLI dynamics [36]. DNS would require to resolve all relevant scales of the problem, whereas LES resolves all dynamically important scales and incorporates the effect of the unresolved scales through a sub-grid scale (SGS) model. Even though LES is computationally less demanding than DNS, LES of multi-scale turbulent flows are still only feasible for a narrow range of conditions. For this reason, previously available numerical studies on STBLI were limited to low and moderate Reynolds numbers, mostly below $Re_\tau \approx 10^3$ and $Re_\theta \approx 10^4$ in terms of friction and momentum-thickness Reynolds number respectively[12]. These values are lower than those in high-Reynolds experiments, e.g., the impinging STBLI case of Humble *et al.* [38, 58] at $Re_\theta \approx 5 \times 10^4$ or the works of Settles *et al.* [59] and Dolling and Murphy [60] on compression ramps at $Re_\theta \approx 7 \times 10^4$, and for an in-depth understanding of the practically relevant high-Reynolds regime of STBLI this

[12]These parameteres are defined in Chapter 6.

gap needs to be closed.

With this aim in mind, we have developed a novel wall-resolved LES database of impinging STBLI that enables an accurate characterization of Reynolds number effects in the flow. The database covers more than a decade of Re_τ (and Re_θ) and otherwise considers equal flow parameters and simulation setup. The investigated cases are at free-stream Mach number $M_0 = 2.0$ and comprise a low-Reynolds STBLI with $Re_\tau = 355$ ($Re_\theta = 1.6 \times 10^3$), a moderate-Reynolds STBLI with $Re_\tau = 1226$ ($Re_\theta = 5.7 \times 10^3$) that is in line with previous numerical works, and a high-Reynolds STBLI with $Re_\tau = 5118$ ($Re_\theta = 26.4 \times 10^3$) that extends the current parameter range of strong interaction. This high-Reynolds case represents a leap towards the high-Reynolds conditions of experimental facilities. All cases exhibit substantial flow reversal and have been integrated for a very long time to properly resolve low-frequency dynamics. Moreover, simulations without the impinging shock have also been performed to characterize the impact of the Reynolds number on the undisturbed TBL. This is particularly instructive for the present analysis since Reynolds number effects in STBLI also stem from the differences in the TBL structure at low and high Reynolds number.

Our analysis of the mean and instantaneous STBLI organization is focused on the differences in interaction scales, bubble topology and turbulent structures that appear with increasing Reynolds number, and we also show that pressure transport in the separation-shock excursion domain becomes an important source of stress at high Reynolds number. Furthermore, the most energetic frequencies in the flow, which are identified by means of temporal spectra of wall-pressure, separation-shock location and separation-bubble volume signals, are related to global flow phenomena via dynamic mode decomposition (DMD [61]) of the LES data. Such modal analysis technique has been commonly applied to two-dimensional datasets in previous impinging STBLI studies, often resulting from spanwise averaging [23, 35, 62]. Here, we instead employ a full three-dimensional dataset that includes the instantaneous streamwise velocity, pressure and streamwise vorticity fields.

The other fundamental aspect that we tackle in the second part of this thesis concerns the aeroelastic coupling between STBLI and a flexible thin-panel. Despite being practically very relevant, studies involving STBLI and elastic components are very scarce due to the complexities in reproducing and characterizing the resulting fluid-structure interaction (FSI) with experiments or numerical simulations [32, 63]. The few available studies confirm that STBLI efficiently triggers low-order modes of panel vibration [64–66]; however, questions related to the coupling mechanism, the corresponding modulation of the STBLI dynamics as a result of surface displacements and the particular role of static and dynamic panel deformation remain still open. The interplay between static surface deformation and STBLI had been studied experimentally [67, 68] and with low-fidelity models [69] but not with high-fidelity simulations to the authors' knowledge.

Motivated by the aforementioned, we thus performed wall-resolved LES of a Mach 2.0 impinging STBLI over a flexible thin-panel in order to investigate the resulting dynamic coupling. A partitioned FSI approach with a finite element (FE) structural solver has been employed together with an adaptive reduced-order model [70] to

achieve long integration times after the initial transient response of the panel, which is discarded from the statistical analysis. In order to distinguish effects that are caused by the mean panel deformation from those that are caused by dynamic panel motion, we have employed the mean panel deflection as a rigid-wall geometry in a second wall-resolved LES, which is integrated over the same time interval as the coupled case. Results are also compared against the baseline configuration, a flat and rigid-wall STBLI at the same flow conditions that corresponds to the moderate-Reynolds interaction employed in the analysis of Reynolds number effects.

1.3. Outline

In chapter 2, we provide details on the numerical and experimental methodology employed in the present work. PART ONE of the thesis then starts with chapter 3, which includes the numerical analysis of unsteady asymmetric SSIs affected by a continuous perturbation. The reader is also introduced in this chapter to the relevant gas-dynamics theory required to calculate the boundaries of the steady-state DSD. The experimental investigation of the SSI response to quasi-steady free-stream Mach number variations is subsequently presented in chapter 4 together with the necessary details of the proposed flow-based postprocessing of schlieren data and synchronous pressure readings. This chapter also reports the variable focal plane study conducted with a focusing schlieren system.

PART TWO of the thesis starts with chapter 5, in which we analyze the differences in TBL structure at low and high Reynolds number. As previously explained, these differences are quantified from LES data generated with the numerical setup of the corresponding STBLI cases but without the shock generator. The impact of the Reynolds number on the organization, dynamics and statistics of STBLI is then numerically investigated in chapter 6. Chapter 7 presents the corresponding computational results of the considered STBLI flow dynamically coupled with a flexible thin-panel. The thesis work is finally concluded in chapter 8.

2

Methodology

This chapter describes the numerical and experimental methodology employed in the present thesis. The former is detailed for two-way FSI simulations, where the flow can dynamically couple with a compliant structure. Such is the case of the simulations reported in chapter 7, which consider the dynamic interaction between STBLI and a flexible thin-panel. The remaining simulations discussed in the thesis, on the other hand, do not involve a deforming solid geometry and were performed with the fluid solver only.

2.1. Numerical method

A partitioned FSI framework with coupled domain-specific solvers is used to advance the system in time. The computational domain thus consists of non-overlapping fluid Ω_F and solid Ω_S domains with a conjoined interface $\Gamma = \Omega_F \cap \Omega_S$ where the normal vector $\boldsymbol{n}^\Gamma$ in spatial configuration points into the fluid domain. Subscripts F and S are used as needed to differentiate between fluid and solid variables[1], and the Einstein summation convention for repeated indices is implied when using index notation, unless otherwise stated.

2.1.1. Governing equations

Fluid

The fluid domain is governed by the three-dimensional compressible Navier-Stokes equations, solved in conservative form

$$\partial_t \boldsymbol{U} + \nabla \cdot \boldsymbol{C}(\boldsymbol{U}) + \nabla \cdot \boldsymbol{H}(\boldsymbol{U}) - \nabla \cdot \boldsymbol{D}(\boldsymbol{U}) = \boldsymbol{0} \quad \text{in } \Omega_F, \tag{2.1}$$

where the state vector $\boldsymbol{U} = [\rho_F, \rho_F u_1, \rho_F u_2, \rho_F u_3, \rho_F E]^{\mathrm{T}}$ consists of the fluid density ρ_F, linear momentum $\rho_F u_i$ for $i = 1, 2, 3$ and total energy $\rho_F E$. The total flux in equation (2.1) consists of advection, $\boldsymbol{C}$, inviscid stresses, $\boldsymbol{H}$, and viscous

[1] These subscripts, however, are omitted in the remainder chapters of the thesis, where we explicitly differentiate between fluid and solid properties in the text.

stresses, $\boldsymbol{D}$,

$$\boldsymbol{C}_i = u_i \boldsymbol{U}, \quad \boldsymbol{H}_i = \begin{bmatrix} 0 \\ \delta_{i1} p \\ \delta_{i2} p \\ \delta_{i3} p \\ u_k \delta_{ik} p \end{bmatrix}, \quad \boldsymbol{D}_i = \begin{bmatrix} 0 \\ \sigma_{i1} \\ \sigma_{i2} \\ \sigma_{i3} \\ u_k \sigma_{ik} + q_i \end{bmatrix}, \tag{2.2}$$

where u_i is the velocity vector and $(\sigma_{ij})_{i,j=1,2,3}$ the viscous stress tensor for a homogeneous and isotropic Newtonian fluid,

$$\sigma_{ij} = \delta_{ij} \lambda_F \partial_k u_k + \mu_F (\partial_j u_i + \partial_i u_j), \tag{2.3}$$

with μ_F being the dynamic viscosity and λ_F the second viscosity coefficient. The total energy $\rho_F E$ is defined as

$$\rho_F E = \rho_F e + \frac{1}{2} \rho_F u_k u_k \quad \text{for } k = 1, 2, 3, \tag{2.4}$$

and the heat flux q_i is given by Fourier's law

$$q_i = \kappa \partial_i T. \tag{2.5}$$

We model air as a perfect gas with a specific heat ratio of $\gamma = c_p / c_v = 1.4$ and a constant molecular Prandtl number of $Pr = 0.72$. Static pressure p and temperature T are determined by the ideal-gas equation of state

$$p = (\gamma - 1) \rho_F e = \mathcal{R} \rho_F T, \tag{2.6}$$

where the specific gas constant is taken as $\mathcal{R} = 287.05 \text{ J(kg K)}^{-1}$.

The dynamic viscosity μ_F is considered a function of the static temperature T and modeled according to

$$\mu_F = \mu_\infty \sqrt{T / T_\infty}, \tag{2.7}$$

where μ_∞ is made case dependent to produce a desired Reynolds number. The second viscosity coefficient λ_F in equation (2.3) is taken as $\lambda_F = -2/3 \mu_F$ following Stokes hypothesis, which establishes σ_{ij} as purely deviatoric. Finally, the thermal conductivity κ is modeled as

$$\kappa = \frac{\gamma \mathcal{R}}{(\gamma - 1) Pr} \mu_F. \tag{2.8}$$

Solid

The solid domain is governed by the local form of the linear momentum balance, also known as Cauchy's first equation of motion, which in the reference (i.e., undeformed) configuration reads

$$\rho_{S;0} \frac{\partial \boldsymbol{d}}{\partial t^2} = \nabla_0 \cdot \boldsymbol{P} + \rho_{S;0} \boldsymbol{b} \quad \text{in } \Omega_S, \tag{2.9}$$

where $\boldsymbol{d}$ represents the vector of unknown displacements, $\rho_{S;0}$ is the material density of the solid, $\nabla_0 \cdot ()$ is the divergence operator, $\boldsymbol{P}$ is the first Piola-Kirchhoff stress tensor, and $\boldsymbol{b}$ denotes the external material body forces. The Cauchy stress tensor $\boldsymbol{T}$ is related to $\boldsymbol{P}$ via

$$\boldsymbol{T} = \frac{1}{J}\boldsymbol{P} \cdot \boldsymbol{F}^T, \tag{2.10}$$

where $\boldsymbol{F}$ is the deformation gradient tensor, which maps a line element in the reference configuration to the current configuration, and $J = \det(\boldsymbol{F})$ is the Jacobian of the mapping. Furthermore, and for later reference, the second Piola-Kirchhoff stress tensor $\boldsymbol{S}$ is defined as $\boldsymbol{S} = \boldsymbol{F}^{-1} \cdot \boldsymbol{P}$ and is symmetric, as opposed to $\boldsymbol{P}$.

The constitutive law used in this work is derived from the hyper-elastic Saint Venant-Kirchhoff material model. Its strain energy function W is defined as

$$W(\boldsymbol{E}) = \mu_S \boldsymbol{E} : \boldsymbol{E} + \frac{1}{2}\lambda_S (\mathrm{tr}(\boldsymbol{E}))^2, \tag{2.11}$$

where λ_S and μ_S are the first and second Lamé parameters and $\boldsymbol{E}$ is the Green-Lagrange strain tensor, i.e.,

$$\boldsymbol{E} = \frac{1}{2}(\boldsymbol{F}^T \cdot \boldsymbol{F} - \boldsymbol{I}). \tag{2.12}$$

The material response is then governed by

$$\boldsymbol{S} = \frac{\partial W}{\partial \boldsymbol{E}}, \tag{2.13}$$

which leads to the employed constitutive law

$$\boldsymbol{S} = \lambda_S (\mathrm{tr}(\boldsymbol{E}))\boldsymbol{I} + 2\mu_S \boldsymbol{E}. \tag{2.14}$$

Note that equation (2.14) is analogous to the constitutive relation in linear elasticity and does not reflect material non-linearities (i.e., stress is still linearly related to strain). However, $\boldsymbol{E}$ includes geometrical non-linearities and is insensitive to rotation, see equation (2.12).

The principle of virtual work is employed to re-write equation (2.9) in an integral form. This involves multiplication of the balance equation by the virtual displacement vector $\delta\boldsymbol{d}$ and integration over the structural subdomain, which upon some manipulation yields

$$\int_{\Omega_{S;0}} (\rho_{S;0}\ddot{\boldsymbol{d}} \cdot \delta\boldsymbol{d} + \boldsymbol{S} : \dot{\boldsymbol{E}} - \rho_{S;0}\boldsymbol{b} \cdot \delta\boldsymbol{d})\, dV_0 - \int_{\partial\Omega_{S;0}} \boldsymbol{p} \cdot \delta\boldsymbol{d}\, dA_0 - \delta W_S^{\Gamma} = 0, \tag{2.15}$$

where the divergence theorem is also applied. Note that all integrals are taken over the reference configuration, with dA_0 and dV_0 being the corresponding infinitesimal surface and volume elements. Additionally, $\dot{\boldsymbol{E}}$ indicates the variation of the Cauchy stress tensor and $\boldsymbol{p}$ denotes the Piola traction.

2.1.2. Numerical discretization

Fluid

The fluid domain is solved with the finite-volume solver INCA[2], which employs the adaptive local deconvolution method (ALDM) for implicit LES of the governing equations [71]. ALDM is a nonlinear solution-adaptive finite-volume method that exploits the discretization of the hyperbolic flux $\boldsymbol{C} + \boldsymbol{H}$ to introduce a physically consistent sub-grid scale turbulence model. Since unresolved turbulence and shock waves require fundamentally different modeling, ALDM relies on a shock sensor to control model parameters. This guarantees the accurate propagation of smooth waves and turbulence without excessive numerical dissipation while providing essentially non-oscillatory solutions at strong discontinuities [71]. Gradients in the viscous flux tensor $\boldsymbol{D}$ are approximated by linear second-order schemes and the third-order total variation diminishing Runge–Kutta scheme of Gottlieb and Shu [72] is employed for time integration. The reader is referred to appendix A for an expanded overview of the ALDM framework and to Hickel *et al.* [71] for implementation details and validation results.

The fluid solver operates on block structured, picewise Cartesian grids, and the cut-cell immersed boundary method (IBM) of Örley *et al.* [73] and Pasquariello *et al.* [74] is employed to accurately represent an arbitrary solid geometry in the Cartesian fluid domain. The discrete surface of the solid comprises several structural interface elements, see section 2.1.2. Each structural element is triangulated and the resulting set of interface triangles Γ_{tri} serves as input to the IBM algorithm. Figure 2.1 shows a Cartesian computational cell $\Omega_{i,j,k}$ that is intersected by the triangulated moving surface, which for illustration purposes includes four different interface triangles. A fluid cell that is intersected by at least one interface triangle is referred to as a cut-cell, whereas an interface triangle segment within the cut-cell is a cut-element $\Gamma_{ele} = \Gamma_{tri} \cap \Omega_{i,j,k}$. For cut-cells, the integral form of equation (2.1) is then evaluated over the fraction of the cell that belongs to the fluid domain Ω_F,

$$\int_{t^n}^{t^{n+1}} \int_{\Omega_{i,j,k} \cap \Omega_F} \partial_t \boldsymbol{U} \, dV \, dt + \int_{t^n}^{t^{n+1}} \int_{\partial(\Omega_{i,j,k} \cap \Omega_F)} \boldsymbol{\mathcal{F}}(\boldsymbol{U}) \cdot \boldsymbol{n} \, dS \, dt = 0, \tag{2.16}$$

and over the time step $\Delta t = t^{n+1} - t^n$. The total flux is here denoted $\boldsymbol{\mathcal{F}}(\boldsymbol{U})$, and dS, dV indicate the infinitesimal surface and volume elements. The area integral, which results from the application of the divergence theorem, is taken over the wetted surface of the computational cell, i.e., $\partial(\Omega_{i,j,k} \cap \Omega_F)$. Applying a volume average of the state vector $\boldsymbol{U}$,

$$\overline{\boldsymbol{U}}_{i,j,k} = \frac{1}{\alpha_{i,j,k} V_{i,j,k}} \int_{\Omega_{i,j,k} \cap \Omega_F} \boldsymbol{U} dx dy dz, \tag{2.17}$$

and considering a forward Euler time integration scheme (for demonstration pur-

[2]For additional details, visit https://www.inca-cfd.com

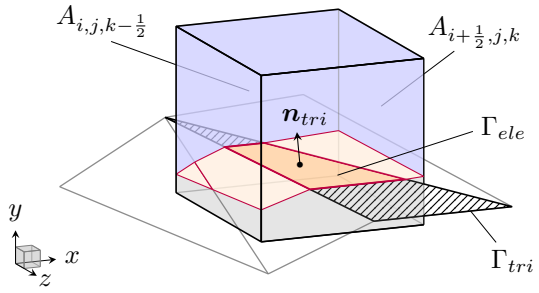

Figure 2.1: Schematics of a computational cell intersected by the triangulated moving surface (here shown with four interface triangles).

poses) yield the following discrete form of equation (2.16)

$$\begin{aligned}\alpha^{n+1}_{i,j,k}\overline{\boldsymbol{U}}^{n+1}_{i,j,k} = \alpha^{n}_{i,j,k}\overline{\boldsymbol{U}}^{n}_{i,j,k} \\ + \frac{\Delta t}{\Delta x_i}[A^n_{i-\frac{1}{2},j,k}\boldsymbol{\mathcal{F}}^{(1)}_{i-\frac{1}{2},j,k} - A^n_{i+\frac{1}{2},j,k}\boldsymbol{\mathcal{F}}^{(1)}_{i+\frac{1}{2},j,k}] \\ + \frac{\Delta t}{\Delta y_j}[A^n_{i,j-\frac{1}{2},k}\boldsymbol{\mathcal{F}}^{(2)}_{i,j-\frac{1}{2},k} - A^n_{i,j+\frac{1}{2},k}\boldsymbol{\mathcal{F}}^{(2)}_{i,j+\frac{1}{2},k}] \\ + \frac{\Delta t}{\Delta z_k}[A^n_{i,j,k-\frac{1}{2}}\boldsymbol{\mathcal{F}}^{(3)}_{i,j,k-\frac{1}{2}} - A^n_{i,j,k+\frac{1}{2}}\boldsymbol{\mathcal{F}}^{(3)}_{i,j,k+\frac{1}{2}}] \\ + \frac{\Delta t}{V_{i,j,k}}\boldsymbol{\chi}_{i,j,k},\end{aligned} \tag{2.18}$$

where $\alpha_{i,j,k}$ is the fluid volume fraction of the cut-cell, $V_{i,j,k} = \Delta x_i \Delta y_j \Delta z_k$ the total cell volume, A the effective fluid wetted cell-face aperture (indicated in blue in figure 2.1) and $\boldsymbol{\mathcal{F}}^{(i)}$ the faced-averaged numerical fluxes across the regular cell faces. The interface exchange term $\boldsymbol{\chi}_{i,j,k} = \sum_{ele} \boldsymbol{\chi}_{ele}$ is added to account for the moving surface $\Gamma_{i,j,k} = \sum_{ele} \Gamma_{ele}$ within the cut-cell, where $\sum_{ele}$ indicates the sum over all cut-elements associated with $\Omega_{i,j,k}$. The cut-element based interface exchange term $\boldsymbol{\chi}_{ele}$ accounts for pressure and viscous stresses, interface work and heat transfer through an individual cut-element. The reader is referred to Örley *et al.* [73] and Pasquariello *et al.* [74] for additional details on the method.

Solid

Equation (2.15) can be seen as the balance of virtual work, which also includes the work at the FSI interface δW^{Γ}_{S}. This equation forms the basis for the finite-element method (FEM) in solid mechanics, which is used for the spatial discretization . The solid domain is composed of n^e elements Ω^e_S with consistent basis functions for representing the displacement field. By assembling the contribution of all elements, the semi-discrete form of equation (2.15) is

$$\boldsymbol{M}\ddot{\boldsymbol{d}} + \boldsymbol{f}_{S;int}(\boldsymbol{d}) - \boldsymbol{f}_{S;ext} - \boldsymbol{f}^{\Gamma}_{S} = \boldsymbol{0}, \tag{2.19}$$

where $\boldsymbol{M}$ is the mass matrix, $\boldsymbol{d}$ and $\ddot{\boldsymbol{d}}$ the discrete vectors of displacements and accelerations, and $\boldsymbol{f}_{S;int}$, $\boldsymbol{f}_{S;ext}$ and $\boldsymbol{f}_S^\Gamma$ the internal, external and interface force vectors.

Equation (2.19) is solved with the finite-element solver CalculiX[3] which uses the Hilbert-Hugues-Taylor α-method [75] for time discretization. This method is an extension of the Newmark method [76] and allows for some degree of numerical dissipation without degrading accuracy. The parameter α, which controls the added numerical dissipation, is here set to -0.3, and the resulting implicit time stepping is solved using a Newton-Raphson method.

The flexible panel in the coupled STBLI simulation is discretized with 20-node hexahedral elements with three degrees of freedom per node (corresponding to the nodal translations in x, y and z). The displacement field within each element is represented with quadratic shape functions. For additional details on the employed solid mesh, see chapter 7.

In order to reduce the computational cost, the adaptive reduced-order model (AROM) of Thari *et al.* [70] is also employed in FSI simulations. The method relies on the linearization of equation (2.19) around a deformed reference state, upon which the number of unknowns is decreased using the mode superposition method [77] with a reduced number of modes.

Consider the Taylor expansion of equation (2.19) around a reference state $\boldsymbol{d}_{ref}$, which can be either the initial condition or an instantaneous solution at the time of the model re-calibration,

$$\boldsymbol{M}\ddot{\boldsymbol{d}}_{ref} + \boldsymbol{f}_{S;int}(\boldsymbol{d}_{ref}) - \boldsymbol{f}_{S;ext} - \boldsymbol{f}_S^\Gamma + \boldsymbol{M}(\ddot{\boldsymbol{d}} - \ddot{\boldsymbol{d}}_{ref}) + \boldsymbol{K}(\boldsymbol{d} - \boldsymbol{d}_{ref}) = \boldsymbol{0}, \quad (2.20)$$

where $\boldsymbol{K}(\boldsymbol{d}_{ref}) = \partial_{\boldsymbol{d}} \boldsymbol{f}_{S;int}|_{\boldsymbol{d}_{ref}}$. The eigenmodes of the structure are obtained by solving the following eigenvalue problem

$$\boldsymbol{K}(\boldsymbol{d}_{ref})\boldsymbol{\Phi} = \boldsymbol{M}\boldsymbol{\Phi}\boldsymbol{\Omega}^{\boldsymbol{2}}, \quad (2.21)$$

where the columns of $\boldsymbol{\Phi} = [\boldsymbol{\phi}_1, \ldots, \boldsymbol{\phi}_m]$ are the orthonormalized (with respect to $\boldsymbol{M}$) eigenvectors, i.e., natural vibration modes, and $\boldsymbol{\Omega} = \mathrm{diag}(\omega_1, \ldots, \omega_m)$ are the corresponding eigenvalues, i.e., natural vibration frequencies in ascending order. For reduced-order modeling, equation (2.20) is projected onto the modal space spanned by the first N_{eig} eigenmodes, where N_{eig} is user-defined. This drastically reduces the number of unknowns, as the system is now rank N_{eig} in modal space. In order to improve the representation of the load vector in modal space, the Modal Truncation Augmentation (MTA) method is additionally employed [78] which increases the rank of the reduced system by 1. Time integration in modal space is then performed with the Newmark method [76].

Note that constructing and updating the above-described AROM is computationally expensive, whereas applying it is cheap. Therefore, the model is re-calibrated when the solution deviates significantly from the reference configuration, i.e., when the maximum absolute deflection δd_{max} exceeds a user-defined threshold ϵ. This

[3]For additional details, visit http://www.calculix.de

threshold thus provides a compromise between simplicity and accuracy of the solution. The limit case of $\epsilon = 0$ corresponds to the full non-linear FEM solution, since the projection onto the modal basis is lossless thanks to the MTA (provided that the same time integration scheme is used). For the present simulations, N_{eig} is set to 10 modes and ϵ to 25% of the panel thickness.

Fluid-structure coupling

A loosely coupled serial staggered scheme is employed to advance the FSI system from t^n to $t^{n+1} = t^n + \Delta t$. The scheme follows the classical Dirichlet-Neumann partitioning, where the fluid (Dirichlet partition) inherits displacements from the structure and the structure (Neumann partition) is loaded by the fluid pressure and viscous stresses:

1. At time t^n, the immersed boundary in the fluid domain is updated with the structural displacements $\boldsymbol{d}^{\Gamma;n}$ and velocities $\dot{\boldsymbol{d}}^{\Gamma;n}$.

2. The fluid domain is advanced in time, from t^n to t^{n+1}. Interface exchange terms are computed from known structural quantities at time t^n.

3. Fluid interface tractions $\boldsymbol{\sigma}_F^{\Gamma;n+1} \cdot \boldsymbol{n}^{\Gamma;n+1}$ are then transferred to the structural interface elements. For details on the load an motion transfer between the non-matching interface, the reader is referred to Thari et al. [70].

4. The solid domain is advanced in time, from t^n to t^{n+1}, with the new fluid tractions as additional Neumann boundary condition.

5. Proceed to the next time step.

The time-step size Δt is determined by the Courant-Friedrichs-Lewy (CFL) stability condition of the Runge-Kutta method used for the fluid solution. We use CFL $\leqslant 1$ everywhere, which guarantees stability and accuracy of the employed methods.

2.2. Experimental method

This section provides infromation about the experimental facility and main flow diagnostics tools employed in the study of shock-shock interactions with variable inflow Mach number reported in chapter 4.

2.2.1. Experimental facility

All experiments were conducted in the transonic-supersonic blow-down wind tunnel (TST-27) of the high-speed aerodynamics laboratory at TU Delft. The facility has a rectangular test section of 280×272 mm and is equipped with a flexible convergent-divergent nozzle that allows the Mach number to be continuously varied during testing. For the current experiments, the total pressure in the settling chamber ranged from 4 to 6 bar, depending on the start-up requirements for each model geometry. The total temperature was approximately 280 K in all cases.

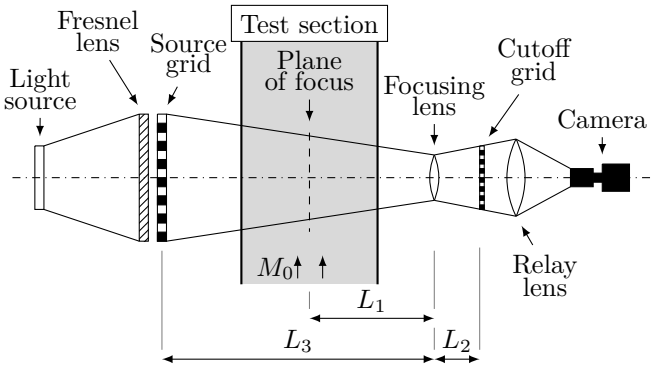

Figure 2.2: Schematic of the focusing schlieren setup.

2.2.2. Flow measurement techniques

The time evolution of the free-stream Mach number was obtained from total and static pressure measurements assuming an isentropic expansion. A pressure sensor located in the settling chamber provided the total pressure readings, while two sensors placed on the side walls of the test section, sufficiently upstream of the model, ensured a precise static pressure measurement. All pressure sensor data was recorded at a sampling rate of 5 kHz.

Schlieren visualization was used as the main flow visualization tool. A continuous white light beam was collimated with a parabolic mirror (focal length $f = 4000$ mm) to create a parallel beam that traversed the test section. This beam was converged using a second parabolic mirror on a vertical knife edge and then recorded with a digital camera. Due to equipment availability, a LaVision High Speed 4M camera at a rate of 125 Hz was used during testing of certain wedge arrangements (i.e., $\vartheta_{2n} = 10°$, 17° and 19°, see chapter 4) whereas a LaVision Imager sCMOS at a frame rate of 50 Hz was used for the remaining geometries. Both systems are essentially similar in optical performance and provided a spatial resolution of approximately 0.04 mm. All schlieren recordings were synchronized with the pressure readings so that a value of the free-stream Mach number could be assigned to every image.

Conventional schlieren visualizations have an infinite depth of focus and therefore show the integrated effect of all density gradients present along the optical path, hence, in the spanwise direction of the test section. This results in undesirable features such as three-dimensional edge effects near the side walls obscuring the target flow features. In order to assess the impact of these effects and to facilitate the correct interpretation of the schlieren data, we additionally set up a focusing schlieren system, which provides sharp images of its focal plane, and examined multiple planes along the optical path. A schematic of the focusing schlieren setup is shown in figure 2.2 with all relevant parameters summarized in table 2.1. The reported values follow from the parametric analysis conducted by Santiago Patterson [79] and the reader is referred to Weinstein [80] for additional details on the particular focusing schlieren

Table 2.1: Summary of relevant parameters of the focusing schlieren setup.

Symbol in figure 2.2	Dimension [mm]	Definition
–	83	Lens aperture
–	250	Focal length of focusing lens
L_1	550	Distance from plane of focus to focusing lens
L_2	323	Distance from focusing lens to cutoff grid
L_3	1100	Distance from source grid to focusing lens
–	1.6	Width of dark strips on the source grid
–	250	Focal length of the relay lens
–	26	Depth of focus (unsharp)

setup used. A relay lens was added to the setup in order to adapt the image size to the camera sensor. The camera used to record the focusing schlieren images was a LaVision Imager sCMOS operated at a frame rate of 50 Hz.

PART ONE

Inviscid shock-shock interactions

3

Response to shock perturbations

In this first part of the thesis, which comprises two chapters, we explore the response of asymmetric shock interactions to external perturbations. The present chapter initiates this exploration by examining different perturbation modes of the lower incident shock with numerical simulations. The investigated perturbation modes aim to emulate the dynamics of the separation shock in STBLI flows, with perturbation amplitudes sufficiently large to bring the starting shock interaction (RI or MI) outside its steady-state stability boundary. The response of the shock system to such perturbations is then characterized in detail, with a focus on the bi-directional RI⇄MI transition and the underlying mechanism by which the MI is found to be more robust than the RI. Gas dynamics concepts relevant to calculating stability boundaries are also presented in this chapter.

3.1. Introduction

As already introduced in chapter 1, SSIs between shock waves of opposite families can be classified as RIs or MIs. The former, which is depicted again in figure 3.1(a), involves five discontinuities: two incident shock waves C_1 and C_2, two reflected shock waves C_3 and C_4, and a slipline s. Following the work of Edney [81], the RI is classified as a type I interference. The compatibility condition for this interaction pattern involves equal static pressure and flow direction in regions (3) and (4), whilst other flow properties differ (only in the particular case of a symmetric interaction both states (3) and (4) are identical and no slipline exists). In the event of a MI, in turn, incident shock waves C_1 and C_2 no longer intersect due to a quasi-normal shock segment appearing in the flow. This wave pattern is classified as a type II interference [81]. Schematics of the MI are also included in figure 3.1(b), in which the quasi-normal shock segment, commonly known as the Mach stem, is

The content of this chapter has been published as: L. Laguarda, S. Hickel, F. F. J. Schrijer and B. W. van Oudheusden. Dynamics of unsteady asymmetric shock interactions, *J. Fluid Mech.* **888**, 2020.

labelled as m. Its presence entails two sliplines s_1 and s_2 that enclose the non-homogeneous region (5) of subsonic flow. A necessary stability requirement is that the slipline pair forms a virtual convergent duct, which allows the subsonic flow in (5) to accelerate. However, this requirement is not sufficient: the presence of (at least) one Prandtl-Meyer expansion fan (PME) is paramount to establish a virtual throat and a divergent duct segment between the slipline pair to enable the enclosed flow to reach supersonic velocities. The resulting Mach stem height is such that all the mass flow through it passes through the virtual slipline throat at sonic conditions. As opposed to the RI, the Mach stem height as well as the spatial extent of the MI are thus linked to a characteristic length scale that relates the incident shock foot locations with the origin of the PME(s) [82–85].

It is common practice to use shock polar theory to establish steady-state stability boundaries between the RI and the MI in the parameter space [86]. A typical shock polar representation in the pressure-deflection plane is included in figure 3.1(c) for free-stream Mach number $M_\infty = 3.0$, specific heat ratio $\gamma = 1.4$ and upper flow deflection $\vartheta_1 = 25°$. Here, the *detachment* condition ϑ_2^d denotes the maximum flow deflection imposed by C_2 for which the polars r_1 and r_2 intersect (in this limit case, they are tangent). Beyond this value, there is no longer a RI configuration capable of providing compatible states (3) and (4), and so the MI materializes. On the contrary, the *von Neumann* criterion ϑ_2^n defines a lower flow deflection for which the three polars, i, r_1 and r_2, intersect at one location. Further reducing ϑ_2 prevents the slipline pair s_1-s_2 from being convergent, which impedes the formation of a stable MI and thus the RI solution prevails thereafter. It is interesting to note that at *von Neumann* both RI and MI provide identical flow states (3) and (4) and therefore they would be in mechanical equilibrium at this condition. Another feature in figure 3.1(c) is the occurrence of a dual solution domain (DSD), shaded in light gray and spanning between $\vartheta_2^n \leqslant \vartheta_2 \leqslant \vartheta_2^d$, for which the two solutions, RI and MI, are both physically possible. As first hypothesized by Hornung *et al.* [87], this allows for a potential flow hysteresis, that is, the solution that materializes and the RI$\rightleftarrows$MI transition conditions can depend on the flow history.

Asymmetric SSIs are present in a wide range of high speed aerodynamics applications [4, 86]. Supersonic inlets are a clear example, comprising a set of oblique shock waves that compress the flow to suitable pressures for combustion, see figure 1.2. Avoiding RI$\rightarrow$MI transition is of paramount importance due to the associated entropy rise, total pressure loss and high risk of engine unstart, see also figure 1.6. Even though steady flow theory provides useful insight on the shock pattern developing inside the inlet, it fails at predicting the premature RI$\rightarrow$MI transition observed when disturbances are present in the free-stream flow [82, 88, 89] eventually preventing the occurrence of any flow hysteresis. On these grounds, only low-noise wind tunnel conditions [90] and disturbance-free numerical computations [91–94] permitted the penetration of the RI inside the steady-state DSD in agreement with theoretical predictions.

A specific class of flow phenomena involving asymmetric SSIs is the STBLI flow, which dominates the aerodynamic environment of supersonic inlets and other high-speed flow devices as discussed in chapter 1. If the adverse pressure gradient imposed

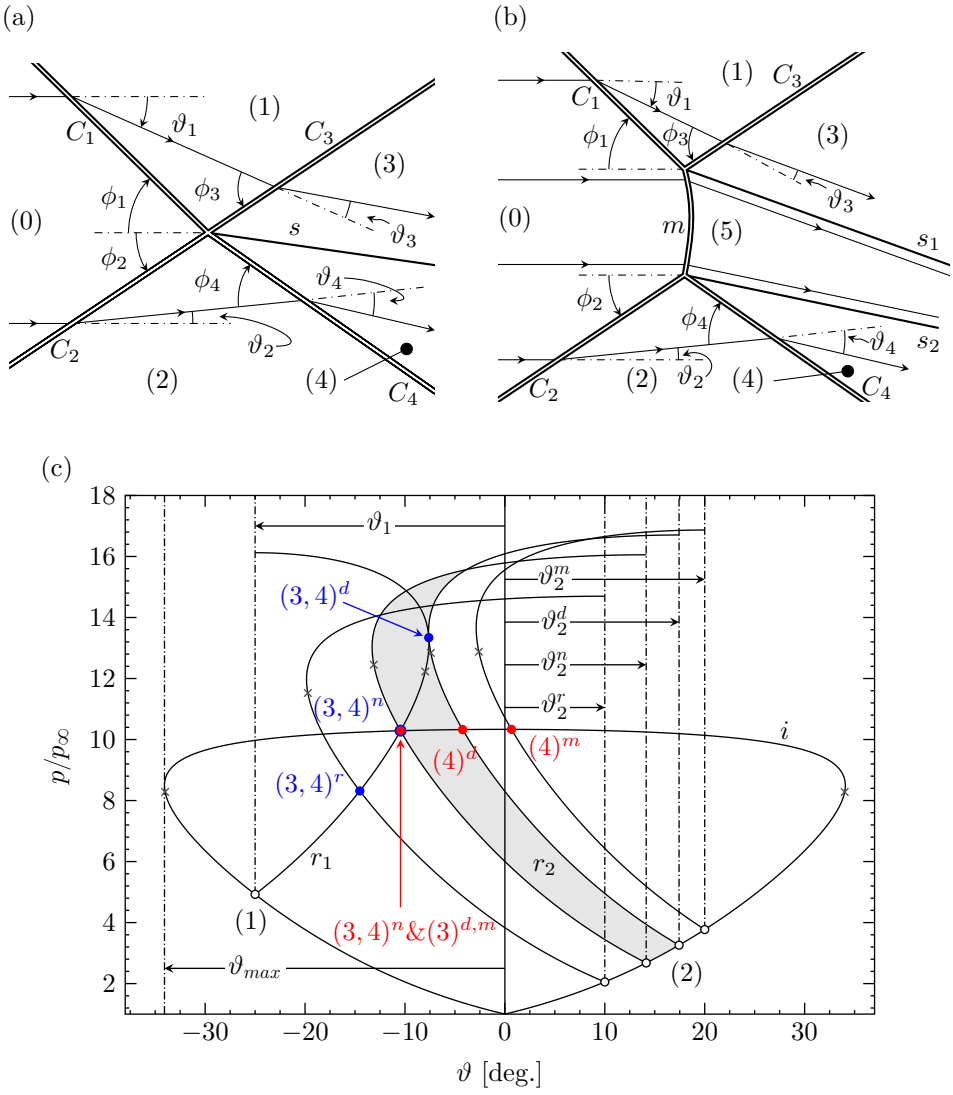

Figure 3.1: Schematic of (a) the regular interaction, (b) the Mach interaction, and shock polar representation (c) in the pressure-deflection plane for $M_\infty = 3$. ϑ_2^r and ϑ_2^m indicate a general solution outside the dual-solution domain for the regular and the Mach interaction, whilst flow states within the dual-solution domain are highlighted in blue for the former and red for the latter. Sonic conditions in (c) are labeled with $\times$.

by the shock is strong enough to cause boundary layer separation, the location and strength of the separation shock becomes highly unsteady and so does its interaction with the incident shock [4, 95]. The work of Matheis and Hickel [46], which was already introduced in section 1.2, provides evidence of the potential implications of such unsteadiness, which can actually cause premature RI→MI transition and

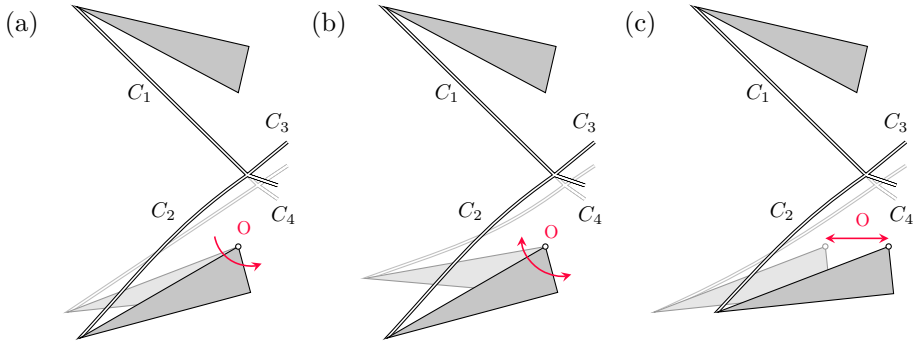

Figure 3.2: Unsteady effects on the incident shock C_2 for the lower wedge excitation mechanisms considered: (a) pitch, (b) periodic deflection oscillation, and (c) periodic streamwise oscillation.

sustain the MI pattern for mean flow conditions beyond its steady-state stability boundary. Previous fundamental research on disturbed shock systems, however, has totally disregarded this practically relevant scenario and has mainly focused on the effect of impulsive disturbances on symmetric SSIs - see section 1.2. An asymmetric shock structure being perturbed in a continuous manner, on the other hand, is much more representative for unsteady internal flows and should therefore be carefully examined.

Motivated by the aforementioned, we thus conduct a set of inviscid computations with the purpose of providing insight on the dynamics of unsteady asymmetric shock interactions affected by a continuous excitation. Two wedges are used to asymmetrically deflect the free-stream flow and introduce the incident shock waves and centered PMEs in the computational domain. After a steady state is reached, the shock system is excited according to three different excitation scenarios depicted respectively in figures 3.2(a–c): pitching of the lower wedge across the steady-state DSD, a periodic (sinusoidal) oscillation of the lower wedge deflection around a mean value both within and outside of the steady-state DSD, and a periodic (sinusoidal) streamwise oscillation of the lower wedge without pitch. These excitation modes, specially the latter two, are aimed at emulating the dynamics of the separation shock in STBLI flows. The response of the system under such forcing is analyzed with a strong focus on the bi-directional RI$\rightleftarrows$MI transition process and the underlying mechanism by which the MI is found to be more robust against periodic perturbations than the RI is discussed. All numerical simulations presented in this chapter are conducted at $M_\infty = 3$ and $\vartheta_1 = 25°$, which are hereafter referred to as the baseline conditions.

3.2. Computational setup

3.2.1. Problem definition

A sketch of the investigated computational domain is given in figure 3.3. We consider two wedges of equal hypotenuse w asymmetrically deflecting the free-stream flow at Mach $M_\infty = 3$ and generating a pair of intersecting waves C_1, C_2 and cen-

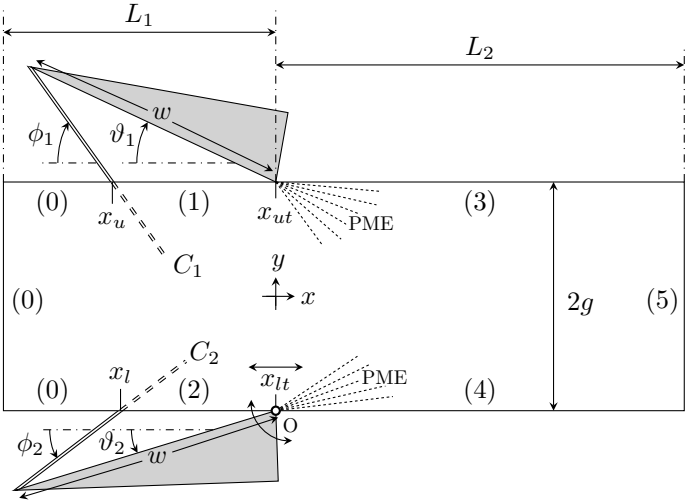

Figure 3.3: Schematic diagram of the computational domain.

tered PMEs. The wedges are not included in the computational domain, however. Instead, we account for their effect through time dependent boundary conditions satisfying the Rankine-Hugoniot relations across the incident shocks C_1 $\{(0) \rightarrow (1)\}$ and C_2 $\{(0) \rightarrow (2)\}$, and Prandtl-Meyer expansion theory for the PMEs in (3) and (4). Note that since each trailing edge, and thus the PME origins, is placed on top of an horizontal domain boundary, states (3) and (4) relate to flow conditions along horizontal expansion rays. Concerning shock generator geometry, one characteristic length scale is the wedge hypotenuse w, which is set to $w = 1$ for all computations. However, the resulting wave system is most sensitive to the geometrical ratio of vertical wedge separation distance ($2g$) to wedge hypotenuse, $2g/w$. This parameter determines whether or not reflected shocks C_3 and C_4 impinge on the wedges, and thus potentially leading to domain unstart, but also imposes a relation between incident shock foot locations and the origin of the centered PMEs. As already mentioned, this influences the spatial extent and the steady-state Mach stem height of the MI configuration. Unless otherwise stated, $2g/w$ is set to 0.84 as commonly used in literature [48, 94]. Rotation and oscillation of the lower wedge deflection occur around point O as indicated in figures 3.2(a–c), and, except for the streamwise oscillation, both wedge trailing edges are positioned at the same x location ($x_{ut} = x_{lt}$ in figure 3.3). Lastly, the upstream length of the domain, $L_1 = w$, establishes free-stream (0) conditions at the left boundary throughout the computations, and $L_2 = 1.4w$ ensures that the flow at the outlet (5) is always supersonic.

3.2.2. Numerical method

For the present analysis, we solve the two-dimensional unsteady Euler equations, meaning that the viscous terms in equation 2.1 as well as those terms associated with the third dimension are dropped. While the finite-volume solver INCA is still em-

ployed for the calculations, the ALDM is no longer used. Instead, fluxes computed at the cell centers are simply projected into the right eigenvector space where a local Lax-Friedrichs flux vector splitting and a third-order weighted essentially non-oscillatory (WENO) reconstruction of the flux through the cell face is performed, see Shu [96]. The resulting fluxes are then projected back to the conserved quantities prior to the time integration step, which is still performed with a third-order explicit Runge-Kutta scheme. We also note that the system of equations is non-dimensionalized using the free-stream velocity u_∞ and the wedge hypotenuse w, which combined define the characteristic time scale w/u_∞ of the problem.

3.2.3. Post-processing

For rapid excitations, unsteady effects manifest and the instantaneous lower wedge deflection is no longer representative of the flow deflection ϑ_2 across C_2 near the interaction point (i.e, C_2 is curved, see figure 3.2). Thus, to properly characterize transition it is imperative to measure quantities of interest, i.e, lower flow deflection $\vartheta_2(t)$, static pressure rise $p/p_\infty(t)$ and entropy jump $\Delta s(t)$, at the interaction location. A custom post-processing algorithm was developed for this purpose. Incident shock waves C_1 and C_2 are tracked by searching for the local maximum of the density gradient magnitude $\sqrt{(\partial\rho/\partial x)^2 + (\partial\rho/\partial y)^2}$ along each row of the grid starting from the left. Depending on whether the shock topology is a MI, the Mach stem is formed. In that case, a marked entropy jump occurs, see figure 3.9(a), accompanied by a clear formation of a minimum and a maximum of vorticity at the upper and lower triple point locations, respectively. Sub-grid resolution for the location of vorticity extrema is achieved by local parabolic reconstruction. The vertical distance between the resulting points thus defines the instantaneous Mach stem height h_{ms}, see figure 3.9(b). Other quantities of interest are determined in their vicinity, e.g, instantaneous ϑ_2 measurements are taken at a distance of $0.01w$ in the negative y-direction from the lower triple point, whilst the pressure rise across the wave system p/p_∞ is recorded $0.01w$ downstream of both triple points, respectively. The instantaneous entropy jump Δs is defined as $s_i - s_\infty$ where s_i is measured at $0.01w$ downstream of the local Mach stem (over the fictional horizontal line that bisects both triple points) and s_∞ is the free-stream value. Magnitudes are averaged with neighboring cells to avoid oscillations. In the case of a RI, the entropy jump is small and C_1 and C_2 intersect. This is considered to be the interaction location, and instantaneous ϑ_2, p/p_∞ and Δs measurements follow in a similar fashion as explained for the MI case.

3.2.4. Grid sensitivity

The flow is discretized on a uniform grid with spacing h in both spatial directions. In order to assess the impact of the grid size on the shock dynamics and the corresponding bi-directional transition process, a grid convergence analysis was performed. For the baseline conditions, both an initial RI and MI were independently considered by setting $\vartheta_{2,0} = 12^\circ$ and $\vartheta_{2,0} = 19^\circ$ respectively. After the steady state was reached, transition to the opposite shock pattern was enforced by linearly changing the lower

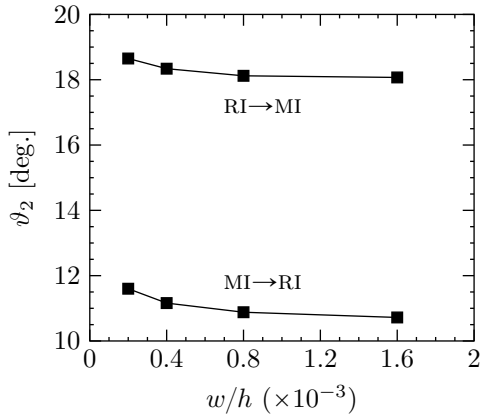

Figure 3.4: Results of the grid sensitivity study.

wedge deflection at a constant rate, i.e, increased to enforce RI→MI transition and decreased in the opposite case. Similar as in Felthun and Skews [53], the rotational velocity of the wedge is defined in terms of the Mach number of the wedge tip M_{tip} divided by the free-stream value M_∞, which is equivalent to the ratio of the wedge tip velocity to the free-stream velocity. For the grid convergence analysis, M_{tip}/M_∞ was set to 0.01. The instantaneous lower flow deflection in the vicinity of the interaction was recorded at transition for four different grid spacings: $w/h = 200, 400, 800$ and 1600, with the corresponding results shown in figure 3.4. As observed, a clear flow deflection convergence is obtained for $w/h = 1600$ regardless of the direction of transition so this value was used for all further computations.

3.3. Results and discussion

3.3.1. Pitch of lower wedge

The first excitation mechanism corresponds to the pitching of the lower wedge across the steady-state DSD. For the baseline conditions ($M_\infty = 3$ and $\vartheta_1 = 25°$), the steady-state DSD extends from the *von Neumann* condition $\vartheta_2^n = 14.14°$ until *detachment* at $\vartheta_2^d = 17.43°$, see figure 3.1(c). Both RI and MI are considered as the starting shock topology by setting the initial lower wedge deflection to $\vartheta_{2,0} = 12°$ for the former and $\vartheta_{2,0} = 19°$ for the latter. After reaching a converged steady state solution, the lower wedge deflection is changed at a linear rate to enforce transition, see section 3.2.4. Rotational velocities corresponding to $M_{tip}/M_\infty = 0.1, 0.01, 0.001$ and 0.0001 are considered. A summary of relevant parameters can be found in table 3.1.

The post-processing method explained in section 3.2.3 proved to be robust and accurate at tracking the evolution of the quantities of interest over the integration time. For every rotational velocity considered, ϑ_2 at transition was recorded when the Mach stem height became larger than zero for RI→MI transition, or became

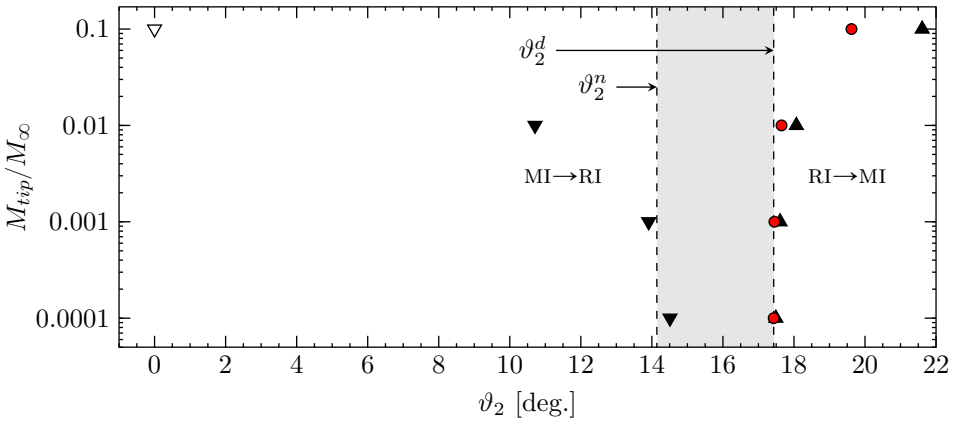

Figure 3.5: Lower flow deflection ϑ_2 at transition as a function of the rotational velocity of the lower wedge: (▾, ▽) numerical data for MI→RI transition, (▲) numerical data for RI→MI transition, (●) RI→MI transition predictions based on shock polar theory evaluated in the (moving) C_2 frame of reference, and (ϑ_2^n) steady-state *von Neumann* and (ϑ_2^d) *detachment* conditions with corresponding DSD shaded in grey. Numerical data was obtained for $2g/w = 0.84$. The flow deflection for the fastest MI→RI transition is labelled with an empty triangle (▽) because the Mach stem was still present when the lower flow deflection at the interaction location was $\vartheta_2 = 0°$.

equal to zero for MI→RI. Results are included in figure 3.5 as up-pointing and down-pointing triangles respectively. As expected, unsteady effects become important for large rotational velocities, meaning that ϑ_2 at transition differs significantly from predictions based on steady flow assumptions. Under these conditions, the MI can penetrate far into the RI domain. As the magnitude of the rotational velocity decreases, however, unsteady effects progressively vanish and the value of ϑ_2 at transition approaches a constant. For RI→MI transition, see up-pointing triangles in figure 3.5, this value is clearly the steady-state theoretical *detachment* boundary ϑ_2^d associated to the baseline conditions. However, ϑ_2 at transition does not approach the theoretical *von Neumann* deflection ϑ_2^n in the MI→RI transition case, as shown by the down-pointing triangles in the same figure. Instead, the data point corresponding to the slowest case falls about 0.4° inside the DSD. We believe this could be a geometry effect related to the selected value of $2g/w$, which imposes a limitation on the minimum ϑ_2 for which a MI is stable. As mentioned, a necessary stability requirement is that the mass flow through the Mach stem should also pass through the virtual throat formed by both slip-lines (s_1 and s_2 in figure 3.1(b)) at sonic conditions. If for a particular wedge arrangement this is not possible, the system response is either a constantly increasing Mach stem until unstart or constantly decreasing until transition to RI. The impelling cause that drives towards one or the other still remains an open question; in our computations the latter occurs. In order to further explore the influence of the geometry parameter $2g/w$, two additional MI→RI transitions at $M_{tip}/M_\infty = 0.0001$ with $2g/w$ ratios of 1.05 and 0.63 were simulated (that is $0.84 \pm 25\%$, see cases P09 and P10 in table 3.1). The results show a shift in the measured ϑ_2 at transition from 14.51° to 14.60° and

Table 3.1: Summary of relevant parameters for the pitch analysis: $\vartheta_{2,0}$ corresponds to the wedge deflection in the initial steady-state; $2g/w$ is the ratio of vertical trailing edge distance to wedge hypotenuse (see figure 3.3); M_{tip}/M_∞ relates the wedge tip Mach number to the free-stream value; ϑ_2^t and ϕ_2^t the measured lower flow deflection and C_2 incidence at transition; $(dh_{ms}/dt)/u_\infty$ the Mach stem characteristic growth rate; and $\vartheta_{2,c}^d$ is the corrected *detachment* condition given by the shock polar analysis in the C_2 (moving) frame of reference. All angles are expressed in degrees.

Case	$\vartheta_{2,0}$	$2g/w$	$\frac{M_{tip}}{M_\infty}$	Direction	ϑ_2^t	ϕ_2^t	$\frac{1}{u_\infty}\frac{dh_{ms}}{dt}$	$\vartheta_{2,c}^d$
P01	12.0	0.84	10^{-1}	RI→MI	21.62	36.16	0.120	19.65
P02	12.0	0.84	10^{-2}	RI→MI	18.07	35.28	0.046	17.65
P03	12.0	0.84	10^{-3}	RI→MI	17.61	35.01	0.035	17.45
P04	12.0	0.84	10^{-4}	RI→MI	17.49	34.90	0.035	17.43
P05	19.0	0.84	10^{-1}	MI→RI	0	-	0.126	-
P06	19.0	0.84	10^{-2}	MI→RI	10.72	28.11	0.066	-
P07	19.0	0.84	10^{-3}	MI→RI	13.91	31.14	0.031	-
P08	19.0	0.84	10^{-4}	MI→RI	14.51	31.74	0.030	-
P09	19.0	1.05	10^{-4}	MI→RI	14.60	31.83	0.025	-
P10	17.0	0.63	10^{-4}	MI→RI	14.45	31.67	0.023	-

14.45° respectively. In line with this finding, relevant geometry effects have been also reported in the recent work of Grossman and Bruce [97] on STBLI at $M_\infty = 2.0$.

We define the characteristic velocity scale associated to the RI→MI transition process as the maximum Mach stem growth rate, $(dh_{ms}/dt)/u_\infty$, occurring when the MI emerges from the interaction location. In a similar fashion as for the transitional ϑ_2, the Mach stem growth becomes independent of the wedge motion as M_t/M_∞ decreases, converging to a constant non-zero magnitude (see table 3.1). This highlights once more the inherent transient character of the transition process. The duration of such growth is also affected by the selected value of $2g/w$ as this ratio influences the target steady-state Mach stem height. This is illustrated in figure 3.6(a) where the evolution of the Mach stem height with respect to the measured lower flow deflection ϑ_2 for the slowest RI→MI case, represented by a solid line and labelled as P04 in table 3.1, shows an abrupt change in trend in the vicinity of point d. This occurrence segregates the transient process into a segment mostly related to the RI→MI transition and a subsequent segment related to the quasi-steady evolution of the MI due to the progressive wedge motion. For larger rotational velocities, as the wedge-motion velocity scale (characterized by M_{tip}/M_∞) becomes of the order of the characteristic Mach stem growth rate $(dh_{ms}/dt)/u_\infty$, this change in trend becomes less abrupt. Another characteristic feature associated to the RI→MI transition is the fact that the free-stream Mach number felt by the Mach stem temporarily increases due to its relative motion towards the free-stream flow. This causes an instantaneous overshoot in the time evolution of the entropy rise across the shock system, see figure 3.9(a), that accentuates for fast rotations.

To illustrate the overall flow topology in the RI→MI transition process, figures 3.7(a–d) include a sequence of flow visualizations corresponding to points a–d in

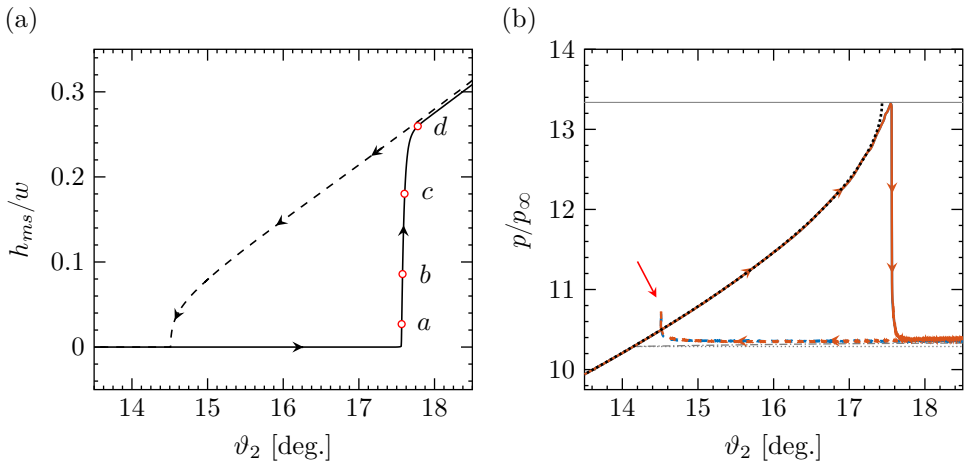

Figure 3.6: Evolution of (a) the Mach stem height, and (b) the pressure jump across the wave system with respect to the measured lower flow deflection ϑ_2 in the vicinity of the interaction location. —— indicate RI→MI transition; - - - MI→RI transition (see respectively cases P04 and P08 in table 3.1); and in (b) colors blue and orange denote pressure measurements obtained downstream of the upper and lower triple point, respectively (solid blue line is hardly visible as it falls below the solid orange line). Theoretical pressure jumps predicted by steady-state shock polar theory are additionally included in (b) as ····· for the RI→MI transition, with —— indicating the theoretical value at *detachment*, and ····· and -·-· the theoretical MI→RI pressure evolution behind the upper and lower triple point, respectively. The red arrow in (b) points towards the pressure peak observed when the Mach stem collapses at the interaction location.

figure 3.6(a). Upon first glance, some characteristic unsteady features such as the increase in spatial extent of the subsonic pocket, embedded within the yellow line denoting sonic conditions, and the associated Mach stem growth are clearly visible. Of particular interest is the flow field depicted in figure 3.7(a), which shows a pressure wave that emanates from the interaction location during the RI→MI transition, similar to that reported by Felthun and Skews [53] for a symmetric interaction. This emerging wave results in a kink in both reflected shocks (see the red arrows in figure 3.7(a)) that segregate, as indicated by the sonic contour, the RI strong-shock solution from the emerging MI weak-shock solution. Continuous pressure measurements behind the shock system, included as solid blue and orange lines in figure 3.6(b), confirm this occurrence and show approximately a 23% pressure drop across the wave. This is in good agreement with the theoretical pressure drop between *detachment* and *von Neumann* conditions given by the steady-state shock polar analysis in figure 3.1(c). Note that the propagation velocity of the pressure wave differs above and below the emerging slipline pair due to the distinct flow properties in these regions. In the absence of both PMEs, the Mach stem would monotonically grow until unstarting the whole computational domain. However, the interaction with the expansion rays results in a converging-diverging slipline configuration that permits the acceleration beyond Mach unity of the enclosed flow (notice the clear sonic throat in figures 3.7(c) and 3.7(d)). A sixth order polynomial fit to each slipline

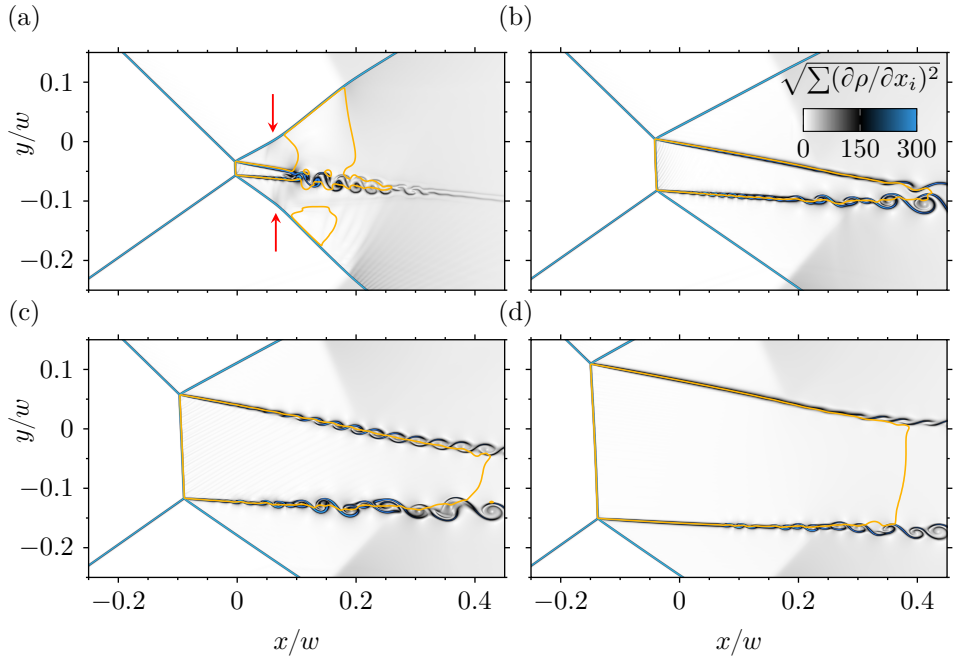

Figure 3.7: Sequence of instantaneous density gradient magnitude (non-dimensionalized with w/ρ_∞) corresponding to points *a*–*d* in figure 3.6(a). Solid yellow lines denote the sonic condition $M = 1$; red arrows point at the kink in both reflected shocks as a consequence of the interaction with the pressure wave generated during RI→MI transition.

allows an estimation of the instantaneous stream-duct inlet-to-throat ratio A/A^* (based on the Mach stem height and the minimum distance between sliplines) and reveals a shift from $A/A^* = 1.65$ to $A/A^* = 1.43$ between figures 3.7(c) and 3.7(d). The latter value agrees well with the theoretical estimate $A/A^* = 1.39$ given by steady one-dimensional isentropic nozzle flow theory at an inlet Mach number corresponding to that after a normal shock at $M_\infty = 3$. Such agreement suggests once more that the transient phase related to RI→MI transition is completed, in line with the change in trend around point *d* of the Mach stem growth in figure 3.6(a). This is further supported by other unsteady flow features vanishing as the MI develops. For instance, a shift in the Mach stem curvature from a forward to a backward bend is observed as predicted by steady-state shock polar theory. A consequence of this process is the generation of weak acoustic waves that reach both sliplines and promote the formation of Kelvin-Helmholtz instabilities. However, once the Mach stem is fully established (figure 3.7(d)), these acoustic waves are no longer present and so slipline instabilities clearly develop further downstream.

Regarding the slowest MI→RI transition case at $2g/w = 0.84$, case P08 in table 3.1, the corresponding Mach stem height and pressure jump evolution are also included as dashed lines in figures 3.6(a) and 3.6(b). As expected from numerical computations absent of free-stream disturbances, the interaction hysteresis first hy-

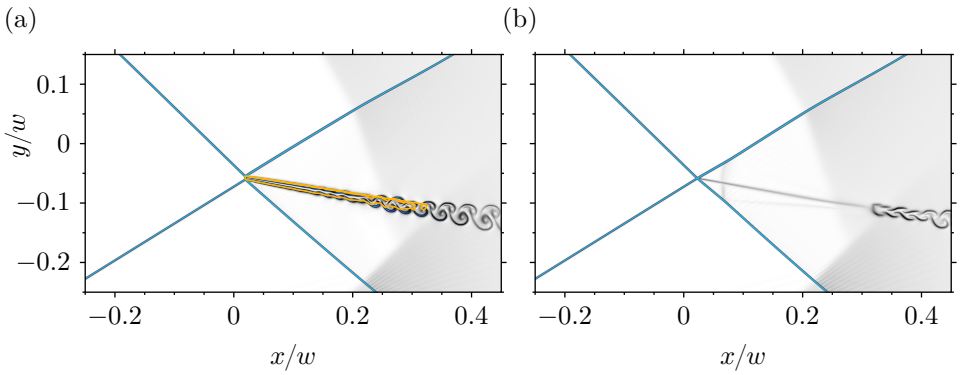

Figure 3.8: Instantaneous density gradient magnitude illustrating the collapse of the Mach stem during MI→RI transition, see case P08 in table 3.1. Solid yellow lines denote the sonic condition $M = 1$.

pothesized by Hornung *et al.* [87] becomes apparent. We define the characteristic velocity scale of the MI→RI transition process as the largest Mach stem shrink rate in absolute magnitude $|dh_{ms}/dt|/u_\infty$. Values are included in table 3.1 for all rotational velocities considered, again showing a convergence towards a non-zero value as M_{tip}/M_∞ decreases. This is a direct consequence of the Mach stem being finite at the precise instant the MI becomes unstable, which also explains the clear change in trend in the Mach stem height evolution (dashed line in figure 3.6(a)) around $h_{ms}/w = 0.05$. Therefore, regardless of the wedge rotation rate, the Mach stem collapse at the interaction location is inherently unsteady and leads to an instantaneous over-pressure at transition (indicated with a red arrow in figure 3.6(b)). Since a mismatch with the pressure level associated to the equivalent RI solution appears, this is accommodated by a weak pressure wave that emanates from the interaction location in a similar fashion as in the RI→MI case. Instantaneous flow impressions included in figures 3.8(a) and 3.8(b) illustrate the aforementioned. Similar as reported by Felthun and Skews [53], we also observe a slight increase in the Mach stem height (prior to the monotonic shrinking) due to a weak expansion wave generated at the lower domain boundary when the shock foot motion is initiated.

Before concluding this section, we would like to highlight a particular feature revealed when considering the spatial evolution of the interaction location over time. As shown in figure 3.9(b) for the fastest rotational velocity $M_{tip}/M_\infty = 0.1$, case P01 in table 3.1, the interaction location moves along C_1 with essentially constant velocity before transition occurs, see the shaded area in the figure. Since this was observed to be the case for all RI→MI transitions triggered by the lower wedge pitch, we could incorporate the shock motion in current shock polar theory by conducting a coordinate transformation to the (moving) frame of reference of the RI interaction location. Its velocity in both x and y directions was taken as the slope of the linear least squares regression to each curve in figure 3.9(b) within the shaded area, respectively. Corrected *detachment* conditions were recalculated and then transformed back into the original frame of reference of the computational domain in

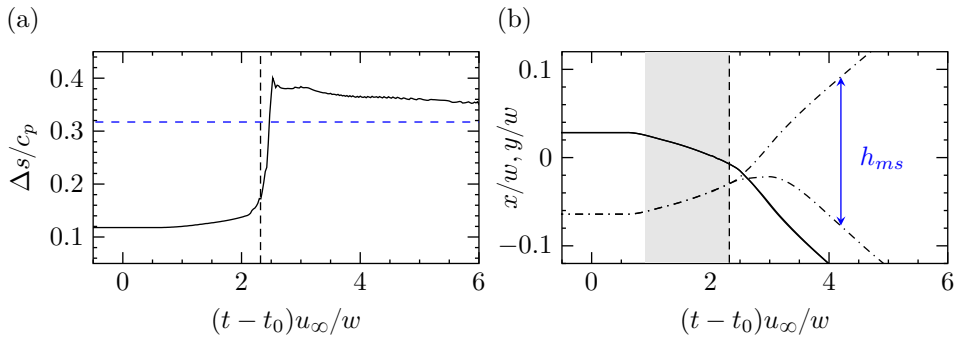

Figure 3.9: Time evolution of (a) the maximum entropy jump Δs across the wave system, and (b) the x-coordinate (——) and y-coordinate (- · - ·) of the interaction location for case P01 in table 3.1. The quasi-inertial region is shaded in gray and the time instant at which RI→MI transition occurs is indicated with a dashed line.

order to allow comparison with numerical data. Results for all rotational velocities are included as red circles in figure 3.5 and under $\vartheta_{2,c}^d$ in table 3.1. As observed, the agreement with numerical data improves significantly. This highlights the impact of rapid rotation on the shock system and the inability of steady shock polar theory to properly predict transition in the absence of unsteady considerations. We attribute the quantitative discrepancy for large rotational velocities to the complex unsteady motion of C_2, which also involves pitching due to the progressive change in shock strength. Thus, although the interaction location moves along C_1 with an apparent constant velocity, flow unsteadiness is still present leading to an overall under-predicted transitional ϑ_2 as observed in figure 3.5. For the MI→RI transition cases, a similar analysis could not be conducted due to the substantial triple point acceleration.

3.3.2. Oscillation of lower wedge deflection

The second excitation mechanism investigated is the sinusoidal oscillation of the lower wedge deflection. We consider two values for the mean lower wedge deflection $\vartheta_{2,i}$; one within the theoretical DSD and one outside it, in the RI domain. For the former, $\vartheta_{2,i} = 15.78°$ is selected with an oscillation amplitude of 2° so that the boundaries of the steady-state DSD in terms of flow deflection ($\vartheta_2^n = 14.14°$ and $\vartheta_2^d = 17.43°$, see figure 3.1(c)) are crossed during every period. The influence of initializing the solution with either a converged RI and MI is examined. For the case outside the steady-state DSD in the RI domain, $\vartheta_{2,i} = 13.89°$ is set with an oscillation amplitude of 4°. Regarding the excitation frequency, we use the available time scale of our setup, w/u_∞, scaled by a factor based on previous works on STBLI. In particular, we were inspired by the LES computations of Matheis and Hickel [46] at a free-stream Mach number $M_\infty = 3$ for which the incoming turbulent boundary layer thickness to shock generator hypotenuse ratio, δ/w, is 78.82. A base excitation frequency of $f_1 = 0.125u_\infty/w$ is therefore chosen to obtain good agreement with the low frequency dynamics of the separation shock in their computations. In order

Table 3.2: Summary of relevant parameters for the oscillation of the lower wedge deflection: $\vartheta_{2,i}$ corresponds to the mean wedge deflection in degrees; A denotes the amplitude of oscillation in degrees; f is the oscillation frequency; θ is the phase of the sinusoid in degrees; and subscripts $+$ and $-$ denote respectively the maximum and minimum value recorded during the first period of oscillation. See table 3.1 for additional remarks.

Case	$\vartheta_{2,i}$	$\frac{M_{tip}}{M_\infty}$	A	$f\frac{w}{u_\infty}$	θ	Initial	Final	$\frac{1}{u_\infty}\left(\frac{dh_{ms}}{dt}\right)_+$	$\frac{1}{u_\infty}\left(\frac{dh_{ms}}{dt}\right)_-$
D01	15.78	0.027	2.0	0.125	0	RI	MI	0.030	0.013
D02	15.78	0.055	2.0	0.250	0	RI	Both	0.016	0.046
D03	15.78	0.110	2.0	0.500	0	RI	Both	0.020	0.055
D04	15.78	0.027	2.0	0.125	180	MI	MI	0.029	0.022
D05	15.78	0.055	2.0	0.250	180	MI	MI	0.033	0.027
D06	15.78	0.110	2.0	0.500	180	MI	MI	0.045	0.038
D07	13.89	0.055	4.0	0.125	0	RI	Both	0.034	0.066
D08	13.89	0.110	4.0	0.250	0	RI	Both	0.028	0.057
D09	13.89	0.219	4.0	0.500	0	RI	Both	0.035	0.081

to assess the effect of increasing excitation frequency in the response of the wave system, higher frequencies $f_2 = 2f_1 = 0.25u_\infty/w$ and $f_3 = 4f_1 = 0.5u_\infty/w$ are additionally investigated.

For the oscillatory motion initiated within the steady-state DSD, the motion direction is set such as to bring the wave pattern towards its stability boundary, i.e, the wedge deflection initially increases for a starting RI and decreases for a MI. In a similar fashion as in section 3.3.1, we define the characteristic velocity scales associated to the RI→MI and MI→RI transition as the maximum Mach stem growth, $(dh_{ms}/dt)_+/u_\infty$, and maximum Mach stem shrink rate, $(dh_{ms}/dt)_-/u_\infty$ (i.e, maximum absolute value of negative Mach stem growth). In this case, they are both measured within the first period of oscillation of the lower flow deflection ϑ_2 at the interaction point. A summary of relevant parameters is given in table 3.2 including the corresponding maximum wedge tip speed in terms of M_{tip}/M_∞.

Figures 3.10(a–d) show the time evolution of the Mach stem height, ϑ_2, static pressure and entropy rise across the shock system for $\vartheta_{2,i} = 15.78°$ and $f_1 = 0.125u_\infty/w$, labelled as case D01 in table 3.2. All quantities are measured in the vicinity of the interaction location as discussed in section 3.2.3, and solid and dashed lines refer to an initially converged RI and MI wave pattern, respectively. In the case of a starting RI (solid line), the Mach stem appears during the first period of oscillation and never disappears thereafter. This observation can be explained as follows: first, the lower wedge oscillation initially brings the RI configuration outside its stability boundary. Close to the peak deviation from the mean deflection $\vartheta_{2,i}$, the RI is most unstable and RI→MI transition occurs. For the considered excitation frequency f_1, the resulting Mach stem growth is accentuated with $(dh_{ms}/dt)_+$ exceeding the corresponding maximum wedge tip speed M_{tip}/M_∞, see table 3.2. The Mach stem keeps growing until the MI is no longer stable, which, due to the existence of the DSD, occurs exclusively when the lower flow deflection ϑ_2 at the interaction location

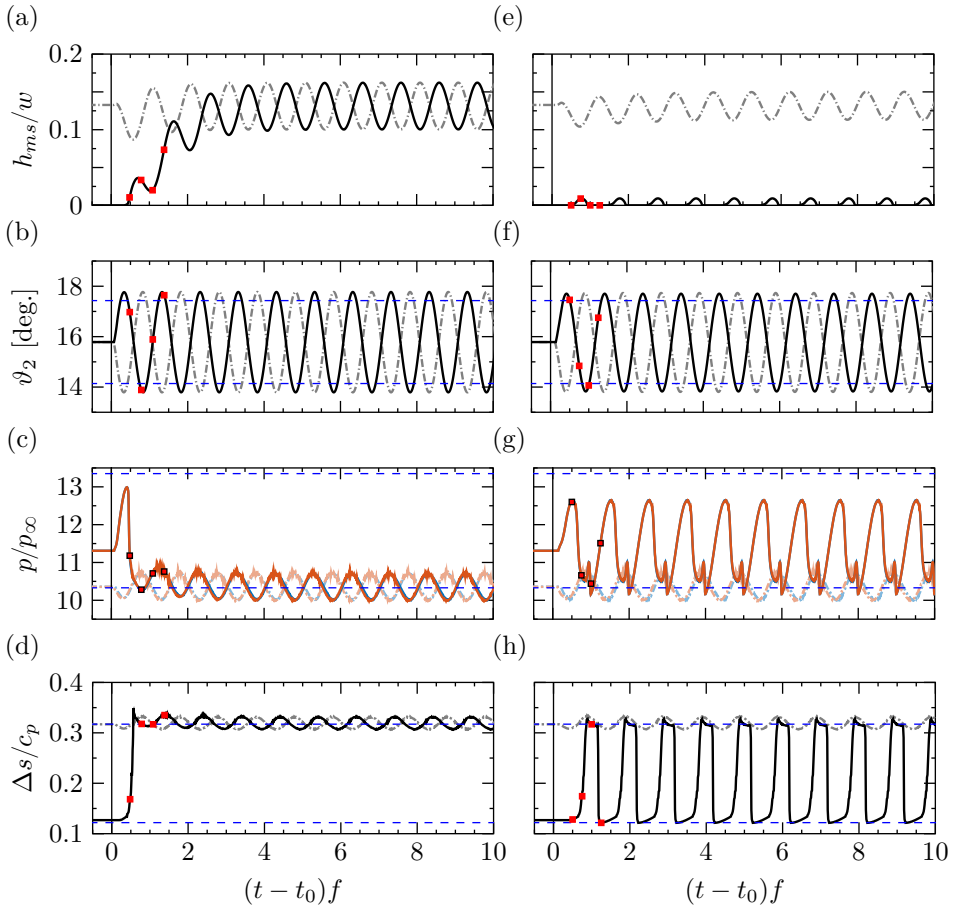

Figure 3.10: Results for the lower wedge deflection oscillation around $\vartheta_{2,i} = 15.78^\circ$ with an amplitude of 2° and excitation frequencies of: (a–d) $f_1 = 0.125u_\infty/w$, and (e–h) $f_2 = 0.25u_\infty/w$. Solid and dash-dotted lines refer to initial RI and MI respectively (the opacity of the latter is additionally set to 50% for clarity). The start time of oscillation is denoted by t_0, and the time axis is non-dimensionalized with the excitation frequency f. Pressure measurements downstream of the upper and lower triple points are included in blue and orange respectively. Dashed horizontal blue lines highlight the values at steady-state *detachment* (upper) and *von Neumann* (lower) conditions for $M_\infty = 3$ and $\vartheta_1 = 25^\circ$.

is close to its minimum. If such flow deflection prevails over a prolonged time, the Mach interaction monotonically shrinks as observed in section 3.3.1. However, because of the periodic excitation, stable conditions for the MI are recovered before the Mach stem collapses, which prevents MI→RI transition and allows the Mach stem to grow again. As a result, the mean Mach stem height increases progressively over several periods until a mean steady state identical to that obtained for an initial MI is reached (compare solid and dashed lines in figure 3.10(a)). Pressure and entropy measurements included in figures 3.10(c) and 3.10(d) respectively confirm this occurrence and illustrate the characteristic dissipative nature of a MI.

A sequence of instantaneous impressions of the density gradient magnitude corresponding to the first period of oscillation of case D01 is included in figures 3.11(a–d) (see also the animation available as supplementary material to the online version of our journal article [98]). Time instances are marked as red squares in figures 3.10(a–d). As the oscillation progresses, an alternation between a convergent and divergent slip-line orientation is observed in line with the characteristic streamwise (upstream and downstream) motion of the Mach stem and the associated Mach stem growth. In a similar fashion as discussed in section 3.3.1 for case P04, a kink in both reflected shocks appears after RI→MI transition occurs due to the presence of a pressure wave accommodating the pressure mismatch between the RI and the emerging MI, see figure 3.11(a). It is interesting to note, however, that the steady-state pressure level at *detachment* is not reached prior to the RI→MI transition (maximum pressure excursion does not lead to the uppermost dashed blue line in figure 3.10(c)). As emphasized in the previous section, this is a consequence of the inability of current steady-state shock polar theory to characterize time-dependent interactions.

Our results thus demonstrate that, for mean flow conditions within the steady-state DSD, periodic flow deflection perturbations across the C_2 incident shock are capable of (1) triggering RI→MI transition, and (2) sustain the MI thereafter. This is a result of the Mach stem dynamics during a period of excitation, exhibiting a large initial growth rate that prevents it from collapsing. A sensitivity study on the excitation frequency reveals, however, a change in the shock interaction response as the excitation frequency increases. For an excitation frequency twice as large as the base frequency, $f_2 = 2f_1 = 0.25u_\infty/w$ (case D02 in table 3.2), RI→MI transition still occurs but the collapse of the Mach stem at the interaction location (and thus transition to RI) follows, see figures 3.10(e–h). In this case, a slower (less impulsive) Mach stem growth than that for case D01 is measured. As documented in table 3.2, the maximum growth $(dh_{ms}/dt)_+/u_\infty$ no longer exceeds the corresponding maximum wedge tip speed M_{tip}/M_∞ nor the maximum shrink rate $(dh_{ms}/dt)_-/u_\infty$. Thus, the fraction of the excitation period for which the Mach stem shrinks is sufficient to permit its collapse. The resulting RI→MI→RI alternation observed within the first period of oscillation becomes periodic with the MI manifesting about 46% of the excitation period. A sequence of instantaneous impressions of the density gradient magnitude is included in figures 3.11(e–h) to illustrate the corresponding flow topology. Time instances of the flow impressions are respectively indicated by red squares in figures 3.10(e–h) during the first period of oscillation. In a similar fashion as for cases P05-P10 considered in section 3.3.1, the maximum Mach stem shrink rate $(dh_{ms}/dt)_-$ is recorded right before MI→RI transition occurs, which leads to the formation of a similar pressure wave that accommodates the pressure difference between both shock configurations (see figures 3.11(g) and 3.11(h)).

It is worth mentioning that in cases D04-D06 featuring an initial MI, transition to RI never occurred within the simulated time. In fact, the Mach stem remains in all cases far from collapsing at the interaction location, with the maximum deviation from the mean decreasing with increasing excitation frequency. This clearly shows that a much lower excitation frequency is required to enforce MI→RI transition than the opposite [48, 49], and thus suggests that any single-time event allowing the

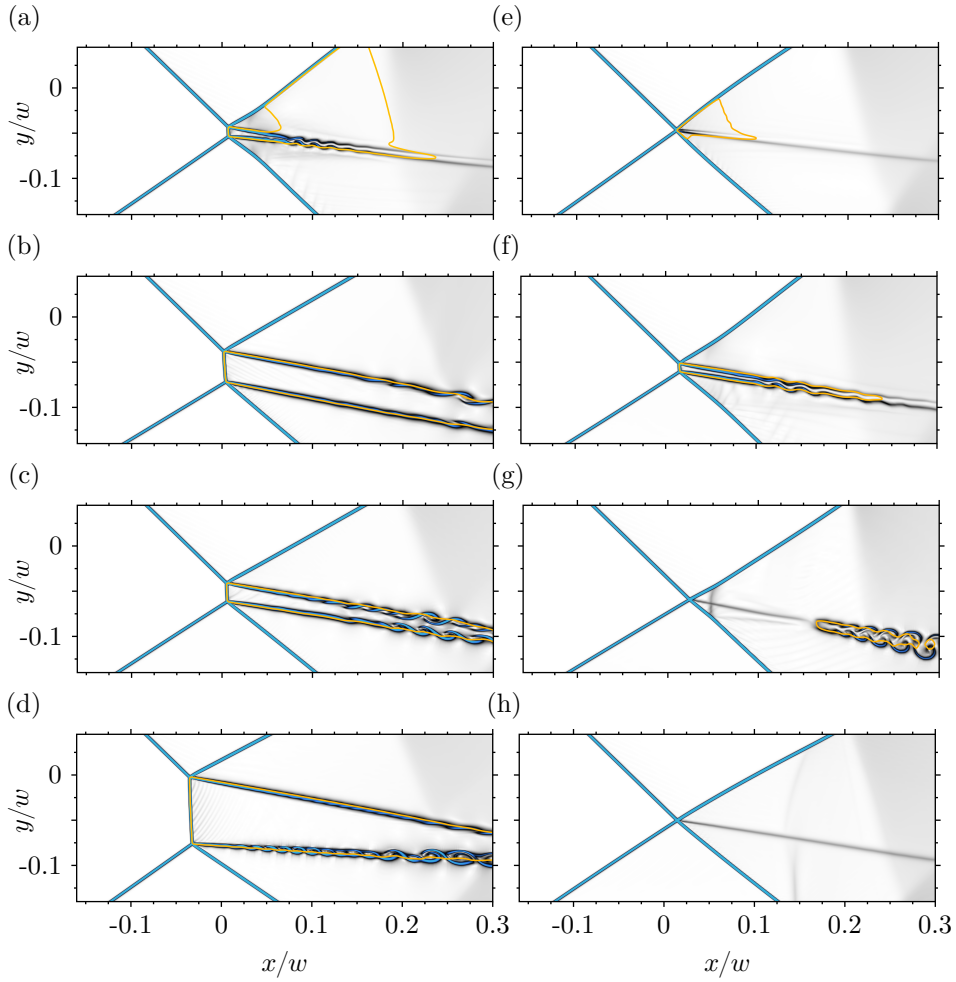

Figure 3.11: Sequence of instantaneous density gradient magnitude for the lower wedge deflection oscillation of 2° amplitude around $\vartheta_{2,i} = 15.78°$ for an initially steady RI. Excitation frequencies correspond to: (a–d) $f_1 = 0.125u_\infty/w$; and (e–h) $f_2 = 0.25u_\infty/w$. Time instances are marked sequentially as red squares in figures 3.10(a–c) and (d–f) respectively for f_1 and f_2. The solid yellow line denotes the sonic condition.

Mach stem to fully develop would lead to a sustained MI thereafter. Results for the excitation frequency f_3 are only included in table 3.2 for brevity, as they exhibit qualitatively the same behaviour as those for f_2.

In view of the above, it is furthermore investigated whether a similar periodic disturbance can also sustain a MI for mean flow conditions that are below the steady-state *von Neumann* boundary, as found in the simulations by Matheis and Hickel [46] for a STBLI at $M_\infty = 2$. In order to investigate if a similar scenario can be supported by unsteady inviscid simulations, additional computations were conducted for the current baseline conditions together with a lower mean wedge deflection $\vartheta_{2,i} =$

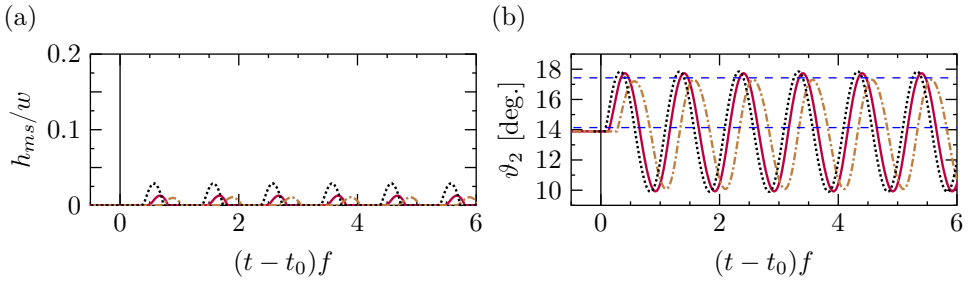

Figure 3.12: Evolution of (a) the Mach stem height h_{ms}, and (b) lower flow deflection below the C_2-C_4 intersection for the lower wedge deflection oscillation of 4° amplitude around $\vartheta_{2,i} = 13.89°$ outside the DSD. Line legend: (·····) results for the excitation frequency $f_1 = 0.125u_\infty/w$; (——) results for $f_2 = 0.25u_\infty/w$; (-·-·-) results for $f_3 = 0.5u_\infty/w$. The start time of oscillation is t_0, and the time axis is non-dimensionalized with the excitation frequency f. Dashed blue lines in (b) highlight the values at *detachment* (upper) and *von Neumann* (lower) conditions.

13.89° slightly below the steady-state *von Neumann* condition ($\vartheta_2^n = 14.14°$, see figure 3.1(c)). The excitation frequencies considered correspond to those defined earlier in this section but combined with an amplitude of oscillation of 4° instead of 2°, such that the maximum instantaneous wedge deflection exceeds the steady-state *detachment* boundary $\vartheta_2^d = 17.43°$. Corresponding time-scales are listed in table 3.2 for all the excitation frequencies, with the resulting Mach stem height and ϑ_2 evolution over time presented in figures 3.12(a) and 3.12(b) respectively. As shown, none of the cases result in a sustained MI over the integrated time. Instead, a periodic RI→MI→RI alternation develops similar to that obtained for cases D02 and D03.

3.3.3. Streamwise oscillation of lower wedge without pitch

Both excitation mechanisms considered above are based on the variation of the lower wedge deflection around its trailing edge, point O in figure 3.3, which remained fixed throughout the computations. We now consider the periodic oscillation of the lower wedge location while its deflection remains unaltered. This excitation mechanism may also be seen as a surrogate of the low-frequency motion of the separation shock foot in STBLI [95]. Baseline conditions together with $\vartheta_2 = 15.78°$ are considered in a similar fashion as in section 3.3.2, with both the RI and MI as starting wave patterns. A starting RI located outside the steady-state DSD with $\vartheta_1 = 13.89°$ is additionally investigated. The motion of the lower wedge is governed by a sinusoidal oscillation of its trailing edge along the lower boundary of the domain with the mean streamwise location equal to the upper wedge trailing edge x_{ut}. The excitation frequencies used to characterize the motion also correspond to those defined in section 3.3.2, and the impact of two different amplitudes of oscillation, $0.05w$ and $0.10w$, is assessed. The former amplitude leads to a maximum streamwise Mach number ratio M_{tip}/M_∞ of 0.039, 0.079 and 0.157 for f_1, f_2 and f_3 respectively, whilst those corresponding to the largest oscillation amplitude $0.10w$ are twice as large, see table 3.3. Oscillation time scales for this case are also defined as in section 3.3.2 but measured within the first period of oscillation for which the entropy jump through the wave system

Table 3.3: Summary of relevant parameters for the streamwise oscillation of the lower wedge without pitch: $\vartheta_{2,i}$ corresponds to the fixed wedge deflection in degrees; A denotes the amplitude of oscillation in terms of the wedge hypotenuse w; and subscripts + and − denote respectively the maximum and minimum value recorded during the first period of oscillation for which the entropy level characteristic of a MI is reached. See table 3.1 for additional remarks.

Case	$\vartheta_{2,i}$	$\frac{M_{tip}}{M_\infty}^+$	$\frac{A}{w}$	$f\frac{w}{u_\infty}$	Initial	Final	$\frac{1}{u_\infty}\left(\frac{dh_{ms}}{dt}\right)_+$	$\frac{1}{u_\infty}\left(\frac{dh_{ms}}{dt}\right)_-$
S01	15.78	0.039	0.05	0.125	RI	RI	0.0	0.0
S02	15.78	0.079	0.05	0.250	RI	MI	0.026	0.010
S03	15.78	0.157	0.05	0.500	RI	MI	0.040	0.040
S04	15.78	0.039	0.05	0.125	MI	MI	0.014	0.016
S05	15.78	0.079	0.05	0.250	MI	MI	0.035	0.032
S06	15.78	0.157	0.05	0.500	MI	MI	0.072	0.076
S07	15.78	0.079	0.10	0.125	RI	MI	0.032	0.010
S08	15.78	0.157	0.10	0.250	RI	MI	0.042	0.043
S09	15.78	0.314	0.10	0.500	RI	Both	0.046	0.073
S10	15.78	0.079	0.10	0.125	MI	MI	0.029	0.029
S11	15.78	0.157	0.10	0.250	MI	MI	0.071	0.063
S12	15.78	0.314	0.10	0.500	MI	MI	0.015	0.015
S13	13.89	0.079	0.05	0.125	RI	RI	0.0	0.0
S14	13.89	0.157	0.05	0.250	RI	RI	0.0	0.0
S15	13.89	0.314	0.05	0.500	RI	RI	0.0	0.0
S16	13.89	0.079	0.10	0.125	RI	RI	0.0	0.0
S17	13.89	0.157	0.10	0.250	RI	Both	0.007	0.003
S18	13.89	0.314	0.10	0.500	RI	Both	0.010	0.020

reaches characteristic values of a MI at $M_\infty = 3.0$.

Results for the $0.05w$ oscillation amplitude are shown in figures 3.13(a–h) for all excitation frequencies. When the initial shock pattern corresponds to a RI, see figures 3.13(a–d), all except the lowest excitation frequency trigger transition to a MI. It is interesting to note the particular Mach stem dynamics exhibited in case S03 (dash-dotted lines in figures 3.13(a–d)). As shown, a MI configuration is eventually sustained but only after 7 periods of oscillation in which the RI→MI→RI alternation occurs. Such alternation, however, is not periodic (the time interval for which the MI is present increases monotonically over consecutive oscillations) which indicates the presence of hysteresis in the flow (an animation for this particular case is also available online). The evident asymmetry in the evolution of ϑ_2 at the interaction location (figure 3.13(b)) further suggests that the streamwise oscillation of the shock generator results in much more complex C_2 shock dynamics than the corresponding oscillation of its incidence. This is additionally supported by the larger deviations in flow deflection and static pressure from the theoretical estimates based on a steady-state shock polar analysis. Under these circumstances, transition appears to be governed by the instantaneous $M_\infty - \vartheta_1 - \vartheta_2$ combination in the (moving) interaction frame of reference no longer able to accommodate a RI configuration. If

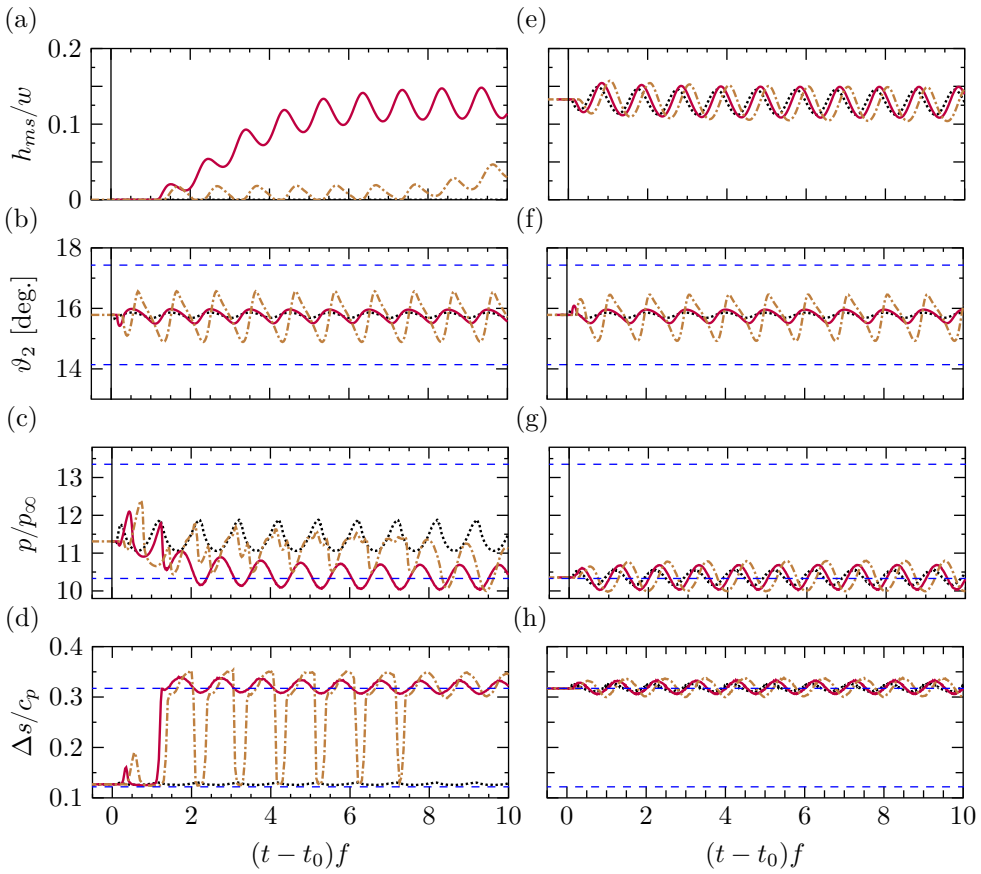

Figure 3.13: Results for the streamwise oscillation of the lower wedge at an amplitude of $0.05w$ and: (a–d) an initial RI pattern, and (e–h) an initial MI pattern; both starting within the steady-state DSD ($\vartheta_2 = 15.78°$). Line legend: (·····) results for the excitation frequency $f_1 = 0.125u_\infty/w$; (——) results for $f_2 = 0.25u_\infty/w$; (- · -) results for $f_3 = 0.5u_\infty/w$. Figures (c) and (f) show the average pressure between measurements taken downstream of both triple points. See caption of figures 3.10 and 3.12 for additional remarks.

such conditions are met, and the Mach stem growth rate is sufficiently large, the MI solution materializes and prevails thereafter. Our results thus demonstrate that low amplitude longitudinal oscillations are also capable of triggering RI→MI transition, and that they are more effective at retaining the MI pattern for large excitation frequencies than deflection oscillations.

Additional computations with a $0.10w$ oscillation amplitude were conducted for the same excitations frequencies, with the resulting time evolution of the Mach stem height shown in figure 3.14 for all cases. Numerical data in figure 3.14(a) involves an initial RI embedded within the steady-state DSD, for the same initial conditions as in the $0.05w$ case, whereas that in figure 3.14(b) corresponds to an initial MI. As it can be observed, the MI was unambiguously sustained for all perturbations except for the highest frequency of oscillation in figures 3.14(a). Such a rapid change of

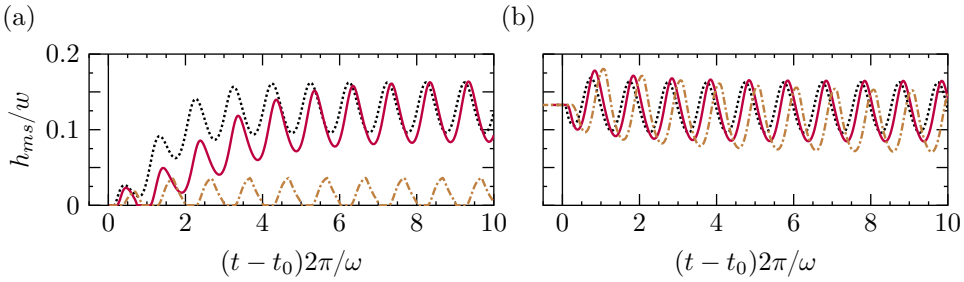

Figure 3.14: Non-dimensional Mach stem height (h_{ms}/w) evolution for an amplitude of oscillation of $0.10w$ and (a) an initial RI pattern, and (b) an initial MI pattern, both embedded within the theoretical DSD ($\vartheta_2 = 15.78°$). Line legend: (·····) results for the excitation frequency $f_1 = 0.125u_\infty/w$; (——) results for $f_2 = 0.25u_\infty/w$; (-·-·-) results for $f_3 = 0.5u_\infty/w$.

boundary conditions prevents the MI from establishing which leads to a continuous RI→MI→RI alternation during every period. This same alternation manifests for all amplitudes and excitation frequencies considered when the initial wave pattern corresponds to a RI outside the steady-state DSD ($\vartheta_{2,0} = 13.89°$).

3.4. Summary

Unsteady asymmetric shock interactions were numerically investigated on a double wedge configuration. Transition between the RI and the MI was triggered by three excitation mechanisms: the pitching of the lower wedge traversing the theoretical DSD, the sinusoidal oscillation of the lower wedge deflection with a mean value both within and outside the DSD, and the streamwise oscillation of the lower wedge location with fixed wedge deflection. Characteristic unsteady flow features such as the Mach stem growth, pressure evolution across the shock system and corresponding flow deflections and entropy rise, were investigated with a focus on the bi-directional RI⇄MI transition process. For periodic excitations, the influence of initializing the solution with either a converged RI and MI was additionally examined.

Regarding pitching of the lower wedge, our results showed the impact of impulsive rotations on the transition limits and revealed, as the rotational velocity was decreased, a mismatch in the MI→RI transition limit with respect to theoretical predictions. This occurrence was probably associated to the particular geometrical wedge arrangement ($2g/w$) imposing a limitation on the minimum Mach stem height for which the MI pattern can be sustained. Furthermore, in an attempt to exploit the prediction capabilities of shock polar theory applied to unsteady problems, a shock polar analysis in the (moving) frame of reference of the RI interaction location was conducted for all RI→MI transition cases, improving the agreement with respect to fast pitching numerical data significantly.

Furthermore, our simulations confirmed that periodic excitations can trigger RI→MI transition and potentially sustain the MI for mean flow conditions within the steady-state DSD. This is a consequence of the impulsive Mach stem growth right after transition, which prevents the remaining oscillatory motion of the lower incident

shock from inducing transition back to the RI pattern. A transient growth of the mean Mach stem height was observed over several periods of oscillation until a mean steady state identical to that obtained for an initial MI was reached. A sensitivity study on the excitation frequency revealed, however, a change in the shock interaction response as the excitation frequency increases. Under these circumstances, such an impulsive Mach stem growth was not permitted, which allowed MI→RI transition to occur. Instead of a MI sustained, we then observed a characteristic RI→MI→RI alternation that appeared to become periodic as the oscillation progressed. It should be noted that such alternation occurred at much higher excitation frequencies for the periodic oscillation of the lower incident shock foot than for the periodic oscillation of the lower flow deflection, indicating that the former mechanism was more effective at sustaining the MI pattern. Regarding the excitations imposed on an initial MI, it was clear that much lower frequencies were required to trigger MI→RI than the opposite since no transition to the RI was observed for the excitation frequencies considered.

In view of all the above, we thus concluded that the MI configuration is more robust against periodic perturbations than the corresponding RI configuration for mean flow conditions within the steady-state DSD. Our computations did not confirm, however, the possibility of a periodic oscillation sustaining the MI for mean flow conditions outside the steady-state DSD on the RI domain.

4

Response to quasi-steady free-stream Mach number variations

The previous chapter dealt with the response of asymmetric shock interaction systems to unsteady perturbations of the lower incident shock. These perturbations corresponded to variations in shock deflection or shock location, while the free-stream flow remained disturbance free. In the present chapter, which is the second and last chapter of PART ONE of the thesis, we investigate the complimentary case, that is, the influence of free-stream Mach number variations on SSIs with nominally fixed shock generator geometry. An experimental campaign was carried out for this purpose, in a wind-tunnel facility that enables a continuous variation of the free-stream Mach number during a run. As the time rate of change of the Mach number was significantly smaller than the characteristic flow time scale, the varying free-stream conditions in the experiments represent a quasi-steady perturbation of the SSI system. This implies that the theoretical framework presented in chapter 3 can be directly used to validate the applied measurements methods. Indeed, a direct comparison between raw data and theoretical predictions reveals the need to correct for off-design effects that contaminate schlieren visualizations of the flow. This is here accomplished with a systematic flow-based post-processing methodology that enables an accurate and reproducible tracking of the evolving shock system. The present chapter also reports a variable focal plane study conducted with a focusing schlieren system that supported the data processing by providing insights into three-dimensional side-wall effects.

The content of this chapter has been published as: L. Laguarda, J. Santiago Patterson, S. Hickel, F. F. J. Schrijer and B. W. van Oudheusden. Experimental investigation of shock–shock interactions with variable inflow Mach number, *Shock Waves* **31** (5), 2021. The author would like to acknowledge the important contribution to the work made by Jaime Santiago Patterson, who realized the experimental setup and generated the experimental results.

4.1. Introduction

As we already saw in chapter 3, gas dynamics theory characterizes SSIs in terms of the free stream Mach M_0, the flow deflections ϑ_1 and ϑ_2 imposed by the incident shocks, and the gas thermodynamic properties. This is often visualized graphically in the form of so-called shock polars [22], like the one in figure 3.1(c). Assuming constant gas properties, stability boundaries for the different interaction types can be calculated in terms of M_0 for fixed flow deflections, or in terms of one of the flow deflections while keeping the other and the free-stream flow properties unchanged [86]. The stability boundary of the MI, as we have already discussed, originates from the necessity of the slip line pair to be convergent so that the subsonic flow after the Mach stem can accelerate. The limit, referred to as the *von Neumann* criterion, defines an upper bound of flow deflection in the $\vartheta_1 - \vartheta_2$ plane (in the case of fixed M_0) and generally a lower M_0 bound in the $M_0 - \vartheta_{1|2}$ plane (for fixed $\vartheta_{2|1}$). The stability condition of the RI, in turn, is purely geometrical, based on whether the shock system is capable of satisfying all flow deflection boundary conditions. The limit, referred to as the *detachment* condition, defines a lower bound of flow deflection or an upper M_0 bound. Of particular interest is the fact that *von Neumann* and *detachment* conditions do not necessarily coincide and so a region exists in the $M_0 - \vartheta_1 - \vartheta_2$ parameter space, the dual-solution domain (DSD), in which the regular and Mach interactions are both realizable - see figure 4.1.

Based on the existence of such a dual-solution domain, Hornung *et al.* [87] speculated about the possibility of hysteresis in the RI→MI→RI cycle. For steady flows, they anticipated the occurrence of RI→MI transition according to the *detachment* condition, whilst the MI→RI transition should abide the *von Neumann* criterion. This hypothesized hysteresis phenomenon turned out to be much easier to be reproduced numerically than experimentally. While numerical works provided unambiguous evidence [47, 99], different experimental investigations [82, 88, 89] yielded different RI→MI transition conditions, all scattered across the theoretical DSD. Ivanov *et al.* [100] attributed the wide spread of experimental results to the different level of free-stream disturbances in each flow facility, which seemed to trigger premature RI→MI transition and thus partially or totally prevent the hysteresis. The same research group later confirmed this hypothesis by successfully observing hysteresis in a low-noise wind tunnel facility [90]. The following works on shock interactions performed by other groups [46, 48, 50–52, 54], which culminate with our investigation presented in chapter 3, made even more evident the sensitivity of the RI→MI transition to flow disturbances and unambiguously identify the MI as more robust under these conditions.

But despite the physical phenomenon being well understood, there is a critical need for improvement in the measurement techniques and post-processing strategies adopted in the experimental investigations of shock interaction transition, as well as in assessing the agreement with theoretical stability boundaries. As means to control the shock generator pitch, electric motors are often used together with pre-calibrated digital transducers to measure the relative position of the model geometry with respect to the free-stream flow. These measurements, generally assumed to be

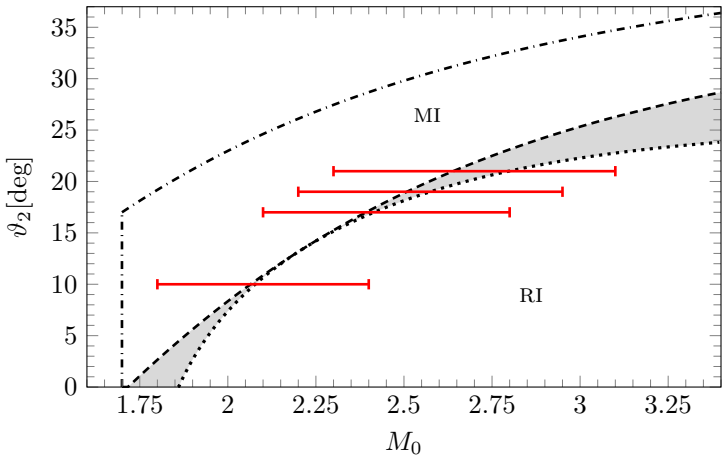

Figure 4.1: $M_0 - \vartheta_2$ plane for $\vartheta_1 = 17°$. The theoretical DSD is shaded in grey. The dotted line corresponds to the *von Neumann* criterion, the dashed line to the *detachment* condition, and the attached shock boundaries for ϑ_1 and ϑ_2 are shown as dash-dotted lines. The free-stream Mach number ranges used in the experiments are also included as solid horizontal lines.

representative of the flow direction, are taken at the location where the device is fixed, which is often at the model supports or at the sting (far away from the shock generators) and disregard potential model deformation induced by the aerodynamic loading. The same holds true for the influence of the boundary layer growth along the shock generator geometry, which is also commonly disregarded. If such effects are not properly accounted for, either with a suitable feedback compensation technique or during post-processing, a non-negligible mismatch between nominal shock generator angle and effective flow deflection appears. Although this mismatch may not alter the main conclusions of the experiment in a qualitative sense, it certainly has an impact on the quantitative results, particularly on the effective flow deflections at transition and the Mach stem height evolution. The importance of providing high-fidelity experimental datasets of such quantities should not be taken lightly, as the validation of low-fidelity simulation as well as reduced order models and analytical descriptions of the phenomenon rely on them.

Motivated by the above considerations, we have developed a flow-based post-processing approach of the experimental data that accounts for off-design effects. Parameters such as flow deflections and Mach stem height are quantified from schlieren visualizations of the shock system, in combination with associated free-stream pressure measurements from which the instantaneous value of the free stream Mach number is determined. The analysis is complemented with the calculation of the stability boundaries consistent with the actual interaction conditions to properly assess hysteresis effects. While most experimental investigations on shock interactions have targeted the flow-deflection-induced hysteresis, that is, homogeneous free-stream conditions and varying shock generator deflections, we perform our analysis for the complimentary case, i.e. the Mach-number-induced hysteresis. Here, the shock generators remain fixed while the free-stream Mach number varies. To our

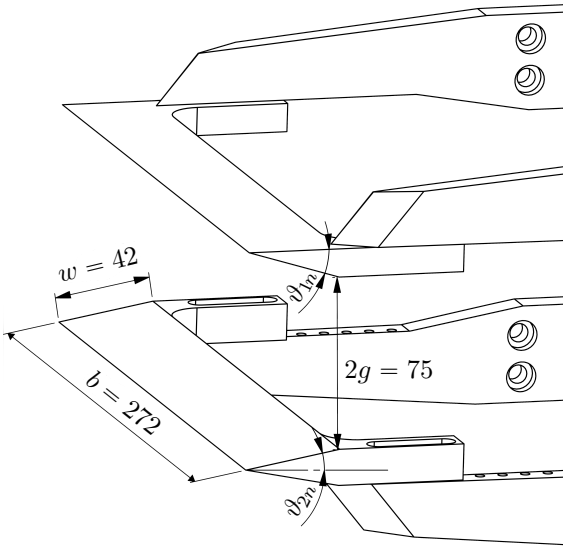

Figure 4.2: Schematic representation of the assembled model with its characteristic dimensions. The wedge hypotenuse w and span b are equal for all wedges. All dimensions are in mm.

knowledge, there is only one reported experimental work using a similar approach [55]. Schlieren visualization is used as the main flow diagnostics tool in our experiments, and a focusing schlieren system is additionally employed to investigate three-dimensional side-wall effects. The combination of these techniques enable the accurate measurement of transition conditions, which is found crucial to achieve agreement with theoretical predictions. We show that RI⇄MI transition, while apparently occurring outside the stability boundaries when their evaluation is based on nominal conditions, either occurs within the DSD or satisfies the *von Neumann* criterion corresponding to the measured flow deflections, which are found to differ noticeably, up to 1.2°, from nominal wedge angles.

4.2. Methodology

Information about the experimental facilities and the flow measurement techniques employed in this study was already provided in section 2.2 of chapter 2. In the following, we describe the investigated test model and the proposed flow-based post-processing methodology.

4.2.1. Setup

A schematic representation of the test model assembly is shown in figure 4.2. It consists of two opposing wedges with equal hypotenuse w that span the complete width of the test section ($b = 272$ mm) in order to minimize the influence of corner effects on the interaction region [101, 102]. Trailing edges of both wedges are

located at the same streamwise location and separated vertically by a distance $2g$. Each wedge is rigidly connected to the side walls by means of a pair of horizontal supports. All wedges used in this study were manufactured out of stainless steel and mechanically polished. To distinguish between nominal wedge angles and measured flow deflections, subscripts n and m are used, respectively. Thus, we refer to the nominal upper wedge angle as ϑ_{1n} and the nominal lower wedge angle as ϑ_{2n}.

A parametric study based on gas dynamics theory was conducted to select the values of w, $2g$, ϑ_{1n}, ϑ_{2n} and the ranges of M_0, such as to maximize the width of the DSD while preventing wind tunnel start-up issues and the expansion fans from intersecting the incident shocks. Based on this analysis, w was chosen to be 42 mm, $2g$ was set to $1.79w = 75$ mm and $\vartheta_{1,n}$ to 17°. The selection of ϑ_{1n} unambiguously determines the shape of the *von Neumann* and *detachment* criteria in the $M_0 - \vartheta_{2n}$ plane and thus the associated DSD, see figure 4.1. The selected values of ϑ_{2n}, namely 10°, 17°, 19° and 21°, include the nominally symmetric interaction and three different asymmetric cases. The chosen M_0 ranges, ensuring RI⇄MI transition within the capabilities of the experimental facility, are indicated in figure 4.1 by the solid horizontal lines.

Tests were conducted as follows. First, the wind tunnel was started at the highest M_0 value within the range associated to a specific wedge arrangement. As observed in figure 4.1, this unambiguously results in a RI. After steady flow conditions were established, M_0 was continuously reduced towards the lowest value of the considered range. This enforced transition towards the MI. Once the lowest value had been reached, M_0 was then again increased towards its starting value to enforce transition back to the RI. The ratio of the time rate of change of the Mach number dM_0/dt, to the characteristic flow time scale u_∞/w was in the order of 10^{-5} in all cases, thus confirming the quasi-steady nature of the interactions [98]. Each wedge arrangement was tested five times in order to increase the statistical significance of the results.

4.2.2. Data processing

We developed a flow-based post-processing approach where accurate instantaneous flow deflection values are extracted from the flow measurement data instead of using the nominal shock generator geometry. This is followed by a consistent calculation of the stability boundaries to properly assess hysteresis effects. The main steps of the proposed methodology are detailed below.

Pre-processing

A pre-processing routine is applied to the raw schlieren images, consisting of cropping and background subtraction. Cropping is performed in order to reduce the image size and zoom into the region of interest, while subtracting the background reduces noise and removes unwanted artifacts, such as dust particles on the camera sensor or imperfections in the windows, from the images. A background image is defined as the average of a series of wind-off images of the test section recorded prior to every experimental run. An example of a pre-processed image compared to the raw counterpart is shown in figure 4.3. Notice that both wedges do not completely

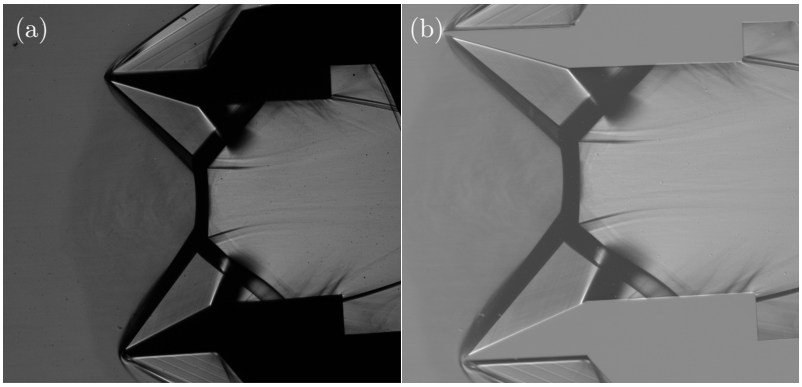

Figure 4.3: Comparison of a MI (a) before pre-processing (raw image), and (b) after pre-processing ($\vartheta_{1n} = 17^\circ$ and $\vartheta_{2n} = 21^\circ$ at $M_0 = 2.3$).

disappear after pre-processing, which highlights the non-negligible deformation of the model due to the aerodynamic loads.

Incident shock angle computation

Next, incident shock angles are computed from the pre-processed images. For this, a search area is defined for each incident shock. We use search windows containing 100 horizontal pixel lines and located such that the closest distance to the corresponding wedge tip (as seen in the background image) is $0.3w$ in the direction perpendicular to the free-stream flow. The horizontal positioning of each window depends on the corresponding incident shock line fit defined in the previous frame; each horizontal pixel row includes 120 pixels towards the free-stream flow from the shock line fit and 30 pixels towards the post-shock region.

For every window, the evolution of the light intensity is examined along each horizontal pixel line in search of the shock wave. A typical light intensity profile is shown in figure 4.4(a). Even though the sudden decrease in light intensity is clearly related to the incident shock, the dark appears too wide to infer with sufficient accuracy the exact shock location at the mid-plane of the test section (where the shock interaction is two-dimensional). Examination of the focusing schlieren data, which is discussed in detail in section 4.3.1, revealed that the trailing edge of the dark region is representative of the true shock location, while most of the remaining thickness can be associated with shock-wave/boundary-layer interactions at the side windows. Therefore, we identify the incident shock by searching for the trailing edge of the dark region. This is done by first computing the gradient of the measured light intensity profile and then searching for the maximum value. In view of the noticeable oscillations, a median filter is applied prior to the gradient computation (dashed red line in figure 4.4(a)). As shown in figure 4.4(b), the trailing edge location of the shock wave on the search line appears now as a sharp peak. We further seek for sub-pixel resolution of the location of extrema by performing a local parabolic reconstruction of the intensity gradient distribution.

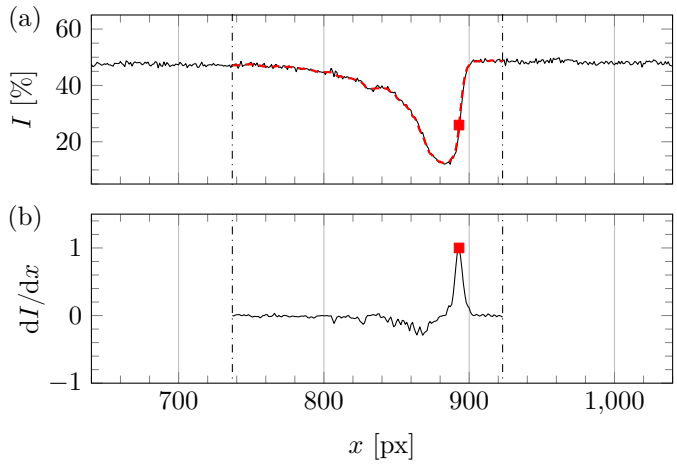

Figure 4.4: (a) Light intensity I along the search line, and (b) corresponding gradient dI/dx normalized with the maximum value. The profile after filtering is included in (a) as a dashed red line, whereas search window limits and the detected shock location are indicated in both figures with dash-dotted lines and red squares respectively.

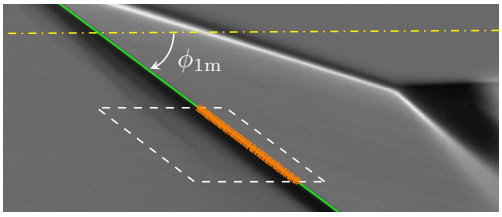

Figure 4.5: Main features of the shock detection and shock angle ϕ_{1m} calculation process. Dash and dash-dotted lines indicate respectively the search window limits and the longitudinal direction of the wind tunnel, the orange × markers depict the detected shock location on each horizontal pixel line, and the green solid line illustrates the resulting shock line fit.

Applying the above-mentioned procedure to all horizontal pixel lines within the search window results in a set of shock location points. An iterative least-square line fitting routine is employed on this set to reduce the number of outliers and optimize the coefficient of determination. We discard all points located beyond three times the RMS of the euclidean point-to-line distance and recalculate the fit iteratively until convergence. The true incident shock angles ϕ_{1m} and ϕ_{2m} are finally determined by computing the angle between the corresponding line fit and the longitudinal direction of the wind tunnel. Figure 4.5 illustrates the key elements of the above-mentioned procedure applied to the upper incident shock and superimposed on the pre-processed schlieren image.

Table 4.1: Estimated uncertainties.

ϑ_{1n}	ϑ_{2n}	$\overline{\Delta M_0}$	$\overline{\Delta\phi_{1m}}$	$\overline{\Delta\phi_{2m}}$	$\overline{\Delta\vartheta_{1m}}$	$\overline{\Delta\vartheta_{2m}}$
17.0°	21.0°	0.0010	0.14°	0.14°	0.13°	0.11°
17.0°	19.0°	0.0017	0.15°	0.22°	0.14°	0.19°
17.0°	17.0°	0.0014	0.15°	0.20°	0.14°	0.18°
17.0°	10.0°	0.0010	0.20°	0.17°	0.17°	0.17°

Flow deflection computation

Once the incident shock angles have been determined, the associated flow deflections follow in a straightforward manner. Due to the synchronous pressure measurements, each schlieren image has an associated free-stream Mach number value. Considering the i-th image in a sequence with a corresponding M_0^i value, if ϕ_{km}^i corresponds to a particular incident shock angle measured with the procedure outlined in section 4.2.2 (with $k = 1$ denoting the upper incident shock and $k = 2$ the lower one), then the corresponding flow deflection ϑ_{km}^i follows from the oblique shock relation

$$\vartheta_{km}^i = f(M_0, \phi, \gamma) = \tan^{-1}\left(\frac{2}{\tan\phi_{km}^i}\frac{(M_0^i \sin\phi_{km}^i)^2 - 1}{M_0^{i\,2}(\gamma + \cos 2\phi_{km}^i) + 2}\right), \tag{4.1}$$

with the specific heat ratio taken as $\gamma = 1.4$.

We consider the propagation of errors in M_0 and ϕ_{km} on equation (4.1) as means to assess the uncertainty associated with the resulting flow deflections ϑ_{km}. For each test run, flow data over a short initial interval corresponding to nominally constant free-stream flow conditions was available (more than 100 visualizations and corresponding pressure measurements). From this data, we estimate the uncertainties on M_0 and ϕ_{km}, namely ΔM_0 and $\Delta\phi_{km}$, as twice the average RMS of the resulting M_0 and ϕ_{km} values (95.4% statistical confidence limit). Since these are independent measurements, i.e. instantaneous errors in M_0 and ϕ_{km} are uncorrelated, we approximate the uncertainty in ϑ_{km}, namely $\Delta\vartheta_{km}$, as the norm

$$\Delta\vartheta_{km} \approx \sqrt{\left(\left.\frac{\partial f}{\partial M_0}\right|_{max}\Delta M_0\right)^2 + \left(\left.\frac{\partial f}{\partial \phi_{km}}\right|_{max}\Delta\phi_{km}\right)^2}, \tag{4.2}$$

where the magnitude of the partial derivatives is taken as the maximum recorded in the run. Resulting uncertainties are reported in table 4.1 per geometry.

Recall that, in order to avoid confusion with nominal conditions, measured quantities are referred with the subscript m, e.g., ϑ_{1n} and ϑ_{2n} denote nominal wedge angles whilst ϑ_{1m} and ϑ_{2m} indicate measured flow deflections.

Intersection point determination

The *intersection point* is defined as the point where the linear fits for the upper and lower incident shocks intersect, which should coincide with the interaction point in case of a RI (the point where the incident shock meet in figure 3.1(a)). In order

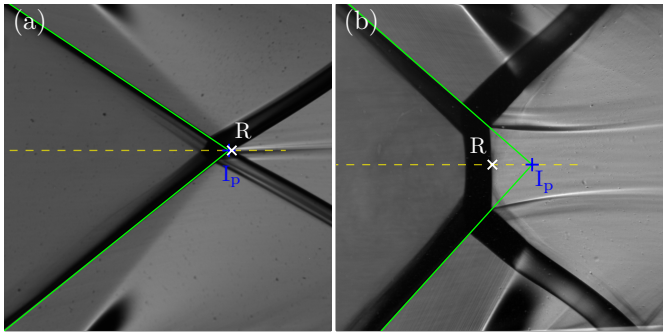

Figure 4.6: Intersection point location I_p and true shock location R for (a) a RI, and (b) a MI. Incident shock line fits are included as solid green lines.

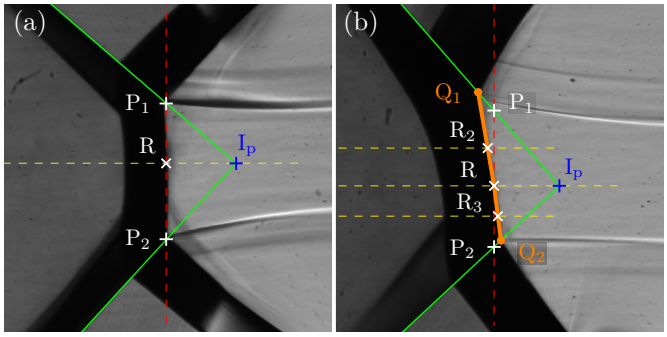

Figure 4.7: Relevant auxiliary parameters for the Mach stem height determination: (a) straight line approach, (b) parabolic approach.

to determine whether or not the current shock configuration agrees with a regular interaction pattern, a horizontal line segment is defined, that extends from a distance $0.1w$ downstream of the intersection point in the upstream direction towards the free-stream flow. The light intensity along this line is examined as explained in section 4.2.2, and the true shock location is determined accordingly. The current shock configuration corresponds to a RI when the shock location R along the horizontal line is located at the intersection point I_p, see figure 4.6(a). Conversely, as depicted in figure 4.6(b), if R is sufficiently far upstream of I_p, the shock system unambiguously corresponds to a MI. The exact occurrence of transition that segregates the RI from the MI, however, is determined according to Mach stem height considerations. This is explained in detail in section 4.2.2, while the procedure to calculate the actual height of the Mach stem is described below.

Mach stem height determination

We define the Mach stem height h_{ms} as the distance between the triple points of the MI, i.e., the points where the incident shocks meet the Mach stem (see figure 3.1(b)), in the direction perpendicular to the free-stream flow. Recalling figure

4.6(b), it can be seen that the true shock location R along the horizontal search line lies on the Mach stem. For shock configurations where the Mach stem is essentially a normal shock wave, see figure 4.7(a), a good approximation of its height is given by the length of the line segment $\overline{P_1P_2}$, where P_1 and P_2 result from intersecting the incident shock fits with the line perpendicular to the free-stream passing through point R.

However, if the Mach stem has non-negligible curvature, as in figure 4.7(b), the straight line approach becomes inaccurate. For this reason, the Mach stem is instead approximated with a quadratic function, requiring two additional points laying on it besides R. These points, labeled as R_2 and R_3 in figure 4.7(b), are obtained by applying the gradient-based method outlined in section 4.2.2 to the light intensity profile over the horizontal lines passing through the midpoints of the line segments $\overline{RP_1}$ and $\overline{RP_2}$, respectively. The unique parabola resulting from the set of points $\{R, R_2, R_3\}$ thus approximates the Mach stem curvature, and the distance in the direction perpendicular to the free-stream between points Q_1 and Q_2, the intersections of the parabola with each incident shock-fitted line, defines the Mach stem height.

For the investigated interactions, we measured deviations between the linear and the parabolic approach of up to 10% in the large Mach stem height range ($h_{ms} > 0.3w$). Therefore, and for the sake of consistency, we use the parabolic approach to approximate the Mach stem height in all cases.

Transition detection

Although very close to each other, in view of measurement uncertainty, points I_p and R will never perfectly coincide in case of a RI, see figure 4.6(a). This leads to a finite non-zero value of the Mach stem height being determined also for these shock patterns. The resulting h_{ms} signal, however, is observed to have a close to zero mean value, which suggests that the measuring procedure, although affected by measurement uncertainty (noise), is not introducing any bias. The computed RMS variation of the h_{ms} signal, of the order of $10^{-2}w$, is used to define the threshold value to determine the occurrence of RI$\rightleftarrows$MI transition. That is, transition is detected when the h_{ms} signal of an image sequence exceeds or falls below $h_{ms}/w = 2 \times 10^{-2}$, and the corresponding ϑ_{1m}, ϑ_{2m} and M_0 values are thus recorded. In case $h_{ms}/w = 2 \times 10^{-2}$ is crossed multiple times due to a local small oscillation, an average value of the aforementioned quantities over the extent of the oscillation is considered instead. It was verified that the transition detection did not critically depend on the threshold value used: the magnitude of the recorded quantities varies by less than one percent when the h_{ms} threshold value is doubled.

Consistent stability boundary calculation

In order to properly assess hysteresis effects, the remaining step is to calculate the actual RI and MI stability boundaries, based on the recorded ϑ_{1m} at transition, to allow for a consistent comparison between measurements and theory.

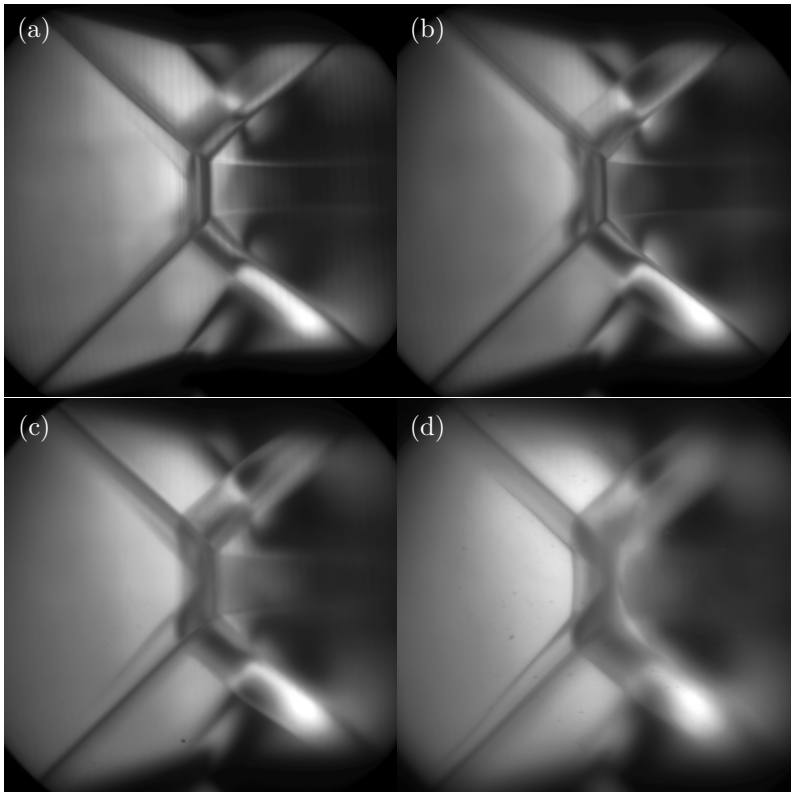

Figure 4.8: Focusing schlieren visualizations of a MI during a variable focal plane study. Focus plane locations: (a) center of the test section; (d) wind tunnel window; (b–c) intermediate locations. The corresponding geometry setup is $\vartheta_{1n} = 17^\circ$ and $\vartheta_{2n} = 21^\circ$ at constant $M_0 = 2.26$.

4.3. Results and discussion

4.3.1. Focusing schlieren diagnostics

As means to investigate the potential impact of three-dimensional effects in our setup, we used the focusing schlieren system presented in section 2.2.2. Visualizations for different focal plane locations were achieved by mounting the camera on a rail allowing it to be moved forward or backwards along the optical path. The plane of focus was initially located at the center of the test section, and after a stable shock interaction was generated, the camera was gradually moved such as to shift the image plane towards one of the wind tunnel windows.

An example of the resulting focusing schlieren visualizations is shown in figures 4.8(a–d) for a MI corresponding to $\vartheta_{1n} = 17^\circ$ and $\vartheta_{2n} = 22^\circ$ at $M_0 = 2.26$. Even though traces from out-of-focus features are still present in the image, it is clear that the MI appears the sharpest when the focal plane is located at the center of the test section, see figure 4.8(a). All characteristic elements, including the concave Mach stem, the expansion fans and the curved slip lines, can be unambiguously

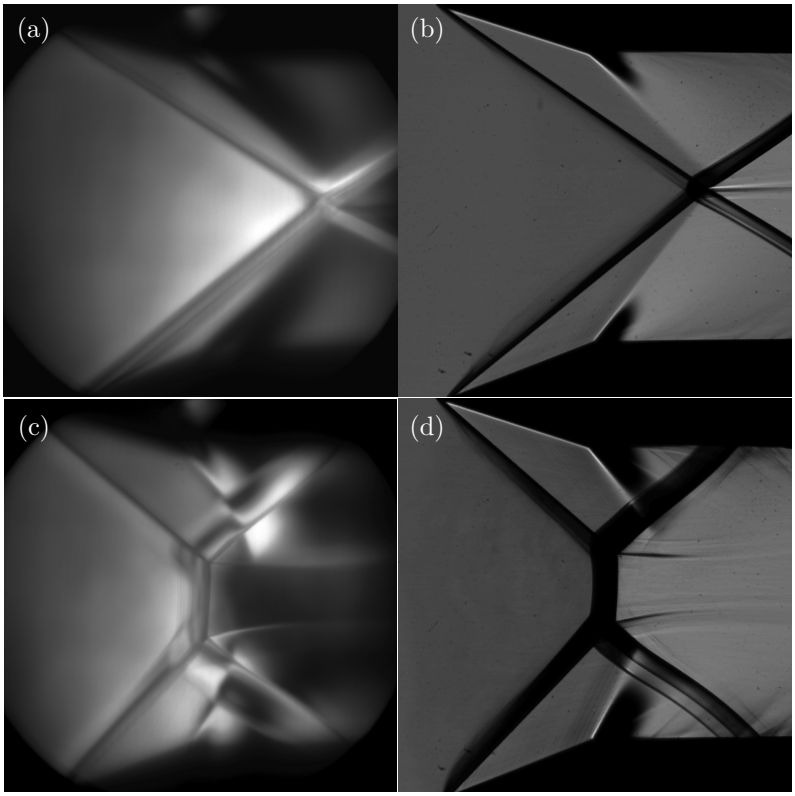

Figure 4.9: Comparison between focusing schlieren and regular schlieren visualizations of (a–b) a RI, and (c–d) a MI, resulting from the wedge arrangement $\vartheta_{1n} = 17^\circ$ and $\vartheta_{2n} = 21^\circ$ at $M_0 = 3.0$ and $M_0 = 2.41$ respectively.

recognized while the shock waves appear considerably thinner than in the regular schlieren visualizations. As the image plane is moved away from the center, the aforementioned features become progressively blurred, see figures 4.8(b) and 4.8(c). At the same time, a considerable thickening of the shock regions is observed, which is attributed to shock-wave/boundary-layer interactions on the side-wall windows. The adverse pressure gradient imposed by the shock wave induces a boundary layer thickening that affects the flow upstream of the impingement point through the subsonic layer [4]. This results in a series of compression waves generated upstream of the impinging shock that contribute to the apparent shock thickening in the visualizations. Such three-dimensional effects appear most predominant when the focal plane is located nearest to the side window, see figure 4.8(d). Notice also the considerable upstream motion of the quasi-normal shock associated with the Mach stem and the disappearance of the slip lines. An animation corresponding to figure 4.8 is available in our data repository [103] (https://doi.org/10.4121/13160954).

When examining MI configurations, we never found a trace of a RI at any position along the span-wise direction; Mach stem and the slip-line pair were present in all planes of the optical path except very near the windows. The same holds true

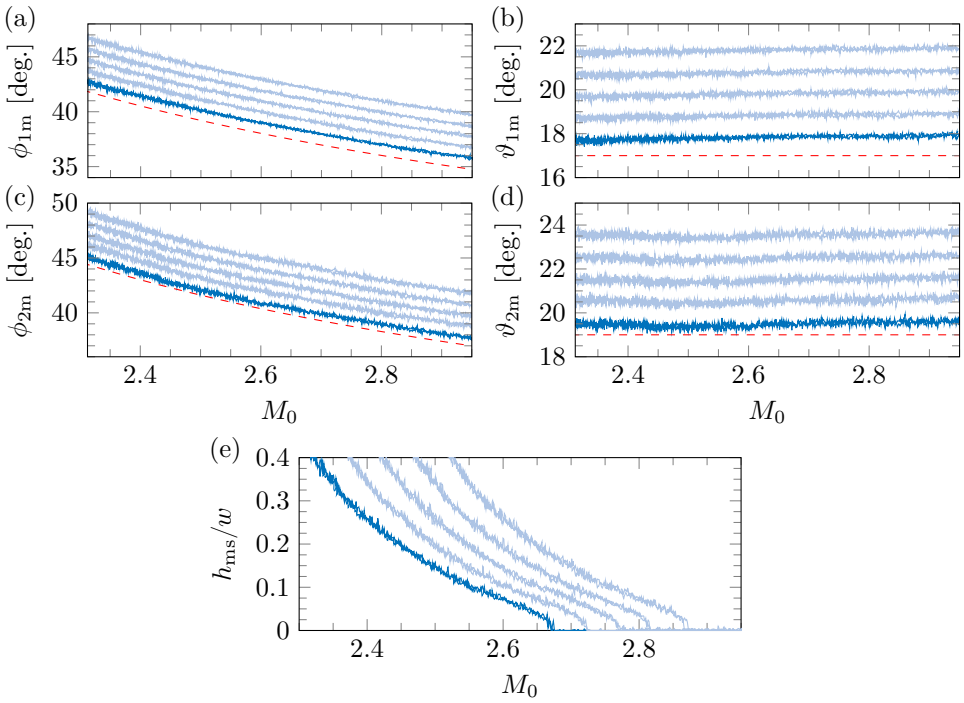

Figure 4.10: Quantitative results obtained with the presented post-processing methodology for all five experimental runs conducted with the wedge arrangement $\vartheta_{1n} = 17^\circ$ and $\vartheta_{2n} = 19^\circ$: (a–b) upper shock angle ϕ_{1m} and flow deflection ϑ_{1m} signals, (c–d) lower shock angle ϕ_{2m} and flow deflection ϑ_{2m} signals, and (e) normalized Mach stem height h_{ms}/w dependency on M_0. Four of the five signals (semi-transparent lines) have been offset $+1^\circ$ vertically from each other in (a–d) and $+0.05$ horizontally in (e) for illustration purposes. Theoretical evolution of shock and flow deflection based on nominal conditions are also included as dashed red lines.

in the opposite case; traces of a MI were never found during examination of the span-wise variation of a RI. In addition, the sharp incident shocks recognized with the image plane at the test section center, figure 4.8(a), appear in all remaining visualizations of the variable focal plane test, figures 4.8(b–d). This confirms that the shock interactions generated with our setup are two-dimensional along most of the wind tunnel width.

It is relevant to note that the incident shocks in the focusing schlieren visualizations, where they appear as dark lines, are always located close to the rear of the blurred regions surrounding them. This observation agrees with the proposed effect of the shock-wave/boundary layer interactions at the side walls, suggesting that most of the thickening of the incident shocks in schlieren visualizations results from the upstream influence effect. Figure 4.9 includes a direct comparison between focusing schlieren and regular schlieren visualizations of a RI and MI. As observed, the trailing edges associated to the shock regions appear as sharp discontinuities in the regular schlieren visualization whilst the leading edges clearly fade out. These findings justify the approach described in section 4.2.2 of searching for the trailing edge

of the incident shock wave footprint during post-processing, as being representative of the actual shock location.

4.3.2. Post-processing results

A total set of 20 schlieren visualization experiments with synchronous pressure readings were conducted as described in section 2.2.2. The resulting sequence of images were analyzed according to the procedure presented in section 4.2.2. Figures 4.10(a–e) show the results for shock angles, flow deflections and corresponding Mach stem height dependency on M_0 for the nominal wedge arrangement $\vartheta_{1n} = 17^\circ$ and $\vartheta_{2n} = 19^\circ$. They contain data from all five runs corresponding to this arrangement, with four of the five signals on each figure accordingly offset for illustration purposes (see the caption for details). The evident similarities between the different recordings highlights the robustness of the processing methodology. The spreading of each signal over the whole M_0 range is also found to be in close agreement with the estimated uncertainties reported in table 4.1.

The theoretical evolution of shock angle and flow deflection based on nominal conditions is also included in figures 4.10(a–d) (red dashed lines), revealing the mismatch between nominal and effective wedge angles. The largest shock angle deviation from nominal conditions in figures 4.10(a) is 1.36° degrees, which translates into a 1.2° flow deflection mismatch with the nominal wedge angle $\vartheta_{1n} = 17^\circ$, the maximum recorded in this work. This mismatch originates from the additional flow displacement through the viscous boundary layers over the wedge surfaces, manufacturing and mounting uncertainties, as well as deformations under high pressure load. Interestingly, the aerodynamic loading on a two-dimensional wedge geometry reaches its maximum at the lowest M_0 value. For a constant total pressure, the free-stream static pressure monotonically increases with decreasing M_0 and this effect dominates over the corresponding decrease in pressure gradient across the shock waves. However, the largest deviations from nominal conditions in our experiments do not agree with the aforementioned. This evidences the complexity of the off-design interaction geometry, and justifies the proposed flow-based post-processing methodology.

4.3.3. Mach stem height dependence on M_0

The evolution of the Mach stem height in figure 4.10(e) appears insensitive to the increase or decrease of M_0 in all five runs, which already indicates the absence of hysteresis for this wedge arrangement. The average normalized Mach stem height h_{ms}/w dependence on M_0 for all geometries is included in figure 4.11. A distinction has been made for the data corresponding to a decreasing M_0 and that for an increasing M_0, but the almost perfect overlap between the two confirms the repeatability, as well as the absence of any measurable hysteresis effects in our experiments. The latter is consistent with past experimental works in noisy facilities [55, 82, 88, 89]. Data shown in figure 4.11 together with the corresponding shock angles and flow deflections is also available in our data repository [103].

The observed growth of the Mach stem height is clearly non-linear in M_0 with a

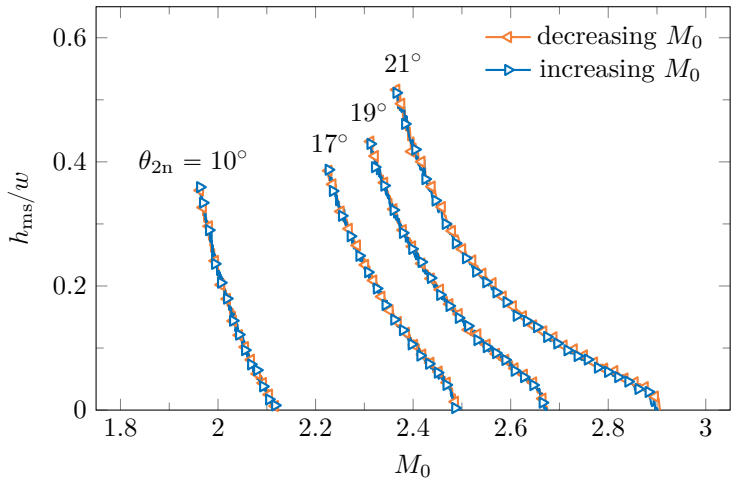

Figure 4.11: Average normalized Mach stem height h_{ms}/w dependence on the free-stream Mach number M_0 for all wedge arrangements.

sharp growth rate increase when approaching the RI⇆MI transition, for all geometries besides $\vartheta_{2n} = 10°$. We consider this effect to be related to the fact that a particular inlet-to-throat ratio in the convergent-divergent slip-line duct behind the Mach stem needs to form for the MI to be stable [98]. After RI→MI transition, this requirement results in a rapid growth of the Mach stem until the mass flow through it can be swallowed at sonic conditions at the throat. In the opposite case, right before MI→RI transition, this translates into a sudden collapse of the finite Mach stem. Whether this abrupt increase in the Mach stem growth rate can be observed or not, i.e. whether h_{ms} is finite in the vicinity of the RI⇆MI transition, depends on the geometrical ratio $2g/w$. As first suggested by Hornung and Robinson [82] for the symmetric MI, $h_{ms}/w = f^+(M_0, \gamma, \vartheta_1, \vartheta_2, 2g/w)$ where f^+ is probably a universal non-dimensional function and $2g/w$ the only scaling parameter.

4.3.4. Remarks on the RI⇆MI transition

The final step in the analysis is to determine to what extent the RI⇄MI transition observed in our experiments corresponds to the stability boundaries that enclose the DSD. The quantities (flow deflections and Mach number) at transition follow from the Mach stem height evolution as explained in section 4.2.2 and the results are summarized in table 4.2 and visualized in figures 4.12(a–h) in the $M_0 - \vartheta_2$ plane. The DSD based on the nominal shock generator angles is indicated in the figure (grey) together with the DSD based on the average measured upper flow deflection ϑ_{1m} (blue) which accounts for the off-design interaction geometry.

It becomes evident that transition in our experiments would appear inconsistent with the theoretical DSD based on the nominal deflections ϑ_{1n} and ϑ_{2n}. However, consistency between experiments and theory is recovered by considering instead the measured deflections ϑ_{1m} and ϑ_{2m} together with the corresponding DSD, which also

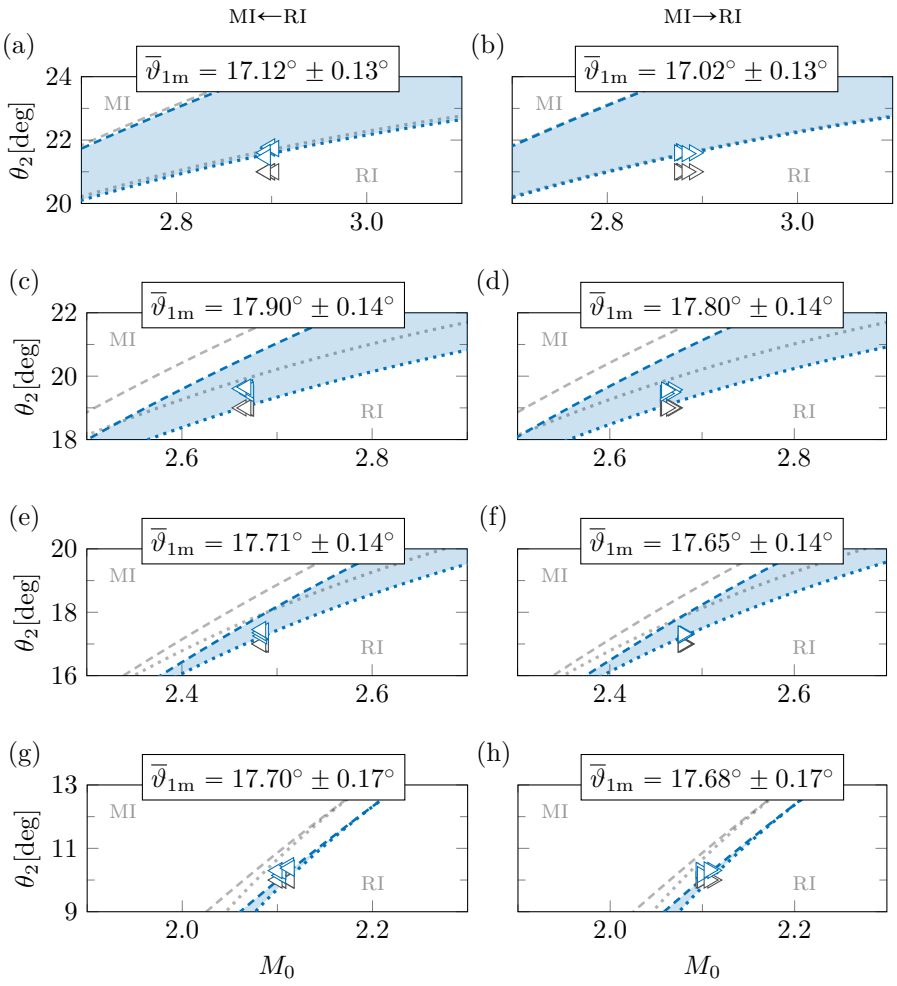

Figure 4.12: Theoretical DSD and resulting RI→MI transition (◁) and MI→RI transition (▷) data based on nominal deflections (grey) and based on measured deflections (blue). Figures (a–b) correspond to $\vartheta_{2n} = 21°$, (c–d) to $\vartheta_{2n} = 19°$, (e–f) to $\vartheta_{2n} = 17°$, and (g–h) to $\vartheta_{2n} = 10°$. Dotted and dashed lines indicate the corresponding *von Neumann* and *detachment* criteria, respectively. The average of the measured upper flow deflection ϑ_{1m} used to recalculate the DSD is indicated at the top of each figure.

confirms that transition in our facilities occurs at (or close to) the *von Neumann* criterion. A very good overlap of the measured transition conditions was found within the expected uncertainty (which is about 0.1°- 0.2°, see table 4.1). The wedge arrangement involving $\vartheta_{2n} = 19°$ is the only geometry for which the detected RI⇄MI transition seems to occur beyond the *von Neumann* criterion but still close to this boundary and within the corresponding DSD.

Table 4.2: Average transition data for all geometries.

geometry		MI←RI			MI→RI		
ϑ_{1n}	ϑ_{2n}	$\overline{M}_0$	$\overline{\vartheta}_{1m}$	$\overline{\vartheta}_{2m}$	$\overline{M}_0$	$\overline{\vartheta}_{1m}$	$\overline{\vartheta}_{2m}$
17.0°	21.0°	2.90	17.12°	21.67°	2.88	17.02°	21.60°
17.0°	19.0°	2.67	17.90°	19.58°	2.66	17.80°	19.52°
17.0°	17.0°	2.48	17.71°	17.37°	2.48	17.65°	17.30°
17.0°	10.0°	2.11	17.70°	10.31°	2.10	17.68°	10.27°

4.4. Summary

Experiments on shock-shock interactions were conducted in a transonic-supersonic wind tunnel with variable free-stream Mach number functionality. Transition between the RI and the MI was induced by variation of the free-stream Mach number. In order to account for possible deformations of the model geometry and other off-design effects, we applied a systematic flow-based post-processing methodology of schlieren visualizations and synchronous pressure readings that enabled accurate tracking of the evolving shock system and precise detection of RI⇄MI transition with high reproducibility. In line with previous works dealing with noisy experimental environments, no transition hysteresis was observed. Due to the measured deviations of the flow deflections from the nominal shock generator angles (of up to 1.2°), calculation of the theoretical DSD consistent with the actual flow conditions was required to confirm that the measured transition data satisfies the *von Neumann* criterion in our experiments. Furthermore, different planes along the optical path were investigated using a focusing schlieren system to assess three-dimensional side-wall effects in the experimental setup. The analysis confirmed that the considerable shock thickening observed in regular schlieren visualizations is caused by shock-wave/boundary-layer interactions at the side-walls, and that the trailing edge of the incident shock footprint is a reliable indicator of the two-dimensional incident shock locations at the mid-plane of the test section.

PART TWO

Shock-wave/turbulent boundary-layer interactions

5

Characterization of the undisturbed turbulent boundary layer

The second part of the present thesis is focused on the physics of STBLIs. But before delving into that, we first take a step back and carefully analyze the undisturbed TBL at different Reynolds numbers. This is particularly instructive for the discussion in chapter 6, which is concerned with Reynolds number effects in STBLIs, since these effects also stem from the differences in the TBL structure at low and high Reynolds number. The analysis of the TBL data, in fact, is not only limited to the aspects that are relevant in the context of STBLIs (e.g., log-layer structures) or that serve to assess the adequacy of the employed numerical setup - it is much more exhaustive than that. The reason for it is the limited availability of high-fidelity TBL datasets in literature, which calls for additional studies in the moderately-high Reynolds number regime. So instead of providing a brief and STBLI-oriented discussion, we decided to expand the content of this chapter and present it as a standalone study on compressible TBLs. In doing so, the resulting discussion will also be of interest to the reader solely concerned with compressible wall-bounded turbulence, since the text makes no explicit reference to the STBLI flow that it is intended to complement. For a discussion of the present TBL data in the context of STBLIs, the reader is then referred to section 6.3.1 of chapter 6, which should be considered after reading the present chapter (section 5.3.3 in particular). Details on the numerical setup employed in the STBLI simulations are also provided in the present chapter, since they only differ from the corresponding TBL setup in the treatment of the top boundary condition.

The content of this chapter has been published as: L. Laguarda, S. Hickel, F. F. J. Schrijer and B. W. van Oudheusden. Assessment of Reynolds number effects in supersonic turbulent boundary layers, *Int J Heat Fluid Flow* **105**, 2024.

5.1. Introduction

In the compressible regime, TBLs are characterized by large mean-property variations, dilatational fluctuations and other phenomena such as localized shocklets [57]. These features emerge as a consequence of the strong non-linear coupling between vorticity, entropy and acoustic fields, which increases the complexity of the flow physics compared to the incompressible case.

Statistical models for the description of TBLs were typically first developed for incompressible flows and later adapted to account for compressibility effects. While some of these effects are still under investigation [104], many models simply revert to the classic hypothesis by Morkovin [105] for the treatment of compressible TBL data at relatively low Mach number. Within this paradigm, compressibility effects are approximated with suitable scalings that account for the mean gradients of temperature, density and viscosity in the boundary layer. The validity of this hypothesis has been assessed in multiple works [106–108] along with the strong Reynolds analogy (SRA), which further assumes negligible total temperature fluctuations and a perfect anti-correlation between the streamwise velocity and temperature fields [105]. Even though their applicability has been shown to be questionable [109–111], these assumptions and related extensions are commonly employed for turbulence modelling due to the lack of better alternatives.

In addition, an important fraction of the available turbulence data has been obtained at relatively low Reynolds numbers. This is specially the case for direct numerical simulations (DNS) of compressible TBL flows, where the Reynolds number dictates the (often prohibitive) grid resolution requirements [112]. The work of Pirozzoli and Bernardini [113] constituted the first DNS investigation that considered a compressible TBL at a moderate viscous Reynolds number of $Re_\tau \approx 1100$, where inner and outer scale separation is emerging. By comparing the corresponding results with low-Reynolds simulations, the authors discuss Reynolds number trends on a wide variety of statistics and further highlight the experimentally observed influence of emerging outer-layer structures on the near-wall turbulence. A follow-up work by the same authors included an additional simulation at $Re_\tau \approx 4000$ [114], where scale separation is much more pronounced. Up to date, this is the highest Reynolds number attained for a supersonic TBL with high-fidelity simulations, which the authors used to complement their previous discussion on Reynold number effects. The analysis of their high-Reynolds data, however, was not as extensive as in the previous study at lower Re_τ. More recently, DNS data at $Re_\tau \approx 1200$ and $Re_\tau \approx 2000$ has also been reported by Huang *et al.* [115] and Cogo *et al.* [116] for TBLs at both supersonic and hypersonic conditions, where the effects of Mach number and strong wall-cooling were also explored.

Clearly, the amount of high-fidelity numerical datasets is nowadays still very limited, which calls for additional studies in the moderately-high Reynolds number regime. While the current parameter range for compressible TBLs can be more easily expanded with experimental investigations [117–119], these alone cannot provide full non-intrusive access to all flow variables and regions of interest. For high-fidelity model development, complementary numerical investigations need to fill in the gaps.

This constitutes a unique opportunity for large-eddy simulations (LES), where a time-accurate prediction of the unsteady flow is obtained at a reduced computational costs compared to DNS [112]. In conventional LES, only the integral scales are resolved by the computational grid and the effect of the unresolved subgrid-scales (SGS) is accounted for with a SGS model. This implies a compromise between accuracy and computational costs; however, under-resolving (and therefore completely modelling) the near-wall structures would put into question the reliability of the resulting dataset for fundamental research. Considering the relevance of the near-wall turbulence cycle and the fact that this region is often inaccessible in experiments, a much more significant approach is to perform wall-resolved LES of the TBL flow. In this case, the local grid resolution close to the wall is typical of DNS rather than conventional LES. While being computationally more expensive, wall-resolved LES is still less demanding than full DNS and the quality of the resulting data, if conducted properly, are essentially the same [120].

In this chapter, we present wall-resolved LES of compressible zero-pressure-gradient TBLs at Mach 2.0 to address the need for additional data as well as to investigate and characterize Reynolds number effects. The resulting database covers more than a decade of Re_τ, from 242 to 5554, which considerably extends the parameter range of current high-fidelity numerical studies. Reynolds number trends are identified on a variety of statistics for skin-friction, velocity, and thermodynamic variables. We further assess the efficacy of recent scaling laws and compressibility effects in the parameter range considered. Particular attention is also placed on the turbulent structures that populate the TBL, with an emphasis on the outer-layer motions at high Reynolds number, which are accurately characterized. In addition, we use the database to investigate uniform momentum regions in the flow [121]. For incompressible wall-bounded turbulence, the average number of uniform regions exhibits a characteristic Reynolds number dependency that could be linked to the meandering motions of the outer-layer structures [122, 123]. Since no such study is available in literature for compressible wall-bounded turbulence, the present LES data is exploited to characterize for the first time the Re_τ-sensitivity of uniform regions in supersonic TBLs. Finally, the distribution of thermodynamic fluctuations as well as their mutual interaction with the velocity field is also analyzed in detail, since these play important roles in compressible turbulence.

5.2. Computational setup

We present wall-resolved LES data for spatially developing zero-pressure-gradient turbulent boundary layers at Mach 2.0 and different Reynolds numbers, from $Re_\tau \approx 250$ to $Re_\tau \approx 5550$. The database comprises three independent simulations, $\mathcal{T}_1$, $\mathcal{T}_2$ and $\mathcal{T}_3$, for which the range of Reynolds number from inflow to outflow plane is provided in table 5.1. As observed, the present study covers more than a decade of Re_τ which allows for a detailed characterization of Reynolds number effects. The line legend is also included in table 5.1 for later reference.

In all cases, the considered fluid is air and details concerning the modelling of its properties are provided in section 2.1.1. The stagnation temperature and pressure

Table 5.1: Details of the TBL simulations. The reported grid spacing is measured at the wall, and $Re_\tau = \overline{\rho}_w u_\tau \delta_0 / \overline{\mu}_w$ is the friction Reynolds number, $Re_\theta = \rho_\infty u_\infty \theta / \mu_\infty$ the momentum-thickness based Reynolds number, and $Re_{\delta_0} = \rho_\infty u_\infty \delta_0 / \mu_\infty$ the velocity-based boundary layer thickness Reynolds number.

Case	Re_τ	Re_θ	Re_{δ_0} $[\times 10^{-3}]$	$\Delta x^+ \times \Delta y^+ \times \Delta z^+$	Legend
$\mathcal{T}_1$	$242 - 402$	$1093 - 1786$	$12.1 - 19.6$	$21.8 \times 0.93 \times 7.7$	---
$\mathcal{T}_2$	$949 - 1338$	$4167 - 6381$	$50.2 - 74.1$	$39.0 \times 0.94 \times 9.8$	-·-·-
$\mathcal{T}_3$	$3897 - 5554$	$20846 - 28892$	$243.4 - 360.3$	$38.5 \times 0.94 \times 10.2$	——

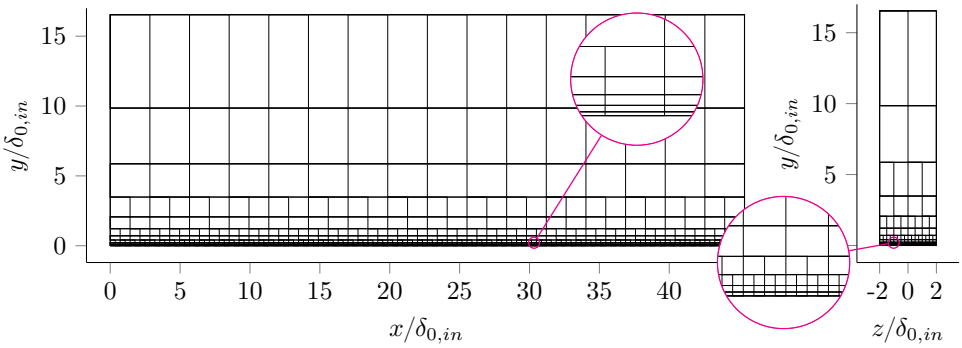

Figure 5.1: Block distribution of the numerical grid for the high-Reynolds case $\mathcal{T}_3$.

are respectively set to $T_0 = 288$ K and $p_0 = 356$ kPa, and the free-stream flow velocity is $u_\infty = 507$ m/s. At the inflow plane, the 99% velocity-based boundary layer thickness $\delta_{0,\,in}$ is 5.2 mm, and a case dependent Reynolds number is achieved by modifying the free-stream dynamic viscosity μ_∞ so as to produce the corresponding values of Re_τ, Re_θ and Re_{δ_0} reported in table 5.1.

The computational domain is rectangular with dimensions $L_x \times L_y \times L_z = 45.5\delta_{0,\,in} \times 16.5\delta_{0,\,in} \times 4.0\delta_{0,\,in}$. Details about the grid spacing in viscous units are also provided in table 5.1. Note that the spatial resolution at the wall is sufficiently large in all cases to properly resolve the wall shear stress $\tau_w = \mu_w \partial u / \partial y|_w$ and the dynamically relevant turbulent structures. Away from the wall plane, a block-wise coarsening is applied in streamwise and spanwise direction as shown in figure 5.1 for the computational domain of the high-Reynolds case $\mathcal{T}_3$. Only one direction is coarsened from one row of blocks to the one above, and always with an expansion ratio of 2. In addition, a grid stretching with constant stretching factor is applied in wall-normal direction. Figure 5.1 also indicates the origin of coordinates, which is placed at the inflow plane, on the wall and half way between the spanwise boundaries.

A non-reflecting boundary condition based on Riemann invariants is used at the top and outflow boundaries of the computational domain [124], and periodicity is imposed in the spanwise direction. The wall is modeled as isothermal at the free-stream stagnation temperature, i.e., $T_w = T_0$. Based on the nominal adiabatic wall-temperature, i.e., $T_{aw} = T_\infty[1 + r(\gamma - 1)M_\infty^2/2]$ with a recovery factor $r = Pr^{1/3}$,

the ratio of wall-temperature to adiabatic wall-temperature is $T_w/T_{aw} = 1.05$. Furthermore, the digital filter technique of Xie and Castro [125] is used at the inflow plane to prescribe adequate turbulent boundary conditions with well-defined space and time correlations. Details about the implementation of the filtering procedure are provided in appendix B and the employed digital filter settings in the present simulations correspond to those of case $A2$ described in the same appendix. These settings include a custom correlation function for tangential directions (equation B.7) which allows for negative values of the correlation and therefore achieves better agreement with DNS data of wall-bounded turbulence [113]. Additionally, three zones with different target length scales are specified at the inflow plane to realistically account for the variation of the TBL structure with wall-distance [126, 127]. The employed scales are specified in table B.2 of appendix B per velocity component, spatial direction and considered zone. Note that only zones 1 and 3 were used in the low-Reynolds case $\mathcal{T}_1$ due to the absence of a fully established quasi-logarithmic layer. The prescribed first and second-order statistical moments at the inflow plane are derived from the DNS database of Pirozzoli and Bernardini [113, 114] for supersonic TBLs at Mach 2.0.

Simulations were performed with the numerical method described in section 2.1.2, and they were carried on as follows. First, an initial transient of 10 flow-through times (FTT) of the full domain length was simulated to ensure a fully developed turbulent flow in statistical equilibrium. This solution interval was discarded from the present analysis. After this transient, simulations were integrated for another 12 FTT of the full domain length. During this second interval, approximately 40000 statistics samples were collected at a sampling interval of $\Delta t u_\infty/\delta_{0,in} \approx 0.013$ and averaged in the homogeneous spanwise direction and in time. In addition, three-dimensional snapshots of the full domain were stored at regular intervals of $\Delta t u_\infty/\delta_{0,in} \approx 2$, leading to an ensemble of approximately 250 snapshots stored per case.

5.3. Results and discussion

The resulting LES database is exploited to characterize the effect of Reynolds number on the flow. Unless otherwise stated, data is extracted at $x/\delta_{0,\,in} = 40$, which corresponds to $Re_\tau \approx 382$, 1291 and 5371 for the three cases.

5.3.1. Skin-friction

The evolution of the skin-friction coefficient starting from $x/\delta_{0,\,in} = 5$ is shown in figure 5.2. The van Driest II transformation [128] is employed to remove Mach number effects and enable comparison with well established correlations for incompressible boundary layers. That is, skin-friction and Reynolds number are reduced to their equivalent incompressible values by means of the following transformation

$$\langle C_{f,inc} \rangle = F_c \langle C_f \rangle, \quad Re_{\theta,\,inc} = \frac{\mu_\infty}{\mu_w} Re_\theta. \tag{5.1}$$

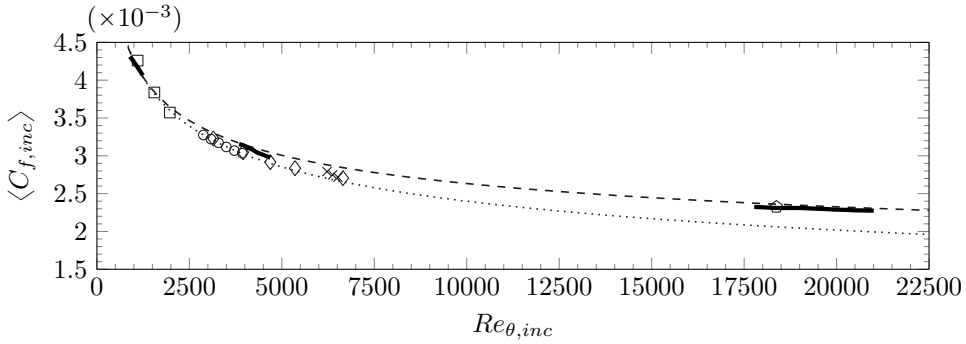

Figure 5.2: Incompressible skin-friction distribution as a function of $Re_{\theta,i}$. Line legend: (——) present LES, (- - -) Kármán-Schoenherr [131], (·····) Smits *et al.* [132]. Symbol legend: (□) Simens *et al.* [133], (◇) Sillero *et al.* [134], (○) Pirozzoli and Bernardini [113], (×) Pasquariello *et al.* [23], (⬠) Bross *et al.* [119].

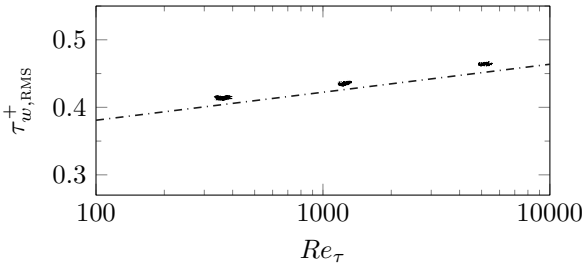

Figure 5.3: Fluctuation magnitude of the wall-shear stress $\tau^+_{w,\mathrm{RMS}}$ for the investigated cases. The dash-dotted line indicates the incompressible relation of Schlatter and Örlü [130].

where F_c is a function of the wall temperature T_w and nominal adiabatic wall temperature T_{aw}, see, e.g., Shahab *et al.* [107] or Hadjadj *et al.* [129]. Incompressible correlations as well as numerical and experimental data at different conditions are also included in figure 5.2 for reference (see caption). As observed, our present LES results are in very good agreement with the reference data, most notably with the Kármán-Schoenherr correlation and the high-Reynolds experimental data of [119] at $Ma = 2.0$ and $Re_\tau = 4680$.

The fluctuation magnitude of the wall-shear stress $\tau^+_{w,\mathrm{RMS}}$ over the second half of the LES domain is shown in figure 5.3. A value in the range of 0.41 to 0.46 is obtained for the considered TBLs, indicating that the fluctuating component of the wall-shear stress amounts to almost half of the corresponding mean value. Figure 5.3 also reveals a clear $\tau^+_{w,\mathrm{RMS}}$ dependency on the Reynolds number, with fluctuation magnitudes increasing with Re_τ. The resulting trend closely follows the linear relation of Schlatter and Örlü [130] derived from incompressible data (dash-dotted line), which confirms the fully developed state of the near-wall turbulence in all cases.

5.3.2. Velocity statistics

In line with previous works at moderate Mach numbers [113, 135], the maximum magnitude of the fluctuating Mach number measured is $\sqrt{M'^2} \approx 0.2$. Therefore, genuine compressibility effects are typically expected to be small [57] and the Morkovin's hypothesis to hold. That is, deviations from incompressible data are mainly associated with the variation of mean thermodynamic quantities across the boundary layer (rather than their fluctuations) and do not fundamentally alter turbulence characteristics [105]. Under this assumption, incompressible velocity statistics should be recovered by simply accounting for mean-property variations.

Figure 5.4(a) shows the van Driest-transformed mean velocity profile u^+_{vD} for each case, where $du^+_{vD} = \sqrt{\overline{\rho}/\overline{\rho}_w}d\overline{u}^+$ accounts for mean density variations. As observed, the transformed profiles exhibit the typical incompressible behavior, with a near-wall viscous sub-layer (where linear scaling $u^+_{vD} = y^+$ holds until $y^+ \approx 5$) and a quasi-logarithmic layer (with close $u^+_{vD} = (1/\kappa)\log y^+ + C$ behavior). The latter is not fully established for case $\mathcal{T}_1$, which is expected at low Reynolds number. For case $\mathcal{T}_3$, on the other hand, the quasi-logarithmic layer extends for more than a decade of inner-scaled wall-distance, from $y^+ \approx 40$ until $y^+ \approx 700$, and conforms to a log-law with a von Kármán constant of $\kappa = 0.4$ and an intercept value of $C = 4.7$. Despite the visually well established logarithmic behavior, however, the diagnostic function $\Xi = y^+ du^+_{vD}/dy^+$ for this case (not shown here) is not constant but rather increases in this region, crossing the theoretical $1/\kappa$ value required for pure logarithmic behavior. As for the wake region, we measure a wake parameter of $\Pi = 0.48$ for case $\mathcal{T}_1$, $\Pi = 0.58$ for case $\mathcal{T}_2$ and $\Pi = 0.63$ for case $\mathcal{T}_3$. These values are consistent with the expected wake parameter dependence on the momentum-thickness Reynolds number and agree well with previous simulations of compressible TBLs [136].

Density-scaled Reynolds stresses are reported in figure 5.4(b) and exemplary illustrate Reynolds number effects in the TBL topology. Most notably, the viscous-scaled fluctuation intensity for the wall-parallel components increases with Re_τ. This is a direct effect of the emergent large-scale coherent motions in the near-logarithmic region, whose contributions to the wall-parallel velocity variances is increasingly significant with Reynolds number [137]. The observed increase in streamwise stress near the wall also reveals the modulating influence that such outer-layer motions have on the near-wall cycle [138]. Despite the fact that the viscous-scaled near-wall turbulence is a self-sustaining process [139, 140], large-scale variations in the velocity fluctuations away from the wall are known to modulate near-wall fluctuations [138] which overall increase with Reynolds number [141]. The formation of a distinct plateau for the shear stress, which is clearly visible for case $\mathcal{T}_3$ in figure 5.4(b), is also a direct Reynolds number effect. This plateau corresponds to the formation of a quasi-equilibrium layer where production of turbulence kinetic energy (TKE) approximately balances dissipation [142]. Other visible Reynolds number effects on the velocity variances concern the wall-normal component, whereby its peak location moves from the inner part to the outer part of the boundary layer at sufficiently high Re_τ.

For reference purposes, DNS data of Pirozzoli and Bernardini [113, 114] for su-

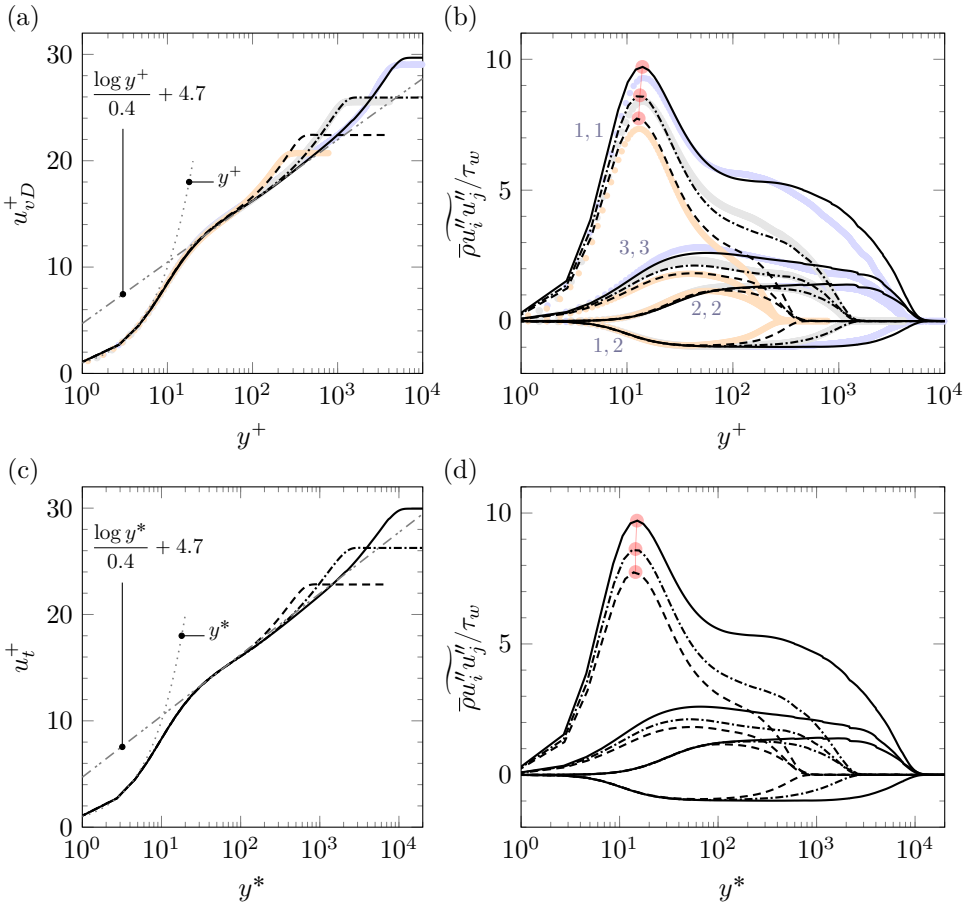

Figure 5.4: First and second order velocity statistics: (a–b) van Driest transformed mean velocity and density-scaled Reynolds stresses over the inner-scaled wall-distance y^+, and (c–d) total-stress-based transformed mean velocity and density-scaled Reynolds stresses over the semi-local wall-distance y^* (see equations (5.2) and (5.3)). For reference, DNS data of Pirozzoli and Bernardini [113, 114] at Mach 2.0 and $Re_\tau \approx [250, 1100, 4000]$ is respectively indicated in panels (a) and (b) with orange, gray and blue markings. The indices i, j for the Reynolds stresses are indicated in panel (b), while red circles in both panels (b) and (d) highlight the peak value of the streamwise stress.

personic TBLs at Mach 2.0 and various Reynolds numbers is also included in figures 5.4(a) and 5.4(b) (indicated with markers). Overall, the present LES data agrees very well with the DNS data, with minor differences attributed to different friction Reynolds numbers (particularly visible at the boundary layer edge). We also note that the peak value for the streamwise stress is very well captured in the present simulations, and closely follows the logarithmic fit to the reference DNS data [114], see figure 5.5.

We recall that the wall-temperature in the present simulations is very close to

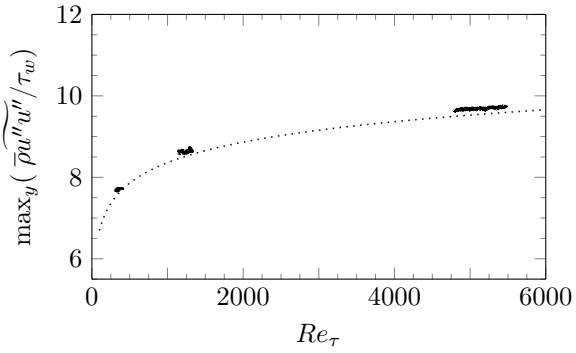

Figure 5.5: Distribution of the peak value for the density-scaled streamwise Reynolds stress. Line legend: (solid) present LES data, (dotted) logarithmic fit to the DNS data of Pirozzoli and Bernardini [113, 114] at Mach 2.0.

its nominal adiabatic value, i.e., $T_w/T_{aw} = 1.05$. However, the employed wall condition is strictly non-adiabatic, and the accuracy of the van Driest transformation is known to deteriorate with (increasing) non-adiabatic conditions [115, 143]. Therefore, alternative transformations to that of van Driest are also considered here to assess whether the collapse of the mean velocity profiles can improve to any extent. Particularly, we consider the transformation proposed by Trettel and Larsson [143], which is identical to that of Patel *et al.* [144], as well as the transformation proposed by Griffin *et al.* [145]. The former is grounded on the premise that a transformed logarithmic law shall preserve the momentum balance in the transformed state. This gives rise to a transformation kernel for both the mean velocity profile as well as the wall-distance coordinate, the later coinciding with the semi-local scaling $y^* = y/l^*$ of Huang *et al.* [110], where

$$l^* = l^+ \frac{\overline{\mu}}{\mu_w} \sqrt{\frac{\rho_w}{\overline{\rho}}}, \tag{5.2}$$

is the semi-local viscous length scale [143]. We also note that the earlier work of Patel *et al.* [144] provides a different foundation for the applicability of the same transformation. By re-scaling the Navier-Stokes equations with local quantities, the authors demonstrate that the van Driest transformed velocity as well as second order turbulent statistics depend on the semi-local viscous Reynolds number $Re_\tau = \delta/l^*$.

The transformation proposed by Patel *et al.* [144] and Trettel and Larsson [143] was tested on the present LES data and led to an increased scatter along the buffer and quasi-logarithmic layers. Other authors have reported similar effects [115, 116, 145] and for the sake of brevity, the resulting transformed profiles are not shown here. As indicated by Griffin *et al.* [145], the increased scatter is attributed to the over-prediction of the mean shear in the beginning of the logarithmic layer, which directly stems from the resulting viscous stress invariance of this transformation throughout the whole boundary layer (instead of only within the viscous sub-layer). In view of this issue, Griffin *et al.* [145] proposed a modified transformation that treats viscous and Reynolds stresses independently and only in their respective domains

of applicability. That is, the semi-local scaling proposed by Patel *et al.* [144] and Trettel and Larsson [143] is recovered for the viscous stresses near the wall while the Reynolds shear stress away from the wall is scaled assuming an approximate balance between turbulence production and dissipation [145]. The resulting transformation is referred to as the total-stress-based transformation $u_t[y^*] = \int S_t^+ dy^*$, where

$$S_t^+ \approx \frac{S_{eq}^+}{1 + S_{eq}^+ + S_v^+}, \tag{5.3}$$

and $S_{eq}^+ = (\mu_w/\overline{\mu})(\partial u^+/\partial y^*)$ and $S_v^+ = (\overline{\mu}/\mu_w)(\partial u^+/\partial y^+)$.

Careful inspection of the total-stress-based transformed mean velocity profiles against the semi-local wall-distance coordinate y^*, which are shown in figure 5.4(c), reveals some improvements in the data collapse along the linear and particularly the buffer layer compared to the van Driest transformed profiles of figure 5.4(a). Additionally, it does not increase the scatter in the quasi-logarithmic layer, overcoming the shortcomings of the transformation proposed by Patel *et al.* [144] and Trettel and Larsson [143]. This shows the enhanced capabilities of the total-stress-based scaling, even for TBLs with quasi-adiabatic wall conditions. As for the boundary layer wake, the data scatter still remains albeit with a slightly reduced deviation from the quasi-logarithmic behavior compared to figure 5.4(a).

Regarding second-order statistics, Patel *et al.* [144] argue that data for variable property flows should also reduce to their constant property counterparts by simply employing the semi-local inner co-ordinate y^*. In order to assess the validity of this scaling for the Reynolds stresses, they are shown in figure 5.4(d) against y^*. Overall, improvements in the data collapse are not apparent when compared to figure 5.4(b). However, the semi-local scaling does improve the overlap of the wall-normal stress profiles in the linear and buffer layer, and leads to a better alignment of the near-wall streamwise stress peak (indicated with red circles).

The effect of Reynolds number on the streamwise velocity statistics is now assessed by inspecting the corresponding skewness $S(u) = \overline{u'^3}/\overline{u'^2}^{3/2}$ and flatness $F(u) = \overline{u'^4}/\overline{u'^2}^2$. These distributions are respectively shown in figures 5.6(a) and 5.6(b) where clear differences can be observed. Most notably, both skewness and flatness increase near the wall at high Reynolds number. This could be attributed to the stronger footprint of the log-layer structures on the near-wall turbulence, which becomes more intermittent. The skewness profiles exhibit a qualitatively similar behavior, that is, positive values very close to the wall and a relaxation towards a nearly Gaussian behavior ($S(u) \approx 0$) above the viscous sub-layer. However, $S(u)$ is clearly negative for case $\mathcal{T}_1$ beyond $y^+ \approx 10$, while the profile for the high-Reynolds case $\mathcal{T}_3$ is much closer to zero, i.e., closer to a purely Gaussian behavior. This could be attributed to the presence of a well-established quasi-logarithmic layer in the latter case. The corresponding flatness distributions in this region approach a value of 3 in all cases, see figure 5.6(b), which confirms the nearly Gaussian behavior observed in the skewness profiles. However, $F(u)$ also exhibits an apparent Reynolds number dependency beyond $y^+ \approx 30$, since increasingly lower values than 3 are observed at higher Reynolds number. This implies that the tailedness of the

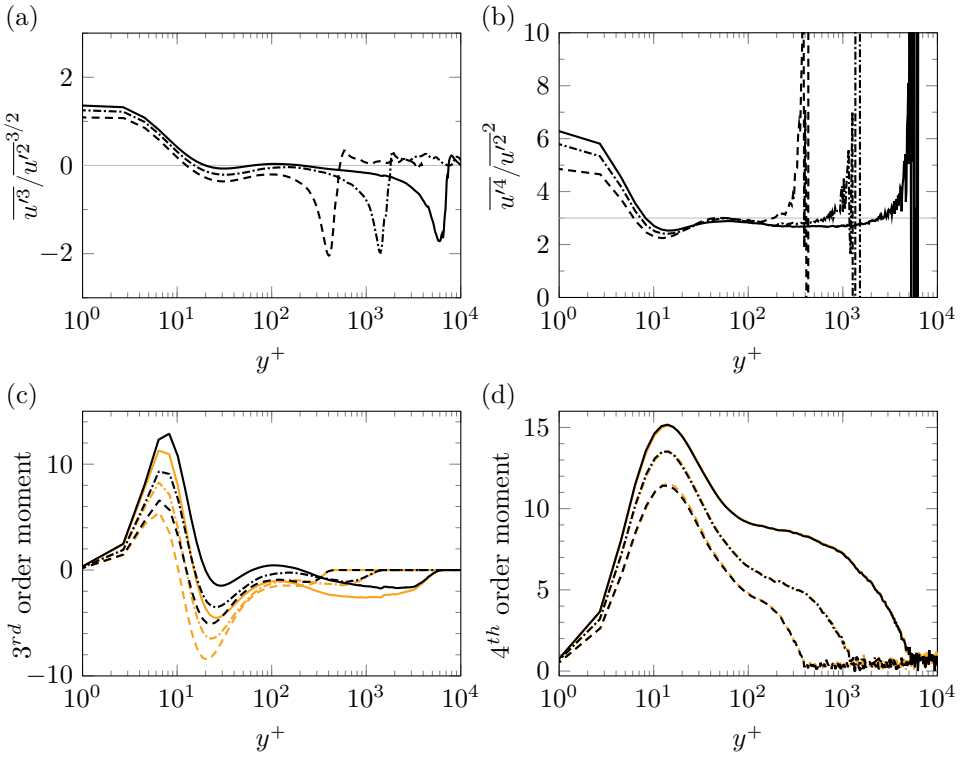

Figure 5.6: Higher-order moments of the streamwise velocity: (a) skewness, (b) flatness, (c) density-scaled third order central moment $\overline{\rho}^{3/2}\overline{u_i'^3}/\tau_w^{3/2}$ (black) and $\overline{\rho}^{3/2}\overline{u_i''^3}/\tau_w^{3/2}$ (orange), and (d) density-scaled fourth order central moment $\overline{\rho}\left(\overline{u_i'^4}\right)^{1/2}/\tau_w$ (black) and $\overline{\rho}\left(\overline{u_i''^4}\right)^{1/2}/\tau_w$ (orange).

corresponding probability distribution decreases with increasing Reynolds number. Moreover, all cases exhibit very similar intermittent behavior towards the edge of the boundary layer, i.e., negative skewness and large flatness, which is caused by outward excursions of low-speed flow into the free-stream. Wall-normal distributions of the intermittency coefficient, defined as the fraction of time that the flow is turbulent, were also computed for the investigated TBLs (not shown here) and do not exhibit any apparent Reynolds number dependency.

Before concluding this section, the influence of density fluctuations, and therefore the validity of Morkovin's hypothesis, on high-order statistics is assessed. As already mentioned, Morkovin's hypothesis implies that any statistical moment is independent of the averaging procedure, i.e., Reynolds or Favre averaging. If that is the case, the following relation would hold for the third order central moment of a velocity component [144]

$$\overline{\rho}^{3/2}\overline{u_i'^3}/\tau_w^{3/2} \stackrel{?}{=} \overline{\rho}^{3/2}\overline{u_i''^3}/\tau_w^{3/2}. \tag{5.4}$$

A single prime denotes a fluctuation from the Reynolds-averaged mean (indicated with an over-bar), while a double prime is used for fluctuations from Favre-averaged quantities. A similar relation would also apply for the fourth order central moment, i.e.,

$$\overline{\rho}\sqrt{\overline{u_i'^4}}/\tau_w \stackrel{?}{=} \overline{\rho}\sqrt{\overline{u_i''^4}}/\tau_w. \tag{5.5}$$

In order to assess whether these relations indeed hold in the present LES data, both averaging procedures are compared in figures 5.6(c) and 5.6(d) for the third-order and fourth-order central moments of the streamwise velocity, respectively. As observed, a clear disagreement is found for the third-order moment, see figure 5.6(c), where the Reynolds-averaged (black) and Favre-averaged (orange) profiles do not collapse for the cases considered. Patel *et al.* [144] reported a similar disagreement for their DNS data of variable-property turbulent channel flows at low Mach number. Our simulations confirm that Morkovin's hypothesis does not hold for third-order statistics of wall-bounded turbulence also in the compressible flow regime. In terms of the fourth order central moments, see figure 5.6(d), good collapse is found between the Reynolds and Favre averaged profiles in all cases, also in agreement with the findings of Patel *et al.* [144]. Note that this also applies for the other velocity components, but for the sake of brevity the corresponding statistical moments are not included in this paper.

5.3.3. Turbulence structure

The effect of Reynolds numbers on the statistical properties of turbulent structures is analyzed next. As a starting point, we consider the pre-multiplied streamwise energy spectra of streamwise velocity fluctuations, which are shown in figure 5.7. Only the last third of the LES domain has been considered for the spectra, which have been calculated at selected wall-normal locations that coincide with the computational grid (no interpolation used) and appear approximately equispaced in logarithmic scale. The spectra have been estimated using Welch's algorithm with Hamming windows and 3 segments with 75% overlap, in addition to the averaging in spanwise direction and in time.

As observed, all spectral distributions bear clear similarities very close to the wall, where a peak corresponding to the signature of energetic near-wall streaks is found at $y^+ \approx 15$ in all cases. The wavelength associated with these high- and low-speed regions is approximately constant in viscous units and equal to $\lambda_x^+ \approx 700$, which is in good agreement with previous studies [115, 138]. Further away from the wall, however, figure 5.7(c) reveals the emergence of energy at high wavelengths for the high-Reynolds case $\mathcal{T}_3$ that is absent in the spectrum for the other cases. This energy increase is already noticeable close to the wall and reaches a local maximum in the quasi-logarithmic region, at about $y/\delta_0 \approx 0.1$. The wavelength associated with this local peak is about $\lambda_x/\delta_0 \approx 6$, which is much larger than the one associated to the near-wall streaks. Clearly, this outer peak is the signature of the emergent large-scale motions in this region. Such bimodal configuration of the streamwise spectra in figure 5.7(c), with two competing energetic peaks at different wavelengths, evidences inner/outer scale separation and the genuinely high-Reynolds nature of case $\mathcal{T}_3$ [138].

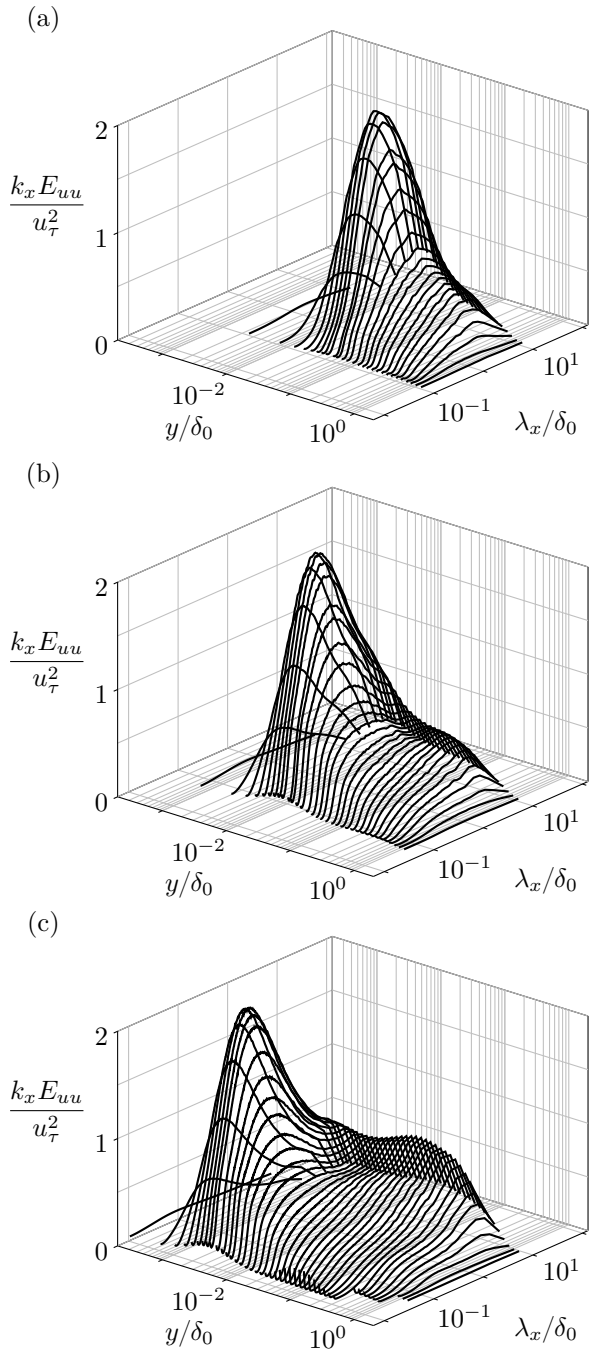

Figure 5.7: Streamwise spectra of streamwise velocity fluctuations for (a) case $\mathcal{T}_1$, (b) case $\mathcal{T}_2$, and (c) case $\mathcal{T}_3$.

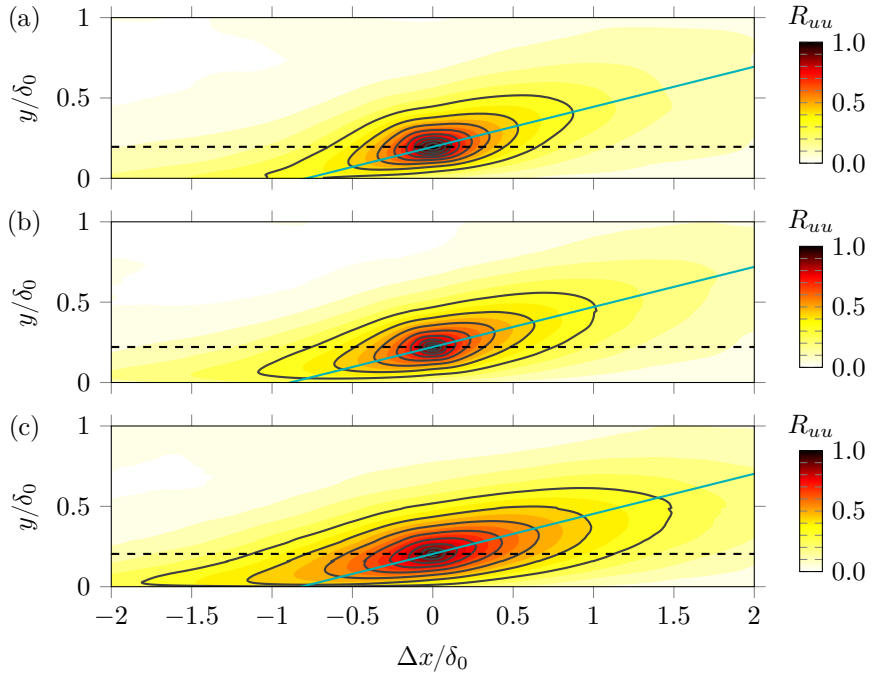

Figure 5.8: Two-point autocorrelation map of streamwise velocity fluctuations $R_{u,u}$ for (a) case $\mathcal{T}_1$, (b) case $\mathcal{T}_2$, and (c) case $\mathcal{T}_3$. The reference wall-normal location is $y_{ref}/\delta_0 = 0.2$ and the solid black lines indicate contour levels from 0.1 to 0.9 in increments of 0.1. In all figures, a blue line with an inclination of 14° intersecting the maximum correlation point is included for reference.

The streamwise-wall-normal organization of the large-scale turbulent structures is further characterized in figure 5.8 by the two-point autocorrelation map of streamwise velocity fluctuations

$$R_{uu}(\Delta x, y) = \frac{\langle u'(x, y, z, t) u'(x + \Delta x, y_{ref}, z, t) \rangle}{\sigma_u(y)\, \sigma_u(y_{ref})}, \tag{5.6}$$

where the reference wall-normal location y_{ref} is set at $0.2\delta_0$ following Bross *et al.* [119]. The angle brackets are employed to denote time-, spanwise-, and also streamwise-averaging, over a domain $4\delta_0$ long and centered at $x/\delta_{0,\,in} = 40$.

The extent of the correlation noticeably increases with increasing Reynolds number, see figure 5.8(c), which evidences the corresponding enlargement of the emergent outer-layer motions. The scale interaction between these structures and the near-wall turbulence is also reflected by the increased correlation magnitudes at the wall. This wall-coherence is established at an oblique angle with respect to the free-stream flow, which implies a forward inclination of the log-layer structures. Despite the scatter of the reported inclination angles in literature [146], recent studies reveal a typical eddy orientation between 12° and 20° [113, 119, 147, 148]. The correlation maps in figures 5.8(a) and 5.8(b) for the low- and moderate-Reynolds

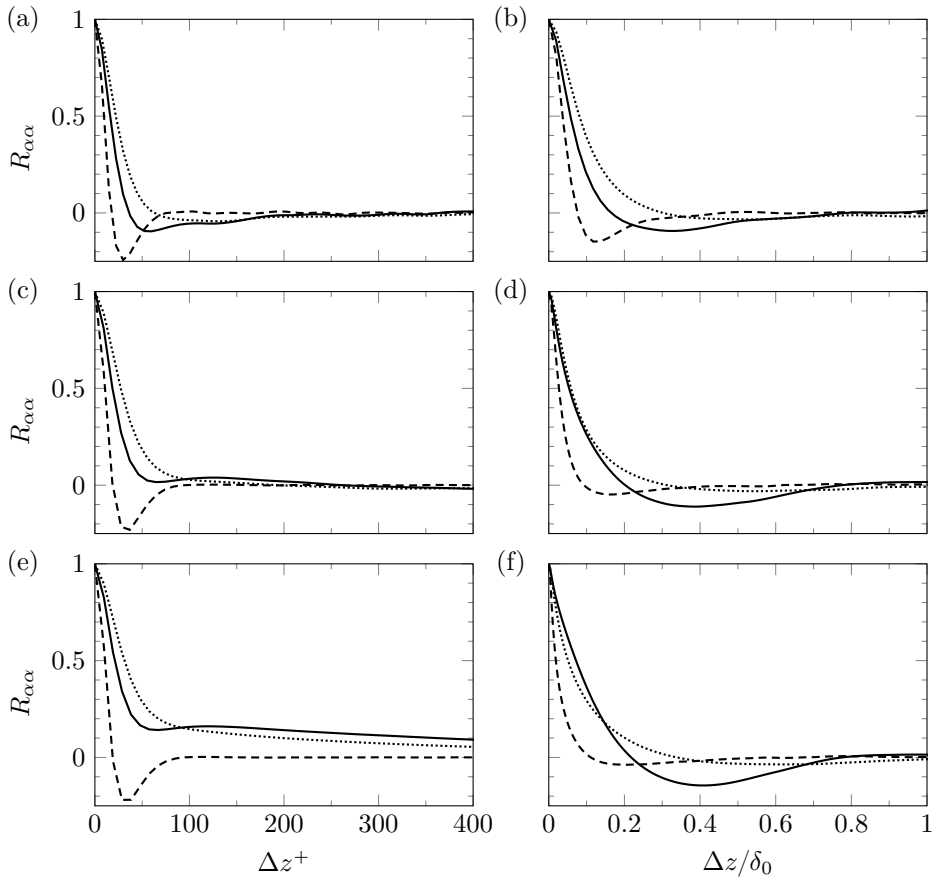

Figure 5.9: Two-point autocorrelation functions of the velocity components in the spanwise direction at (left) $y^+ \approx 15$, and (right) $y/\delta_0 \approx 0.1$. Panels (a) and (b) correspond to case $\mathcal{T}_1$, panels (c) and (d) to case $\mathcal{T}_2$, and panels (e) and (f) to case $\mathcal{T}_3$. Line styles legend: streamwise velocity (——), wall-normal velocity (- - -), and spanwise velocity (·····).

cases conform well with an inclination of 14° in the outer part of the boundary layer, which corresponds to the value reported by Marusic and Heuer [147] over a wide range of Reynolds numbers. This inclination is indicated in the figures with a solid blue line. The high-Reynolds case $\mathcal{T}_3$, in turn, exhibits a slightly smaller inclination above y_{ref} of approximately 10°, see figure 5.8(c). We also note that all correlation maps conform to more shallow angles between 8° and 11° near the wall (in the region below the reference height). In view of this, a line fit of the peak points in wall-normal direction is considered to be a poor representation of the inclination of the correlation map, and would certainly lead to a smaller inclination angle than 14° in all cases.

The average spanwise spacing of the dominant turbulent structures is assessed from spanwise autocorrelation functions and related spectra to better understand

their three-dimensional arrangement. Correlation functions of the velocity components at two different wall-normal locations, i.e., $y^+ \approx 15$ and $y/\delta_0 \approx 0.1$, are shown in figure 5.9. Correlations have been obtained by first applying the Fourier transform to the instantaneous fluctuation distribution in the spanwise direction, then computing the power spectrum and averaging (in Fourier space) over all instances, and finally transforming back to physical space. Note that all variables (also thermodynamic variables, which are not shown) fully de-correlate for a spacing corresponding to δ_0, see the rights panels of figure 5.9, which is smaller than the domain half-width $L_z/2$. This confirms that turbulence dynamics in the present simulations do not suffer from limited-span effects.

In all cases, the streamwise velocity correlation calculated at $y^+ \approx 15$ has a local minimum at $\Delta z^+ \approx 50$. This provides an indication of the spanwise spacing between adjacent near-wall streaks, which are characterized by velocity fluctuations of opposite sign. In reference investigations of compressible TBLs at lower Reynolds numbers [135, 149], such local minimum is actually global and associated with negative correlation values. As shown in the left panels of figure 5.9, this is true for the low-Reynolds case but no longer holds for the moderate and high-Reynolds TBLs, where the local minimum near the axis is found at $R_{uu} \approx 0$ and $R_{uu} \approx 0.15$ respectively. While the alternating streak pattern of low- and high-momentum regions near the wall is still present in these cases, the increasingly positive value of the local minimum highlights the organizing influence of the emergent outer-layer motions on the small-scale fluctuations near the wall. This influence is better illustrated in figure 5.10 which directly compares the streamwise velocity correlation at $y^+ \approx 15$ with the one obtained at $y/\delta_0 \approx 0.1$. For the high-Reynolds case, see figure 5.10(b), the global minimum of the near-wall correlation (black line) clearly coincides with the global minimum of the correlation at $y/\delta_0 \approx 0.1$ (orange line). This further evidences the imprint of the log-layer on the near-wall region at high Reynolds number. Inspired by the analysis of Hutchins and Marusic [138], we also show correlations computed from spatially high-pass filtered and spatially low-pass filtered instantaneous data at $y^+ \approx 15$ to highlight the separate contribution of small scales and large scales to the total correlation, see figure 5.10(b). Filtering is performed in spanwise direction with a finite impulse response (FIR) filter and cutoff wavelengths $\lambda_z^+ = 300$ for the high-pass and $\lambda_z/\delta_0 = 0.2$ for the low-pass filtering operation. The correlation obtained from the spatially low-pass filtered flowfield (dash-dotted line) closely follows the correlation calculated at $y/\delta_0 \approx 0.1$ for large spacing, which shows that the large-scale contribution at $y^+ \approx 15$ can be associated with the imprint of log-layer structures. The correlation computed from the spatially high-pass filtered flow field, on the other hand, recovers the negative peak near the axis (see the dotted line) thus regaining qualitative agreement with low-Reynolds TBL data in absence of scale separation.

Besides the alternating streaks of high- and low-speed fluid, the near-wall region is also populated with vortical structures [146]. Together, these two types of coherent motions are responsible for the near-wall turbulence regeneration cycle [140, 150]. The presence of such vortices, mostly oriented in the streamwise direction, explains the observed near-wall distribution of the wall-normal velocity correlation functions

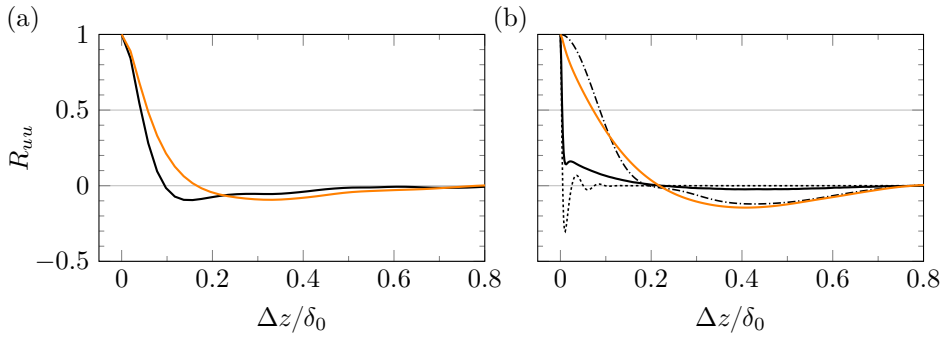

Figure 5.10: Spanwise autocorrelation function of streamwise velocity fluctuations for (a) the low-Reynolds case $\mathcal{T}_1$, and (b) the high-Reynolds case $\mathcal{T}_3$ at $y^+ \approx 15$ (black solid line) and $y/\delta_0 \approx 0.1$ (orange line). Panel (b) additionally includes the correlation computed from the spatially high-pass filtered flowfield (dotted line) and the spatially low-pass filtered flowfield (dash-dotted line) at $y^+ \approx 15$.

in figure 5.9. The global minimum, located at $\Delta z^+ \approx 35$, provides an indication of the average vortex spacing in spanwise direction. In agreement with previous works [135, 146], profiles of streamwise vorticity fluctuations in the wall-normal direction (not shown here) have a local maximum at $y^+ \approx 15$ and a local minimum at $y^+ \approx 5$ in all cases. These heights provide additional insights into the average vortex core location and radial extent [135, 140] and appear insensitive to the Reynolds number in the present simulations.

The spanwise spectra associated with the spanwise velocity correlation functions in figure 5.9 is included in figure 5.11. At $y^+ \approx 15$, see figure 5.11(a), the inner-scaled spectra excellently collapse at low wavelengths up to the local peak at $\lambda_z^+ \approx 100$, which is a global peak for case $\mathcal{T}_1$. This confirms the characteristic spanwise spacing of the near-wall streaks inferred from the spatial correlations, which is in good agreement with previous works [114, 135]. The location of the spectral peak for the higher-Reynolds cases, however, is found at much higher wavelengths than $\lambda_z^+ \approx 100$, and is associated with increasing energy levels. This trend is attributed to the imprint of the emergent outer-layer motions, which appear spaced much further apart in spanwise direction [113]. Their approximate spacing is deduced from the spectra at $y/\delta_0 \approx 0.1$, which is shown in figure 5.11(b) in outer scaling. As observed, all spectra exhibit a peak at $\lambda_z \approx 0.7\delta_0$ that reveals the average spacing of outer-layer structures. While the peak energy is higher for case $\mathcal{T}_3$, the fact that the corresponding wavelength remains unaffected by Reynolds number indicates its negligible impact on the width of turbulent structures away from the wall. This observation is in agreement with the experimental results of Hutchins and Marusic [137] and Bross *et al.* [119]. Figure 5.11(b) also highlights the collapse of the spectral distributions for cases $\mathcal{T}_2$ and $\mathcal{T}_3$ along the inertial sub-range, which extends for over a decade with close $\kappa_z^{-5/3} = (2\pi/\lambda_z)^{-5/3}$ behavior characteristic of local isotropy (indicated with a dotted line).

The characteristic size of turbulent structures is further established by means of

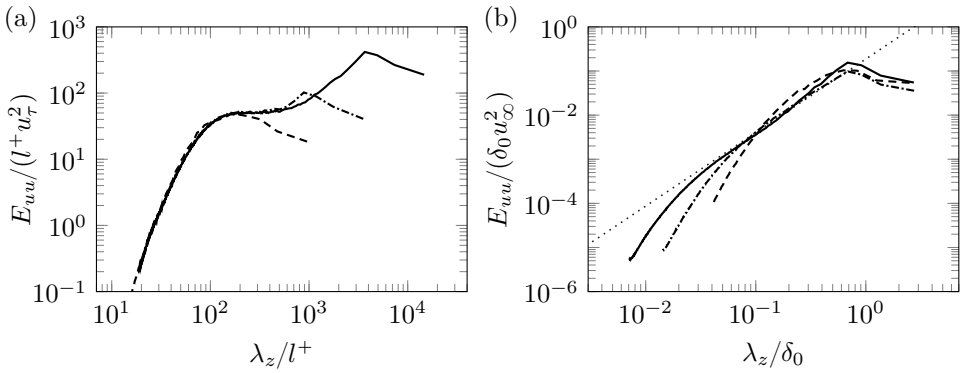

Figure 5.11: Spanwise spectra of streamwise velocity fluctuations at (a) $y^+ \approx 15$ in inner scaling, and (b) $y/\delta_0 \approx 0.1$ in outer scaling. The dotted line in (b) indicates $\kappa_z^{-5/3} = (2\pi/\lambda_z)^{-5/3}$ behavior.

5

the corresponding streamwise and spanwise integral length scales, which are reported in figure 5.12 for all cases. Length scales are here defined as the area between the corresponding correlation function and the isoline $R_{\alpha\alpha}/R_{\alpha\alpha}(0) = 0.05$ [113]. The largest streamwise length scales, as shown in figures 5.12(a–c), are clearly associated with the streamwise velocity component (indicated with upward pointing triangles). For the low-Reynolds case $\mathcal{T}_1$, the maximum value of the corresponding scale distribution for this variable is found at $y^+ \approx 15$ and is related to the near-wall streaks. For the other cases, however, there is a scale increase from the wall towards the quasi-log layer, where the peak value is found at $y/\delta_0 \approx 0.1 - 0.2$. This scale increase is related to the emergent coherent structures in this region, whose mean streamwise elongation is also Reynolds number dependent. As observed, the largest length-scales are found for the high-Reynolds case $\mathcal{T}_3$ which evidences the enlargement of the outer-layer motions with increasing Reynolds number. The corresponding values, which exceed $1.3\delta_0$ at $y/\delta_0 \approx 0.1$, are slightly lower than those experimentally measured by Ganapathisubramani [151] on a Mach 2.0 TBL at $Re_\tau = 5800$, where the peak value was attained at $y/\delta_0 \approx 0.4$. This could be attributed to the lower Reynolds number of case $\mathcal{T}_3$ compared to the experiments. In figure 5.12(c), an emerging local peak is visible at approximately half the boundary layer thickness, and this peak could eventually become global at higher Reynolds numbers. Regarding the streamwise scales associated with the temperature field, indicated with circles in figures 5.12(a–c), they follow the same trend as those for the streamwise velocity, albeit with approximately half the magnitude. This is in very good agreement with the observations of Pirozzoli and Bernardini [113]. The cross-stream velocity components, in turn, exhibit much smaller streamwise length scales, with comparable values ranging from $0.1\delta_0$ to $0.3\delta_0$. In addition, they appear weakly dependent on the Reynolds number, with slightly lower values measured for the high-Reynolds case $\mathcal{T}_3$.

Spanwise length scales for the considered variables are included in figures 5.12(d–f). In all cases, the streamwise velocity, spanwise velocity and temperature scale distributions exhibit a steep rise near the wall, and they progressively relax towards

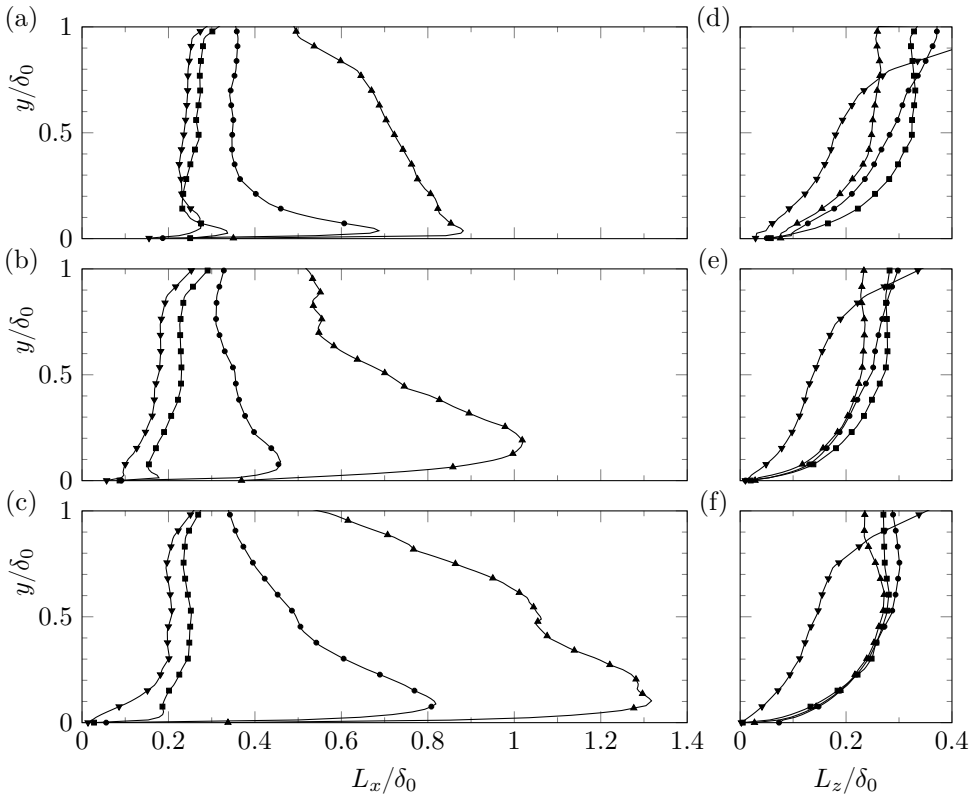

Figure 5.12: Integral length scale distributions measured in the streamwise direction (L_x, top panels) and spanwise direction (L_z, bottom panels) for: (a,d) case $\mathcal{T}_1$; (b,e) case $\mathcal{T}_2$; (c,f) case $\mathcal{T}_3$. Marker legend: streamwise velocity (▲), wall-normal velocity (▾), spanwise velocity (■) and temperature (●).

values between $0.2\delta_0$ to $0.3\delta_0$ within half the boundary layer thickness. Interestingly, the aforementioned scale distributions appear to overlap at high Reynolds number, see figure 5.12(f) for case $\mathcal{T}_3$. At low Reynolds number, where these structures are absent, the reported scale distributions are visibly different, see figure 5.12(d) for case $\mathcal{T}_1$, and the largest scales are associated with the spanwise velocity. In terms of the wall-normal velocity, its corresponding scales present a different behavior than the rest. As observed, they first exhibit a moderate increase near the wall in all cases, which becomes steeper in the outer part of the boundary layer where the scales become the largest.

Another aspect connected to the turbulence structure in TBL flows involves the presence of confined zones with relatively uniform streamwise momentum, the so-called uniform momentum regions (UMZs). Adrian *et al.* [121] attributed UMZs to coherent hairpin vortices in the flow, which tend to align in streamwise direction and form packets with similar convection speeds. Within this paradigm, thin regions of high $\partial u/\partial y$ appear due to the continuous passage of hairpin heads, which translates

into wall-normal step-like jumps in the instantaneous streamwise momentum rather than a smooth variation [122]. More recently, the experimental work of Laskari *et al.* [123] linked the existence of UMZs to different large-scale events in the quasi-logarithmic layer, which meander in spanwise direction and generate instantaneous low- and high-momentum regions across the measurement plane.

The presence of UMZs and their dependence on the Reynolds number is well documented for incompressible TBLs [121–123] but very few studies are available for compressible TBLs. The experimental works of Williams *et al.* [152] and Bross *et al.* [119] are among the few studies that provide evidence for the presence of UMZs in high-speed TBLs, which appear to be similar to their incompressible counterparts. More recently, Cogo *et al.* [116] also observed a zonal distribution for the static temperature in their DNS data of high-speed TBLs with heat transfer. The present LES database offers a unique opportunity to further support these claims as well as effectively quantify Reynolds number effects on the resulting number of UMZs, which has not been yet documented for compressible TBLs.

The streamwise velocity u/u_∞ as well as the static temperature T/T_∞ are therefore considered for the detection of uniform zones (UZs), which proceeds as follows. First, the quantity of interest is sampled within a streamwise-wall-normal slice to generate its corresponding (instantaneous) probability density function (PDF). The required bins for the construction of the PDF are defined in steps of $0.5u_\tau$ for $u/u_\infty \in [0, 1.05]$. The associated bin size for $T/T_\infty \in [0.95, T_w/T_\infty]$, in turn, is selected so as to match the number of bins employed for u/u_∞. Once the target PDFs are assembled, a peak detection algorithm identifies the location of the various peaks within each PDF as well as the least probable value between peaks. The resulting number of peaks thus corresponds to the number of UZs for the quantity of interest in the considered slice, while the least probable values between the detected peaks define the boundaries of the UZs. The parameter set for the peak detection algorithm is adopted from Laskari *et al.* [123] and corresponds to a minimum peak height of 0.3, a minimum prominence (i.e., distance from neighboring values) of 0.05, and at least two bins between adjacent peaks.

For an optimum evaluation of UZs, the flow above the turbulent/non-turbulent interface (TNTI) is excluded from the analysis. This is required to prevent the free-stream velocity from creating a dominant peak in the corresponding PDF that would inhibit the detection of other peaks in its vicinity [122]. The employed definition for the TNTI is adopted from Cogo *et al.* [116] and is based on the square of the momentum defect $\Delta\mathrm{p}$ induced by the TBL, i.e,

$$\Delta\mathrm{p} = \frac{(\rho u - \rho_\infty u_\infty)^2 + (\rho v - \rho_\infty v_\infty)^2}{(\rho_\infty u_\infty)^2 + (\rho_\infty v_\infty)^2} = 0.001. \tag{5.7}$$

In addition, the region below $y^+ = 100$ is also excluded for consistency with experimental datasets, since this region is often unavailable in experiments [122]. In streamwise direction, the considered domain is also finite to prevent the resulting PDF from being smoothed out [122]. Following Laskari *et al.* [123], we consider a length of approximately $2600l^+$ in streamwise direction and centered around $x/\delta_{0,in} = 40$.

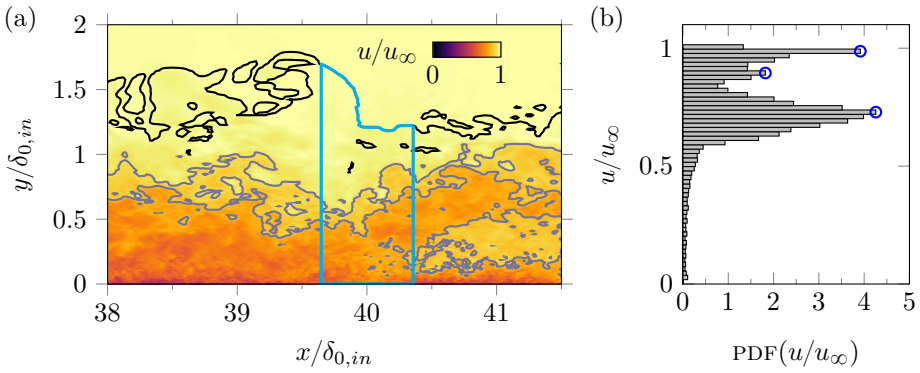

Figure 5.13: (a) Instantaneous impression of the streamwise velocity field, and (b) corresponding PDF of the streamwise velocity magnitude. In (a), the TNTI and the edge of the identified UZs are respectively indicated with black and gray lines, while the region considered for the analysis of UZs is outlined in blue. In (b), peak values identified with the peak search algorithm are indicated with blue circles.

5

Figure 5.13(a) includes an example of an instantaneous streamwise velocity field for case $\mathcal{T}_3$ where the region considered for the detection of UZs is outlined in blue. The boundaries of the detected UZs are indicated in gray, and the TNTI is shown in black. As observed, the identified boundaries of the UZs are in very good qualitative agreement with the instantaneous flow organization, which conforms to a zonal structure. The corresponding instantaneous PDF of the sampling region of figure 5.13(a) is included in figure 5.13(b) and shows the three distinct peaks that correspond to the modal velocities of the identified UZs [121].

To accurately assess Reynolds number effects on the number of UZs, we consider two slices per instantaneous snapshot, which leads to an ensemble of $\sim$500 slices per case. The extracted slices within one snapshot are separated over a distance $1.3\delta_0$ in spanwise direction to ensure proper data decorrelation. The corresponding number of UZs is then identified for each slice, and the PDF of the number of UZs is assembled per variable and for each of the investigated TBLs. The resulting PDFs are shown in figure 5.14(a) and confirm the observation of de Silva *et al.* [122] for incompressible wall-bounded flows that the corresponding number of UZs increases with the Reynolds number. This is not only valid for the streamwise velocity (shown in black) but also for the temperature field (shown in red), which exhibits an average factor of 1.4 more zones than the streamwise velocity. This value is close to the $\sim$1.6 factor reported by Cogo *et al.* [116]. We also note that the PDF for the streamwise velocity field of $\mathcal{T}_2$ is in very good agreement with the corresponding PDF for the lowest Reynolds case of de Silva *et al.* [122] ($Re_\tau \approx 1200$) which suggests that the UZs are not strongly affected by compressibility.

Figure 5.14(b) shows the variation of the average number of UZs ($\overline{N}_{\text{UZ}}$) with Re_τ for the cases considered, with black and red markers distinguishing between streamwise velocity and temperature data. As observed, both distributions exhibit an increase with Reynolds number that conforms with the logarithmic trend de-

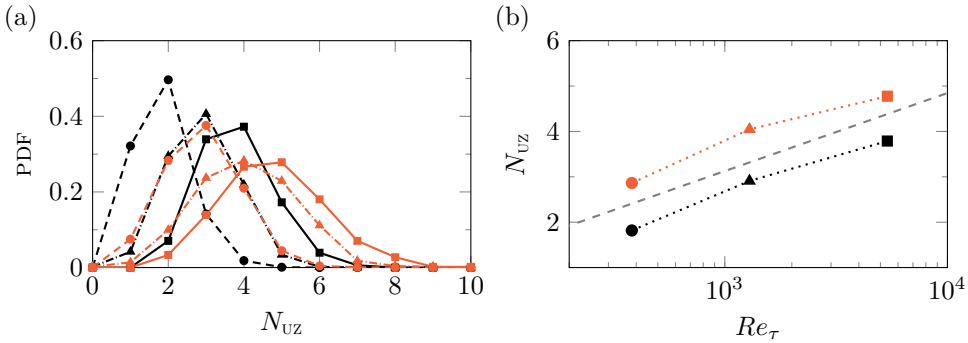

Figure 5.14: (a) PDF of UZs for the investigated TBLs, and (b) evolution of the average number of UZs with Re_τ. Color legend: streamwise velocity (black) and static temperature (red).

rived by de Silva *et al.* [122] from incompressible streamwise velocity data, which is indicated with a dashed line. This further supports the intrinsic relation between UZs and outer-layer motions, and confirms the negligible influence of compressibility effects on the UZ characteristics. Note that the actual value of $\overline{N}_{UZ}$ for the streamwise velocity appears slightly under-predicted compared to the incompressible data; however, the analysis should only concern trends rather than absolute values, and these appear insensitive to the employed parameter set in the peak search algorithm (confirmed with a separate parametric study). As previously stated, the employed parameters were adopted from previous works and modifications to deliberately match $\overline{N}_{UZ}$ with reported values in literature were not attempted.

Before concluding this section, we consider the instantaneous flow organization to provide a visual impression of the above-described turbulent structures. Streamwise velocity fluctuations are shown in figure 5.15 at two wall-parallel planes, $y^+ \approx 15$ and $y/\delta_0 \approx 0.1$, to illustrate the emerging scale separation and associated scale interaction with increasing Reynolds number. At $y^+ \approx 15$, see the left panels of figure 5.15, the characteristic streaky pattern of low- and high-momentum flow is present in all cases. However, since these structures become progressively finer with Reynolds number, they are hardly visible in figure 5.15(e) for case $\mathcal{T}_3$. At $y/\delta_0 \approx 0.1$, in contrast, the corresponding velocity structures for this case are much larger and recognizable, see figure 5.15(f). In addition, they leave a very distinct signature near the wall, since the large-scale fluctuations in figure 5.15(e) conform closely to the large-scale structures in figure 5.15(f). This illustrates the correspondence between the log-layer and the near-wall region, which is not so apparent for the moderate Reynolds case $\mathcal{T}_2$ when comparing figures 5.15(c) and 5.15(d). For the low-Reynolds case $\mathcal{T}_1$, the observed structures at $y/\delta_0 \approx 0.1$ exhibit similar sizes to those in the viscous sub-layer, see figures 5.15(a) and 5.15(b), which is expected in the absence of scale separation.

A three-dimensional view of velocity structures is included in figure 5.16 for each case, the Reynolds number increasing from top to bottom. In addition, the swirling strength criterion λ_{ci} is employed to reveal the corresponding vortical structures [153]. As observed, velocity streaks with similar spanwise spacing are present in

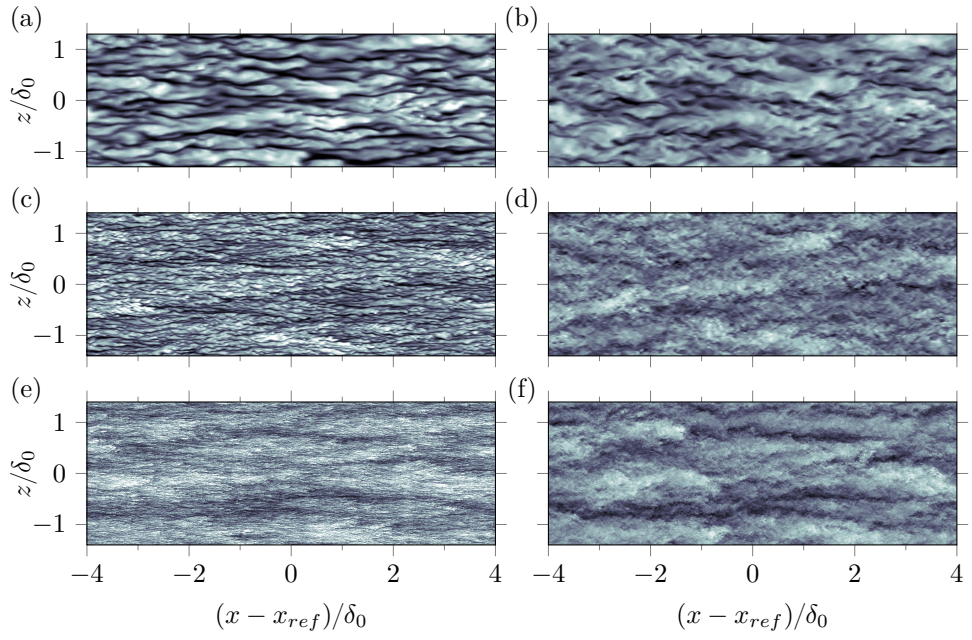

Figure 5.15: Instantaneous streamwise velocity field at $y^+ \approx 15$ (left panels) and $y/\delta_0 \approx 0.1$ (right panels): (a,b) case $\mathcal{T}_1$; (c,d) case $\mathcal{T}_2$; (e,f) case $\mathcal{T}_3$. Contour levels from $u'/u_\infty = -0.25$ (dark shade) to $u'/u_\infty = 0.25$ (light shade).

all cases. For the low-Reynolds case $\mathcal{T}_1$, see figure 5.16(a), the corresponding vortical structures are of considerable size and resemble hairpin vortices. The higher Reynolds cases $\mathcal{T}_2$ and $\mathcal{T}_3$, in contrast, exhibit vortical structures of much smaller size, see figures 5.16(b) and 5.16(c), which have not been filtered out by the employed computational grid. In agreement with the observations of Pirozzoli and Bernardini [113], these small-scale structures exhibit a tubular shape that does not conform to the classical hairpin eddy (see the close-up view on the right panels).

5.3.4. Thermodynamic statistics

The transport of internal energy, the transfer between kinetic and internal energy, and the corresponding fluctuations of the thermodynamic state properties play important roles in compressible turbulence. As a consequence, an accurate characterization of thermodynamic fluctuations and their mutual interaction with the velocity field is necessary for model development.

Figure 5.17 reports fluctuation profiles of thermodynamic variables in both inner scaling (left panels) and semi-local scaling (right panels). As observed, the isothermal boundary condition inhibits temperature fluctuations at the wall, which leads to density and pressure fluctuations of similar normalized magnitudes in the linear sub-layer. Additionally, their fluctuation intensity at the wall is observed to progressively increase with Reynolds number, see figures 5.17(a,c). This is a consequence

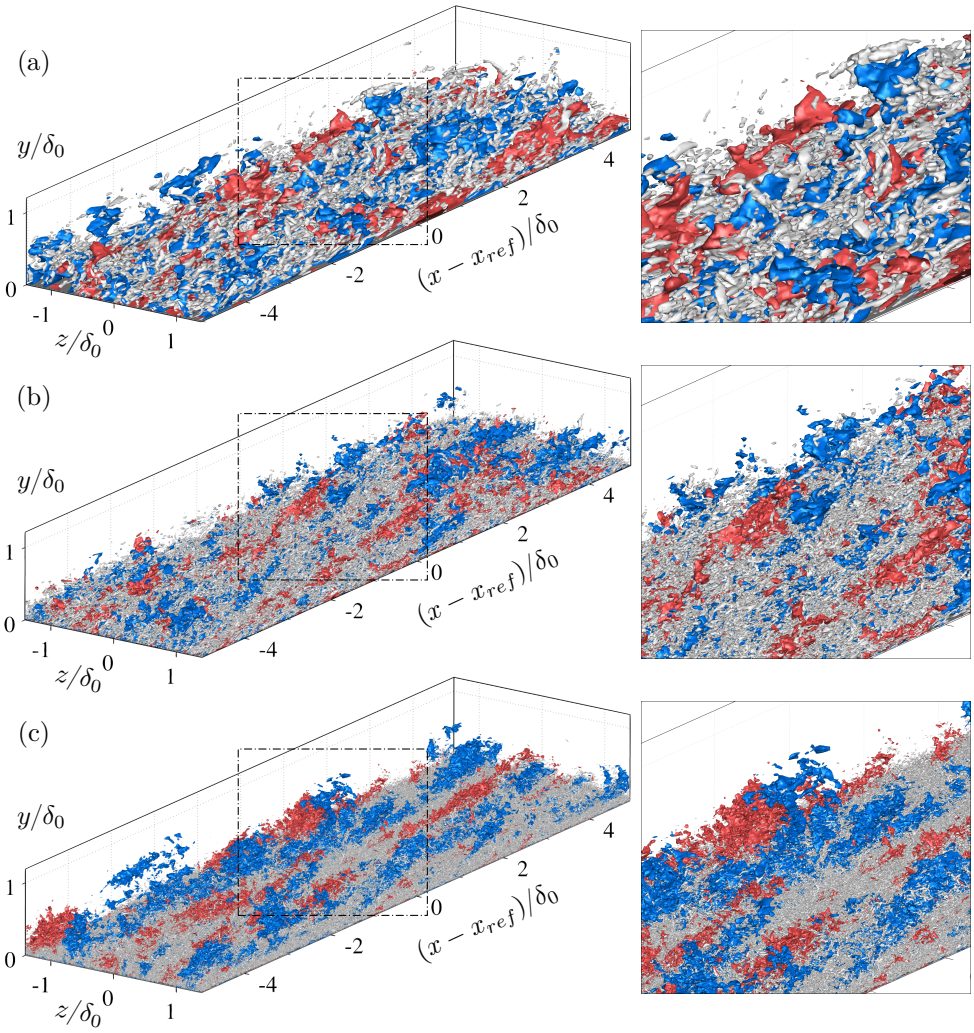

Figure 5.16: Instantaneous three-dimensional flow organization for (a) case $\mathcal{T}_1$, (b) case $\mathcal{T}_2$, and (c) case $\mathcal{T}_3$. Isosurfaces correspond to $u'/u_\infty = -0.12$ (blue), $u'/u_\infty = 0.12$ (red) and $\lambda_{ci} = 2\overline{\lambda}_{ci}$ (gray), where $\overline{\lambda}_{ci}$ is the average value of the swirling strength at $y/\delta_0 = 0.1$. Dash-dotted lines indicate the location of the close-up view on the right panels.

of the modulating influence of the outer layer motions [113]. Experimental evidence suggest a logarithmic increase of the inner-scaled wall-pressure fluctuations with Re_τ. While the corresponding values for cases $\mathcal{T}_1$ and $\mathcal{T}_2$ conform well with the empirical correlation of Farabee and Casarella [154], within 2% and 7% error from the respective predicted values, inner-scaled wall-pressure fluctuations for $\mathcal{T}_3$ exceed the predicted values by a slightly larger margin. This is attributed to the spurious

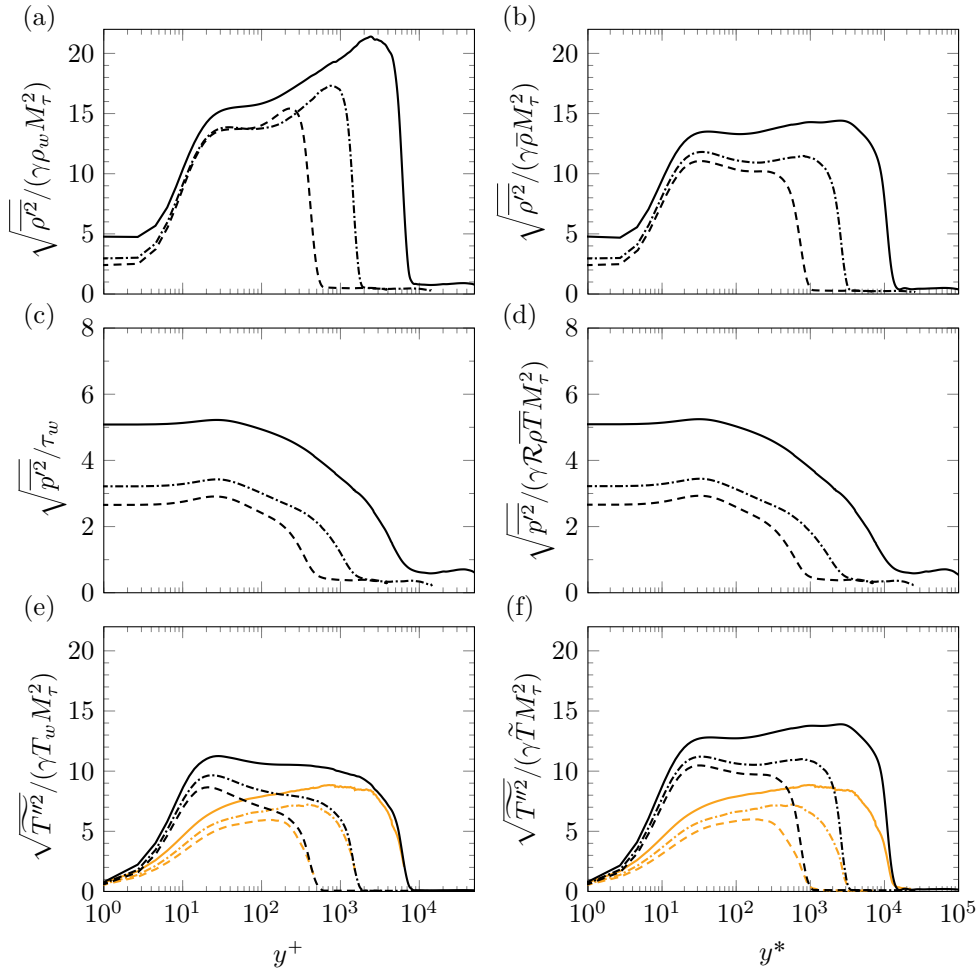

Figure 5.17: Wall-normal distribution of the inner-scaled (left panels) and semi-locally scaled (right panels) thermodynamic fluctuations: (a,b) density; (c,d) temperature; (e,f) pressure. The distribution of total temperature fluctuations is additionally included in panels (e) and (f) (orange lines), and $M_\tau = u_\tau(\gamma\mathcal{R}T_w)^{-1/2}$.

noise generated by the digital filter, which increases in magnitude with the inflow Reynolds number and requires long distances to relax [116].

Away from the wall, inner-scaled temperature fluctuations attain their peak value in the buffer layer, see figure 5.17(e), while the inner-scaled density fluctuations in figure 5.17(a) clearly peak at the boundary layer edge. This is a consequence of the mean temperature and density distributions in wall-normal direction, which stimulate their corresponding fluctuations in opposite ways [116]. If mean-property variation effects are taken into account, for instance, by considering the semi-local scaling shown on figures 5.17(b,f), temperature and density fluctuations exhibit very

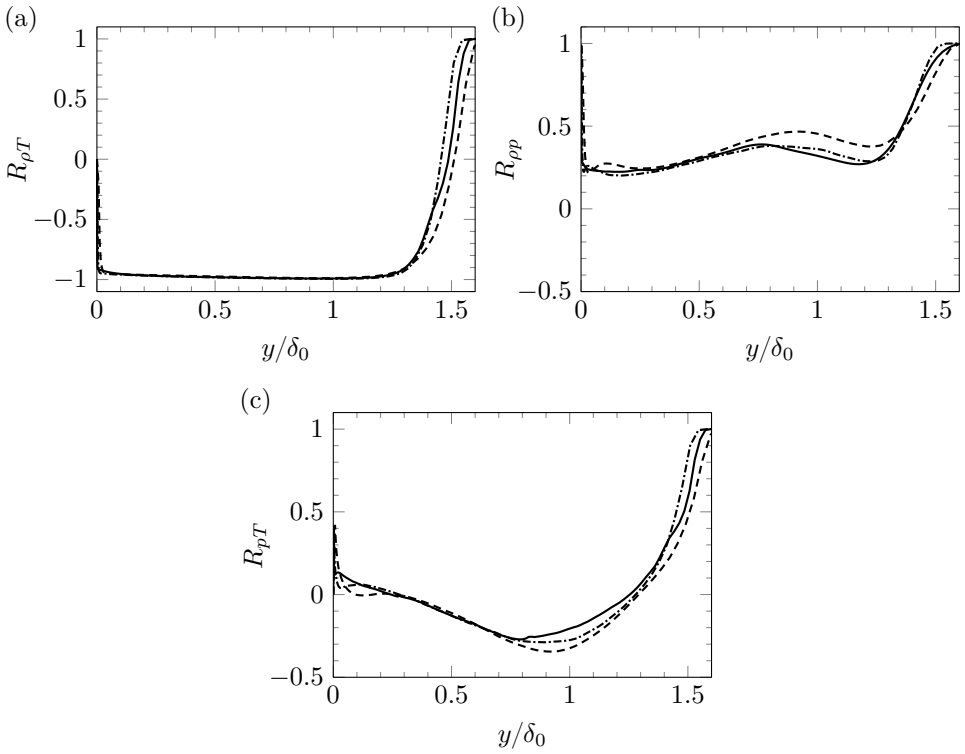

Figure 5.18: Wall-normal distribution of the correlation coefficients between (a) density and temperature, (b) density and pressure, and (c) pressure and temperature.

similar behavior across the boundary layer (except for the near-wall region). This highlights the close relation between these two variables in compressible TBLs. The resulting fluctuation profiles are almost flat from the upper end of the buffer layer until the boundary layer edge, where a peak seems to emerge at high Reynolds number. In addition, the intensity of the fluctuations across the boundary layer is also dependent on the Reynolds number.

The fluctuating pressure, on the other hand, is not modulated by mean-property variation effects because the mean-pressure is approximately constant. At the same time, the corresponding fluctuations across the layer do not resemble those associated with the temperature and density in any of the considered scalings, which indicates a lower degree of correlation, i.e., higher decoupling, between them (see next paragraph). As observed in figures 5.17(c,d), pressure fluctuations are largest in the near-wall region, where the strongest vorticity fluctuations are found, and progressively decrease along the quasi-logarithmic region and towards the free-stream flow. While their behavior is qualitatively similar for the different TBLs considered, the intensity of the pressure fluctuations is clearly sensitive to the Reynolds number across the whole layer, being highest for case $\mathcal{T}_3$.

The correlation coefficients between thermodynamic variables are shown in fig-

ure 5.18, where no systematic Reynolds number effects are observed. The density-temperature correlation of figure 5.18(a) confirms the close relation between these two variables, with $R_{\rho T}$ being approximately -0.9 in the buffer layer and continuing to approach -1 with increasing wall-distance. The fact that they are anti-correlated clearly depicts the non-isentropic behavior of the thermodynamic fluctuations inside the boundary layer. Beyond the boundary layer edge, in turn, the correlation changes drastically and approaches unity within half a boundary layer thickness. This is a consequence of the acoustic disturbances dominating the free-stream flow, which are of isentropic nature. The density-pressure correlation, see figure 5.18(b), is unity at the wall due to the isothermal boundary condition, which inhibits temperature fluctuations. The correlation then drops to a value of about 0.2 within the buffer layer and increases slightly towards the intermittent boundary layer edge, where it levels off and starts to decrease again. Similar as for the density-temperature correlation, the density-pressure correlation changes trend outside the TBL and reaches unity within $1.5\delta_0$ from the wall. This is also the case for the pressure-temperature correlation in figure 5.18(c). Interestingly, this correlation is positive near the wall but changes sign inside the boundary layer. As observed, a local maximum of approximately 0.4 is first attained in the viscous sub-layer and is followed by a progressive decrease that crosses $R_{pT} = 0$ at $y/\delta_0 \approx 0.3$. The correlation then levels off to a value of about -0.3 to -0.4 near the edge of the boundary layer.

The turbulent pressure diffusion is analyzed in figures 5.19(a) and 5.19(b), where the coefficients for the pressure-streamwise velocity and pressure-wall-normal velocity correlations are respectively shown. In agreement with the DNS data of Gerolymos and Vallet [155] for compressible channel flows, both correlations are very weak within the boundary layer except for R_{vp} in the near-wall region $y^+ \lesssim 10$. This local increase is associated with considerable transport of TKE away from the wall, since the corresponding pressure-diffusion term in the TKE transport equation is $-\partial_y[\overline{p'v''}]$ [111]. Furthermore, R_{up} also becomes increasingly negative at the boundary layer edge, see figure 5.19(a), which is attributed to outward excursions of low-speed rotational fluid towards the free-stream. The pressure-velocity correlations do not exhibit any strong or consistent Reynolds number dependence.

The relationship between the streamwise velocity and the temperature fields is considered next. Under the assumption of constant mean total temperature and negligible total temperature fluctuations, Morkovin [105] proposed a series of relations for a equilibrium zero-pressure gradient TBL over an adiabatic wall, the so-called strong Reynolds analogies (SRA). Three of these relations are

$$\frac{\sqrt{\widetilde{T''^2}}/\widetilde{T}}{(\gamma-1)M^2\sqrt{\widetilde{u''^2}}/\widetilde{u}} \approx 1, \tag{5.8}$$

$$R_{uT} = \frac{\widetilde{u''T''}}{\sqrt{\widetilde{u''^2}}\sqrt{\widetilde{T''^2}}} \approx -1, \tag{5.9}$$

$$Pr_t = \frac{[-\overline{\rho u''v''}](\partial\widetilde{T}/\partial y)}{[-\overline{\rho v''T''}](\partial\widetilde{u}/\partial y)} \approx 1, \tag{5.10}$$

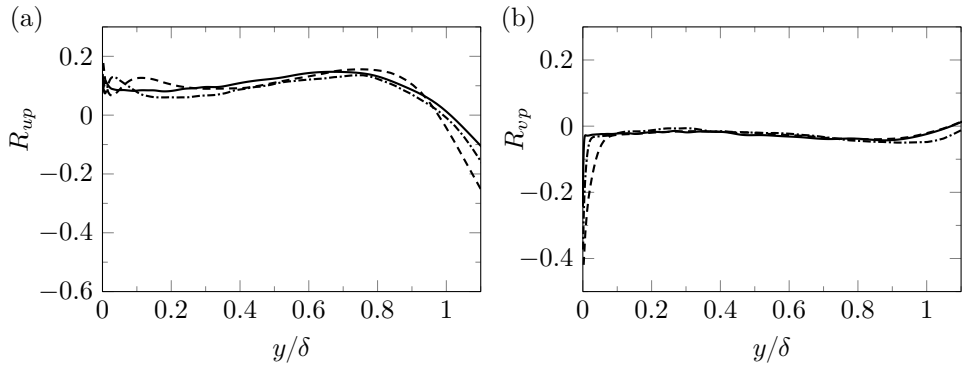

Figure 5.19: Wall-normal distribution of the correlation coefficients between the pressure and (a) the streamwise velocity, and (b) the wall-normal velocity.

with $M^2 = \widetilde{u}^2/\gamma\mathcal{R}\widetilde{T}$.

These relations have been extensively employed for modeling purposes despite their rather questionable agreement with experimental or numerical data [106, 111, 113, 115]. For instance, the assumption of constant total temperature is a fair approximation for the present quasi-adiabatic LES data (variations do not exceed 1.5% of $T_{0,\infty} = T_w$), while negligible total temperature fluctuations is not. The distribution of total temperature fluctuations in wall-normal direction is also included in figures 5.17(e) and 5.17(f) for the investigated TBLs, where it is clear that $\widetilde{T_0''^2}$ exhibits comparable magnitudes as $\widetilde{T''^2}$.

Evaluation of equations (5.8)–(5.10) reflects the aforementioned deviation from the SRA assumptions. For instance, the streamwise velocity-temperature correlations and the turbulent Prandtl number shown in figures 5.20(a) and 5.20(b) are clearly not unity throughout the boundary layer. The distribution for $-R_{uT}$ exhibits a peak value of approximately 0.9 in the buffer layer. In agreement with the DNS data of Pirozzoli and Bernardini [113], the correlation appears weakly dependent on the Reynolds number near the wall. However, no apparent Reynolds number dependence can be identified above $y/\delta_0 \approx 0.3$, where all correlations exhibit a value between 0.5 and 0.6 before dropping again at the boundary layer edge. The turbulent Prandtl number in figure 5.20(b) exhibits a somewhat similar trend as $-R_{uT}$ throughout most of the boundary layer, with values slightly closer to unity (between 0.6 and 0.8). At the edge of the boundary layer, however, its magnitude starts to increase rather than decrease.

The SRA relation (5.8) is evaluated in figure 5.21(a). Interestingly, all cases exhibit a nearly-constant value close to unity within the first half of the boundary layer. However, this is no longer true in the outer region, where all distributions largely overshoot the expected unity value of the SRA paradigm. In view of these deviations, Huang *et al.* [110] proposed a so-called modified SRA, in an attempt to improve the agreement with non-adiabatic TBL data. The resulting expression,

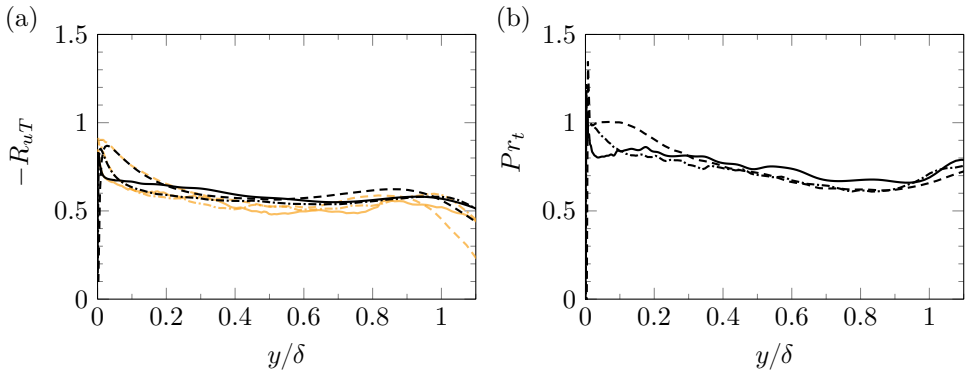

Figure 5.20: Wall-normal distribution of (a) the correlation coefficient between streamwise velocity and temperature, and (b) the turbulent Prandtl number. Orange lines in (a) indicate the corresponding distributions obtained with equation (5.13).

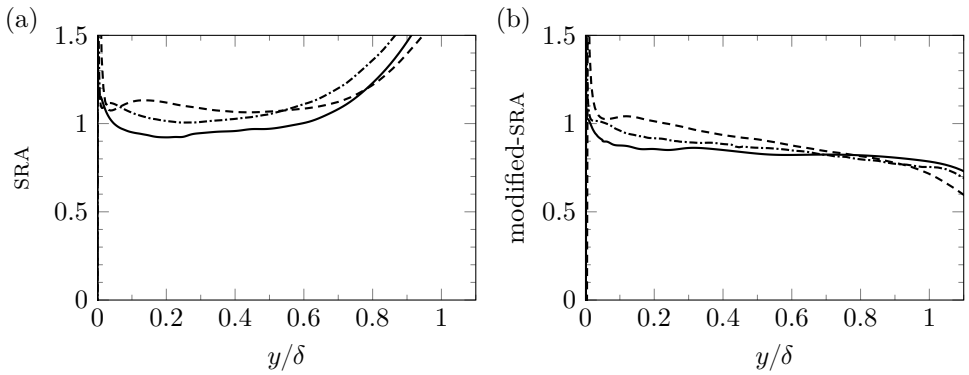

Figure 5.21: Evaluation of (a) the SRA relation (equation (5.8)), and (b) the modified version by Huang *et al.* [110] (equation (5.11)).

which takes into account heat fluxes at the wall, is

$$\frac{\sqrt{\widetilde{T''^2}}/\widetilde{T}}{(\gamma-1)M^2\sqrt{\widetilde{u''^2}}/\widetilde{u}} \approx \frac{1}{Pr_t[1-(\partial\widetilde{T_0}/\partial\widetilde{T})]}. \tag{5.11}$$

We multiply the left-hand side by the denominator on the right-hand side, which leads to a modified-SRA indicator that also predicts unity. This indicator is evaluated in figure 5.21(b) and shows clear improvements in the outer layer with respect to the SRA, in very good agreement with previous findings [106, 111, 113, 115]. Interestingly, the modified-SRA also reveals a weak Reynolds number dependence that is consistent throughout the boundary layer.

As shown by Guarini *et al.* [111], an improved expression for the streamwise velocity-temperature correlation can be derived by considering the modified-SRA

version of Huang *et al.* [110] in the presence of non-negligible total temperature fluctuations. By retaining only those terms that are linear in the fluctuations, total temperature fluctuations can be expressed as

$$\overline{T_0''^2} \approx \overline{T''^2} + \frac{\widetilde{u}^2}{c_p^2}\overline{u''^2} + 2\frac{\widetilde{u}}{c_p}\sqrt{\overline{T''^2}}\sqrt{\overline{u''^2}}R_{uT}. \tag{5.12}$$

Substituting equation (5.11) into equation (5.12) and solving for R_{uT} yields

$$R_{uT} \approx \frac{[\overline{T_0''^2}/\overline{T''^2} - 1]}{[2Pr_t(1 - \partial\widetilde{T_0}/\partial\widetilde{T})]} - \frac{Pr_t}{2}\left(1 - \frac{\partial\widetilde{T_0}}{\partial\widetilde{T}}\right). \tag{5.13}$$

This expression is evaluated for the considered TBLs, and the corresponding distributions are included in figure 5.20(a) for comparison (orange lines). As observed, they are in excellent agreement with the present LES data. This further confirms the relevance of total temperature fluctuations in compressible TBLs as well as the enhanced performance of the modified-SRA relation by Huang *et al.* [110], even for quasi-adiabatic wall conditions.

5.4. Summary

In this chapter, we have presented and discussed a database of compressible TBLs that covers more than a decade of friction Reynolds number Re_τ, from 242 to 5554. Effects of Reynolds number have been quantified on a variety of statistics, with special attention on the size and topology of the turbulent structures populating the TBL at high Reynolds number. Streamwise spectra of streamwise velocity fluctuations show a clear separation between inner and outer scales in the high Reynolds case, where energetic peaks are found at wavelengths of $\lambda_x^+ \approx 700$ and $\lambda_x/\delta_0 \approx 5$-6. The latter peak corresponds to the signature of large-scale coherent structures in the outer region, which exert a modulating influence on the near-wall turbulence that is clearly visible in many of the metrics discussed. The spanwise spacing of outer-layer motions, on the other hand, is found to be insensitive to the Reynolds number and equal to $\sim 0.7\delta_0$. Moreover, the Re_τ-sensitivity of uniform momentum regions (UMZs) in the flow, which have been recently associated with outer-layer motions, has also been assessed in this chapter. The resulting probability density function of the UMZs as well as the observed logarithmic increase in UMZ count with Re_τ is found to agree well with incompressible data, indicating that outer-layer dynamics are not strongly influenced by compressibility at Mach 2.0. And last but not least, the remaining part of the chapter is devoted to the analysis of thermodynamic fluctuations, which are clearly sensitive to the Reynolds number across the whole boundary layer. When mean-property variation effects are taken into account, temperature and density fluctuations are found to exhibit very similar behavior (except for the near-wall region). The fluctuating pressure, in turn, is not modulated by mean-property variation effects and does not resemble the fluctuating temperature or density.

6

Reynolds number effects in the baseline interaction

Having characterized the incoming TBL in detail (chapter 5), our attention is now focused on the STBLI flow of interest. The scope of this chapter is thus to 1) present the essential features of strong STBLI over flat-rigid walls, which complements our discussion in the introduction chapter, and 2) to systematically asses the effect of Reynolds number on multiple aspects of the interaction. Reynolds number effects are quantified from a new wall-resolved LES database that covers more than a decade of Re_τ (until $Re_\tau = 5118$) and otherwise considers the same flow parameters and simulation setup. The moderate-Reynolds STBLI case presented in this chapter ($Re_\tau = 1226$) is then further investigated in chapter 7 in presence of a compliant thin-panel located underneath the interaction.

6.1. Introduction

A relevant aspect concerning the physics of STBLI is the effect of Reynolds number on the interaction dynamics [156]. This knowledge is of paramount importance for the extrapolation of laboratory data to full-scale flight conditions. Experimental investigations of compression ramp and impinging-shock configurations have been conducted for a wide variety of flow conditions [56] and have established a foundation on the effect of this parameter along with Mach number and shock strength. For instance, at high Reynolds number the separation shock emerges from deep within the boundary layer which results in a highly intermittent wall-pressure signal [60]. For low-Reynolds interactions, in contrast, the compression at separation is more diffused and the shock is located further away from the wall, which attenuates the intermittency of the wall-pressure [157]. The low-frequency unsteadiness of the separation shock, however, appears rather unaffected by Reynolds number outside of the boundary layer [158]. In a compression ramp flow at Mach 2.9, Settles *et al.* [59]

The content of this chapter has been accepted for publication in *J. Fluid Mech.* as: L. Laguarda, S. Hickel, F. F. J. Schrijer and B. W. van Oudheusden. Reynolds number effects in shock-wave/turbulent boundary-layer interactions, 2024.

additionally found that the upstream influence length, that is, the distance between the onset of separation and the corner location, consistently decreased with increasing Reynolds number. The required shock strength for incipient separation, in turn, was not so much affected in their experiments. Furthermore, three-dimensional effects become more important at high Reynolds number; Muck *et al.* [159] found that the separation shock front becomes spanwise nonuniform, exhibiting a rippling appearance. This has been attributed to the incoming turbulent structures [160, 161], more specifically to the passage of streamwise-elongated regions of relatively low- and high-speed fluid that emerge in the approaching TBL at high Reynolds number [38]. While an increasing body of work disproves the hypothesis by Ganapathisubramani *et al.* [37, 162] that these very-long structures (often termed superstructures) drive the low-frequency unsteadiness of strong STBLIs, they still exert an important modulating influence.

High-fidelity numerical simulations are an attractive choice for the analysis of complex flow phenomena in STBLIs [56]. Thanks to the ever-increasing spatio-temporal resolution combined with non-intrusive access to all flow variables, simulations overcome inherent experimental limitations and potentially offer better insights into the interaction dynamics. A wide variety of configurations, shock strengths, and Mach numbers have been numerically investigated. These studies have significantly contributed to the fundamental understanding of STBLI, see for example the recent review paper of Gaitonde and Adler [192].

However, it is important to acknowledge that numerical works on STBLI are generally available at lower Reynolds number than complementary experiments. This is illustrated in table 6.1 which shows a compilation of relevant numerical and experimental studies on canonical impinging STBLIs conducted over the past two decades. Only high-fidelity simulations, i.e., DNS and LES, have been reported in the table since these are the only numerical frameworks capable of capturing all relevant STBLI dynamics [36]. The very often prohibitive resolution requirements of DNS are somewhat alleviated by LES, but even LES simulations of multi-scale turbulent flows are still only feasible for a narrow range of conditions. For this reason, available numerical studies on STBLI are limited to low and moderate Reynolds numbers, mostly below $Re_\tau \approx 10^3$ and $Re_\theta \approx 10^4$ in terms of friction and momentum-thickness Reynolds number respectively, see table 6.1. These values are lower than those in high-Reynolds experiments, e.g., Humble *et al.* [38, 58] or the works of Settles *et al.* [59] and Dolling and Murphy [60] on compression ramps at $Re_\theta \approx 7 \times 10^4$. For an in-depth understanding of the practically relevant high-Reynolds regime of STBLI, this gap needs to be closed.

With this aim in mind, we numerically investigate the effect of Reynolds number on impinging STBLI with strong mean flow separation. The various Reynolds number effects are quantified from a new wall-resolved LES database that covers more than a decade of Re_τ (and Re_θ) and otherwise considers the same flow parameters and simulation setup. Specifically, the database is at free-stream Mach number $M_\infty = 2.0$ and includes a low-Reynolds interaction, with $Re_\tau = 355$ ($Re_\theta = 1.6 \times 10^3$), a moderate-Reynolds interaction, with $Re_\tau = 1226$ ($Re_\theta = 5.7 \times 10^3$), in line with previous numerical works as shown in table 6.1, and a high-Reynolds interaction,

Table 6.1: Summary of turbulence-resolving numerical simulations and experimental studies on canonical impinging STBLIs conducted over the past two decades (for adiabatic or quasi-adiabatic wall conditions and up to $M_\infty = 3.0$). The flow deflection induced by the impinging shock is indicated as ϑ, and Re_τ values with an asterix have been estimated from velocity profiLES reported in the corresponding work. $Re_\theta = \rho_\infty u_\infty \theta / \mu_\infty$; $Re_\tau = \overline{\rho}_w u_\tau \delta_0 / \overline{\mu}_w$.

Authors	M_∞	ϑ [deg.]	Re_θ	Re_τ	notes
Pirozzoli and Grasso [40]	2.25	8	3725	800*	DNS
Priebe *et al.* [163]	2.9	12	2300	300*	DNS
Touber and Sandham [34, 164]	1.7-2.4	6-8	3000-5300	600*	LES
Morgan *et al.* [165]	2.05	8	2194	500*	LES
Pirozzoli *et al.* [166]	2.28	8	2280	-	LES
Pirozzoli and Bernardini [167]	2.28	8	2344	466	DNS
Agostini *et al.* [168]	2.3	6.3-9.5	5100	800*	LES
Hadjadj [169]	2.28	8	5350	1000*	LES
Aubard *et al.* [170]	2.25	8	3725	600*	LES
Morgan *et al.* [36]	2.28	8	4800	500*	LES
Mullenix and Gaitonde [171]	2.33	9	3048	1000*	LES
Pasquariello *et al.* [172]	2.3	8.8	-	900	LES
Agostini *et al.* [39]	2.0	9.5	5100	-	LES
Matheis and Hickel [46]	2.0, 3.0	11-24.5	-	671	LES
Wang *et al.* [173]	2.7	9	4300	500*	LES
Jiang *et al.* [174]	2.0	8.5	4850	1000*	LES
Nichols *et al.* [62]	2.28	8, 9.5	2300	500*	LES
Pasquariello *et al.* [23]	3.0	19.6	14000	1523	LES
Vyas *et al.* [175]	2.29	8	4640	800*	LES
Fang *et al.* [176]	2.25	8	3700	590	DNS
Gao *et al.* [177]	2.0	7-10	1628	500*	LES
Gross *et al.* [178]	2.3	12.5	1100, 4300	-	LES
Bernardini *et al.* [179]	2.28	8	6882	1100	DNS
Present low-Re case ($\mathcal{B}_1$)	2.0	10.66	1600	355	LES
Present mid-Re case ($\mathcal{B}_2$)	2.0	10.66	5700	1226	LES
Present high-Re case ($\mathcal{B}_3$)	2.0	10.66	26400	5118	LES
Bookey *et al.* [180]	2.9	12	2400	300*	Exp.
Dupont *et al.* [181]	2.3	8	6900	-	Exp.
Humble *et al.* [38, 58]	2.05	8, 10	49200	8600	Exp.
Piponniau *et al.* [42]	2.28	8	5100	1100	Exp.
Souverein *et al.* [182]	1.7	6	50000	-	Exp.
Van Oudheusden *et al.* [183]	2.05	8	49200	8600	Exp.
Webb *et al.* [184, 185]	2.33	7-10	24800	-	Exp.
Giepman *et al.* [186]	2.0	12	-	3765	Exp.
Schreyer *et al.* [187]	2.0	8.5	5000	-	Exp.
Daub *et al.* [29]	3.0	17.5, 20	14000	-	Exp.
Threadgill and Bruce [188]	2.0	7-10	7700-8800	-	Exp.
Rabey and Bruce [189]	2.0	10	7900	-	Exp.
Grossman and Bruce [97]	2.0	12	10000	-	Exp.
Dupont *et al.* [190]	2.3	8, 9.5	5100	800*	Exp.
Rabey *et al.* [191]	2.0	12	10000	-	Exp.

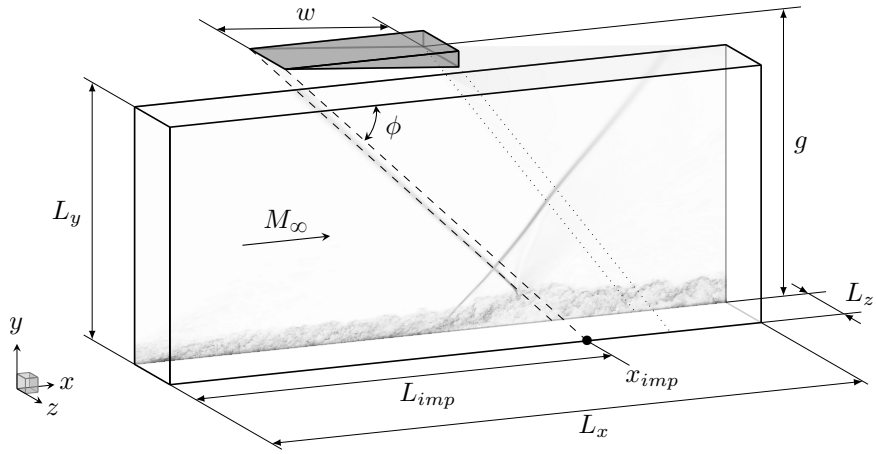

Figure 6.1: Schematics of the computational domain.

with $Re_\tau = 5118$ ($Re_\theta = 26.4 \times 10^3$). Notably, the latter significantly broadens the parameter range of strong STBLIs covered with high-fidelity simulations, extending towards the high-Reynolds conditions of experimental facilities. All cases exhibit substantial flow reversal and have been integrated for a very long time, i.e., over 90 FFT of the full domain length, to properly resolve low-frequency dynamics.

6.2. Computational setup

We consider an oblique shock impinging on a flat-plate TBL as illustrated in figure 6.1. Three LES simulations have been performed for the investigated geometry, with different Reynolds numbers but otherwise equal flow parameters. Table 6.2 summarizes common flow parameters. The free-stream Mach number is $M_\infty = 2.0$ and stagnation temperature and pressure are $T_0 = 288$ K and $p_0 = 356$ kPa. The 99% velocity-based boundary layer thickness at the inflow plane $\delta_{0,in}$ is set to 5.2 mm in all cases. The virtual shock generator is located outside of the computational domain at a distance $g = 18.46\delta_{0,i}$ above the wall-plane, see figure 6.1, and induces a free-stream flow deflection of $\vartheta = 10.66°$. This value is 2° smaller than the maximum theoretical value for a regular shock reflection at the investigated Mach number and corresponds to an incident shock wave angle of $\phi = 40.04°$. The channel height to wedge hypotenuse ratio is $g/w = 1.16$.

The considered fluid is air and details concerning the modelling of its properties are provided in section 2.1.1. A case dependent Reynolds number is achieved by modifying the free-stream dynamic viscosity μ_∞, see table 6.3, which also states the corresponding velocity-based boundary layer thickness Reynolds number $Re_{\delta_{0,i}}$ and friction Reynolds number $Re_{\tau,i}$ at the inflow plane for each case. We hereafter refer to the low-Reynolds STBLI as case $\mathcal{B}_1$, to the moderate-Reynolds STBLI as case $\mathcal{B}_2$, and to the high-Reynolds STBLI as case $\mathcal{B}_3$.

The computational domain is exactly the same as the one employed for the

Table 6.2: Common flow parameters of all simulations.

M_∞	T_0	p_0	u_∞	$\delta_{0,in}$	ϕ	ϑ
2.0	288.2 K	355.6 kPa	507 m/s	5.2 mm	40.04°	10.66°

Table 6.3: Case dependent flow parameters. Subscript *in* refers to the inflow plane.

Case	μ_∞ [kg (m s)$^{-1}$]	$Re_{\delta_{0,in}}$	$Re_{\tau,in}$
$\mathcal{B}_1$	22.5×10^{-5}	11.6×10^3	250
$\mathcal{B}_2$	5.34×10^{-5}	50.1×10^3	935
$\mathcal{B}_3$	1.10×10^{-5}	238×10^3	3725

analysis of the undisturbed TBL, see section 5.2 of the previous chapter. The only difference is that here, in order to generate the STBLI flow of interest, we also introduce an incident shock and a trailing-edge expansion fan at the non-reflecting top boundary, see figure 6.1. This is achieved by prescribing boundary conditions according to the Rankine-Hugoniot relations and Prandtl-Meyer theory. The virtual impingement point on the wall, referred to as x_{imp}, is located far downstream of the inflow plane, at a distance $L_{imp} = 32\delta_{0,in}$, to ensure proper boundary layer relaxation to an equilibrium state before it interacts with the incident shock.

The adequacy of the selected grid resolution and domain size for the simulation of STBLI flows was verified through a preliminary grid- and domain-sensitivity study conducted for case $\mathcal{B}_2$. This study involved four distinct grid resolutions and domain dimensions, and the findings, presented in appendix C, confirm the convergence of the STBLI statistics at the selected inner-scaled grid resolution and outer-scaled domain size, which are common to all cases.

Computations were performed with the numerical method described in section 2.1.2 and carried out as follows. First, the computational domain was initialized with the inviscid shock reflection solution. An initial transient of 15 FTT of the full domain length was next considered to allow the STBLI flow to fully develop. This initial transient was discarded from the statistical analysis. After that, the fully developed STBLI was then integrated for over 90 FTT to properly resolve low-frequency dynamics. Flow statistics, obtained by averaging the instantaneous three-dimensional solution in time and spanwise direction, were collected at a sampling rate of $\Delta t u_\infty/\delta_{0,in} \approx 0.013$. Additionally, instantaneous three-dimensional snapshots of the interaction region were stored every $\Delta t \approx 0.5\delta_{0,in}/u_\infty$ for processing purposes, yielding an ensemble size of 8192 snapshots per case.

6.3. Results and discussion

6.3.1. Incoming turbulence

Characterizing the undisturbed TBL is particularly instructive for the present analysis since Reynolds number effects in STBLI also stem from the differences in the

Table 6.4: Undisturbed TBL parameters at the virtual impingement point x_{imp} without the shock (computed from the wall-resolved LES data presented in chapter 5). Re_{δ_0} and Re_θ are defined in terms of free-stream quantities, see tables 6.3 and 6.2.

Case		δ_0	H	u_τ	$\overline{\rho}_w$	Re_{δ_0}	Re_θ	Re_τ
STBLI	TBL[a]	[mm]	[-]	[m s^{-1}]	[kg m^{-3}]	[$\times 10^{-3}$]	[$\times 10^{-3}$]	[-]
$\mathcal{B}_1$	$\mathcal{T}_1$	7.66	3.15	25.1	0.56	17.1	1.6	355
$\mathcal{B}_2$	$\mathcal{T}_2$	7.15	3.19	21.6	0.56	67.1	5.7	1226
$\mathcal{B}_3$	$\mathcal{T}_3$	7.23	3.12	18.8	0.55	331	26.4	5118

[a] Corresponding undisturbed TBL case in chapter 5.

TBL structure at low and high Reynolds number. As the reader may recall, these differences were quantified on a wide variety of statistics in chapter 5, with special attention on the size and topology of the turbulent structures populating the TBL. The analysis on that chapter revealed that the structures located at $y/\delta_0 \approx 0.1$ are 5-6 boundary layer thicknesses long for the high-Reynolds case $\mathcal{T}_3$, the corresponding undisturbed TBL of case $\mathcal{B}_3$, and approximately $\approx 0.7\delta_0$ wide for all cases.

To asses the potential modulating influence that these structures can exert on the STBLI dynamics, figure 6.2 presents two-dimensional power spectral density (PSD) maps of streamwise velocity fluctuations in the spanwise direction and in time at various wall-normal locations. The corresponding fluctuation signals have been extracted from the STBLI simulations upstream of the interaction, with a 90 FTT time history that allows for the resolution of potential low-frequency tones that could influence the interaction dynamics. The Strouhal number $St = fL/u_\infty$ is calculated using $L = \delta_0$ on the right y-axis and $L = L_{sep}$ on the left y-axis, where L_{sep} corresponds to the separation length, which is the distance between the mean separation and reattachment points in impinging STBLIs. For the estimation of the two-dimensional spectra, signals have been divided into 10 overlapping segments along the time axis (with a 65% overlap) and windowed with the Hann window function.

Spectral distributions in figure 6.2 highlight the decrease in length and time scales of near-wall turbulence as the Reynolds number increases. The left panel of figure 6.2(c) additionally shows the emergence of an energetic branch at high-wavelengths ($\lambda_z/\delta_0 > 0.1$) for the high-Reynolds at $y^+ \approx 15$, indicating the presence of energetic outer-layer structures influencing the near-wall cycle. Further away from the wall, at $y \approx 0.1\delta_0$, spectra exhibit the broadest widening for the high-Reynolds case, with spectral energy shifting towards lower frequencies. The most energetic Strouhal numbers, however, are still only measured down to $St_{L_{sep}} \approx 0.1$ (see the left y-axis), which is higher than the typical $0.03 - 0.06$ range reported in literature for the low-frequency unsteadiness of STBLIs [30]. This observation suggests that, in line with many other works in the literature, the dynamics of strong interactions at $St_{L_{sep}} < 0.1$ are primarily induced by a mechanism other than the passage of incoming long-wavelength structures in our simulations.

Furthermore, figure 6.2 reveals the modulating influence of outer-layer struc-

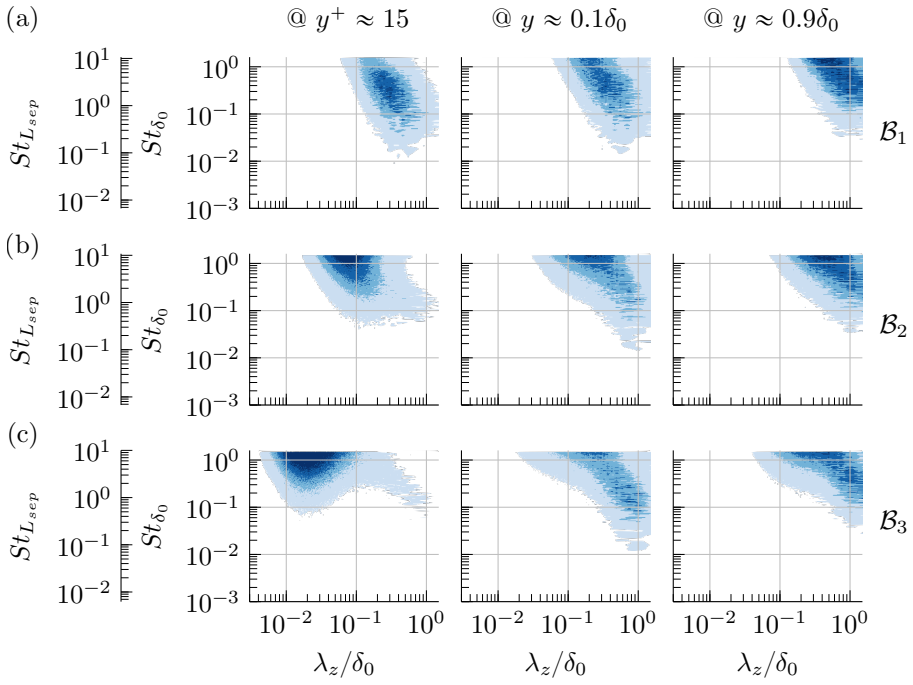

Figure 6.2: Two-dimensional power spectral density maps of streamwise velocity fluctuations in the homogeneous spanwise direction and in time at three wall-normal locations upstream of the investigated STBLIs. Spectral maps are presented in pre-multiplied form and normalized by the variance, with blue-filled contours depicting 4 isocontours from 0.075 to 0.3. Data has been extracted at $Re_\tau = 310$ for case $\mathcal{B}_1$, $Re_\tau = 1150$ for case $\mathcal{B}_2$ and $Re_\tau = 4800$ for case $\mathcal{B}_3$.

tures and bulges on the STBLI flow. These structures, characterized by energetic spanwise scales of order 0.1 to $1\delta_0$ in all cases, can contribute to both moderate-frequency ($St_{L_{sep}} \sim 0.1$–1) and high-frequency ($St_{L_{sep}} \sim 10$) spanwise wrinkling of the separation-shock foot [159, 178].

A summary of relevant undisturbed TBL parameters evaluated at x_{imp} is provided in table 6.4 for reference, where δ_0 is used for scaling purposes in the following unless otherwise stated.

6.3.2. Instantaneous STBLI configuration

We now turn our attention to the interaction between the above discussed TBLs and an oblique shock wave deflecting the free-stream flow by 10.66°, see figure 6.1. These interactions lead to the formation of the strong STBLIs of interest.

Instantaneous impressions of the temperature fields are provided in figure 6.3 to illustrate the resulting STBLI topology. Solid lines indicate instantaneous (yellow) and mean (white) contours of zero streamwise velocity, and they show that the adverse pressure gradient imposed by the incident shock is strong enough to cause

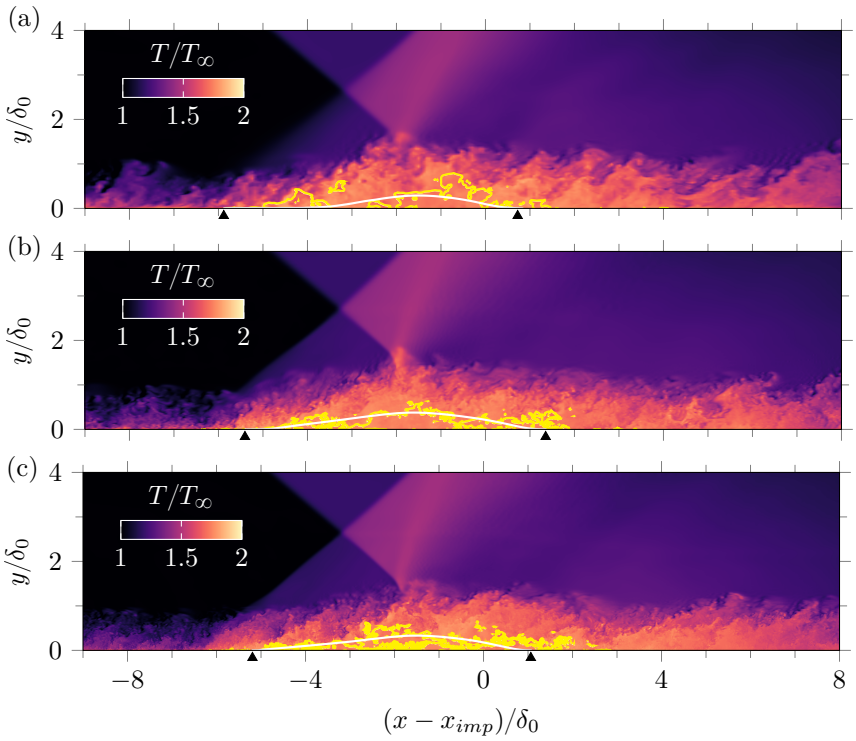

Figure 6.3: Instantaneous temperature fields: (a) case $\mathcal{B}_1$, (b) case $\mathcal{B}_2$, and (c) case $\mathcal{B}_3$. Solid lines indicate instantaneous (yellow) and mean (white) isocontours of zero streamwise velocity, and ▲ indicate mean separation and reattachment locations.

substantial flow separation in all cases. For the higher-Reynolds cases, that is, cases $\mathcal{B}_2$ and $\mathcal{B}_3$, the separation shock emanates from deep within the TBL; for the low-Reynolds case $\mathcal{B}_1$, the compression fan generated at the leading edge of the separated flow region is only coalescing into a shock wave well outside the TBL. This is directly linked to the height and curvature of the sonic line (from which compression waves emanate), which is Reynolds number dependent and dictates the intensity of the separation shock footprint on the surface [60].

At the separation shock foot, the flow is strongly decelerated and starts to detach. Turbulent structures from the upstream TBL are seeded into the free shear layer, and grow in size as they move away from the wall. The upper limit of the separation bubble is eventually established as a result of the interaction between the detached shear layer and the incident-transmitted shock, which turns the flow back towards the surface and initiates the reattachment process. All STBLI cases exhibit a very mild concave streamline curvature near reattachment, which translates into a weak compression fan instead of a coalesced reattachment shock. We also note that the intersection between the incident and the separation shock occurs approximately $2.5\delta_0$ above the wall in all cases.

The organization of the investigated STBLI flows is further examined by employing the swirling strength criterion λ_{ci} to visualize instantaneous turbulent structures. This criterion is based on local spiraling motion, which in the vicinity of vortex cores translates into a real eigenvalue λ_r plus a pair of complex conjugate eigenvalues $\lambda_{cr} \pm i\lambda_{ci}$ of the velocity gradient tensor [153]. In figure 6.4, coherent vortical structures in the investigated STBLI flows are visualized by plotting an isosurface of the magnitude of the imaginary part of the complex conjugate eigenvalue λ_{ci}. In this figure, turbulent structures are also colored by the local streamwise velocity, and a numerical schlieren visualization is included in the background of each rendering for reference. The Reynolds number increases from top to bottom.

Figure 6.4 reveals clear differences in terms of size and organization of turbulent structures at low and high Reynolds number. Starting from the upstream TBL, structures resembling hairpin vortices can be observed for the low-Reynolds case $\mathcal{B}_1$, see figure 6.4(a). The higher Reynolds cases $\mathcal{B}_2$ and $\mathcal{B}_3$, in contrast, exhibit structures of much smaller size that do not conform to the canonical hairpin vortex. This is in agreement with the observations made by Pirozzoli and Bernardini [113] on a $M_\infty = 2.0$ TBL flow at $Re_\tau \approx 1100$.

At the leading edge of the interaction, where incoming turbulence is compressed and the shear layer detaches from the wall, spanwise variations become more pronounced at high Reynolds number, see figures 6.4(b) and 6.4(c). Based on the color of the structures in the detaching shear layer, which indicates the magnitude of the local streamwise velocity, such variations are associated with alternating regions of low- and high-momentum fluid. Furthermore, within and above the high-speed streaks, larger vortical structures emerge in the detached shear layer as it moves away from the wall. These structures then break at the bubble apex, where the overall turbulence intensity is reduced. Past the interaction region, the boundary layer has clearly thickened and all cases exhibit more turbulent structures in the outer region compared to the upstream (undisturbed) TBL.

The background schlieren visualizations emphasize the origin of the separation shock deep within the TBL at high-Reynolds number, as seen when comparing figures 6.4(a) and 6.4(c). Furthermore, the schlieren visualization in figure 6.4(b) captures the precise instant when the separation-shock front for the moderate-Reynolds case $\mathcal{B}_2$ is instantaneously deformed by the passage of outer-layer bulges. These structures, of order δ_0 in span, contribute to the wrinkling of the separation-shock foot at both moderate and high frequencies, as discussed in section 6.3.1.

We have emphasized above that, despite the shift towards lower energetic frequencies, the energetic frequency scales of the incoming turbulence for case $\mathcal{B}_3$ remain too high to significantly impact the low-frequency dynamics of STBLI. However, these structures, associated with larger streamwise wavelengths, still play a crucial role in modulating the flow organization. This is illustrated in figure 6.5, which shows instantaneous streamwise velocity fluctuations for case $\mathcal{B}_3$ at the same time instance as in figure 6.4(c).

Three-dimensional isosurfaces of positive (red) and negative (blue) streamwise velocity fluctuations are shown in figure 6.5(a), while figures 6.5(b–g) depict two-dimensional contours on yz slices at $(x - x_{imp})/\delta_0 = \{-8.4, -5.6, -4.2, -2, 1, 5\}$.

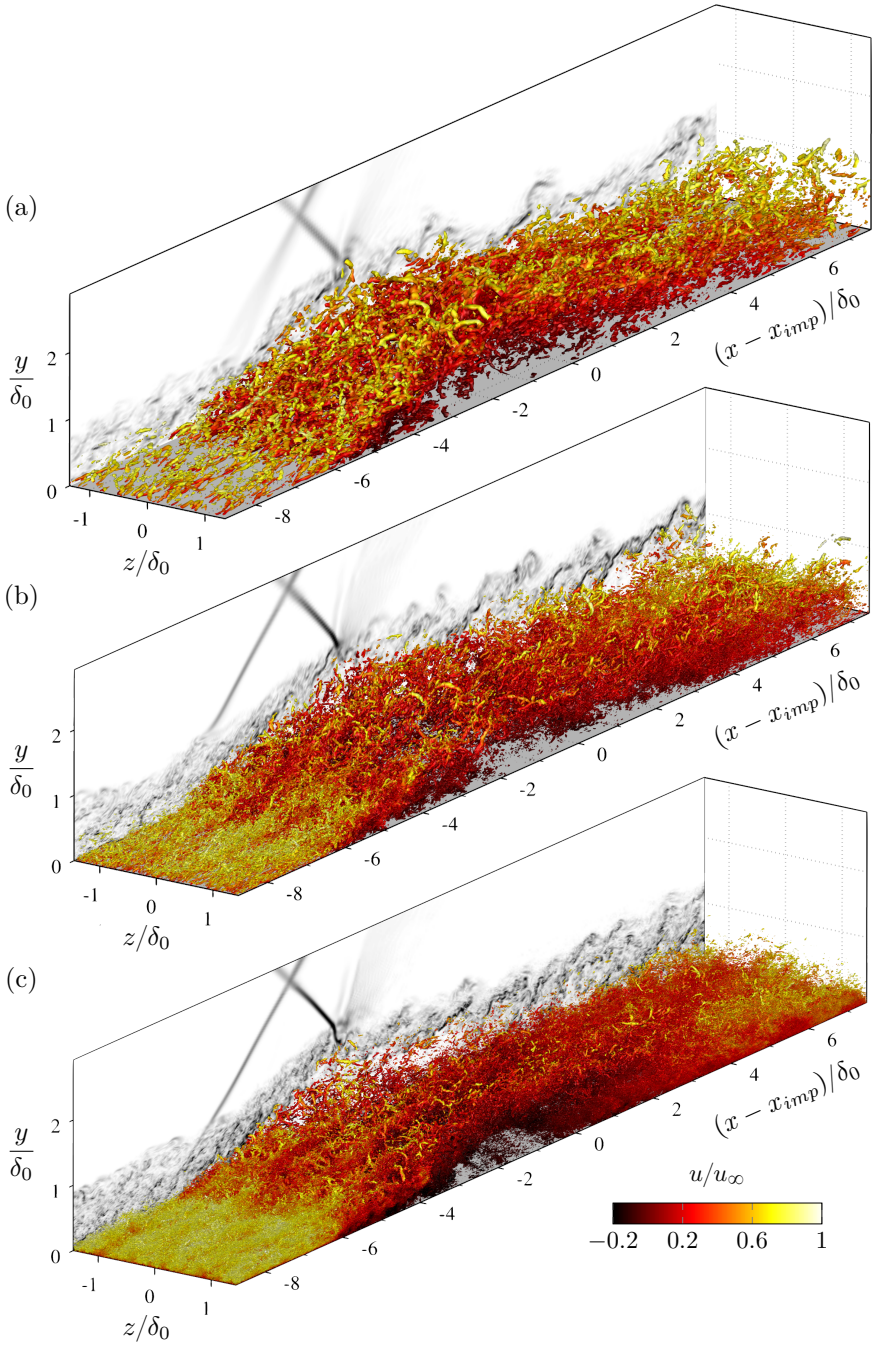

Figure 6.4: Instantaneous vortical structures visualized with the λ_{ci} criterion and coloured by the local streamwise velocity: (a) case $\mathcal{B}_1$ ($|\lambda_{ci}|\delta_0/u_\infty = 2.2$), (b) case $\mathcal{B}_2$ ($|\lambda_{ci}|\delta_0/u_\infty = 3.8$), and (c) case $\mathcal{B}_3$ ($|\lambda_{ci}|\delta_0/u_\infty = 5.6$). A numerical schlieren is shown in the background slice for each case, and the streamwise velocity colorbar applies to all renders.

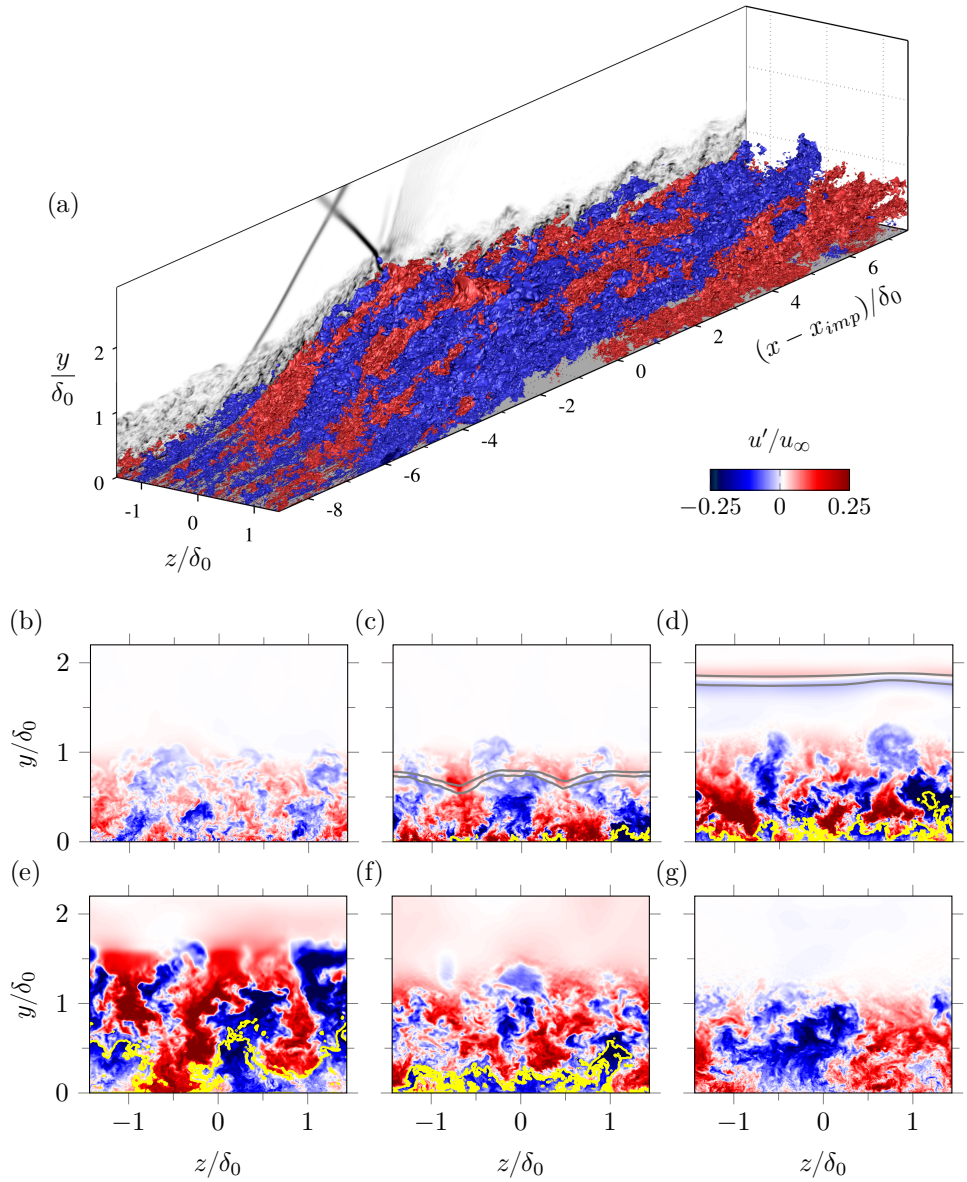

Figure 6.5: Instantaneous streamwise velocity fluctuations for case $\mathcal{B}_3$ at the same time instance as figure 6.4(c). Isosurfaces in (a) correspond to $u'/u_\infty = -0.12$ (blue) and $u'/u_\infty = 0.12$ (red), and panels (b–g) illustrate streamwise-normal cuts of (a) at $(x - x_{imp})/\delta_0 = \{-8.4, -5.6, -4.2, -2, 1, 5\}$ respectively. A numerical schlieren visualization is shown in the background slice of (a) for reference while solid lines in (b–g) indicate the instantaneous isocontour of zero streamwise velocity (yellow) and pressure gradient $|\nabla p|\delta_0/p_\infty = 4$ (gray).

These visualizations reveal clear correlations between spanwise variations of the separation shock (gray lines) and the edge of the reverse-flow bubble (yellow lines) with

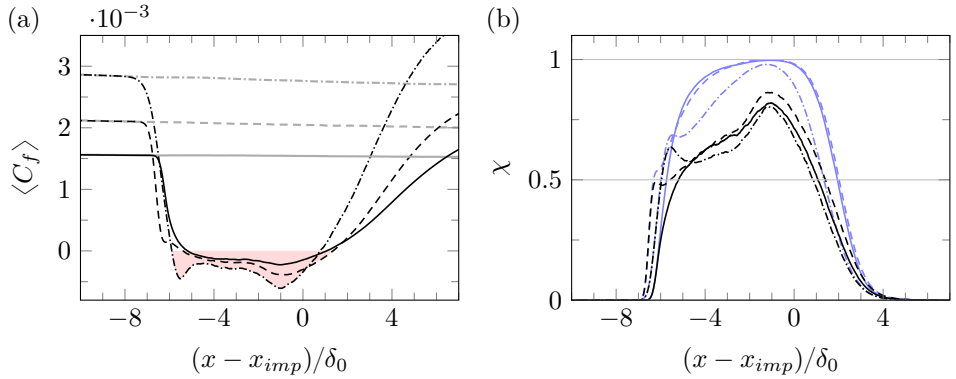

Figure 6.6: (a) Time- and spanwise-averaged skin-friction evolution, and (b) probability of reverse flow: (-·-·-) case $\mathcal{B}_1$, (- - -) case $\mathcal{B}_2$, (——) case $\mathcal{B}_3$. Separated regions in (a) are shaded in red and the gray lines denote the corresponding skin friction distribution for the undisturbed TBL. Distributions in (b) denote the probability of reverse flow at the wall (black) and its maximum value in wall-normal direction (blue).

alternating regions of low- and high-momentum fluid in the incoming TBL. At the leading edge of the interaction, they strongly modulate the separation-shock foot, see figure 6.5(c), where the passage of high-speed fluid brings the shock foot closer to the wall and also delays separation right at the surface. Moreover, as these velocity structures traverse the interaction, they reorganize and progressively exhibit much stronger spatial coherence. This is evident when comparing figures 6.5(b), representing the upstream TBL, with figure 6.5(g), corresponding to a location downstream of the interaction region. Spanwise autocorrelation functions at this two locations (not shown here) clearly highlight this increase in coherence, which is observed across all investigated Reynolds numbers.

Previous works have identified the resulting large-scale velocity structures beyond reattachment as the imprint of Görtler-like vortices in the interaction region [23, 43, 193]. While these studies also argue that such structures could play a pivotal role in driving the low-frequency unsteadiness of STBLIs, their actual relevance remains unclear. We attempted to extract any large-scale vortex from the turbulent background by filtering the three-dimensional snapshot data, following the approach by Pasquariello *et al.* [23]. However, the large-scale circulation is so weak compared to the small-scale turbulence in the present interactions that it was not possible to discern Görtler-like vortices in the filtered instantaneous snapshots. Their visualization is, however, possible with modal decomposition techniques applied to the full time series, as will be discussed in section 6.3.7.

6.3.3. Characteristics of the reverse-flow region

The spatial distributions of the average skin-friction coefficient, see figure 6.6(a), exhibit a large and connected separation region characteristic of strong interactions. The figure also shows that the location of the global minimum in $\langle C_f \rangle$ is not affected by Reynolds number and occurs approximately $1\delta_0$ upstream of the inviscid

Table 6.5: Topological properties of the interaction region.

Case	$\frac{L_{sep}}{\delta_0}$	$\frac{L_\chi}{\delta_0}$	$\frac{\Delta x_{ui}}{\delta_0}$	ϑ_{sep}	ϕ_{sep}	$\frac{H_{sep}}{L_{sep}}$	$\frac{A_{sep}}{\frac{1}{2}H_{sep}L_{sep}}$	$\frac{L_u}{L_{sep}}$	$\frac{A_u}{A_{sep}}$
$\mathcal{B}_1$	6.65	10.62	7.57	12.15°	41.75°	0.044	0.78	0.66	0.54
$\mathcal{B}_2$	6.74	11.16	7.19	12.24°	41.86°	0.056	1.04	0.56	0.53
$\mathcal{B}_3$	6.24	10.64	6.62	12.05°	41.63°	0.053	1.08	0.59	0.57

impingement point x_{imp}. The overall skin-friction distribution within the reverse-flow region, on the other hand, is noticeably different at low and high Reynolds number. The low-Reynolds case $\mathcal{B}_1$, indicated with a dash-dotted line in figure 6.6(a), exhibits a W-shaped distribution characteristic of low-Reynolds interactions [163, 170, 172], with a second negative peak right after separation. The higher Reynolds cases have a skin-friction plateau in the first half of the separation bubble that precedes the global minimum on the second half. Despite the aforementioned differences, the separation length L_{sep}, i.e., the distance between mean separation and reattachment points, does not appear to change noticeably in the investigated Reynolds number range, see also table 6.5. This finding is in agreement with the experimental work of Souverein *et al.* [182] and the comparative numerical study of Morgan *et al.* [36] over the range $Re_\theta = 1500$-–4800, where L_{sep} was also found insensitive to the Reynolds number. Interestingly, though, the largest L_{sep} value in our LES database is found for case $\mathcal{B}_2$ ($L_{sep} = 6.74\delta_0$), which indicates that the effect of Reynolds number on the interaction topology is non-monotonic.

Figure 6.6(a) also includes the skin-friction distribution of the corresponding undisturbed TBLs (dash-dotted lines) in order to better appreciate the upstream influence of the STBLI. Inspired by Settles *et al.* [59], we define the upstream influence parameter $\Delta x_{ui} = x_{imp} - x_{ui}$ for impinging STBLI as the distance between the inviscid impingement point x_{imp} and the streamwise location where the skin-friction falls by 1% with respect to the undisturbed TBL distribution, denoted by x_{ui}. The resulting values for this parameter are also reported in table 6.5. They confirm the Reynolds number dependency of the upstream influence effect that was previously observed in compression ramp flows, that is, a reduced upstream influence with increasing Re_τ. We find that the logarithmic fit $\Delta x_{ui}/\delta_0 = -0.357 \ln Re_\tau + 9.689$ approximates the present data with an R^2 value of 0.995.

A final remark on figure 6.6(a) concerns the skin-friction distribution downstream of the interaction. As observed, all curves overshoot the corresponding values of the undisturbed TBLs beyond the reattachment point. This is due to the presence of the expansion fan that originates at the trailing edge of the (virtual) shock generator.

The probability of reverse flow χ is shown in figure 6.6(b) to further illustrate Reynolds number effects in the shock-induced flow separation. Solid lines indicate the probability at the wall, i.e., the fraction of the total time when $C_f < 0$, and dashed lines consider the maximum value in wall-normal direction, i.e., the fraction of the total time when $u < 0$ at any point above the wall.

Initially, both probability distributions initially overlap for the lower Reynolds

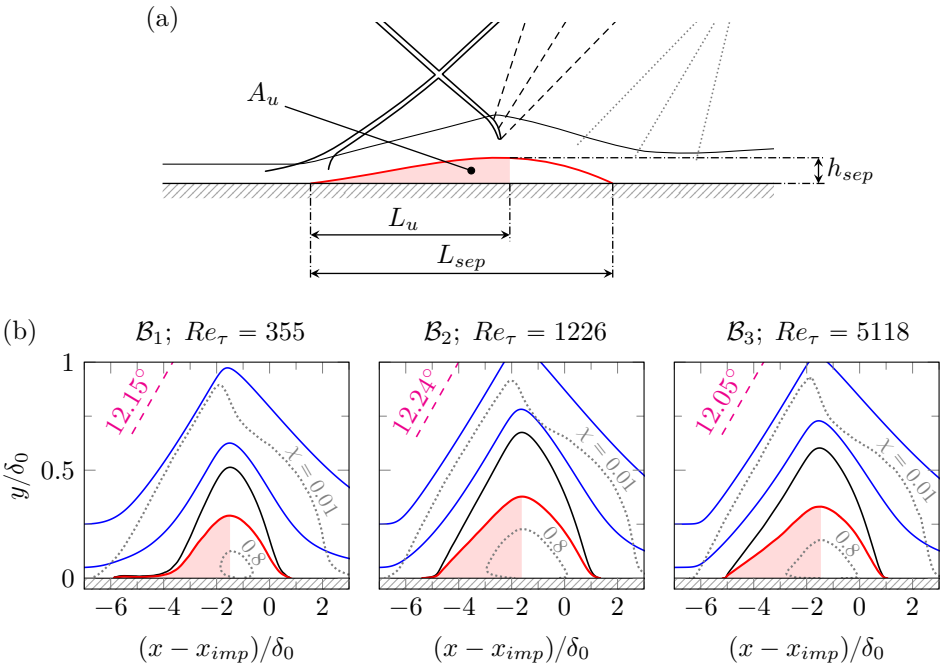

Figure 6.7: (a) Relevant definitions concerning the interaction topology, and (b) close-up view of the recirculation region. Dividing streamlines are marked with solid black lines in (b), and blue lines are streamlines passing through $y/\delta_0 = \{0.05, 0.3\}$ at $x - x_{imp} = -7\delta_0$. Dotted gray lines indicate isocontours of reverse-flow probability ($\chi = 0.01$ and 0.8), and dashed magenta lines show the free-stream flow deflection.

cases $\mathcal{B}_1$ and $\mathcal{B}_2$, see the corresponding blue and black lines in figure 6.6(b), until $\chi \approx 0.60$ and 0.45 respectively. This overlap ends with a local peak in χ at the wall that reveals the occurrence of partial flow reattachment near the leading edge of the interaction. Interestingly, the location of the local peak for case $\mathcal{B}_1$, found at $(x - x_{imp})/\delta_0 \approx -5.6$, coincides with the local minimum in skin-friction near separation in figure 6.6(a). This correspondence suggests that the characteristic W-shaped distribution of $\langle C_f \rangle$ in low-Reynolds interactions is a result of partial flow reattachment right after separation.

For the high-Reynolds case $\mathcal{B}_3$, both probability distributions in figure 6.6(b) only overlap until $\chi \approx 0.25$. Moreover, all cases exhibit a maximum in reversed-flow probability at $x - x_{imp} = -\delta_0$, where χ is almost unity for cases $\mathcal{B}_2$ and $\mathcal{B}_3$ when considering the maximum value in wall-normal direction (see the corresponding blue lines). The location of this peak is also associated with a negative peak in $\langle C_f \rangle$, see figure 6.6(a), in this case the global minimum.

The effect of Reynolds number on the recirculation bubble topology is further quantified with a set of topology parameters that we define in figure 6.7(a) and report in table 6.5. They include the aspect ratio of the bubble, i.e., its height H_{sep} normalized by L_{sep}, and the bubble area A_{sep}, i.e., its volume per unit span.

The latter is normalized by the area of the triangle formed by the separation point, bubble apex and reattachment point locations to highlight the degree of compliance with a perfect triangular shape (with area $H_{sep}L_{sep}/2$).

For the higher-Reynolds cases $\mathcal{B}_2$ and $\mathcal{B}_3$, the normalized A_{sep} is very close to unity, see table 6.5, which indicates that the corresponding bubbles are closely triangular. The recirculation bubble for the low-Reynolds case $\mathcal{B}_1$, in contrast, is characterized by a smaller normalized A_{sep} of 0.78. A close-up view of the different recirculation regions in figure 6.7(b) shows that the reversed flow is initially restricted to the wall for this case, over a distance of approximately $2\delta_0$, before the shear layer moves away from the wall. This condition is consistent with the presence of a compression fan instead of a coalesced separation shock at the leading edge of the interaction, and explains the larger degree of non-compliance of the bubble shape with a perfect triangle.

Additionally, the corresponding dividing streamline (black line) and two other streamlines above the separation region (blue lines) are also included in figure 6.7(b). For the low-Reynolds case $\mathcal{B}_1$, they clearly exhibit a much larger curvature radius around the leading edge of the separation bubble. The post-shock flow deflection ϑ_{sep} is slightly larger than 12° in all cases and essentially independent of the Reynolds number. This deflection is also indicated in figure 6.7(b) and reported in table 6.5 along with the corresponding theoretical shock angle ϕ_{sep}.

Furthermore, table 6.5 provides additional parameters that quantify the degree of symmetry between the leading and trailing portions of the bubble. These include the corresponding distance between the separation point and the streamwise location of the bubble apex, which is denoted L_u following the nomenclature employed by Giepman [194] for laminar and transitional interactions; see also figure 6.7(a). The associated bubble volume above this segment, A_u, is also reported and indicated with a red shade in figure 6.7. Interestingly, both symmetry parameters reveal that the separation bubble for case $\mathcal{B}_2$ is the most symmetric in shape, with $L_u = 0.56L_{sep}$ and $A_u = 0.53A_{sep}$. This can also be recognized by visual inspection of figure 6.7(b). The reverse-flow probability within the bubble, however, is clearly asymmetric in all cases, see the $\chi = 0.8$ isocontour.

The isocontour of $\chi = 0.01$ is included in figure 6.7(b) to illustrate the extent of the instantaneous reverse flow. Following Simpson's terminology for turbulent boundary layer separation, $\chi = 0.01$ is the condition for incipient separation [195]. This isocontour is an essentially straight line at the leading edge of the bubble in all cases, see figure 6.7(b), and closely follows the post-shock deflection of the outer flow. The maximum height above the wall of the $\chi = 0.01$ isocontour is approximately $0.9\delta_0$, which is two to three times higher than the mean bubble height H_{sep}. At the trailing edge of the bubble, the contour line is curved and eventually meets the wall approximately $2\delta_0$ downstream of the reattachment point. We use the streamwise distance over which the reversed-flow probability is higher than $\chi = 0.01$ to define the reverse-flow based length scale L_χ. This parameter could be an alternative to L_{sep} in the case of weakly separated STBLIs with partitioned bubbles. For the present strong interactions, L_χ is approximately $11\delta_0$ and insensitive to the Reynolds number, see table 6.5.

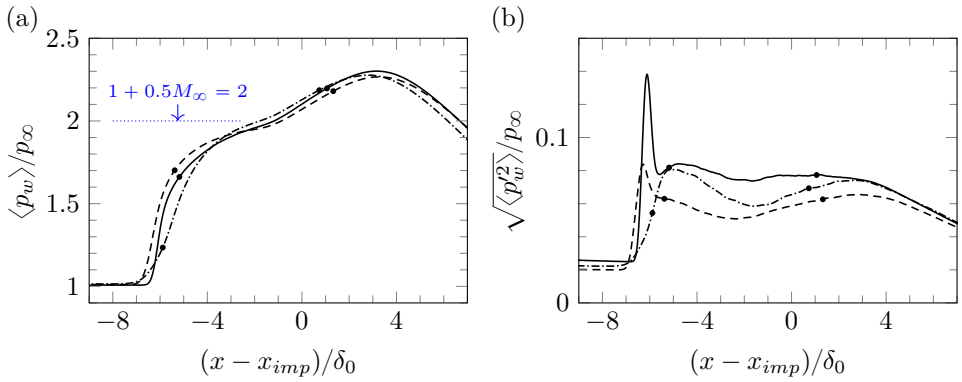

Figure 6.8: Time- and spanwise-averaged (a) wall-pressure, and (b) wall-pressure fluctuation intensity. For the line legend, see caption of figure 6.6. Mean separation and reattachment points are indicated with a marker (•), and the plateau pressure computed according to the empirical formula by Zukoski [196] is also shown in (a).

6.3.4. Mean and fluctuating wall-pressure

After discussing the corresponding differences in recirculation-bubble topology, we now consider the impact of Reynolds number on wall-pressure characteristics of STBLI. Figure 6.8(a) shows the mean wall-pressure distribution for the investigated interactions, which all exhibit the typical features of strong STBLI with substantial flow separation [23, 46]. Characteristic inflection points associated with separation, the onset of reattachment and the reattachment compression can be identified on each curve [197]. The low-Reynolds case $\mathcal{B}_1$, however, shows a more gradual pressure rise at the leading edge of the interaction as a result of the diffuse separation-shock foot, while the higher Reynolds cases $\mathcal{B}_2$ and $\mathcal{B}_3$ exhibit a more abrupt pressure increase. The pressure plateau is not fully established in any of the cases, and its magnitude, in close agreement with the predictions by Zukoski [196], appears insensitive to the Reynolds number.

The corresponding wall-pressure fluctuation intensities are presented in figure 6.8(b). The low-Reynolds case $\mathcal{B}_1$ does not exhibit any discernible peak at the leading edge of the interaction, which is indicative of attenuated wall-pressure intermittency [163]. A distinct peak, in contrast, is clearly visible for the higher Reynolds interactions as a result of the sharper separation-shock footprint on the surface, where the peak intensity is almost twice as large for case $\mathcal{B}_3$ as compared to that of case $\mathcal{B}_2$. Furthermore, case $\mathcal{B}_3$ exhibits the largest wall-pressure fluctuation intensities throughout the interaction, while the lowest values are found for case $\mathcal{B}_2$. This observation further evidences the non-monotonic effect of Reynolds number on the interaction dynamics. Despite the difference in magnitude, however, curves in figure 6.8(b) exhibit common features that are in good qualitative agreement with previous works on impinging STBLI [23, 181]. In particular, all distributions show an increased level of fluctuation intensity after separation (corresponding to a global maximum for case $\mathcal{B}_1$ and a local maximum for case $\mathcal{B}_3$) which is attributed to the

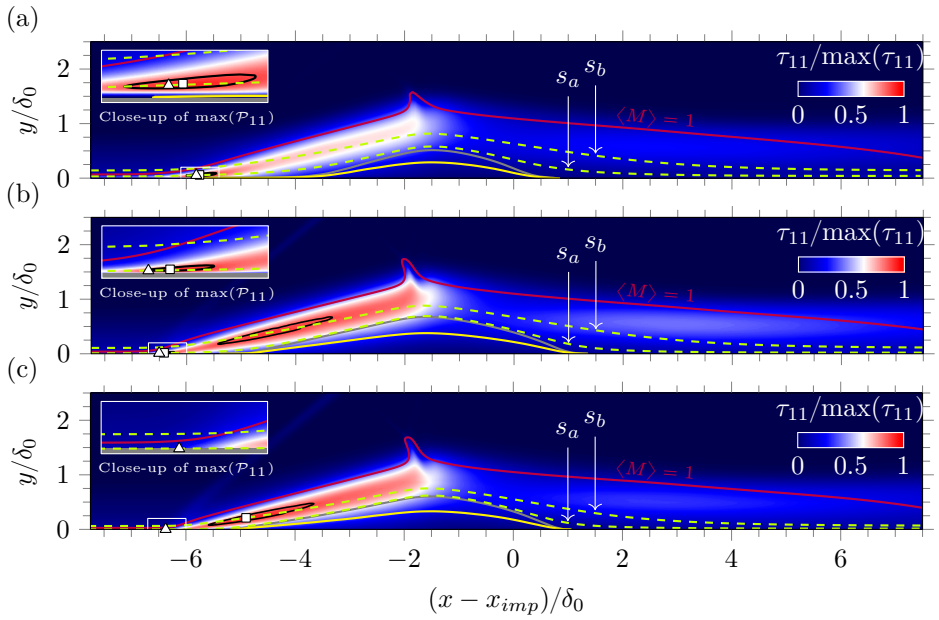

Figure 6.9: Time- and spanwise-averaged streamwise Reynolds stress $\tau_{11} = \widetilde{u''u''}$ for (a) case $\mathcal{B}_1$, (b) case $\mathcal{B}_2$, and (c) case $\mathcal{B}_3$. Solid line color legend: (yellow) $\langle u\rangle = 0$; (gray) dividing streamline; (purple) $\langle M\rangle = 1$; (black) 95% of max(τ_{11}). Green dashed lines mark selected streamlines, and ▫ and △ indicate the locations of max(τ_{11}) and max($\mathcal{P}_{11}$), respectively.

flapping motion of the shear layer [181]. This is followed by a small drop in pressure fluctuation intensity within the separated region before increasing again as a result of the reattaching shear layer vortices.

Moreover, the wall-pressure statistics in figure 6.8 indicate that mean separation occurs downstream of the excursion domain of the separation shock (i.e., beyond the pressure fluctuation intensity peak in figure 6.8(b)) for the interactions at higher Reynolds number. We attribute this to the moderate incident-shock strength in the investigated STBLIs, which results in a deeper penetration of the high-momentum flow into the interaction before the formation of the separation bubble.

6.3.5. Reynolds stresses

The effect of Reynolds number on second-order velocity statistics is analyzed next. Figure 6.9 shows contours of the Favre-averaged streamwise Reynolds stress $\tau_{11} = \widetilde{u''u''}$. Qualitatively, all cases bear similarities in terms of the location of increased fluctuation intensity, which is mainly confined to the shear layer at the leading edge of the separated region. This is in good agreement with previous works [23, 166, 198]. Additionally, τ_{11} is highly damped by the strong convex curvature at the bubble apex in all cases. As pointed out by Sandham [199], such curvature effects are strongest for this stress component.

One notable observation concerns the disparity in the location of maximum τ_{11}

across the different cases, as indicated by the ▫ symbols in figure 6.9. It is evident that in figures 6.9(a,b), for the lower-Reynolds cases $\mathcal{B}_1$ and $\mathcal{B}_2$, this point is found near the separation-shock foot, where the production of τ_{11}, i.e., $\mathcal{P}_{11}$, is highest. This point is indicated with a △ symbol. Conversely, for the high-Reynolds case $\mathcal{B}_3$ in figure 6.9(c), the streamwise stress distinctly peaks within the detached shear layer, which is no longer correlated with $\max(\mathcal{P}_{11})$ (see also the isocontours of 95% of $\max(\tau_{11})$ shown as black solid lines).

Previous numerical studies, such as Fang *et al.* [176] and the recent work of Kang and Lee [200], which have examined turbulence amplification across canonical STBLIs, consistently identified peak locations of τ_{11} and turbulence kinetic energy (TKE) beneath the separation-shock foot and near the point of maximum stress production. While these findings are consistent with our observations in the lower-Reynolds cases, the observed disparity in stress peak locations for case $\mathcal{B}_3$ suggests that the widely accepted τ_{11} amplification mechanism proposed in literature, which is associated with the deceleration of the mean-flow, may not be the primary source of stress at high Reynolds number.

To clarify this, we analyze the corresponding transport budgets along two mean-flow streamlines crossing the interaction. The first streamline, labeled s_a in figure 6.9, intersects the point of $\max(\mathcal{P}_{11})$ in all cases, which is consistently located in the near-wall region beneath the separation-shock foot. As shown in the inset panels of figures 6.9(a,b), this point is indeed in close proximity to the point of maximum τ_{11} for the lower-Reynolds cases $\mathcal{B}_1$ and $\mathcal{B}_2$. The second selected streamline, labeled as s_b, cuts through the shear layer as shown in figure 6.9. Notably, this intersection highlights the misalignment between the mean-flow and the track of maximum stress in the detached shear layer. For the high-Reynolds case $\mathcal{B}_3$, s_b is selected such that it intersects the location of maximum τ_{11} over the interaction (i.e., the ▫ symbol in figure 6.9(c)).

The transport equation for the Favre-averaged Reynolds stress $\tau_{ij} = \widetilde{u_i'' u_j''}$ in convective form is

$$\frac{\partial \tau_{ij}}{\partial t} + \widetilde{u}_k \frac{\partial \tau_{ij}}{\partial x_k} = \mathcal{P}_{ij} + \mathcal{D}_{ij} + \Pi_{ij} + \mathcal{M}_{ij} - \epsilon_{ij}, \tag{6.1}$$

where the mass averaged form of the continuity equation is used to simplify the left-hand side. Terms on the right-hand side represent the contributions due to production $\mathcal{P}_{ij} = -\tau_{ik}\partial_{x_k}\widetilde{u}_j - \tau_{jk}\partial_{x_k}\widetilde{u}_i$, transport processes $\mathcal{D}_{ij} = (\mathcal{D}^{\nu}_{ij} + \mathcal{D}^{t}_{ij} + \mathcal{D}^{p}_{ij})/\overline{\rho}$ that comprise viscous diffusion $\mathcal{D}^{\nu}_{ij} = \partial_{x_k}[\overline{\sigma'_{ik}u'_j + \sigma'_{jk}u'_i}]$, turbulent convection $\mathcal{D}^{t}_{ij} = -\partial_{x_k}[\overline{\rho u_i'' u_j'' u_k''}]$, and pressure transport $\mathcal{D}^{p}_{ij} = -\partial_{x_k}[\overline{p'u'_i}\delta_{jk} + \overline{p'u'_j}\delta_{ik}]$, the pressure-strain correlation $\overline{\rho}\Pi_{ij} = \overline{p'(\partial_{x_i}u'_j + \partial_{x_j}u'_i)}$, dissipation $\overline{\rho}\epsilon_{ij} = \overline{\sigma'_{ik}\partial_{x_k}u'_j + \sigma'_{jk}\partial_{x_k}u'_i}$, and turbulent mass flux $\overline{\rho}\mathcal{M}_{ij} = \overline{u_i''}(\partial_{x_k}\overline{\sigma}_{jk} - \partial_{x_j}\overline{p}) + \overline{u_j''}(\partial_{x_k}\overline{\sigma}_{ik} - \partial_{x_i}\overline{p})$. Over-bars and tildes indicate Reynolds and Favre averages, respectively.

Resulting distributions of the τ_{11} transport budgets along the previously defined streamlines are shown in figure 6.10. The convective term of the material derivative is evaluated as it appears on the left-hand side of equation (6.1) (with the sign unchanged) so that it serve as an indication of net τ_{11} gain. Additionally, for clarity,

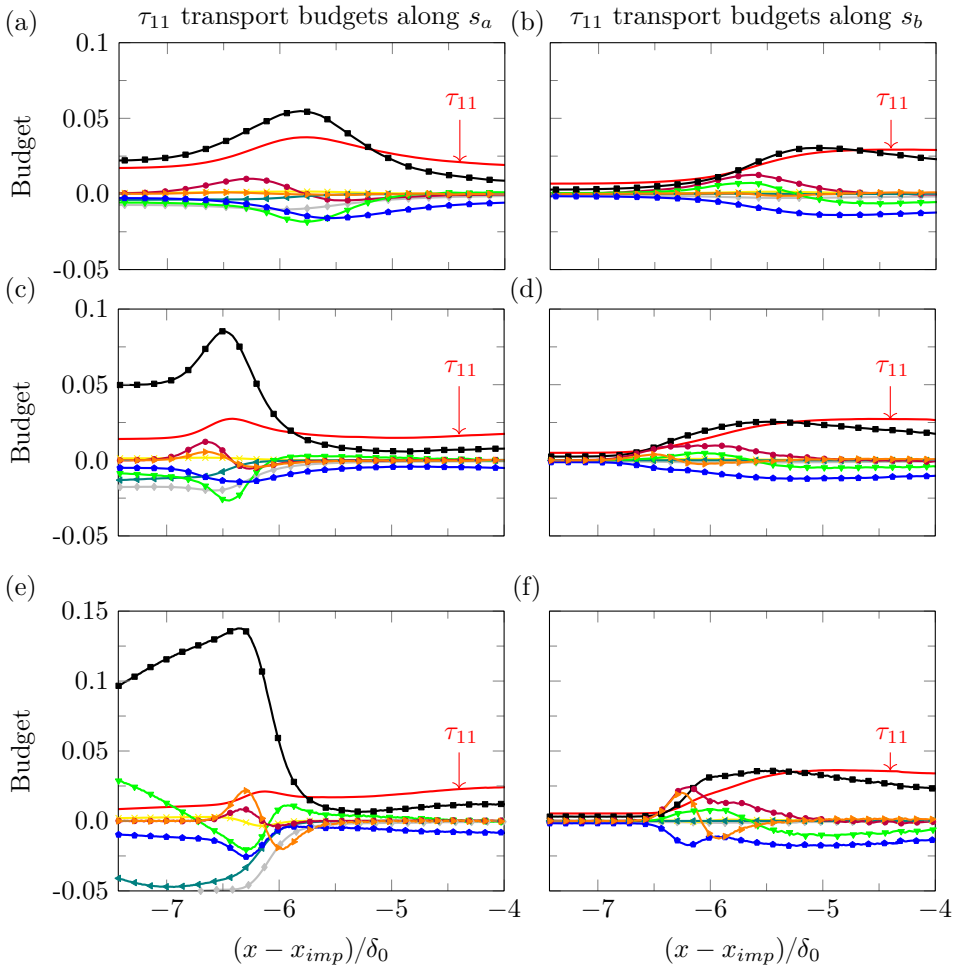

Figure 6.10: Transport budgets for τ_{11} along streamlines s_a (left panels) and s_b (right panels): (a,b) case $\mathcal{B}_1$, (c,d) case $\mathcal{B}_2$, and (e,f) case $\mathcal{B}_3$. Symbol legend: production $\mathcal{P}_{11}$ (■, black), viscous diffusion $\mathcal{D}^{\nu}_{11}/\overline{\rho}$ (◂, teal), turbulent convection $\mathcal{D}^{t}_{11}/\overline{\rho}$ (▼, green), pressure transport $\mathcal{D}^{p}_{11}/\overline{\rho}$ (▸, orange), pressure-strain correlation Π_{11} (⬟, blue), turbulent mass flux $\mathcal{M}_{11}$ (×, yellow), dissipation ϵ (♦, gray) and convection $\widetilde{u}_k\partial_k\tau_{11}$ (●, magenta). For reference, the evolution of τ_{11} (normalized by u^2_∞) is also indicated with a solid red line.

two-dimensional contours of the most relevant terms are also shown in figure 6.11, and they should be considered alongside the discussion of figure 6.10.

We consider first the corresponding budget distributions along s_a, which are depicted on the left panels of figure 6.10. It is clear that the magnitude of the production term at the separation-shock foot is largest for the high-Reynolds case $\mathcal{B}_3$ in figure 6.10(e). However, the amplification of $\mathcal{P}_{11}$ with respect to that of the undisturbed TBL is only 1.06 , which indicates a minor impact of the mean-flow deceleration in the near-wall production at high Reynolds number. For the other

cases, the amplification of this term is much larger; 1.58 for case $\mathcal{B}_2$ in figure 6.10(c), and 2.44 for case $\mathcal{B}_1$ in figure 6.10(a). In addition, the fact that $\mathcal{P}_{11}$ for case $\mathcal{B}_3$ exhibits a progressive increase in the upstream boundary layer is simply a result of the selected streamline deviating away from the wall, from $y^+ \approx 6$ on the left of figure 6.10(e) to $y^+ \approx 10$ at the peak production. This deviation naturally alters the value of the production term as well as other terms like turbulent transport $\mathcal{D}^t_{11}$, which changes from a positive to a negative value. Thus, an indication of the STBLI onset is where previously inactive terms in the undisturbed TBL, like convection or pressure transport, become active.

Figures 6.10(c,e) reveal that the convection term, which indicates net τ_{11} gain, is correlated with the initial amplification of the pressure transport term for the higher Reynolds cases $\mathcal{B}_2$ and $\mathcal{B}_3$. This is caused by the stronger footprint of the separation-shock dynamics at the wall, which leads to large negative values of the pressure−streamwise-velocity correlation for these cases and consequently a sharp rate of change in streamwise direction. The streamwise extent of increased pressure transport $\mathcal{D}^p_{11}$, including both positive and negative values, thus reflects the streamwise excursion range of the separation shock. For the low-Reynolds case $\mathcal{B}_1$, in contrast, the more gradual compression and thus weaker footprint of the separation-shock dynamics at the wall result in negligible pressure transport contributions. Here, the increase in τ_{11} is solely attributed to the amplification of $\mathcal{P}_{11}$ driven by the deceleration of the mean flow, see figure 6.10(a). This corresponds to the amplification mechanism previously reported in literature [176], which this analysis demonstrates to be predominant only at low Reynolds numbers. Furthermore, the increase in pressure-strain correlation Π_{11} eventually brings the amplification of τ_{11} to an end in all cases. The pressure-strain correlation is responsible for the redistribution of energy from the longitudinal stress τ_{11} towards the transverse stresses τ_{22} and τ_{33} (and indirectly to the shear stress τ_{12}) which exhibit large positive values of Π_{ij} at the separation shock foot (not shown here).

The role of pressure transport on the amplification of τ_{11} at high Reynolds number is further highlighted in the budget distributions along the streamline s_b, which are shown on the right panels of figure 6.10 for all cases. The level of $\mathcal{P}_{11}$ in the upstream TBL is much lower along this streamline, as expected away from the wall. For case $\mathcal{B}_1$, the progressive amplification of the production term together with increased turbulent convection $\mathcal{D}^t_{11}$ lead to a net gain in streamwise stress, see figure 6.10(b). A similar scenario is observed for case $\mathcal{B}_2$ in figure 6.10(d), with an additional contribution of pressure transport, albeit very moderate, at the leading edge of the interaction. The role of pressure transport, however, is much more significant for case $\mathcal{B}_3$ in figure 6.10(f). As shown, the evolution of the convection term at the leading edge of the interaction is highly correlated with the pressure transport budget, specially its initial steep rise and peak value (occurring at $y^+ \approx 350$). This results in the largest rate of change of τ_{11}, which also contributes to the rapid amplification of $\mathcal{P}_{11}$. Even though the magnitude of the production term is much lower than the global production peak observed in the near-wall region (see figure 6.10(e)), it undergoes a much larger amplification from the free-stream value along this streamline. Once the pressure-transport contribution becomes negative,

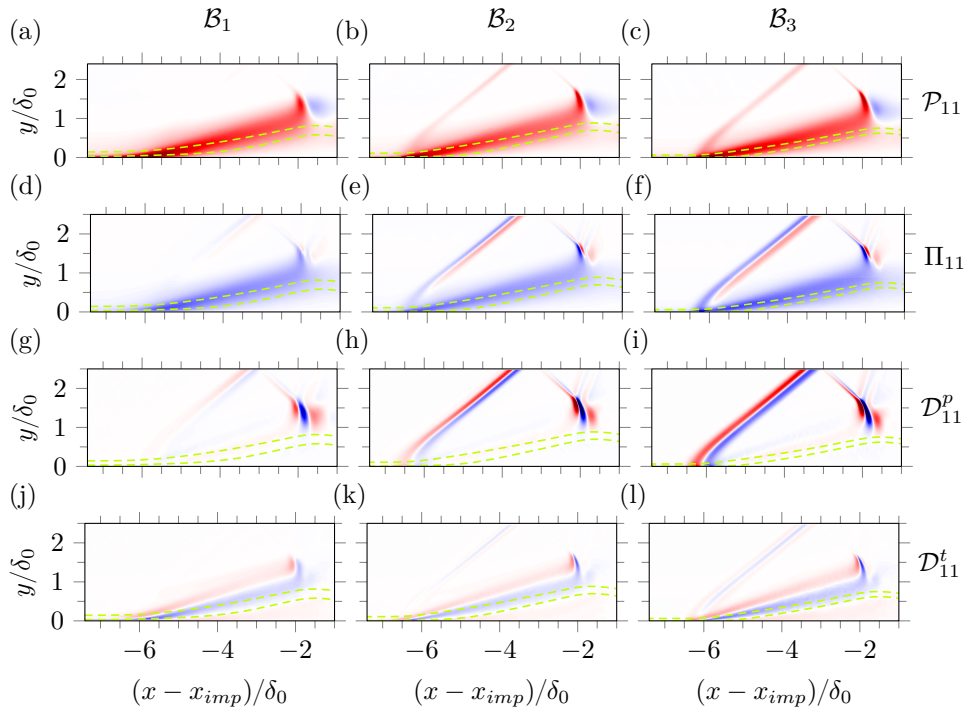

Figure 6.11: Contours of selected τ_{11} transport budgets: (a–c) production $\mathcal{P}_{11}$, (d–f) pressure-strain correlation Π_{11}, (g–i) pressure transport $\mathcal{D}^p_{11}$, and (j–l) turbulent convection $\mathcal{D}^t_{11}$. Each column of panels corresponds to a different case, as indicated at top of the figure. Contour levels are shown from $-0.05u^3_\infty/\delta_0$ (dark blue) to $0.05u^3_\infty/\delta_0$ (dark red).

the increased production (also affected by the mean flow deceleration) and turbulent diffusion terms still enable a net gain in τ_{11} for over half a boundary layer thickness in streamwise direction, eventually leading to the global peak stress along the detached shear layer.

The present analysis thus demonstrates that the maximum amplification of τ_{11} at high Reynolds number no longer correlates with the peak in streamwise-stress production near the wall. This peak is influenced by both the near-wall cycle of the approaching TBL and the mean-flow deceleration at the leading edge of the interaction. Instead, we demonstrate that the maximum τ_{11} amplification correlates with increased pressure transport in the separation-shock excursion domain, further away from the wall. This increase is attributed to the unsteadiness of the sharp separation shock at high Reynolds number, originating deep within the TBL. The contours of τ_{11} production, pressure-strain, pressure-transport and turbulent convection shown at the leading edge of the interaction in figure 6.11 further illustrate the effect of Reynolds number on the budget terms. In particular, figures 6.11(g–i) show the τ_{11} pressure-transport budget $\mathcal{D}^p_{11}$, where visible differences in the separation-shock foot region are observed.

Moving on to the cross-stream and shear stress components, they do not exhibit

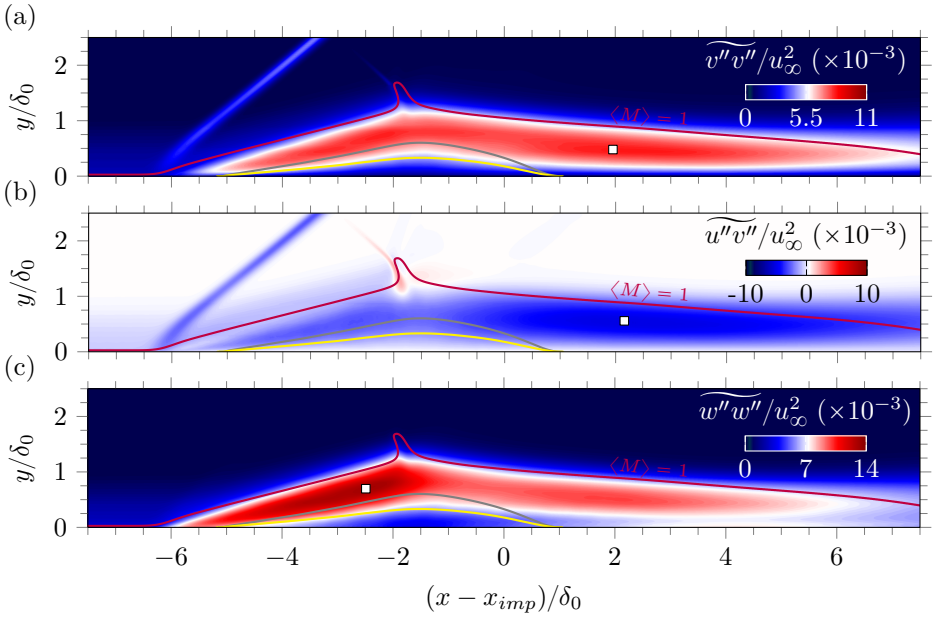

Figure 6.12: Time- and spanwise-averaged Reynolds stresses (other than τ_{11}) for case $\mathcal{B}_3$: (a) $\tau_{22} = \widetilde{v''v''}$, (b) $\tau_{12} = \widetilde{u''v''}$, (c) $\tau_{33} = \widetilde{w''w''}$. Locations of maximum stress are indicated with ▫. For line legend, see caption of figure 6.9.

any strong Reynolds number dependency over the investigated Reynolds number range. For the sake of conciseness, we only show them for the high-Reynolds case $\mathcal{B}_3$ in figure 6.12. The location of the corresponding stress peaks are also indicated with ▫. The wall-normal stress $\tau_{22} = \widetilde{v''v''}$ shows increased fluctuation levels in the excursion range of the separation shock and along the shear layer, see figure 6.12(a). The global maximum is located around the reattachment location but away from the wall, where shear layer vortices are compressed as a result of the concave streamline curvature. This is in very good agreement with the LES data of [23], where slightly larger values of τ_{22} were found due to the stronger reattachment compression (a reattachment shock is clearly visible in their STBLI). The distribution of the Reynolds shear stress $\tau_{12} = \widetilde{u''v''}$, see figure 6.12(b), is very much in line with τ_{22}, including the (negative) peak location. The flapping motion of the incident-transmitted shock results in a region of positive shear stress, which is most intense for the high-Reynolds case $\mathcal{B}_3$. The low-Reynolds case $\mathcal{B}_1$, on the other hand, presents slightly larger (negative) stress values at the separation-shock foot. Neither τ_{22} nor τ_{12} appear significantly damped at the bubble apex, in agreement with the observations of Sandham [199].

The spanwise Reynolds stress $\tau_{33} = \widetilde{w''w''}$ bears clear similarities with both τ_{11} and τ_{22}. These include a significant intensity decrease at the bubble apex. However, the location of peak stress is found further away from the wall within the detached shear layer at the leading edge of the separation bubble in all cases. Interestingly,

this is not in line with the LES data of Pasquariello *et al.* [23] where the τ_{33} peak was found approximately $3\delta_0$ downstream of the reattachment location and very close to the wall. Inspection of figure 6.12 also reveals a moderate τ_{33} increase at the same location in our LES data, but the intensity is substantially lower than in the majority of the shear layer. Pasquariello *et al.* [23] attribute the increased intensity to the presence of Görtler-like vortices resulting from the concave streamline curvature at reattachment. Although above the critical Görtler number, this curvature is rather mild in the present STBLIs, which involve a weaker incident shock than that of Pasquariello *et al.* [23]. We observe a reorganization of velocity fluctuations across the interaction that is consistent with the presence of streamwise-aligned vortices, see section 6.3.2. Their apparenlty limited impact on τ_{33} is consistent with the observed lower vortex strength and suggests a less pivotal role in the low-frequency dynamics in our cases.

6.3.6. Spectral analysis

In order to assess Reynolds number effects in the dynamics of the investigated STBLIs, we analyze temporal spectra of wall-pressure data, separation-shock location and bubble-volume variations. The most energetic frequencies are then linked to global flow phenomena via dynamic mode decomposition (DMD [61]) of the LES data. In previous impinging STBLI, such modal analysis technique has been commonly applied to two-dimensional datasets, often resulting from spanwise averaging [23, 35, 62]. Here, we instead employ a full three-dimensional dataset that includes the instantaneous streamwise velocity, pressure and streamwise vorticity fields. In addition, the sparsity-promoting variant of the DMD algorithm (known as SPDMD [201]) is employed to seek a low-rank representation of the most relevant dynamics for each of the investigated Reynolds numbers.

Wall-pressure

Figure 6.13 shows the pre-multiplied PSD map of the wall-pressure for each of the investigated interactions. The corresponding signals were obtained from wall-pressure taps equispaced in the streamwise direction along the domain centerline and sampled at a frequency $f_s \approx 37u_\infty/\delta_0$ ($\sim$2.5 MHz). Spectra have been estimated using Welch's algorithm, with Hamming windows and 10 segments with 65% overlap. The segment length is longer than $100L_{sep}/u_\infty$ in all cases.

The wall-pressure PSD maps in figure 6.13 illustrate one of the most prominent features of STBLI: the shifting of the frequency of the most energetic fluctuations in the incoming TBL to much lower frequencies. Consistent with previous works, the separation shock exhibits broadband low-frequency dynamics at a separation-length based Strouhal number $0.01 \lesssim St_{L_{sep}} \lesssim 0.1$. The spatial extent associated with such low-frequency dynamics, indicative of the streamwise excursion domain of the separation shock, is approximately δ_0 for the higher-Reynolds number cases $\mathcal{B}_2$ and $\mathcal{B}_3$, see figures 6.13(b,c). The low-frequency content of the low-Reynolds case $\mathcal{B}_1$ extends for almost $2\delta_0$ in streamwise direction but appears much less energetic, as seen in figure 6.13(a). This lower energy level is expected considering the diffused character of the separation-shock foot. Moreover, the separation point for this case

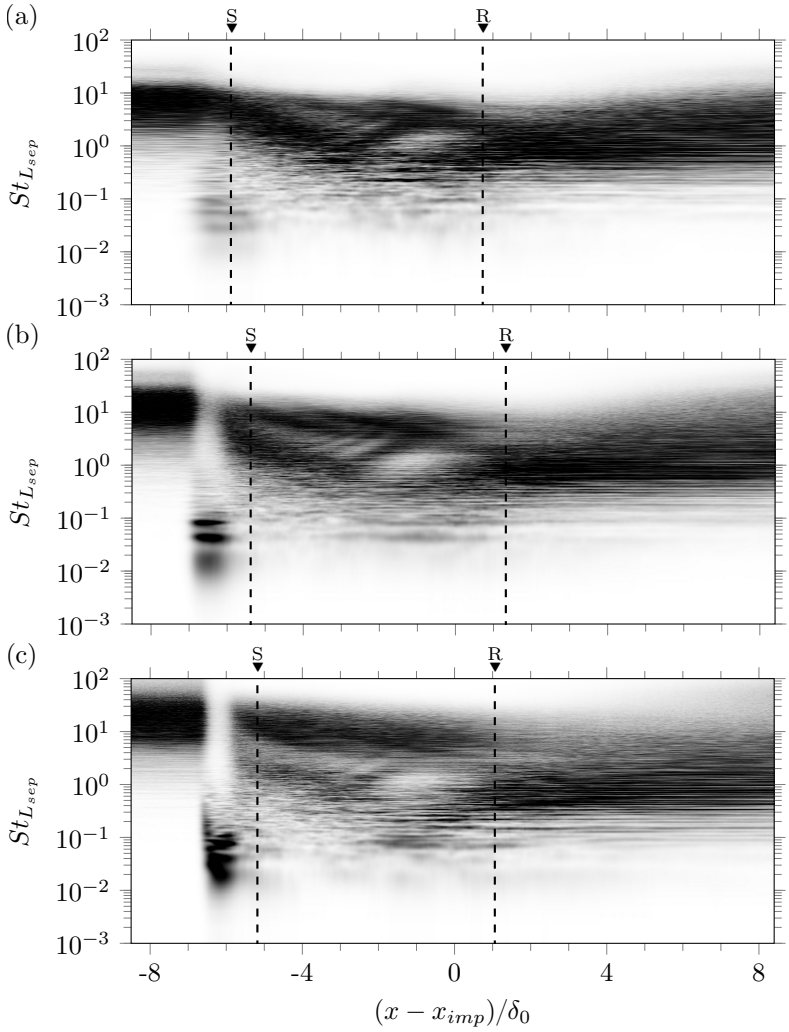

Figure 6.13: Frequency-weighted and normalized power spectral density map of wall-pressure at the center line: (a) case $\mathcal{B}_1$, (b) case $\mathcal{B}_2$, and (c) case $\mathcal{B}_3$. Dashed lines indicate mean separation S and reattachment R locations for each case. Contour levels range from zero (white) to 0.3 (black).

(labeled S) occurs within the low-frequency region, while it is found downstream of the separation-shock excursion domain for cases $\mathcal{B}_2$ and $\mathcal{B}_3$. This observation is consistent with the analysis of wall-pressure fluctuations in figure 6.8(b).

Beyond the region of low-frequency unsteadiness, energetic frequencies of turbulent fluctuations notably decrease, and this trend is preserved well into the reverse-flow bubble in all cases. This observation confirms the formation of larger turbulent structures in the detached shear layer, associated with lower frequencies. Within the recirculation region, a spectral peak around $St_{L_{sep}} \lesssim 0.1$ is also visible in all cases at

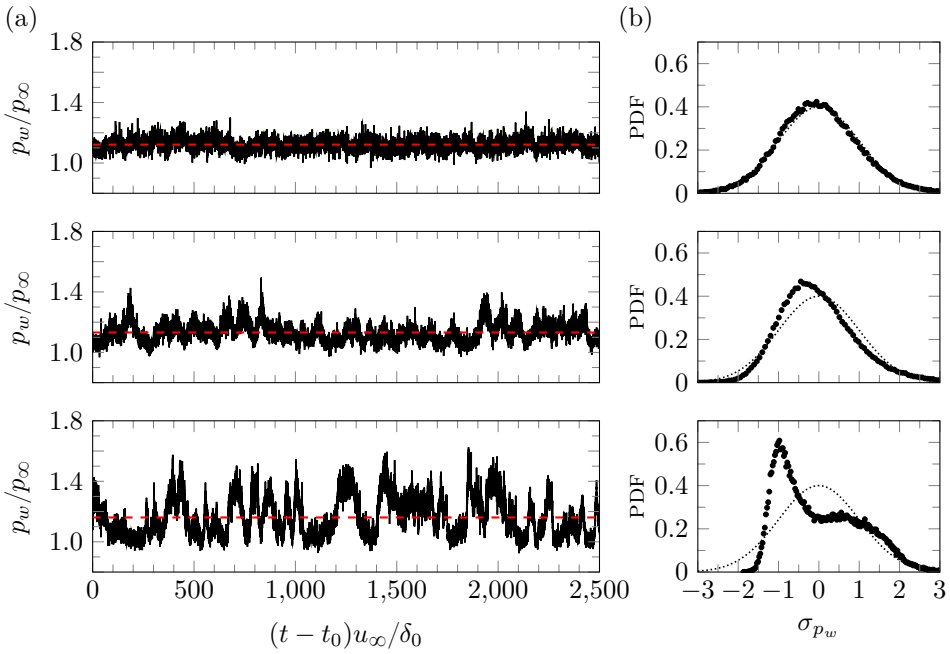

Figure 6.14: (a) Instantaneous wall-pressure signal near the separation shock foot, and (b) corresponding normalized PDF: (top) case $\mathcal{B}_1$, (middle) case $\mathcal{B}_2$, (bottom), case $\mathcal{B}_3$. Dashed lines in (a) indicate the mean value of the corresponding signal, and dotted lines in (b) depict a reference Gaussian distribution.

$(x - x_{imp})/\delta_0 \approx -1$, which corresponds to the point where the skin-friction exhibits a global minimum in figure 6.6(a). Beyond this point, and near the reattachment location (labeled R), energetic frequencies are highly broadband in all cases, spanning over two decades of $St_{L_{sep}}$. These frequencies include: (1) $St_{L_{sep}}$ larger than unity, characteristic of small-scale turbulence (but larger than in the upstream TBL); (2) intermediate frequencies centered around $St_{L_{sep}} \approx 0.5$, related to the reattaching shear layer vortices [181]; and 3) $St_{L_{sep}} \approx 0.1$, possibly associated with shear-layer dynamics, akin to the behavior observed in step flows where this frequency is linked to the flapping motion of the shear layer [193]. Finally, far downstream of the interaction, the spectra relax towards a state characteristic of canonical wall-turbulence in all cases.

The intermittent character of the wall-pressure at the separation-shock foot is illustrated in figure 6.14. In figure 6.14(a), the wall-pressure signal of a tap embedded within the separation-shock excursion domain is shown for each STBLI, while figure 6.14(b) includes the corresponding normalized PDF of the signal.

These data clearly illustrate the accentuated intermittency of the wall-pressure at high Reynolds number; notably, the signal for the high-Reynolds case $\mathcal{B}_3$ in the bottom panel of figure 6.14(a) exhibits a strongly bi-modal behavior, alternating between p_∞ and the post-shock pressure level [202]. Moreover, the signal is also clearly

aperiodic, consistent with the broadband nature of the low-frequency unsteadiness. These observations are in very good agreement with previous high-Reynolds experiments on the impinging shock configuration [60, 181, 189].

Furthermore, the corresponding p.d.f of the high-Reynolds wall-pressure signal, shown in the bottom panel of figure 6.14(b), exhibits high right-skewness (skewness coefficient of $\alpha_3 = 0.56$), with the major apex at $-\sigma_{p_w}$ and the minor apex at $+0.6\sigma_{p_w}$. As noted by Dolling and Or [202], the former peak reflects the high likelihood of encountering a value in a narrow range around p_∞, while the latter indicates the probability of observing a broader range of post-shock pressure levels.

For the low-Reynolds case $\mathcal{B}_1$, in contrast, wall-pressure fluctuations at the separation-shock foot exhibit an almost perfectly Gaussian distribution, see the top panel of figure 6.14(b), which is characteristic of low-Reynolds interactions with a diffused separation-shock foot, where intermittency is attenuated [158]. Case $\mathcal{B}_2$ lies midway between cases $\mathcal{B}_1$ and $\mathcal{B}_3$ in terms of intermittent behavior. Although the wall-pressure signal beneath the separation shock exhibits moderate intermittency, deviations from the free-stream pressure level are not as pronounced or distinct as those observed at high Reynolds number.

Separation shock and reverse-flow bubble

The effect of Reynolds number on the STBLI unsteadiness is further examined in figures 6.15 and 6.16, which respectively show the time variation of the spanwise-averaged separation-shock location and bubble-volume signals for all cases, alongside their respective spectral content. The instantaneous separation-shock location is extracted from three-dimensional snapshots by searching for peak values of the pressure gradient field $|\nabla p|$ in a wall-normal slice outside the TBL (at $1.5\delta_0$ from the wall, before intersecting the incident shock), and then averaging the resulting shock front in the spanwise direction. The instantaneous volume of the separation bubble, on the other hand, is estimated as the volume of reverse flow (i.e., $u < 0$) in the corresponding three-dimensional snapshot.

Starting with the separation-shock location signals in figure 6.15, it is evident that all signals exhibit noticeable low-frequency unsteadiness, with deviations from the mean location of up to $0.4\delta_0$ for the high-Reynolds interaction. The spectra of the signals, which are shown in pre-multiplied form, highlight that frequencies in the range $0.01 < St_{L_{sep}} < 0.1$ make the largest contributions to the signal variance. This observation indicates that there are mechanisms driving the low-frequency dynamics of STBLIs that are fundamentally independent of Reynolds number.

Despite the spanwise averaging, higher frequencies are found relatively energetic in the shock-location signal for case $\mathcal{B}_1$, in contrast to the higher Reynolds number cases. This is again attributed to the diffused character of the separation shock at low Reynolds number, which is much more sensitive to turbulent fluctuations. Instantaneous visualizations of the flow for this case (not shown here) show that incoming turbulent structures induce variations in the separation-shock front that are comparable to the range of motion of the shock at low frequencies.

Figure 6.16 shows the time evolution of the reverse-bubble volume and the corresponding spectral energy for the investigated interactions. Several similarities and

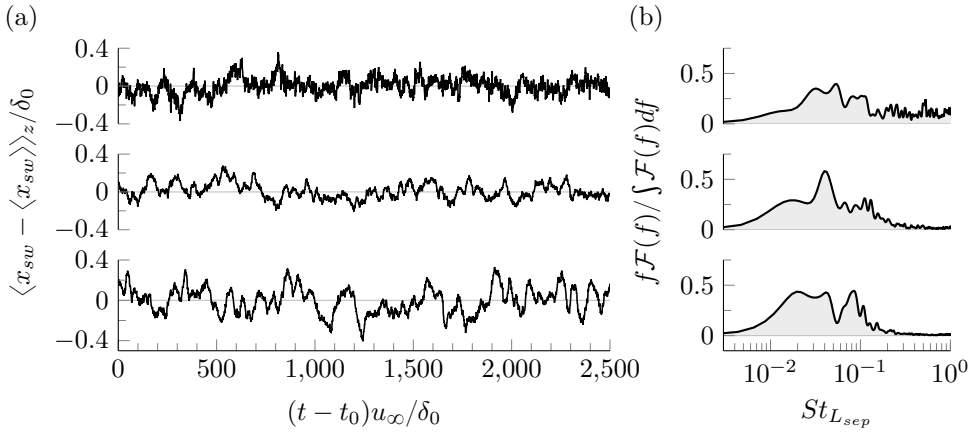

Figure 6.15: (a) Time variation of the spanwise-averaged separation-shock location at $y = 1.5\delta_0$, and (b) corresponding pre-multiplied and normalized PSD of the signal: (top) case $\mathcal{B}_1$; (middle) case $\mathcal{B}_2$; (bottom) case $\mathcal{B}_3$.

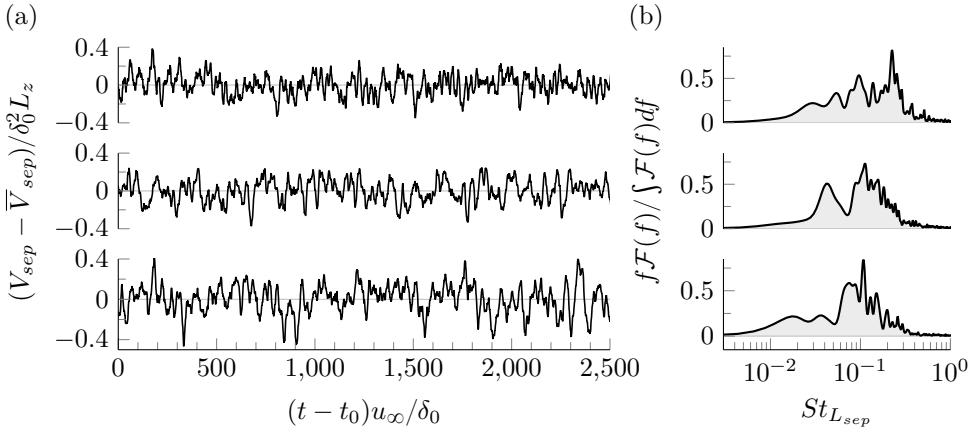

Figure 6.16: (a) Time variation of the separation-bubble volume, and (b) corresponding pre-multiplied and normalized PSD of the signal: (top) case $\mathcal{B}_1$; (middle) case $\mathcal{B}_2$; (bottom) case $\mathcal{B}_3$.

differences can be discerned when comparing this data to that of figure 6.15. All bubble-volume signals exhibit noticeable low-frequency unsteadiness at $St_{L_{sep}} < 0.1$, which can be associated with expansions and contraction of the re-circulation region from both ends. However, these low-frequency dynamics are not the dominant contributors to the signal variance; instead, all PSD peak at a distinct higher frequency oscillation centered around $St_{L_{sep}} \approx 0.1$–0.2, see figure 6.15(b).

This observation is in agreement with the numerical works of Morgan *et al.*

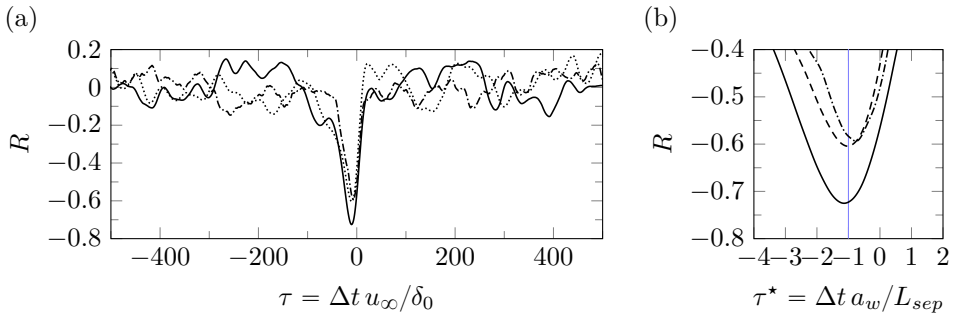

Figure 6.17: Cross-correlation between the separation-bubble volume and the spanwise-averaged separation-shock location signals, with the time lag normalized by (a) δ_0/u_∞, and (b) L_{sep} over the sound speed at the wall, a_w. Line legend: (-·-·-) case $\mathcal{B}_1$, (- - -) case $\mathcal{B}_2$, (——) case $\mathcal{B}_3$.

[36] and Adler and Gaitonde [203] on impinging STBLIs, where the most significant bubble oscillations were found around $St_{L_{sep}} \approx 0.1$. As previously pointed out, such frequency is prominent in subsonic detached shear layers [204, 205] and supersonic backward-facing step flows [193], where it is linked to the flapping motion of the shear layer. A similar phenomenon may occur in the investigated STBLIs, for which animations show visible oscillations in shear layer deflection. These oscillations have the potential to influence the entrainment process and re-injection of fluid into the bubble [41, 42], which could explain the observed spectral peak at $St_{L_{sep}} \approx 0.1$.

Furthermore, the fact that the spectra in figure 6.16(b) for the low-Reynolds case $\mathcal{B}_1$ peak at a higher frequency, around $St_{L_{sep}} \approx 0.2$, while for the high Reynolds case $\mathcal{B}_3$ the peak is found at $St_{L_{sep}} \approx 0.1$, suggests a possible correlation between these dynamics and the characteristic scales of the incoming turbulence, although this correlation is not yet clear.

A final remark concerns the relationship between the reverse-flow bubble volume and the location of the separation shock. In line with previous studies [36, 41, 203], we also find a significant correlation between both signals for a small negative lag, see figure 6.17(a), which indicates that separation-shock excursions are preceded by bubble-volume variations. In fact, we find that the time lag between both signals is approximately the acoustic propagation time from reattachment to separation; the cross-correlation peak is found at $\tau^\star = \Delta t\, a_w/L_{sep} \approx 1.0$ in all cases, as shown in figure 6.17(b), with a_w denoting the speed of sound at the wall. This remarkable consistency in the normalized time lag provides compelling evidence for a downstream mechanism being responsible for the motion of the separation shock.

We also note that the reverse-flow region and the separation-shock location are expected to exhibit correlations at various other time scales associated with multi-scale turbulent fluctuations. However, the use of the separation-shock location in spanwise-averaged form effectively removes such correlations and only preserves the observed acoustic connection.

6.3.7. Modal analysis

In this section, we aim to establish connections between the most energetic frequencies identified in the already discussed temporal spectra and global flow phenomena through SPDMD [201]. This decomposition method is a variant of the standard DMD algorithm described by Schmid [61], which seeks to decompose a data sequence into a set of modes that optimally represent its evolution. In the SPDMD framework, the standard DMD solution is additionally sparsified to produce a low-rank representation of the system dynamics. The sparsity-promoting step is controlled by a user-defined regularization parameter that determines the trades-off between accuracy and sparsity. For algorithmic details, the reader is referred to appendix D.

The database for the SPDMD analysis consists of 8192 three-dimensional snapshots per case, recorded at a sampling interval of $0.5\delta_{0,i}/u_\infty$. Each snapshot includes the instantaneous streamwise velocity, pressure and streamwise vorticity fields to establish coherent links among these variables. All fields are stored in single precision to alleviate memory requirements, and the decomposition algorithm is parallelized following the approach described by Sayadi and Schmid [206].

The regularization parameter of the SPDMD algorithm is selected to yield a sparse representation comprising 41 modes per case. Since the resulting convex optimization problem in the SPDMD method involves regularizing the least-squares deviation between the snapshot matrix and the linear combination of standard DMD modes (see equation D.9 in D), each field in the snapshot matrix (velocity, pressure, vorticity) is appropriately re-scaled to ensure that it contributes approximately a third of the ℓ_2-norm. To guarantee the statistical significance of the sparse representation, dynamic modes with oscillation periods exceeding one-third of the total simulation time are excluded from selection by the SPDMD algorithm.

Figure 6.18 shows the resulting modal amplitudes and frequencies of the standard DMD solution (gray circles) and SPDMD solution (red crosses) for each case. The SPDMD solution exhibits a consistent structure characterized by a dominant mean mode and 20 complex conjugate pairs primarily concentrated in the low-frequency range ($St_{L_{sep}} < 0.1$) and extending into the moderate-frequency range ($St_{L_{sep}} \approx 0.1$ to 0.6). Notably, as the Reynolds number increases, there is a higher concentration of the retained modes at low frequencies, where modes generally exhibit the largest amplitudes. For instance, in case $\mathcal{B}_1$, the highest frequency in the sparse representation is $St_{L_{sep}} = 0.712$, while for case $\mathcal{B}_3$, it is $St_{L_{sep}} = 0.375$.

We also note that the SPDMD algorithm has excluded dynamic modes with frequencies above $St_{L_{sep}} \approx 0.7$ from all sparse solutions, for this reason the high-frequency range $St_{L_{sep}} > 1.0$ is omitted in figure 6.18. However, the maximum modal frequency in each standard DMD solution is $St_{L_{sep}} \approx 10$.

The performance loss of the SPDMD solution, i.e., the fraction of energy that is not captured by the retained dynamic modes (see equation (D.10) in appendix D), is less than 14% in all cases. We also find that the SPDMD solution requires a factor 10 more modes to reduce the performance loss by another 1-2%, which is consistent with the broadband nature of the flow. This observation aligns with the findings of Priebe *et al.* [43], who noted the necessity of including all DMD modes within a particular frequency range to accurately reconstruct the variance of the

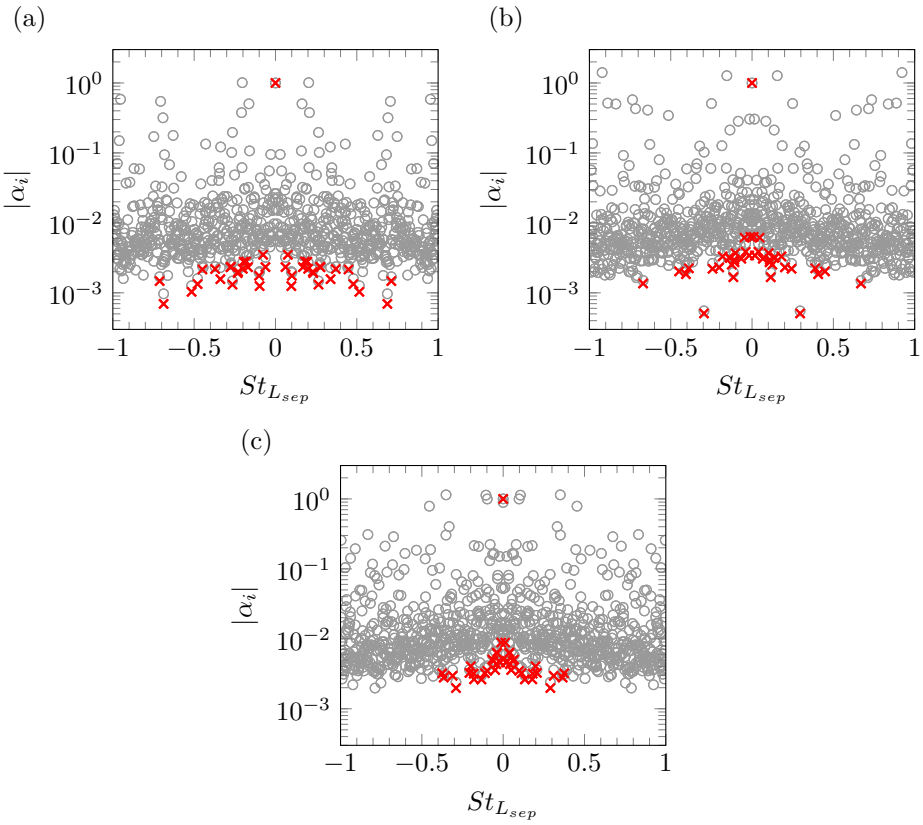

Figure 6.18: Modal amplitude $|\alpha_i|$ and frequency distribution of the standard DMD solution (○, gray) and SPDMD solution (×, red) for (a) case $\mathcal{B}_1$, (b) case $\mathcal{B}_2$, and (c) case $\mathcal{B}_3$. Modal amplitudes are normalized with respect to the amplitude of the mean mode in the corresponding SPDMD solution.

corresponding dynamics.

Despite these considerations, our focus remains on the corresponding flow structures contained in the retained modes, which can provide valuable insights into the physical mechanisms driving the energetic STBLI dynamics.

A representative low-frequency mode from the SPDMD solution of cases $\mathcal{B}_1$ and $\mathcal{B}_3$ are depicted in figures 6.19 and 6.20. The corresponding modal frequencies are $St_{L_{sep}} = 0.076$ and $St_{L_{sep}} = 0.039$, and the associated modal amplitudes represent the largest and second largest amplitudes after that of the mean mode. Isosurfaces of modal pressure (top panels), streamwise velocity (center panels) and streamwise vorticity fluctuations (bottom panels) are shown in the figures at two phases. These phases correspond to the instant when the separation shock is most upstream (left panels) and a quarter of a cycle afterwards when it moves fastest downstream (right panels). For visualization purposes, a top-hat filter with a constant filer width of

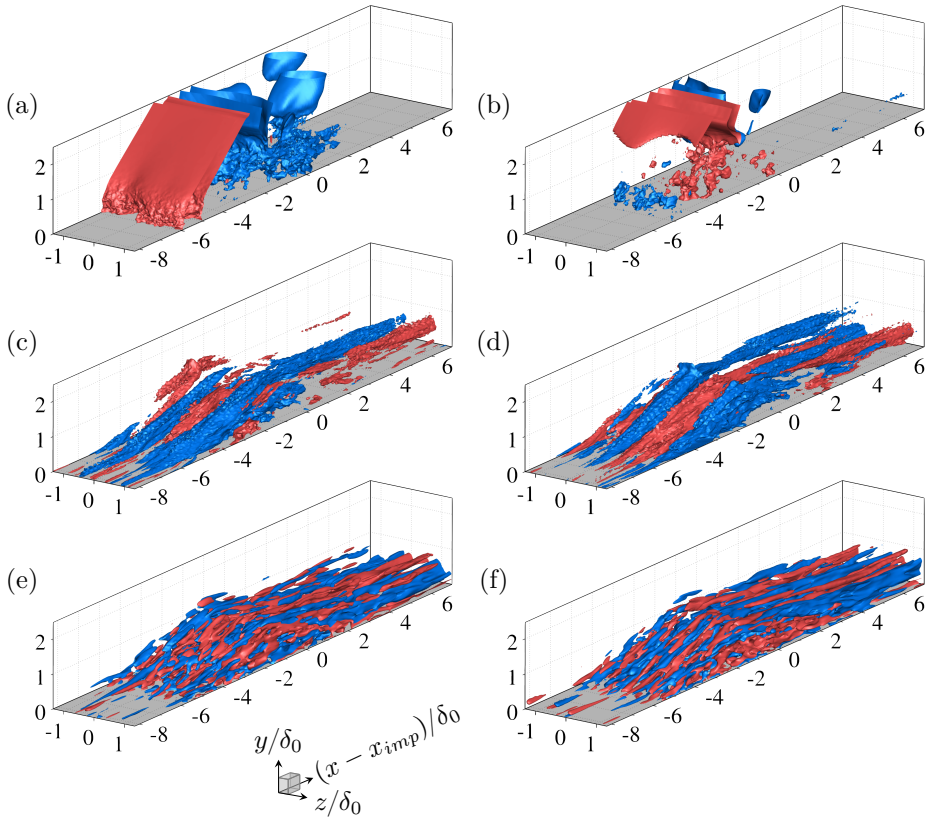

Figure 6.19: Isosurfaces of positive (red) and negative (blue) fluctuation from a representative low-frequency mode ($St_{L_{sep}} = 0.076$) in the SPDMD solution of case $\mathcal{B}_1$: (a,b) pressure, (c,d) streamwise velocity, and (e,f) streamwise vorticity. There is a phase shift of $\Delta\theta_m = \pi/4$ between left and right panels.

$\Delta = 0.1\delta_0$ in all directions has been applied to the vorticity field, since the vorticity includes more small-scale noise than the other variables. In addition, animations of the dynamic modes described are available in our data repository [207] and should be considered in conjunction with the discussion.

The low-frequency modes in figures 6.19 and 6.20 reveal that the characteristic large-amplitude excursion of the separation shock accounts for most of the energy in the pressure field, see the top panels. Its upstream motion is linked to negative pressure fluctuations of the reattachment compression, and vice-versa, which is consistent with expansions and contractions of the recirculation bubble from both ends. The incident-transmitted shock, on the other hand, exhibits considerable pitching motion that is not consistent with a pure translation of the shock-shock interaction point. This suggest a non-negligible change in separation-shock deflection at low-frequencies. An asynchronous motion between the separation shock and the incident-transmitted shock is also observed, characterized by a phase shift of

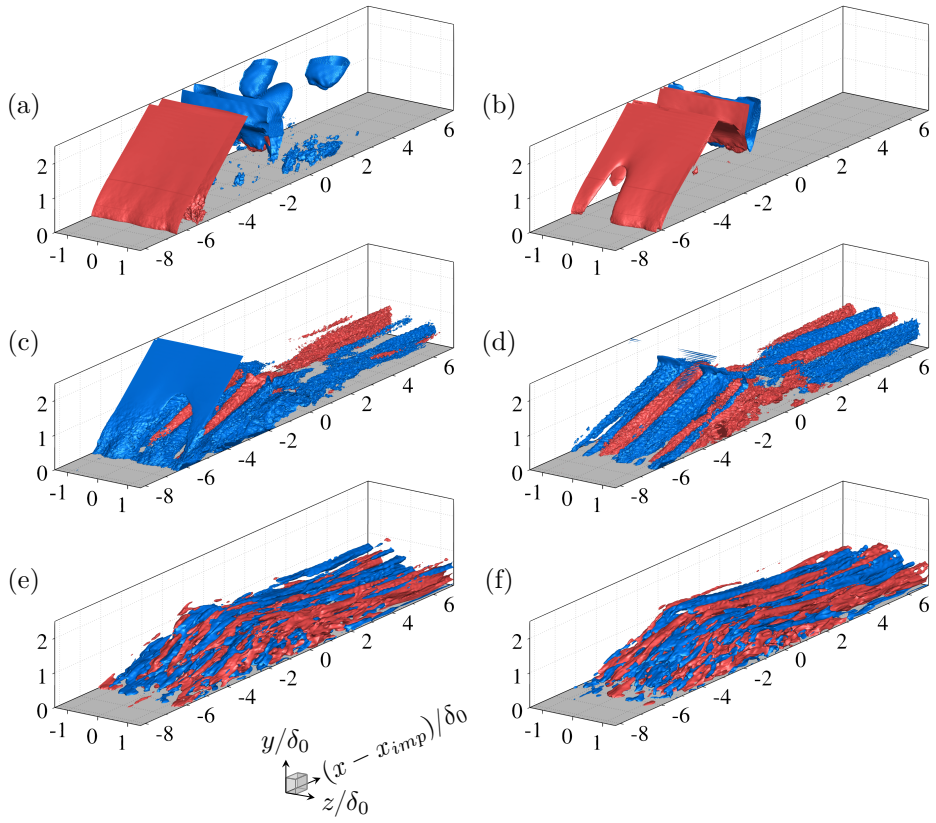

Figure 6.20: Isosurfaces of positive (red) and negative (blue) fluctuation from a representative low-frequency mode ($St_{L_{sep}} = 0.039$) in the SPDMD solution of case $\mathcal{B}_3$: (a,b) pressure, (c,d) streamwise velocity, and (e,f) streamwise vorticity. There is a phase shift of $\Delta\theta_m = \pi/4$ between left and right panels.

approximately $\Delta\theta_m = \pi/2$. Furthermore, the fluctuating streamwise velocity field in the center panels shows the presence of large-scale streaky structures statistically linked to the low-frequency dynamics of the separation shock. These streaks emerge at the separation-shock foot and convect downstream. Their strength is reduced at the bubble apex, as a result of the resulting expansion, and increases again throughout the reattachment compression.

Priebe *et al.* [43] identified very similar streaks in their DNS data of a compression ramp flow at Mach 2.9 by performing DMD of the three-dimensional streamwise mass-flux field. The authors argue that the observed elongated structures emerge as a result of Görtler-like vortices that play a key role in the low-frequency unsteadiness of the interaction, see also [23]. Inspection of streamwise vorticity fluctuations in panels (e,f) of figures 6.19 and 6.20 indeed reveals the emergence of counter-rotating, large-scale streamwise vortices near separation and, more prominently, around the reattachment location. This observation confirms, at the very least, a correlation

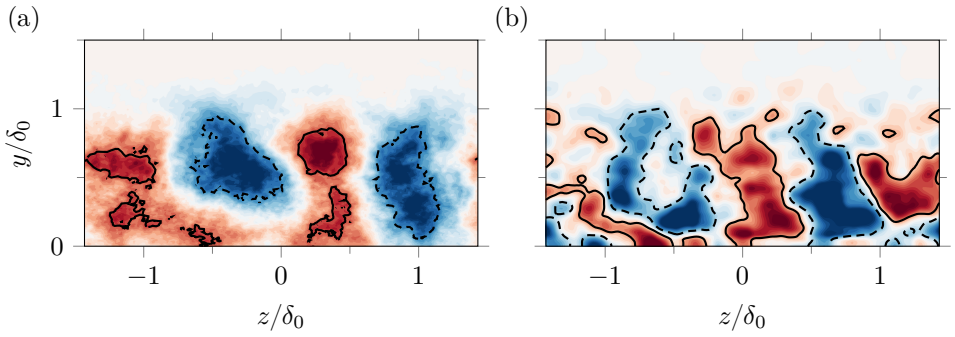

Figure 6.21: Contours of (a) modal streamwise velocity, and (b) modal streamwise vorticity from the selected low-frequency mode of case $\mathcal{B}_3$ ($St_{L_{sep}} = 0.039$) at $(x - x_{imp})/\delta_0 = 4$. Isosurfaces of positive and negative fluctuation in figure 6.20 are here indicated with solid and dashed lines, respectively.

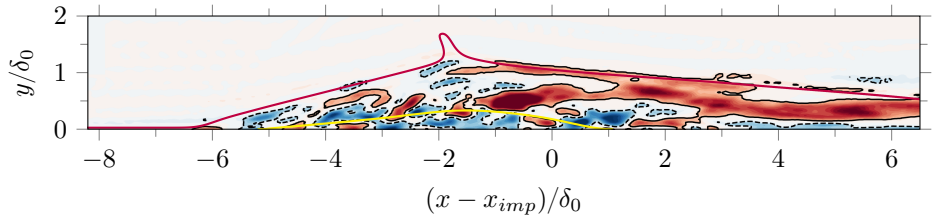

Figure 6.22: Contours of modal streamwise vorticity from the selected low-frequency mode of case $\mathcal{B}_3$ ($St_{L_{sep}} = 0.039$) at $z/\delta_0 = 1.1$. Mean zero streamwise velocity and mean sonic lines are indicated with yellow and purple lines, respectively. For additional details, see caption of figure 6.21.

between the vortical activity throughout the interaction and the characteristic longitudinal excursions of the separation shock at the front.

The observed large-scale vortices, successfully isolated from the turbulent background with the employed modal decomposition technique (unlike with traditional averaging methods), exhibit varying strength throughout an oscillation cycle. This variation is accompanied by a translation of the vortex core primarily along the spanwise direction. Moreover, the streamwise vorticity is clearly in phase with the streamwise velocity field at reattachment, where both large-scale streaks and vortices appear and disappear at the same time instants within the oscillation cycle (see also the animation available online). The separation shock is moving fastest when these structures are established, and it reaches either end of its excursion domain when both streaks and vortices weaken and recombine. This observation provides further support for a direct coupling between the separation-shock motion and the flow dynamics at reattachment.

The specific arrangement of velocity streaks and streamwise vortices for the selected low-frequency mode of case $\mathcal{B}_3$ is depicted in more detail in figure 6.21, which shows contours of streamwise velocity and streamwise vorticity fluctuations

on a streamwise-normal slice at $(x - x_{imp})/\delta_0 = 4$, downstream of the interaction. The phase depicted corresponds to that of the right panels in figure 6.20, and the isosurfaces of positive and negative fluctuation employed in the three-dimensional renderings are here indicated with solid and dashed lines, respectively.

Large-scale structures are clearly visible in both the streamwise velocity and vorticity fields in figure 6.21. Specifically, two counter-rotating vortex pairs are visible, arranged in a staggered pattern relative to the velocity streaks, which is consistent with a vortex-induced upwash or downwash. Additionally, the streak and vortex spacing is approximately $0.7\delta_0$ in span, and their corresponding cores are found at a distance 0.3–$0.5\delta_0$ from the wall.

Figure 6.22 includes a spanwise-normal slice of the modal vorticity field at $z/\delta_0 = 1.1$ that further highlights the topology of an individual large-scale, counter-clockwise rotating streamwise vortex at the trailing edge of the interaction. The figure clearly shows that the vortex does not extend to the surface but is accompanied by a region of clockwise vorticity fluctuation (opposite to that of the vortex) close to the wall, beyond $(x - x_{imp})/\delta_0 \approx 3$. These observations align with the findings of Pasquariello *et al.* [23] regarding the presence of streamwise-aligned vortices in impinging STBLI and the associated τ_{33} increase in the near-wall region beyond reattachment. However, as noted in section 6.3.5, the increased stress magnitude in this region does not lead to a global peak in the investigated interactions. This discrepancy is likely a consequence of the selected aerodynamic parameters, which result in a milder reattachment compression, thereby reducing the impact of the observed large-scale vortices on the spanwise velocity variance relative to other turbulent fluctuations.

Our data thus confirms the statistical link among velocity streaks, vortical structures and large-scale oscillations of the separation shock at low-frequencies, which was previously postulated by Priebe *et al.* [43] and Pasquariello *et al.* [23] but only supported by single-field analyses. The general characteristics of the modal shapes discussed above are consistent across the low-frequency range $St_{L_{sep}} < 0.1$ in the various sparse representations considered. The main differences in fact lie in the number of low-frequency modes selected by the SPDMD algorithm (3 for case $\mathcal{B}_1$, 5 for case $\mathcal{B}_2$ and 9 for case $\mathcal{B}_3$). Flow structures are very similar for all cases, which is why data for case $\mathcal{B}_2$ is omitted here. An animation of a representative low-frequency mode for case $\mathcal{B}_2$ is also available in our data repository (the associated $St_{L_{sep}}$ is 0.047).

A final note on the low-frequency modes pertains to the dynamics of the bubble. While the separation shock shows spanwise-coherent behavior, see figures 6.19 and 6.20, the characteristic quasi-two-dimensional breathing motion of the reverse-flow bubble becomes apparent only when the corresponding spanwise-averaged modal shape is superimposed on the mean-flow. Such animations are also available in our data repository. However, when considering three-dimensional modal shapes, the observed streaks appear to obscure the expected behavior of the bubble. This observation challenges the traditional conceptualization of the bubble motion at low frequencies and highlights the complexity of the actual dynamics involved.

Given the importance of $St_{L_{sep}} \approx 0.1$–0.2 in the spectra of the reverse-flow bub-

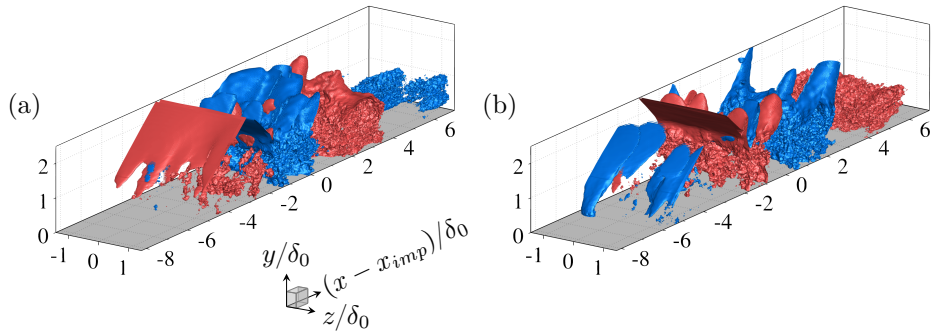

Figure 6.23: Pressure fluctuations associated with a high-frequency mode ($St_{L_{sep}} = 0.375$) in the SPDMD solution of case $\mathcal{B}_3$. There is a phase shift of $\Delta\theta_m = \pi/4$ between the left and right panel.

ble, we also examined SPDMD modes at these frequencies. These modes exhibit qualitative similarities to the low-frequency modes previously discussed. Consequently, they have been omitted from the paper for brevity (animations are still available online). Overall, a significant fraction of the modal pressure variance at this frequency is still concentrated around the separation shock, which exhibits a shorter excursion domain and slightly more pronounced spanwise variations. Streaky structures are also observed in the corresponding modal streamwise velocity fields, correlated with the separation-shock motion in a similar fashion as in the low-frequency modes. The same remark applies to the modal streamwise vorticity, where large-scale structures persist throughout and beyond the interaction region. These findings, along with further analysis of these modal shapes, suggest that the potential flapping motion of the shear layer at $St_{L_{sep}} \approx 0.1$, manifests as a highly three-dimensional phenomenon. Furthermore, the presence of large-scale streaks and vortical structures is not limited to low-frequency modes; instead, they appear over a broad frequency range, which raises questions about their role in the low-frequency dynamics of STBLIs.

For completeness, contours of modal pressure for a high-frequency SPDMD mode of case $\mathcal{B}_3$ ($St_{L_{sep}} = 0.375$) are shown in figure 6.23 to illustrate the complete SPDMD reduced-order representation (an animation is also available in our data repository). At this frequency, shock oscillations are clearly associated with shear layer vortices that convect downstream, potentially inducing eddy Mach waves in the supersonic region of the flow [62]. This particular modal shape is consistent across all high-frequency modes of the SPDMD representations and is correlated with small-scale velocity and vorticity fluctuations (not shown here).

6.4. Summary

In this chapter, we have discussed the effect of Reynolds number on a Mach 2.0 impinging STBLI flow with strong mean flow separation. Reynolds number effects have been analyzed based on a new wall-resolved and long-integrated LES database

that involves three different simulations at friction Reynolds number $Re_\tau = 355$, 1226 and 5118, and otherwise equal flow parameters. The high-Reynolds case, at $Re_\tau = 5118$, significantly extends the available parameter range of strong STBLI covered with high-fidelity simulations.

A detailed characterization of the instantaneous and mean STBLI organization has been presented, focusing on differences in interaction scales, bubble topology and turbulent structures. For the high-Reynolds interaction, it is found that the maximum amplification of the streamwise stress is no longer correlated with the production peak at the separation-shock foot, but rather, with increased pressure transport in the separation-shock excursion domain. The wall-pressure underneath the separation shock also becomes progressively intermittent as Re_τ increases, exhibiting broadband and energetic low-frequency content. When tracked above the shear layer, however, the separation-shock motion shows broadband energetic low-frequency content in all cases, at a separation-length-based Strouhal number $St_{L_{sep}} < 0.1$. This observation confirms that the mechanisms driving the low-frequency dynamics of STBLIs are fundamentally independent of Reynolds number.

Spectra of the separation-bubble volume additionally exhibit a peak at $St_{L_{sep}} \approx$ 0.1–0.2. This particular frequency is similarly found energetic in subsonic detached shear layers as well as supersonic backward-facing steps, where it is linked to the flapping motion of the shear layer. Furthermore, variations in bubble size are found to precede the separation shock motion in all the investigated cases, with a time lag corresponding to the acoustic propagation time from reattachment to separation. This finding is consistent with a downstream mechanism being responsible for the separation-shock motion.

Lastly, we have performed sparsity-promoting dynamic mode decomposition of the three-dimensional pressure, streamwise velocity and streamwise vorticity fields to relate energetic frequencies in the temporal spectra with global flow phenomena. We found that the subset of dynamically relevant modes exhibits an increased concentration at low-frequencies with increasing Reynolds number. Inspection of the corresponding low-frequency modes confirms a consistent statistical link among large-amplitude excursions of the separation shock, large-scale velocity streaks and streamwise-aligned vortices across all cases.

7

Fluid-structure coupling with a compliant thin-panel

In preceding chapters, we discussed the fundamental characteristics of strong STBLIs and investigated the effect of Reynolds number on both the interaction as well as the upstream TBL. In this chapter, which corresponds to the final chapter of PART TWO of this thesis, we take the analysis one step further and explore the dynamic coupling between STBLI and a compliant thin-panel. Coupled FSI simulations involving wall-resolved LES are conducted for this purpose, at the same flow conditions as the moderate-Reynolds interaction discussed in the previous chapter ($Re_\tau = 1226$). We show that the flexible panel exhibits self-sustained oscillatory behavior under these conditions, confirming the strong and complex dynamic coupling with the flow. The resulting mean panel deflection is also employed as a rigid-wall geometry in a separate simulation to discern between effects caused by the mean panel deformation and those caused by the panel motion.

7.1. Introduction

A central aspect in the structural design of high-speed systems is long-duration exposure to STBLI. As we have already discussed multiple times throughout this thesis, such complex multi-scale flow phenomena exhibit energetic low-frequency motions that impose intermittent and high-amplitude loads on nearby components [4, 30, 181]. Lightweight skin panels may resonate under these conditions and potentially collapse due to vibrational fatigue [33, 208]. At hypersonic speeds, STBLI additionally lead to severe localized heating since local heat transfer rates greatly exceed those associated with attached TBLs [45]. These thermal effects may further degrade the mechanical properties of aircraft components, thereby becoming more prone to failure. The accurate characterization of dynamic FSI is therefore paramount for the design of next-generation high-speed flight vehicles with expanded operational

The content of this chapter has been published as: L. Laguarda, S. Hickel, F. F. J. Schrijer and B. W. van Oudheusden. Shock-wave/turbulent boundary-layer interaction with a flexible panel, *Phys. Fluids* **36** (1), 2024.

envelopes [63, 156].

Due to their practical relevance, STBLI have been extensively investigated since the late 1940s [56]. The wide range of Mach number, Reynolds number and shock strength covered through experimentation, and more recently, with high-fidelity numerical simulations, has helped shape our fundamental understanding of the relevant flow physics [44]. In the presence of substantial flow separation, the interaction is known to exhibit a very broad range of energetic frequencies as we have seen in chapter 6. The high-frequency content is associated with small-scale turbulence, while shear layer dynamics are a major source of unsteadiness at moderate frequencies that promote the mass exchange with the reverse-flow region [42, 190]. The lower end of the energetic spectrum, in turn, is related to pulsating motions of the separation bubble and the associated longitudinal excursions of the separation shock [23]. The fact that the corresponding mechanisms driving these low-frequency motions remain still unclear, despite the large volume of work, highlights the complexity of the phenomenon and the need for further fundamental research.

In addition, the extensive literature on STBLI mostly considers rigid geometries, which are often canonical like flat plates, compression ramps and steps [56]. Studies involving elastic components, on the other hand, are far more scarce due to the additional complexities in reproducing and characterizing the resulting FSI system with experiments or numerical simulations [32, 63]. From the experimental side, recording simultaneous field measurements of the flow and structural displacements is a challenging task [208]. Spottswood *et al.* [64] were among the first to concurrently employ surface pressure measurements and digital image correlation (DIC) to characterize the response of a clamped elastic panel subject to STBLI at Mach 2.0. They observed a strong dynamic coupling between the flow and the panel, with the panel response exhibiting low-frequency content and being highly sensitive to small changes in shock impingement location. A strong dynamic coupling was also observed by Ahn *et al.* [209] and Musta *et al.* [210] in a Mach 2.0 compression-ramp STBLI over a fully clamped elastic panel. Proper-orthogonal decomposition (POD) of DIC and surface pressure measurements revealed a dominant low-frequency coupling associated with the first bending mode of panel oscillation [210]. More recently, D'Aguanno *et al.* [66] performed simultaneous DIC and particle-image velocimetry (PIV) measurements to investigate the response of a compliant panel subject to impinging STBLI at Mach 2.0, with the panel clamped on the front and rear edges and free on the sides. Their time-record extends for over 400 cycles of the first bending mode, which together with the third bending mode account for over 90% of the variance of the structural displacement field. These two discrete frequencies appear also energetic in the spectra of the separation shock location, which the authors extracted from the PIV data. Other experimental works on STBLI over flexible panels include Spottswood *et al.* [33], Brouwer *et al.* [211], Tripathi *et al.* [212, 213], and Eitner *et al.* [214] and they further confirm the aforementioned observations.

The numerical simulation of aeroelastic problems involving STBLI has also its challenges [32]. Turbulence-resolving strategies are required to properly capture the STBLI dynamics, which determine the unsteady loads on the compliant structure [36], and fluid and solid domains need to be coupled within a monolithic or

partitioned FSI framework [215]. The time-varying solid geometry requires explicit representation within the fluid domain, either with dynamic mesh deformation or via IBMs, and motion and load transfer at the interface is non-trivial when fluid and solid discretizations do not match [216]. As a result, numerical simulations of complex FSI systems are computationally very expensive, which contributes to the limited range of flow conditions and panel response time-records available in literature.

The first high-fidelity simulation of a TBL over an elastic panel subject to fast-moving shock impingement was performed by Pasquariello *et al.* [217] with a partitioned FSI solver combining wall-resolved LES of the flow with a FE solver for the structure. The work aimed to replicate the experimental results of Daub *et al.* [218] at Mach 3.0. An overall good agreement between numerical and experimental data was found in terms of flow configuration and static panel deflection, but not in terms of dynamic behavior. While self-sustained panel motion was obtained in the numerical investigation, experimental results showed a different oscillatory frequency and a clear damping. This highlights how challenging it can be to properly model and resolve these complex FSI systems. Hoy and Bermejo-Moreno [219] further attempted to replicate the experimental results of Daub *et al.* [218] at Mach 3.0 combining wall-modeled LES and a FE solver with structural damping. The computational savings attained with the wall-model enabled longer integration times and the resulting dynamic deflection of the panel was in better agreement with the experimental signal than the results of Pasquariello *et al.* [217]. The volume of the reverse-flow region was found to increase considerably in the presence of the flexible panel, and the spectral analysis of wall-pressure additionally revealed enlarged excursions of the separation shock. Very recently, Shinde *et al.* [65] explored the effect of one-way versus two-way coupling between impinging STBLI and a fully clamped flexible panel at Mach 4.0. One-way coupling results were obtained by transferring wall-pressure fields from a rigid-wall STBLI simulation to the structural solver to compute the instantaneous panel response. Despite the quantitative discrepancies, an overall qualitative agreement was observed in the panel response for both approaches. Namely, a dominant first bending mode of panel oscillation.

The few available studies thus confirm that STBLI efficiently triggers low-order modes of panel vibration; however, questions related to the coupling mechanism, the corresponding modulation of the STBLI dynamics as a result of surface displacements and the particular role of static and dynamic panel deformation remain still open. The interplay between static surface deformation and STBLI has been studied experimentally [67, 68] and with low-fidelity models [69] but not with high-fidelity simulations to the authors' knowledge.

In the present study, we perform wall-resolved LES of a Mach 2.0 impinging STBLI over a flexible thin-panel. As discussed in chapter 2, a partitioned FSI approach comprising our in-house fluid solver and a FE structural solver is employed for the calculations together with the AROM of Thari *et al.* [70] to achieve long integration times, that is, more than 90 FFTs of the full domain length after the initial transient response of the panel. In order to distinguish effects that are caused by the mean panel deformation from those that are caused by dynamic panel motion, we employ

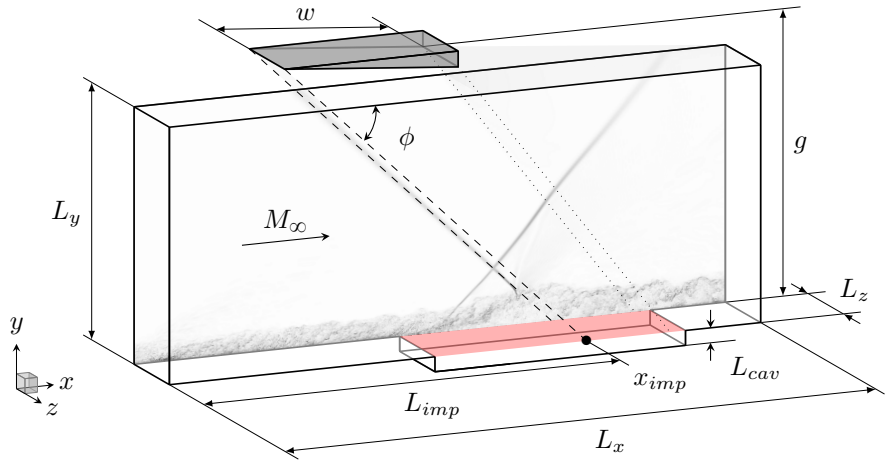

Figure 7.1: Schematics of the computational domain.

the mean panel deflection as a rigid-wall geometry in a second simulation, which is integrated over the same time interval as the coupled case. Results are compared against the baseline configuration, a flat and rigid-wall STBLI at the same flow conditions.

7.2. Computational setup

The investigated flow geometry is outlined in figure 7.1. It involves an oblique shock wave impinging on a TBL over a compliant panel (the latter shown in red). The selected flow conditions correspond to those of the moderate-Reynolds case $\mathcal{B}_2$ discussed in the previous chapter, which are repeated here for clarity. The incoming flow of air is at Mach number $M_\infty = 2.0$ and has a stagnation temperature and pressure of $T_0 = 288$ K and $p_0 = 356$ kPa respectively. The 99% velocity-based boundary layer thickness at the inflow plane $\delta_{0,in}$ is 5.2 mm, and the corresponding Reynolds number based on free-stream quantities, $Re_\infty = \rho_\infty u_\infty \delta_{0,in}/\mu_\infty$, is 50.1×10^3. The flow deflection induced by the virtual shock generator is $\vartheta = 10.66°$ which results in an oblique shock wave with wave angle $\phi = 40.04°$ and pressure ratio $p_2/p_\infty = 1.76$. The shock generator is placed at a height $g = 96$ mm above the surface, while its streamwise position is set such that the theoretical inviscid shock impingement point x_{imp} occurs at 60% of the panel length and is located $L_{imp} = 32\delta_{0,in}$ downstream of the inflow plane. The considered channel height to wedge hypotenuse ratio is $g/w = 1.16$.

The elastic panel has a thickness $h = 0.25$ mm and consists of Aluminum 7075-T6 with a Young's modulus of $E = 71.1$ GPa, a Poisson ratio of $\nu = 0.33$ and a density of 2800 kg m^{-3}. The length of the panel is $a = 100$ mm and the panel is clamped at the front and the rear with free side edges. The corresponding non-dimensional dynamic pressure parameter, commonly used in panel flutter studies,

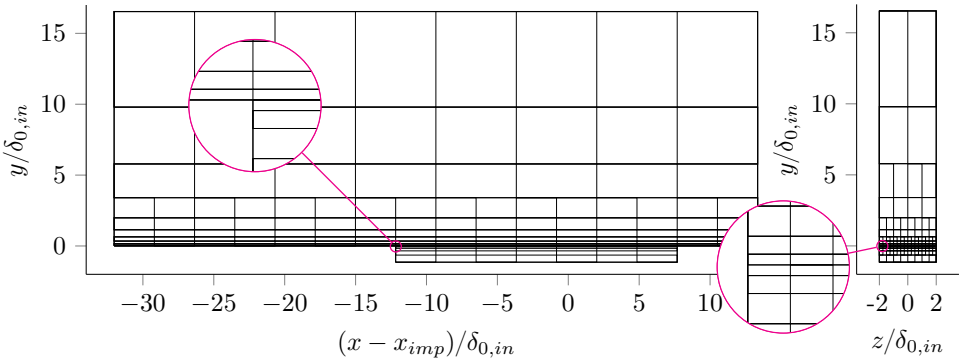

Figure 7.2: Block distribution of the employed computational grid.

is $\lambda_{dp} = \rho_\infty u_\infty^2 a^3 D^{-1} = 2440$, where $D = Eh^3/(12(1-\nu^2))$ is the flexural rigidity of the panel. Moreover, a constant pressure of $1.87p_\infty$ is prescribed in the cavity, where p_∞ is the free-stream static pressure of the flow. This value corresponds to the mean wall-pressure of the flat rigid-wall STBLI over the panel.

Chapter 2 of this thesis provides the necessary details concerning the numerical strategy employed for the coupled simulations, which are performed using a partitioned FSI that combines wall-resolved LES for the fluid with a FE structural solver combined with the AROM of Thari *et al.* [70]. The employed block distribution for the present simulations is shown in figure 7.2 and corresponds to that of case $\mathcal{B}_2$ discussed in the previous chapter. The only difference is that here we add a small cavity underneath the panel ($L_{cav} = \delta_{0,in}$, see figure 7.1) to allow for negative displacements of the moving boundary. The grid distribution within the cavity has been generated by mirroring the grid distribution above the cavity around $y = 0$, see figure 7.2. In terms of the solid mesh employed for the panel, it consists of 196 elements in streamwise direction and two elements along its thickness; the panel is restricted to purely two-dimensional motion (no torsion) so only one element is used across the span.

7.3. Results and discussion

Selected results for the baseline STBLI, the coupled STBLI with the flexible panel and the STBLI over a rigid panel with the mean deformation of the coupled case are presented and discussed. When necessary, the different configurations will be referred with acronyms that follow from the corresponding panel characteristics. That is, the baseline flat wall, which is equivalent to an undeformed and rigid panel, is referred to as UR, the deformed and rigid wall shaped with the mean panel displacements is DR, and the flexible panel dynamically coupled with the flow is denoted as FC.

All simulations have been integrated for over 90 FFTs of the full domain length after the corresponding initial transients. The last instantaneous solution of the

baseline case served as initial condition for the coupled simulation, in which the flat panel was allowed to deform. Quantities of interest have been extracted from three-dimensional snapshots, that were recorded at a sampling interval of $0.5\delta_{0,in}/u_\infty$ leading to an ensemble of 8200 snapshots per case.

7.3.1. Undisturbed turbulent boundary layer

Details concerning the undisturbed TBL over a flat-rigid wall are provided in chapter 5 of this thesis (case $\mathcal{T}_2$). The boundary layer thickness at the inviscid impingement point without the shock is $\delta_0 = 7.15$ mm (see table 6.4), and this parameter will be used for scaling purposes unless otherwise stated.

7.3.2. Panel response

The time evolution of vertical panel displacements is shown in figure 7.3 for the quarter point, mid point and three-quarter point locations along the panel length. The largest displacements are found within the first $\sim$15 FFTs after the flexible panel is released, which corresponds to the initial transient period required to reach the mean deformation state. This initial transient (indicated in red in figure 7.3) is excluded from the statistical analysis. For the remaining simulation time, a self-sustained oscillatory behavior with varying oscillation amplitude is observed, which confirms the strong and complex dynamic coupling between the panel and the flow.

Figure 7.4(a) shows the mean panel deformation along with the envelope of all instantaneous deflection states after the initial transient. The observed mean shape is consistent with the pressure difference, resulting from the pressure distribution caused by the STBLI on top and the constant imposed cavity pressure at the bottom, and has a maximum downward deflection that exceeds $3h$ around 70% of the panel length. The corresponding PSD map of panel displacements is included in figure 7.4(b) and provides an indication of the dominant vibration modes and their respective frequencies. In this work, all PSDs have been estimated using Welch's algorithm, with Hamming windows and 10 segments with 65% overlap (segment length of approximately $650\delta_0/u_\infty$).

As shown in figure 7.4(b), the first three bending modes account for most of the variance of the displacement signals while higher-order modes contribute only marginally. This is in good agreement with previous works [64–66, 210]. Interestingly, the first bending mode is not symmetric; rather, its largest contribution is found in the second quarter of the panel, see figure 7.4(b). The second bending mode is also highly asymmetric and has energetic contributions predominantly in the second half of the panel. Its frequency is very close to that of the third bending mode, which as opposed to the previous two has a symmetric effect with respect to the panel half-length.

Note that large static displacements increase the effective stiffness of the panel, thereby requiring higher driving frequencies to resonate. Table 7.1 reports the first three natural oscillation frequencies for the unloaded flat panel and the pre-stressed deformed panel, which confirm the effective stiffening. These values were obtained with a free-vibration analysis performed with the structural solver, which in the

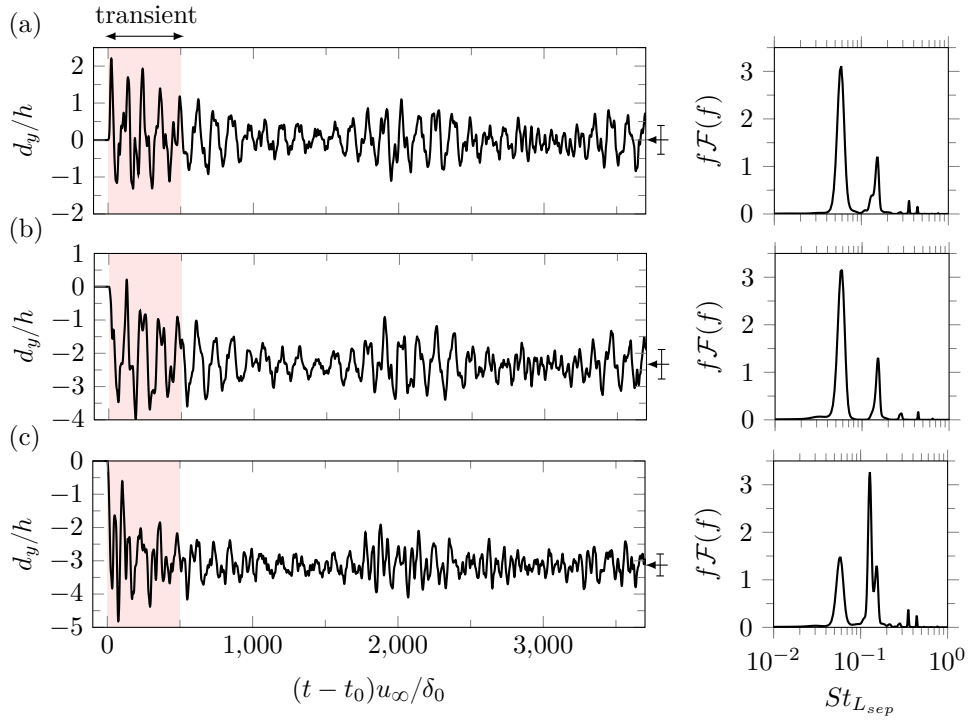

Figure 7.3: Instantaneous vertical panel displacements for the (a) quarter point, (b) mid point, and (c) three-quarter point locations along the panel length. Arrows and vertical bars (at the right hand scale) indicate the corresponding mean displacement and its standard deviation. The panels to the right include the pre-multiplied and normalized PSD of the signals.

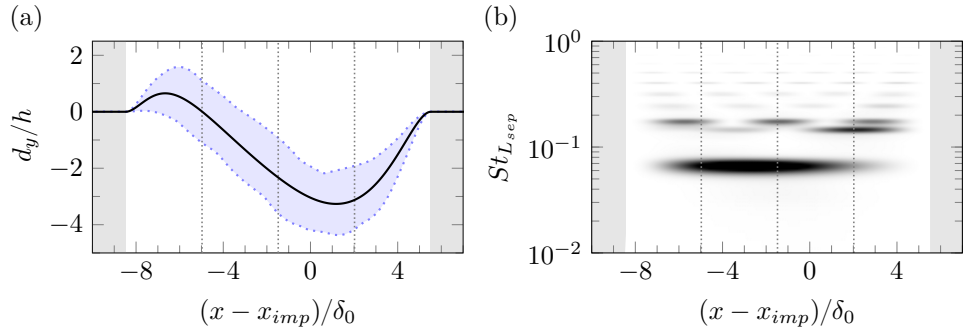

Figure 7.4: (a) Mean panel deflection (black) together with the envelope of all instantaneous deflection shapes (blue shade), and (b) pre-multiplied PSD map of displacement signals (increasing linearly from white to black). Vertical dotted lines indicate the quarter point, mid point, and three-quarter point locations along the panel length, and the rigid portion of the wall is shaded in gray

Table 7.1: Panel oscillation frequencies.

Natural				Measured	
Flat		Pre-stressed			
Hz	$St_{L_{sep}}$	Hz	$St_{L_{sep}}$	Hz	$St_{L_{sep}}$
134	0.013	538	0.051	593	0.056
375	0.036	1351	0.128	1338	0.127
739	0.070	1554	0.148	1625	0.154

pre-stressed case involved pre-loading the panel with the mean wall-pressure of the coupled simulation. For comparison, table 7.1 also includes the energetic frequencies identified in the displacement signal of the three-quarter point along the panel length (shown in figure 7.3(c) with its corresponding PSD). These frequencies are in close agreement with natural frequencies of the pre-stressed panel, rather than those for the flat panel, which highlights the importance of mean displacements in the dynamic response of the panel when exposed to STBLI. We also note that the frequency of the first bending mode of the pre-stressed panel lays within the characteristic low-frequency range of STBLI, i.e., a separation-length-based Strouhal number $St_{L_{sep}}$ below 0.1.

7.3.3. Instantaneous and mean-flow organization

An instantaneous impression of the temperature field is provided in figure 7.5 for the coupled interaction to illustrate the investigated STBLI topology. Contours of instantaneous (black) and mean (yellow) zero streamwise velocity show the massive flow separation, which is characteristic of strong interactions. Beyond the separation point, upstream TBL disturbances grow into larger vortical structures as the shear layer moves away from the wall, and they eventually interact with the incident-transmitted shock tip at the bubble apex. Such shock-vortex interaction and the strong flow deceleration near separation correspond to visible peaks in the TKE production [172]. Immediately after the bubble apex, the flow is turned towards the wall and the reattachment process is initiated. All simulations exhibit a very mild concave streamline curvature at reattachment, which results in a weak compression fan instead of a coalesced reattachment shock.

Relevant wall-properties are shown in figure 7.6 to highlight the impact of static and dynamic surface displacements on the flow. Skin-friction distributions in figure 7.6(a) show an increase of 15.6% in the streamwise extent of the reverse-flow bubble for the coupled interaction, shown in blue, with respect to the baseline case, which is indicated in gray. The corresponding separation length L_{sep}, defined as the streamwise distance between mean separation and reattachment points, increases from $6.62\delta_0$ to $7.64\delta_0$ (the separation point moves $0.42\delta_0$ upstream and the reattachment point moves $0.61\delta_0$ downstream). The initial skin-friction drop and partial recovery at the leading edge of the panel are consistent with the upward mean panel deflection at this location, see figure 7.4(a). The following decrease in $\langle C_f \rangle$, on the other hand,

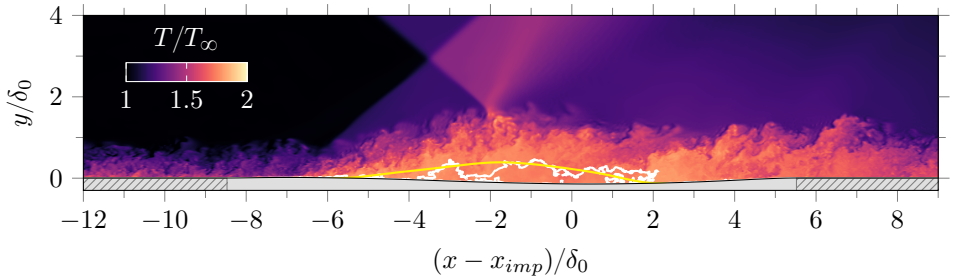

Figure 7.5: Instantaneous flow organization of STBLI over the flexible panel. Solid lines indicate instantaneous (white) and mean (yellow) iso-contours of zero streamwise velocity. The wall region is colored in gray with stripe patterns highlighting the rigid segments.

is attributed to the STBLI and reveals the upstream shift of the separation shock in the presence of the moving panel, see figure 7.6(a). Interestingly, the skin-friction profile for the STBLI over the rigid mean deformed panel geometry, that is, the DR configuration, is almost identical to that of the coupled interaction, including the magnitude of L_{sep}, which is $7.49\delta_0$. This case is indicated in figure 7.6(a) with a red line. The strong skin-friction similarity between the DR and FC configurations suggests a dominant role of mean surface deformation on the resulting STBLI organization over a moving panel. This is also confirmed by the probability of reverse-flow in figure 7.6(b), where these two configurations exhibit a very similar increase in reverse-flow probability compared to the baseline.

The corresponding mean and RMS wall-pressure evolution for each configuration are shown in figures 7.6(c) and 7.6(d). Interestingly, the incipient pressure plateau in the separated region appears more established for the DR and FC configurations in figure 7.6(c), without noticeable differences between the two. A more distinct pressure plateau is generally associated with a stronger interaction [197], which highlights the impact of the mean surface deformation on STBLI. The dynamic component of panel displacements, in turn, plays an important role in the corresponding wall-pressure fluctuation intensities, which are shown in figure 7.6(d) for all cases. It can be clearly observed that only the FC configuration exhibits a higher peak at the separation-shock foot than the baseline, being approximately 30% larger. This shows the non-negligible modulation of the separation-shock dynamics due to the moving panel, which leads to a stronger separation-shock footprint on the surface. We will further elaborate on the separation-shock dynamics in the next section. The mean separation-shock location, on the other hand, is still mostly determined by the mean deformation of the panel, since wall-pressure fluctuation peaks for the DR and FC configurations are aligned. These configurations also exhibit very similar fluctuation intensities beyond the reattachment location in figure 7.6(d), which are noticeably larger than those for the baseline (UR) interaction.

To better characterize the size of the mean recirculation bubble, different quantities such as its length, height and volume are reported in table 7.2 for the investigated configurations. In agreement with the above-discussed results, the presented bubble metrics are very similar for the DR and FC configurations, which confirms the strong

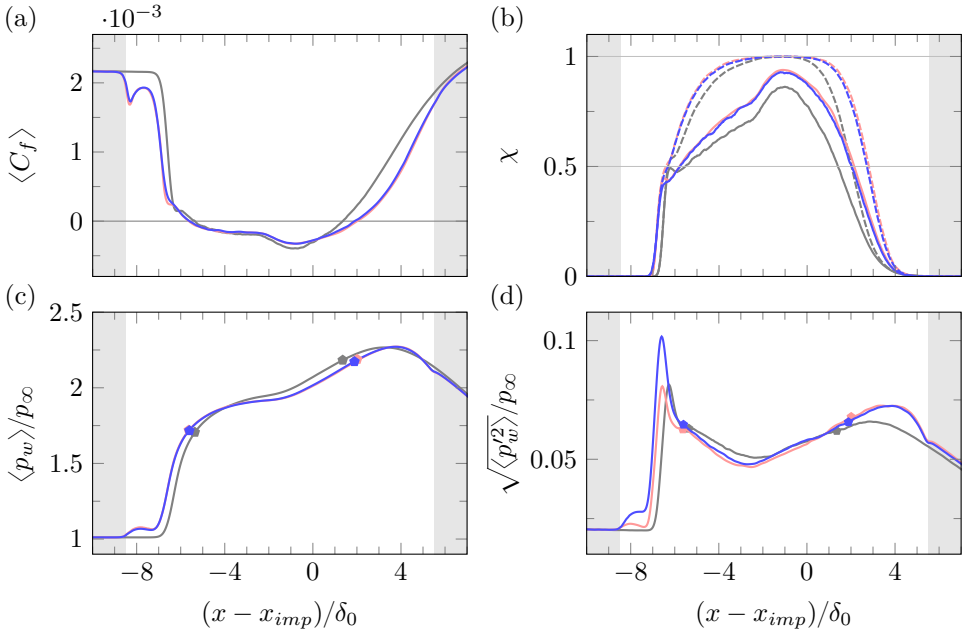

Figure 7.6: Time- and spanwise-averaged (a) skin-friction, (b) probability of reverse-flow, (c) wall-pressure and (d) wall-pressure RMS. Line legend: STBLI over a (gray) flat-rigid panel - UR configuration, (red) deformed-rigid panel - DR configuration, and (blue) flexible panel - FC configuration. Pentagon markers denote the corresponding mean separation and reattachment points, while solid and dashed lines in (b) indicate the reverse-flow probability at the wall and the maximum wall-normal value, respectively. In addition, the rigid-wall segment for the FC configuration is shaded in gray in all panels.

sensitivity of the separated flow to mean surface deformations. Furthermore, the resulting height and reverse-flow bubble volume for these cases are much closer to the baseline values when considering only $y \geqslant 0$. This suggests that the expansion of the reverse-flow region is primarily a consequence of the mean panel deflection being predominantly downward, see figure 7.4(a). The two-dimensional probability of reverse-flow is presented in figure 7.7 and shows that the recirculation region is mostly located above a segment of the panel with negative deflection and where the surface curvature is concave. This condition further compresses the flow and contributes to the observed longitudinal expansion of the bubble from both ends.

The influence of static and dynamic panel displacements on the turbulence intensity is analyzed next. Figure 7.8 shows contours of TKE for the investigated configurations, and all cases exhibit the typical distribution associated with impinging STBLIs [40]. That is, turbulence is first amplified in the detached shear layer, then undergoes a noticeable damping at the bubble apex and finally re-amplifies again at reattachment. The most noticeable differences are found near and past the reattachment location, where the DR and FC configurations exhibit higher levels of TKE compared to the baseline. This stems from the effective increase in streamline curvature as a result of the mean downward deflection of the panel, and does not

Table 7.2: Mean-flow quantities of the recirculation region for the investigated cases.

Flow parameters		UR	DR	FC
Separation length	L_{sep}/δ_0	6.72	7.49	7.64
Bubble height	H_{sep}/δ_0			
• from wall		0.37	0.47	0.47
• from $y = 0$		0.37	0.39	0.39
Bubble volume	$V_{sep}/\delta_0^2 L_z$			
• integral		1.63	2.43	2.35
• above $y = 0$		1.63	1.81	1.75

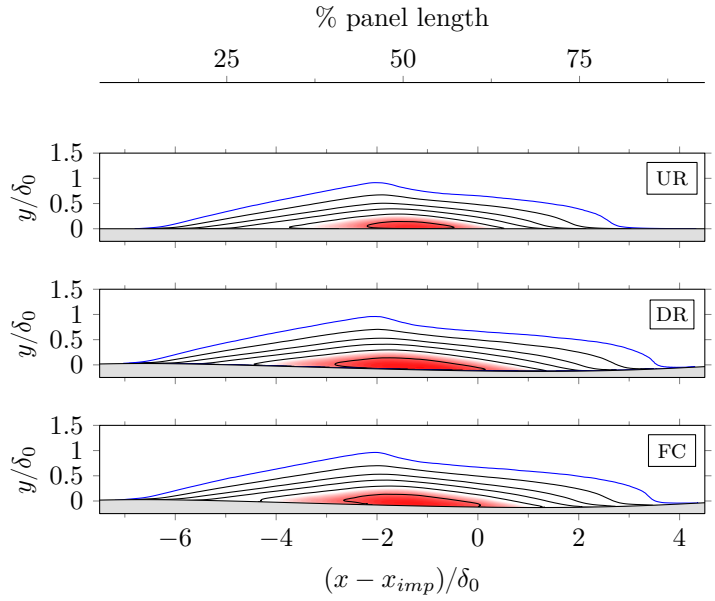

Figure 7.7: Two-dimensional probability of reverse-flow for the investigated configurations. Black lines indicate contour levels from 10% to 90% reverse-flow probability in steps of 20%, while the blue line indicates the 1% contour. For the selected colormap, transition from white to red starts at 75%.

appear to be meaningfully altered by the unsteady panel motion.

Table 7.3 reports amplification factors for the TKE and the individual Reynolds stresses. Amplification factors are here defined as the ratio between the maximum value within the interaction region and the maximum value in the undisturbed TBL measured at the inviscid impingement point. For the baseline interaction, that is, the UR configuration, the corresponding factors are in good agreement with previous high-fidelity numerical simulations [172, 176]. A comparison of these factors with those associated with the DR and FC configurations then prompts the following observations. First, the maximum TKE amplification does not appear to be

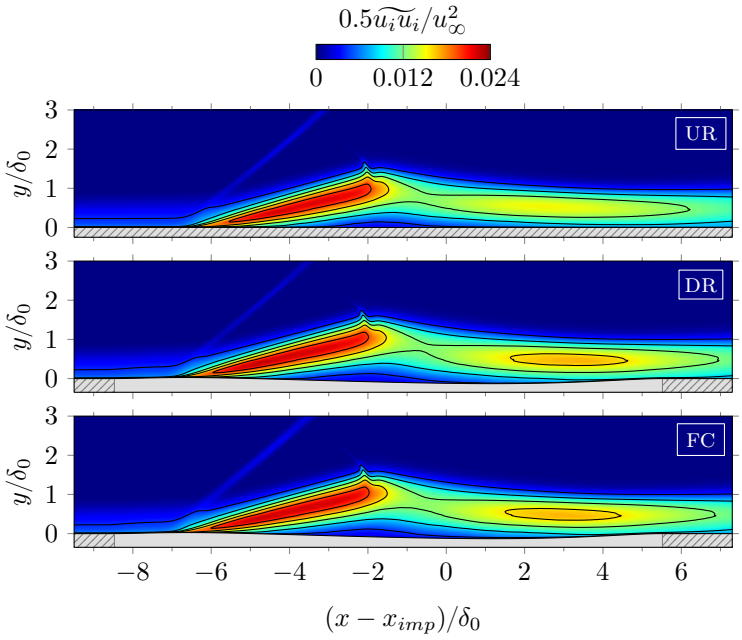

Figure 7.8: Turbulence kinetic energy (TKE) for the investigated configurations. Black lines correspond to seven equispaced contours, and the wall region is colored in gray with stripe patterns highlighting the rigid segments for each case.

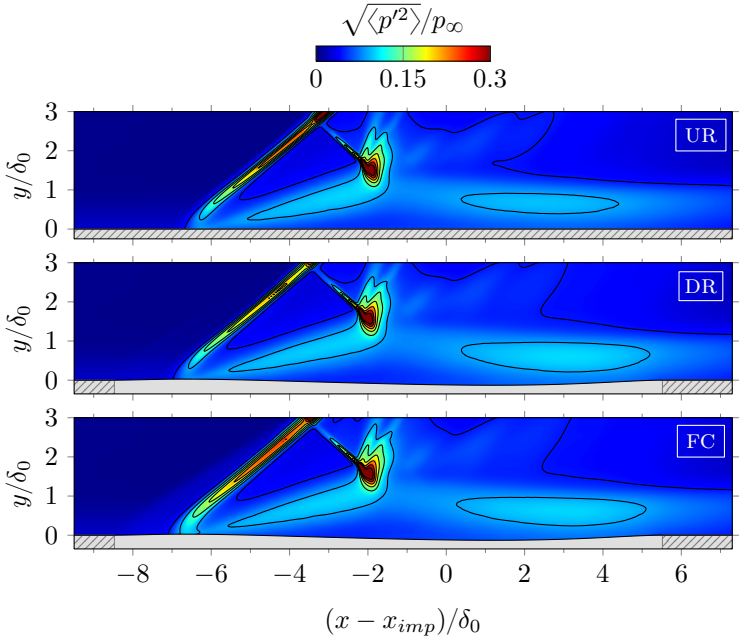

Figure 7.9: Pressure fluctuation intensity for the investigated configurations. For additional details, see figure 7.8.

Table 7.3: Turbulence amplification factors.

Case	Stress amplification factor				
	$0.5\widetilde{u_i''u_i''}$	$\widetilde{u''u''}$	$\widetilde{v''v''}$	$\widetilde{w''w''}$	$\widetilde{u''v''}$
UR	2.60	1.97	4.35	3.57	3.97
DR	2.65	2.05	4.75	3.59	4.39
FC	2.63	2.39	4.72	3.62	4.37

meaningfully altered by the resulting mean or dynamic panel displacements. As observed in figure 7.8, this amplification occurs in the detaching shear layer where all cases exhibit a very similar behavior. The same can be said for the amplification of the spanwise Reynolds stress, which also remains effectively unaltered. The wall-normal and shear stress components, on the other hand, undergo approximately 10% higher amplification in the DR and FC configurations. This amplification is related to the shear layer dynamics close to the reattachment point, which are more intense for these cases. The maximum amplification of the streamwise Reynolds stress is substantially higher in the presence of the moving panel, about 20% larger than in the UR or DR configurations. Inspection of the corresponding transport budgets for this stress reveals enhanced pressure transport at the separation shock foot (not shown here) which contributes to the additional amplification. As already highlighted in the wall-pressure RMS of figure 7.6(d), the dynamic coupling between the flow and the panel accentuates the separation-shock unsteadiness, which yields a stronger footprint in the pressure fluctuation intensity map of figure 7.9, where the separation shock exhibits increased fluctuation levels as well as a slightly larger longitudinal excursion range in the FC configuration. Figure 7.9 also highlights the increased shear layer activity near reattachment in the presence of mean surface displacements, with the panel motion having a marginal influence as already discussed.

7.3.4. Flow dynamics

In order to identify dominant frequencies contributing to the modulation of the STBLI dynamics as a result of mean and dynamic panel displacements, temporal spectra of wall-pressure, separation-shock location and bubble-volume variations have been analyzed for the different configurations. For consistency, the separation length L_{sep} from the baseline interaction is employed in the definition of $St_{L_{sep}}$ in all cases.

The pre-multiplied and normalized PSD map of wall-pressure in figure 7.10 is considered first. Dashed lines denote the corresponding mean separation and reattachment points for each case while the leading and trailing edges of the panel are indicated with dotted lines. The excursion range of the separation shock, which is of order δ_0, is located in front of the reverse-flow region in all cases, and exhibits a distinct low-frequency signature compared to the incoming TBL. In the separated region, high-frequency content characteristic of small-scale turbulence coexists with

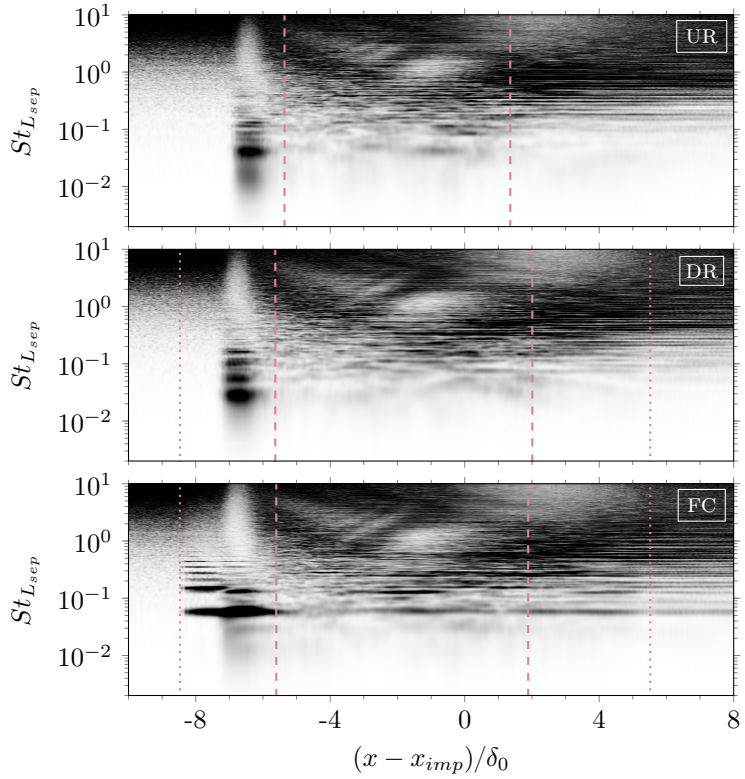

Figure 7.10: Pre-multiplied and normalized PSD map of wall-pressure along the centerline of the investigated configurations. Dashed lines indicate the mean separation and reattachment locations, and dotted lines mark the leading and trailing edges of the flexible panel. Contour levels range from zero (white) to 0.3 (black).

moderate frequencies, extending from $St_{L_{sep}} \approx 1$ to 0.1 and below. The energetic content is centered around $St_{L_{sep}} \approx 0.5$ near the reattachment location in all cases, and then progressively relaxes towards the post-interaction TBL state.

In the presence of both static and dynamic panel displacements, that is, for the DR and FC configurations, the energy density of the low-frequency content is noticeably different compared to the baseline configuration. For instance, the PSD map for the DR configuration exhibits significant higher harmonic content at the separation-shock foot. This illustrates the non-negligible modulating influence of the deformed surface geometry on the shock unsteadiness. The spectra for the FC configuration, in turn, show that the separation-shock motion resonates with the panel oscillation. The most energetic peaks in the low-frequency range for this configuration correspond to the first and second bending modes of the panel, which are also found energetic upstream of the separation shock range, throughout the reverse-flow region and beyond reattachment. Energetic content associated with the panel motion, particularly at the first bending frequency ($St_{L_{sep}} \approx 0.056$), is

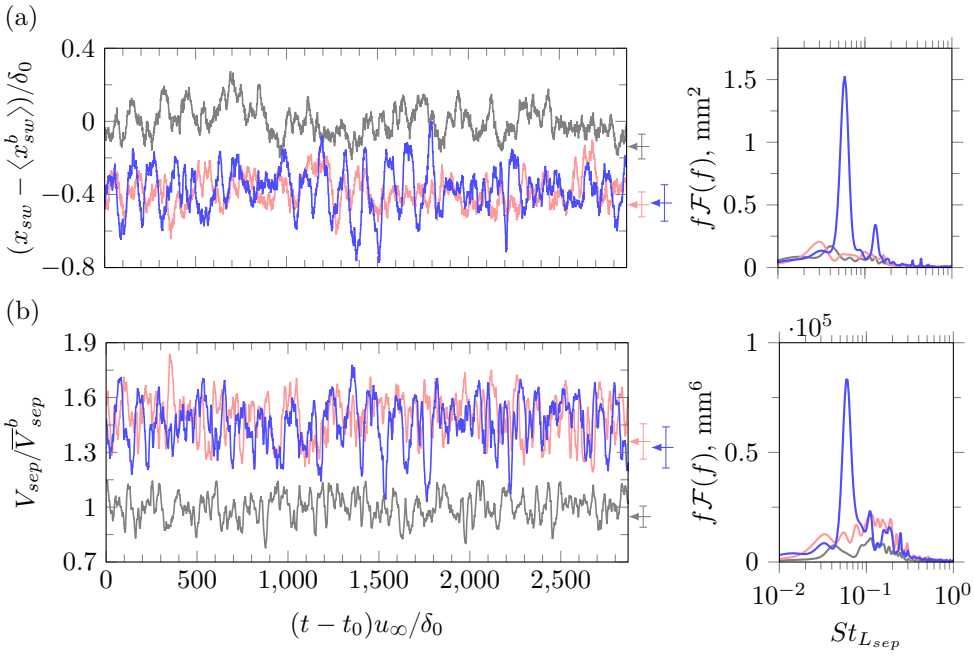

Figure 7.11: Time evolution of (a) spanwise-averaged shock position, and (b) separation bubble volume. Color legend: (gray) baseline UR configuration, (red) DR configuration, and (blue) FC configuration. The shock position is referenced with respect to the mean shock location of the baseline, i.e., $\langle x^b_{sw} \rangle$, and the bubble volume signal is normalized with the mean bubble volume of the baseline, i.e., $\overline{V}^b_{sep}$. Arrows and vertical bars indicate the corresponding mean value and its standard deviation, and right panels include the pre-multiplied PSD of the signals.

also visible downstream of the trailing edge of the panel. This suggests that the dynamic fluid-structure coupling results in pressure disturbances that propagate into the downstream flow.

Further insights on the separation shock dynamics are obtained by inspecting the time evolution of the separation-shock location signal and its pre-multiplied PSD, which are shown in figure 7.11(a) for the different configurations. Instantaneous shock locations were extracted from the corresponding three-dimensional snapshot sequence, by searching for peak values of the pressure gradient field $|\nabla p|$ in a wall-normal slice outside the boundary layer (at $y = 1.5\delta_0$, before intersecting the incident shock) and then averaging the resulting shock front in span. Note that the shock location in figure 7.11(a) is referenced with respect to the mean separation shock location of the baseline case $\langle x^b_{sw} \rangle$ for ease of comparison.

In agreement with the analysis in the previous section, the separation shock is clearly located more upstream in the presence of mean surface displacements, see the left panel of figure 7.11(a). The arrows on the side, which indicate the mean value of each signal, also make clear that the effect of the panel motion on the mean separation-shock location is secondary to the effect of the mean panel deformation.

As observed, the corresponding signals for the DR and FC configurations, which are indicated in red and blue respectively, have an almost identical mean value. The FC configuration, however, is characterized by noticeably larger excursions of the separation shock from its mean location, which translates into a larger standard deviation of the signal. This is indicated by the vertical bars on the left panel of figure 7.11(a). The present results thus confirm that the excursion domain of the separation shock is effectively increased in the presence of the moving panel, while its mean location is determined by mean (rather than dynamic) surface displacements.

The dominant peak in the corresponding PSD of the separation-shock location signal, shown in the right panel of figure 7.11(a), also confirms that the dynamic FSI coupling is mainly established through the first bending mode of the panel oscillation. The dominant peak of the signal is located at $St_{L_{sep}} \approx 0.058$, which is very close to the spectral peak of panel displacements found at $St_{L_{sep}} \approx 0.056$, see table 7.1. A secondary peak is also visible in the spectra for the coupled case, see figure 7.11(a), at a frequency $St_{L_{sep}} \approx 0.130$. This is very close to that of the second bending mode of the panel oscillation, which is found at $St_{L_{sep}} \approx 0.127$. Frequencies below the first bending frequency of the panel oscillation are also energetic in the shock location signal of the coupled interaction, and their level is comparable to the low-frequency content of the other configurations (PSDs are not normalized in this figure). This suggests that the low-frequency dynamics characteristic of flat and rigid-wall STBLIs coexist with those emerging from the dynamic coupling with the moving panel, rather than being replaced by them.

We also note that the broadband low-frequency range below the first bending frequency of the panel is centered around $St_{L_{sep}} \approx 0.03$ for the FC configuration. This peak is aligned with the global spectral peak of the DR configuration, see figure 7.11(a), which further supports the coexistence of FSI and non-FSI low-frequency dynamics in the coupled interaction. Interestingly, the corresponding low-frequency peak for the baseline case is found at $St_{L_{sep}} \approx 0.04$. This difference in peak location cannot be accounted by employing the particular L_{sep} of each configuration, rather than the baseline L_{sep}, in the definition of its corresponding Strouhal number. As deduced from table 7.2, L_{sep} is only about 11-13% larger in the DR and FC configurations compared to the baseline, which does not account for the observed discrepancy. Our results thus indicate that $St_{L_{sep}}$ is ineffective in collapsing low-frequency dynamics of flat-wall and deformed-wall STBLIs at the same flow conditions.

The time evolution of the reverse-flow bubble volume is shown in figure 7.11(b), and most of the observed changes in the presence of the flexible panel are in close qualitative agreement with those discussed for the separation shock location. For ease of comparison, volume signals have also been normalized with the corresponding mean value for the baseline case $\overline{V}^b_{sep}$. As observed, the mean bubble volume increases by approximately 50% in the presence of mean surface displacements, see also table 7.2, and is not substantially altered by the panel oscillation (if only the fluid domain above $y = 0$ is considered, the increase in bubble volume is 15%). The standard deviation of the bubble-volume signal for the DR configuration, however, is much closer to that of the FC configuration rather than the baseline. This suggests that bubble dynamics are also largely affected by mean surface displacements. From

the corresponding PSDs, shown on the right panel of figure 7.11(b), it is clear that the dominant frequency in the signal for the coupled interaction is also associated with the first bending mode of panel oscillation. Higher frequencies appear also energetic, but a direct connection with a dominant frequency of the panel oscillation cannot be established. We also note that all cases exhibit a peak at $St_{L_{sep}} \approx 0.1$, which is global for the UR and DR configurations. In agreement with the observations made in the analysis of the separation shock unsteadiness, the presence of this common peak indicates that some of the energetic bubble motions are not altered by the surface geometry and coexist with those induced by the considered surface displacements.

7.3.5. Modal analysis

For the coupled interaction, our results have so far shown that the STBLI flow strongly resonates with the first bending mode of panel oscillation. This emerging narrow-banded behavior in an otherwise broadband spectrum makes the investigated FSI particularly suitable for the dimensionality reduction that a data-driven decomposition technique like SPDMD can grant [201]. So in order to relate global flow phenomena to the first and other bending frequencies of the panel, we perform SPDMD of the LES data. The reader is referred to appendix D for algorithmic details.

In the present modal analysis, we use a total of $N_s = 8200$ snapshots per case to produce a modal decomposition with high statistical significance. The considered snapshots, which were recorded at a sampling interval of $0.68\delta_0/u_\infty$, include the instantaneous three-dimensional streamwise velocity and pressure fields. For the coupled interaction, panel displacements are also appended to the instantaneous snapshot data so that a statistical link between flow dynamics and panel motion can be established. Moreover, the regularization parameter of the SPDMD algorithm is chosen such that the number of retained DMD modes is 41 per case, and the statistical significance of the lowest frequencies is guaranteed in a similar fashion as in chapter 6. That is, by preventing DMD modes with a period of oscillation larger than a third of the total simulation time from being selected by the SPDMD algorithm as dynamically relevant.

Figure 7.12 shows the corresponding modal amplitudes and frequencies of the resulting DMD modes for each case as well as those retained by the SPDMD algorithm, referred to as SPDMD modes. All modes with non-zero frequencies arise as complex conjugate pairs because the original snapshot data is real-valued. The SPDMD mode set highlights those modes that are dynamically relevant in the DMD solution and that are therefore worth inspecting. These modes are indicated with red crosses in each panel of figure 7.12. The amplitudes of the SPDMD modes are slightly different from the DMD amplitudes because the algorithm recomputes them for an optimal representation of the original data sequence with the retained sparse structure. For the sake of clarity, the spectrum of figure 7.12 only shows Strouhal numbers up to $St_{L_{sep}} = 0.25$ because this low-frequency range already encompasses the SPDMD mode set of the DR and FC configurations. The corresponding SPDMD solution for the baseline case, on the other hand, contains a few modes with higher oscillation frequencies, up to $St_{L_{sep}} \approx 0.65$, which suggests that the lower end of the energetic

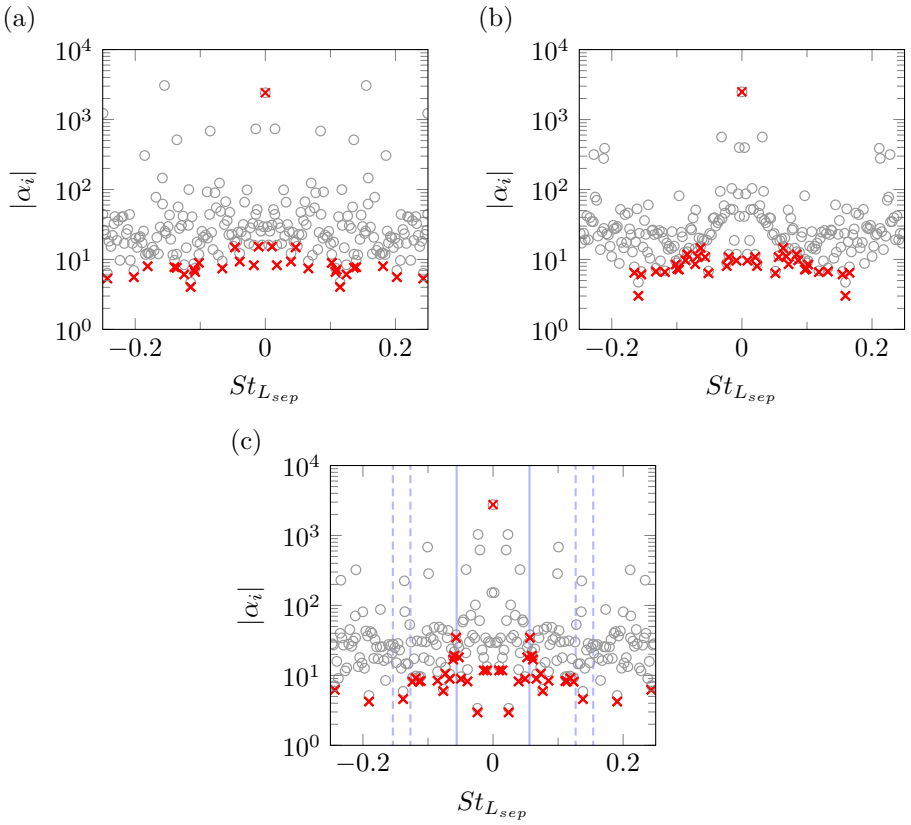

Figure 7.12: Dynamic-mode amplitude distribution for (a) the baseline UR configuration, (b) the DR configuration, and (c) the FC configuration. Symbol legend: (circles) standard DMD solution; (crosses) SPDMD solution containing 41 modes. Solid blue lines in (c) indicate the first measured bending mode of the panel oscillation, see table 7.1, while dashed blue lines denote the high-order ones (second and third).

spectrum of STBLI is more dynamically relevant in the presence of the investigated surface deformations than in the case of a flat wall. We also note that low-frequency modes below $St_{L_{sep}} = 0.1$ exhibit the largest amplitudes in all cases.

The SPDMD solution of the coupled interaction, see figure 7.12(c), excellently captures the first bending mode of panel oscillation. The corresponding Strouhal number as measured from the PSD of panel displacements is indicated with a solid blue line in the figure, and it intersects the largest SPDMD modal amplitude with non-zero frequency almost perfectly. This confirms the excellent capabilities of the SPDMD method in detecting and isolating the main system dynamics. In addition to this tone, the SPDMD solution of the coupled interaction also includes dynamic low-frequency modes below the first bending frequency of the panel oscillation, and their amplitudes are very much in line with the corresponding SPDMD modes of the UR and DR configurations, see figures 7.12(a) and 7.12(b). This further confirms

the observations made in the previous section regarding the emerging FSI dynamics, which coexist with rather than replace the characteristic non-FSI low-frequency dynamics of STBLI. Concerning the higher-order modes of panel oscillation, indicated with dashed lines in figure 7.12(c), the second bending mode also appears to be captured by the SPDMD algorithm in the coupled case. However, it does not emerge as a distinct tone like the first bending mode. The third bending mode of the panel, in turn, cannot be directly associated with a particular SPDMD mode, indicating that the STBLI flow does not resonate at this frequency.

Based on the above considerations, three SPDMD modes of the coupled interaction are selected and described in the following. These include a representative low-frequency mode below the first bending frequency of the panel oscillation, as well as the dynamic modes closest to the first and second bending frequencies of the panel. Animations of the depicted modal shapes are available as in our data repository [220] and should be considered in conjunction with the following discussion.

The selected low-frequency mode below the first bending frequency of panel oscillation, at $St_{L_{sep}} \approx 0.015$, is depicted in figures 7.13(a) and 7.13(b) at two discrete phase angles, $\omega_i t = 0$ and $\omega_i t = \pi/2$. The associated modal pressure, modal streamwise velocity and modal displacement fields are shown in the top, center and bottom panels of the figures. The modal pressure clearly highlights the connection between the low-frequency unsteadiness of STBLI and longitudinal excursions of the separation shock, in agreement with the observations made in chapter 6. These excursions are associated with pressure fluctuations of opposite sign near reattachment, which is consistent with expansions and contractions of the reverse-flow bubble from both ends. The modal streamwise velocity field additionally reveals the statistical link between the low-frequency unsteadiness of the separation shock and streamwise velocity streaks that originate near the separation point. The strongest velocity fluctuations are found at the leading edge of the bubble and in the downstream flow, whereas the streak strength is highly damped at the bubble apex due to the interaction with the incident-transmitted shock. These observations are also in excellent agreement with the SPDMD results for the rigid-wall interaction discussed in the previous chapter. In fact, we find that both the DR and FC configurations exhibit low-frequency modes with very similar modal shapes as those obtained for the baseline UR configuration. This provides strong evidence of the coexistence of non-FSI low-frequency dynamics of STBLI with those emerging from the dynamic coupling with the moving panel. The corresponding modal displacement field for the FC configuration further supports this conclusion, since it shows that the panel passively adapts to the pressure variations induced by the oscillating flow (see bottom panels of figure 7.13).

Figures 7.14(a) and 7.14(b) show two discrete phases of the dynamic mode associated with the first bending frequency of the panel oscillation, with a modal frequency of $St_{L_{sep}} \approx 0.056$. The phase difference between both figures is again $\omega_i \Delta t = \pi/2$. This mode differs in many aspects from the low-frequency mode shown in figure 7.13. Most notably, it presents an increased spanwise coherence that is consistent with the two-dimensional motion of the panel. The modal pressure, see the top panels of figure 7.14, exhibits strong fluctuations at the front end of the panel due

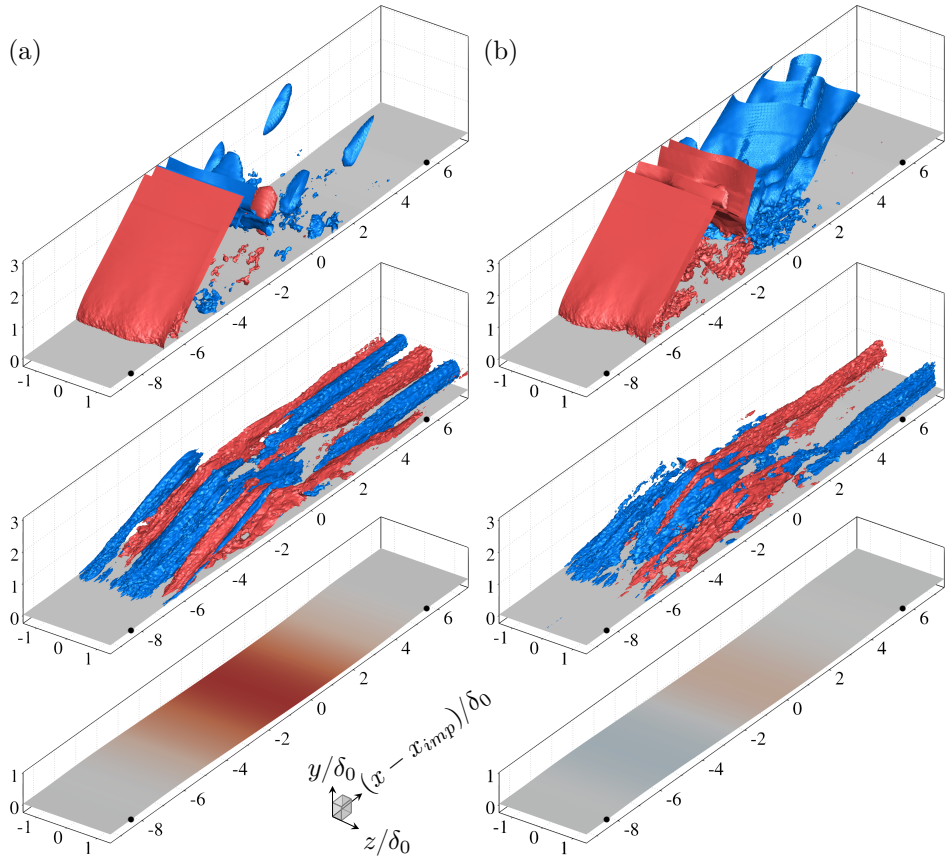

Figure 7.13: Representative dynamic low-frequency mode of the coupled interaction ($St_{L_{sep}} \approx 0.015$) at two different phase angles: (a) $\omega_i t = 0$, and (b) $\omega_i t = \pi/2$. The different panels include the modal pressure (top), the modal streamwise velocity (center), and the modal displacements (bottom). Front and rear edges of the flexible panel are indicated with black circles. Iso-contours in the top and center panels indicate strong positive (red) and negative (blue) fluctuations, and the corresponding surface geometry is indicated in gray. In the bottom panels, the surface geometry is colored by the modal displacements.

to the unsteady motion of the upward-deflected leading edge (both edges of the panel are indicated with black circles in the figures). A similar observation can be made for the fluctuations at the trailing edge of the panel, behind the interaction region, where the unsteady bending motion induces pressure disturbances that propagate into the downstream flow. The signature of these structures is also visible in the wall-pressure PSD of figure 7.10. The spanwise coherence of this mode is particularly evident in the modal streamwise velocity field, which exhibits large-scale fluctuations of the entire shear layer instead of a distinct three-dimensional streak structure. The accompanying modal displacements, which are shown on the bottom panels of figure 7.14, are clearly asymmetric in streamwise direction around the

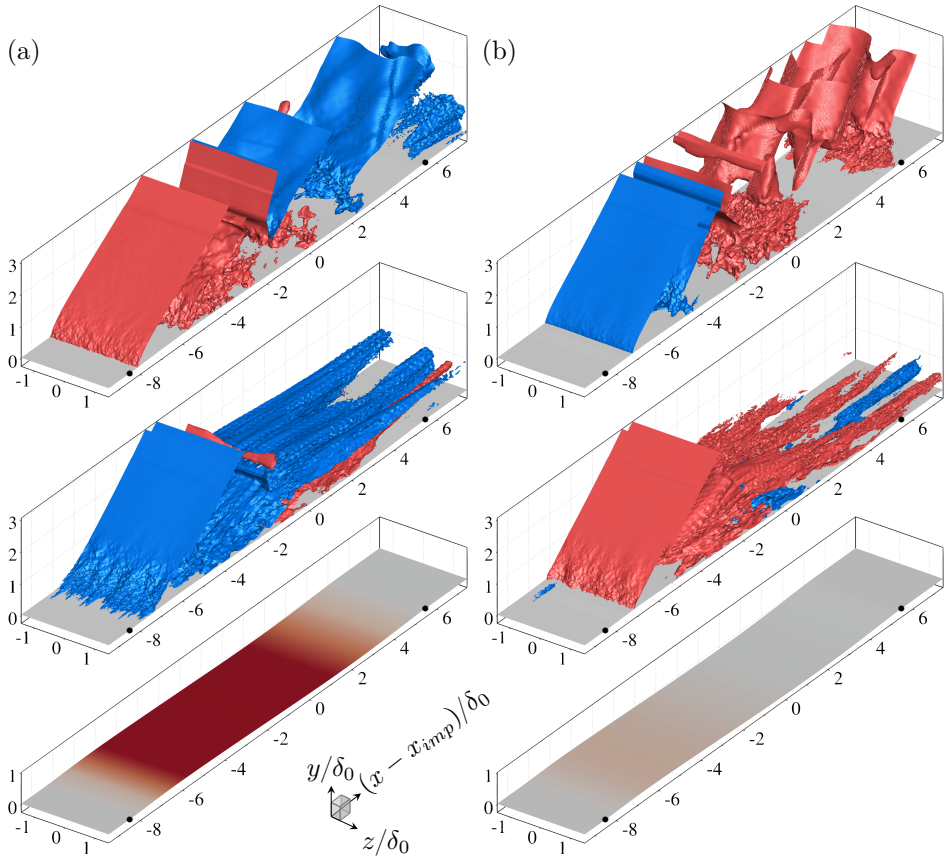

Figure 7.14: Dynamic mode associated with the first bending mode of the panel oscillation ($St_{L_{sep}} \approx 0.056$). The phases portrayed in (a) and (b) respectively correspond to phases θ_1 and θ_2 in figure 7.16, respectively. For additional details, see figure 7.13.

panel half-length. This is in agreement with the PSD map of panel displacements shown in figure 7.4(b).

In order to better understand the dynamic coupling at the first bending frequency of the panel, we reconstruct the FSI dynamics by superposing the corresponding SPDMD mode of figure 7.14, hereby referred to as $\boldsymbol{\phi}_1$, on the mean mode. Due to the noticeable spanwise coherence of $\boldsymbol{\phi}_1$, we consider the spanwise-averaged modal fields and reconstruct the corresponding purely two-dimensional dynamics. When doing so, the amplitude of $\boldsymbol{\phi}_1$ is also amplified by a factor 2 to better appreciate its effect on the mean flow. The resulting reconstructed velocity field is shown on the left panels of figure 7.15 at four equally spaced phase angles, such that figures 7.15(a) and 7.15(c) correspond to the maximum and minimum deflection of the centerpoint of the panel, while figures 7.15(b) and 7.15(d) depict the intermediate

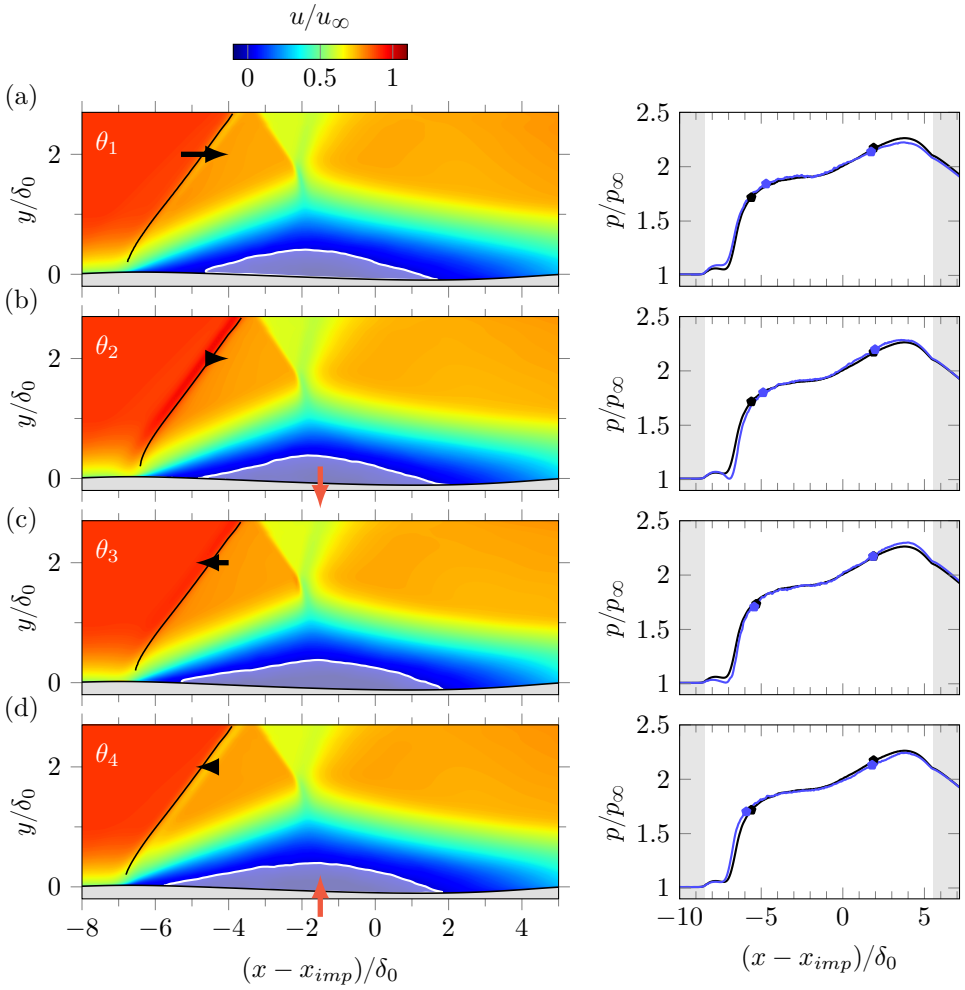

Figure 7.15: Reconstructed streamwise velocity field based on the mean flow plus the spanwise-averaged dynamic mode corresponding to the first bending frequency of t he panel oscillation. The selected phases within one cycle, which are labeled on the left corner of each contour map, are indicated in figure 7.16. The instantaneous separation shock front is delineated with a black line, and a white line delimits the reverse-flow region (which is also shaded in white). Black and red arrows indicate the direction of separation shock and panel motion, respectively. The corresponding reconstructed instantaneous wall-pressure (blue) together with its mean distribution (black) are shown on the right panels, where markers indicate separation and reattachment points.

phases. For clarity, the separation shock and the reverse-flow region are indicated with solid lines, and arrows are used to mark the direction of the separation shock and panel bending motion. The right panels of figure 7.15 include the corresponding variation of the reconstructed wall-pressure (blue line) together with the mean wall-pressure (black line) for reference. The discussion of figure 7.15 should be considered

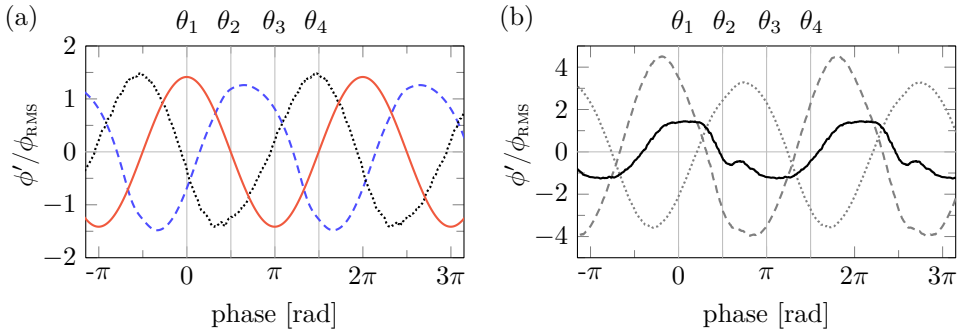

Figure 7.16: Fluctuations of different quantities for the pure oscillation based on the spanwise-averaged dynamic mode associated with the first bending frequency of the panel oscillation: (a) evolution of the mid point displacement (solid red), the separation shock location (dashed blue) and the reverse-flow bubble volume (dotted black); (b) evolution of the the integrated load over the full panel (solid black) and contributions over the first half (dashed gray) and over the second half of the panel (dotted gray). Four different phases within one cycle are indicated at the top, and they correspond to the reconstructed fields shown in figure 7.15.

in conjunction with figure 7.16, which shows the corresponding evolution of the midpoint displacement of the panel, the separation-shock location, the volume of the reverse-flow bubble and the integral panel load. Note that the equally spaced phases shown in figure 7.15(a–d) are labeled as θ_1-θ_4 in figure 7.16.

The reconstructed velocity field in figure 7.15 reveals that the reverse-flow bubble volume lags behind the bending motion of the panel by approximately $\pi/2$. In a hypothetical very slow oscillation (i.e., quasi-steady), one would expect that the most downward deflection of the panel would lead to the largest reverse-flow bubble volume, since the mean-flow of the coupled case shows an enlarged bubble in the presence of mostly-downward mean surface displacements compared to the baseline interaction, see section 7.3.3. The unsteady nature of the coupling, however, introduces a phase offset between both signals that is particularly evident in figure 7.16(a) (compare solid and dotted lines). As indicated by the dashed blue line of figure 7.16(a), the separation shock motion is also characterized by asymmetric excursions around its mean location, with larger upstream excursions that persist for less than half of the period. Figure 7.16(a) also indicates that the separation shock location signal is approximately anti-correlated with the reverse-flow bubble volume, which is expected considering that the first bending frequency of panel oscillation is found within the broadband low-frequency range of STBLI [31, 221]. The cross-correlation between the bubble volume and the separation shock location signals, however, reveals a small negative time lag between the two. This time lag is visible in 7.16(a) and indicates that the shock motion is preceded by variations in the extent of the recirculation region. Interestingly, we find that the observed time lag corresponds precisely to the time required by a pressure disturbance generated at the mean reattachment location to reach the separation line, i.e., $\Delta t \approx L_{sep}/a_w$ where a_w is the speed of sound at the wall. This finding could support the hy-

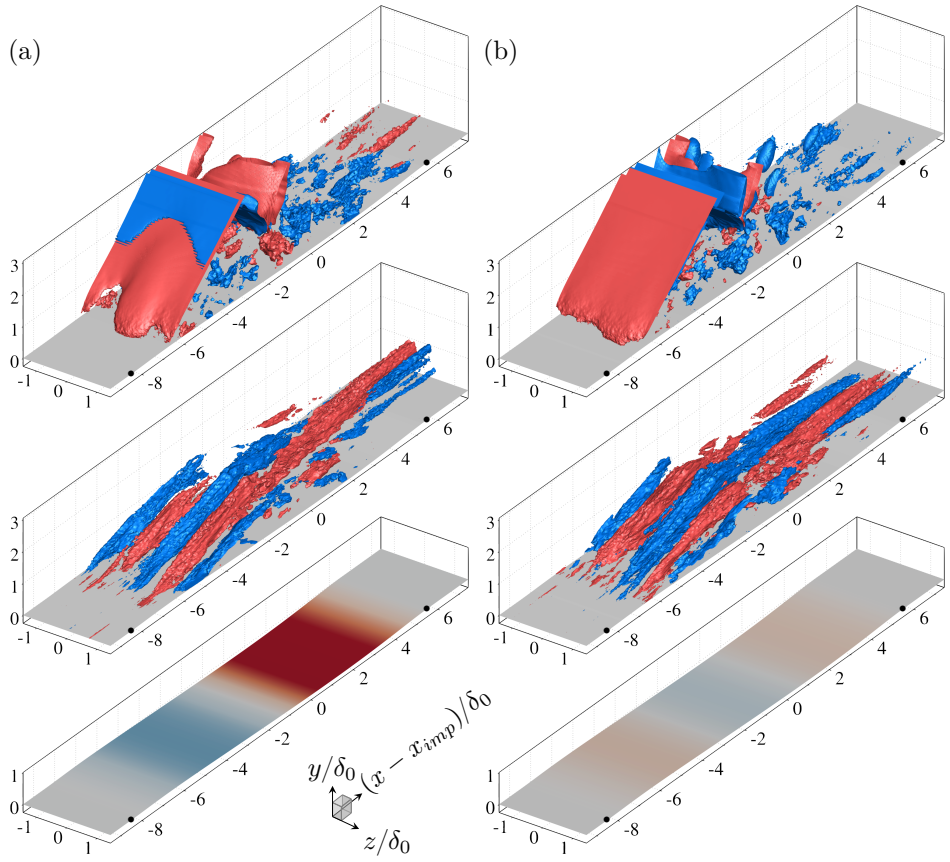

Figure 7.17: Dynamic mode associated with the second bending mode of the panel oscillation ($St_{L_{sep}} \approx 0.124$). For additional details, see figure 7.13.

pothesis that a downstream instability is the main driver of the separation-shock unsteadiness [30].

Another relevant element in the considered fluid-structure coupling is the panel load. Together with the resulting elastic forces and the considered cavity pressure, the panel load ultimately drives the panel motion. Figure 7.16(b) shows the evolution of the integral panel load within the cycle (black solid line), which also presents an asymmetric behavior around its mean value. The panel load on the first and second half of the panel, which together constitute the integral panel load, are also indicated in figure 7.16(b) as dashed and dotted gray lines, respectively. By comparing figures 7.16(a) and 7.16(b), it is clear that the separation-shock location determines the load on the first half, while the trailing edge of the bubble, that is, the reattachment process, influences the load on the second half. The particular evolution of these signals, as well as their relative offset, leads to an integral panel

load that essentially increases during the upward bending and decreases during the downward bending, see figure 7.16(b). This is characteristic of a restoring load.

Figure 7.17 shows a dynamic mode with a characteristic frequency of $St_{L_{sep}} \approx 0.124$, which is very close to the second bending frequency of the panel oscillation, see table 7.1. Qualitatively, the flow characteristics of this mode appear similar as those of the low-frequency mode included in figure 7.13. Differences are mainly found in the modal pressure at the separation shock, which is characterized by narrower longitudinal excursions, noticeable variations in shock deflection and increased spanwise shock wrinkling. The corresponding modal displacements have an asymmetric effect around the panel half-length with larger fluctuations in the second half of the panel. This behavior is consistent with the PSD map of panel displacements in figure 7.4(b). Since the first and second half of the panel also oscillate with a different phase within the mode, the observed asymmetry makes the oscillation at times reminiscent of a third bending mode. We also note that the other configurations exhibit similar modal shapes for the flow variables around this frequency (not shown here), which suggests that the STBLI flow is only weakly coupled with this bending mode.

7.4. Summary

In this chapter, we discussed the dynamic coupling between a Mach 2.0 TBL flow, an oblique impinging shock wave, and a flexible panel. This phenomenon was captured with a coupled FSI simulation that combined wall-resolved LES for the fluid with a FE structural solver for the panel. To assess the different effects of mean and dynamic panel displacements on the STBLI dynamics, the resulting mean panel deflection was also employed as a rigid-wall geometry in a second simulation, integrated over the same time interval as the coupled case. Results were compared with a flat rigid-wall STBLI at the same flow conditions, corresponding to the moderate-Reynolds case $\mathcal{B}_2$ discussed in chapter 6.

Our results showed that the flexible panel exhibited self-sustained oscillatory behavior over a broad frequency range, confirming the strong and complex FSI. The first three bending modes of the panel oscillation were found to contribute most to the unsteady panel response, at frequencies in close agreement with natural frequencies of the pre-stressed panel rather than those for the flat (unloaded) panel, which differed significantly. Moreover, the mean panel deflection was found to enlarge the reverse-flow region, whereas the dynamic panel motion around the mean deflection had a negligible influence on the mean-bubble volume. The separation-shock unsteadiness, however, was enhanced by the panel motion, leading to higher wall-pressure fluctuations at its foot. Spectral analysis of the separation-shock location and bubble-volume signals revealed that the fluid-structure coupling was predominantly established via the first bending mode of the panel oscillation. Modal analysis of the flow and displacement data further supported this coupling and helped identify the mechanism sustaining it.

Epilogue

8

Conclusions

The aim of the present work was to improve our understanding of the underlying physics of shock-shock interactions (SSIs) and shock-wave/turbulent boundary-layer interactions (STBLIs). Both phenomena are omnipresent in high-speed aerodynamics and can severely affect the efficiency and structural integrity of multiple aircraft components when uncontrolled.

8.1. Shock-shock interactions

Response to periodic excitations

The first part of the thesis was focused on the response of asymmetric SSIs to different excitation mechanisms that mimic the disturbance environment of supersonic inlets and other internal flows. In chapter 3, we considered perturbation modes of the lower incident shock, which included pitching across the dual-solution domain, a periodic (sinusoidal) oscillation of the imposed deflection around a mean value (both within and outside of the DSD), and a periodic (sinusoidal) streamwise oscillation without pitch. These excitation modes, specially the latter two, were aimed at emulating the dynamics of the separation shock in STBLI flows.

Our simulations unambiguously confirmed that excitations of this kind can trigger RI→MI transition and potentially sustain the MI for mean flow conditions within the steady-state DSD. This is a consequence of the impulsive Mach stem growth right after transition, which prevented the remaining oscillatory motion of the lower incident shock from inducing transition back to a stable RI pattern. A transient growth of the mean Mach stem height was in fact observed over several periods of oscillation until a mean steady state identical to that obtained for an initial MI was reached. In relation to the excitation applied to an initial MI, significantly lower frequencies were required to induce the collapse of the Mach stem and trigger MI→RI transition, compared to the opposite case. No transition to the RI was observed for the excitation frequencies considered. This suggests that any single-time event encountered in real life conditions for which a stable Mach stem can develop could lead to a sustained MI thereafter.

In view of the aforementioned, we thus conclude that the MI configuration is more robust against periodic perturbations than the corresponding RI configuration for mean flow conditions within the steady-state DSD. This is in agreement with previous experiments in wind tunnel facilities with a high level of free-stream disturbances, for which the MI configuration was observed to prevail within most of the extent of the DSD with hardly any visible hysteresis. Our computations did not confirm, however, the possibility of a periodic oscillation sustaining the MI for mean flow conditions outside the steady-state DSD on the RI domain. This is consistent with case SWBLI_6 of Matheis and Hickel [46] in which, for the same free-stream Mach number and similar mean flow deflections outside the DSD, RI→MI transition due to the dynamics of the separation shock was not observed. Computations for which they did observe such phenomenon were conducted at $M_0 = 2.0$ and mean flow deflections for which no steady-state DSD exists, and for which additional acoustic perturbations emitted by the TBL may play a decisive role.

Effect of variable inflow Mach number

In the second and last chapter of PART ONE, which corresponds to chapter 4, we investigated the complimentary excitation mechanism to those described above, that is, the influence of free-stream Mach number variations on SSIs with nominally fixed shock generator geometry. An experimental campaign was carried out for this purpose in the transonic-supersonic blow-down wind tunnel (TST-27) of the high-speed aerodynamics laboratory at TU Delft, which enabled a continuous variation of the free-stream Mach number during a run. Since the time rate of change of the Mach number was much smaller than the characteristic flow time scale, the varying free-stream conditions represented a quasi-steady perturbation of the SSI system.

In line with previous works dealing with noisy experimental environments, no transition hysteresis was observed in our experiments and the MI was found to persist throughout most of the steady-state DSD. However, achieving experimental agreement with the *von Neumann* criterion required very accurate measurements of flow deflection alongside the Mach number. This was accomplished through a systematic flow-based post-processing methodology that extracted the correct state of the flow from schlieren visualizations and synchronous pressure readings. The maximum observed deviation between flow deflection measurements and nominal wedge angles was 1.2°.

Furthermore, different planes along the optical path were investigated with a focusing schlieren system to assess three-dimensional side-wall effects in the experimental setup. The analysis confirmed that the considerable shock thickening observed in regular schlieren visualizations was caused by STBLIs at the side-walls, and that the trailing edge of the incident-shock footprint was a reliable indicator of the two-dimensional incident-shock locations at the mid-plane of the test section. To the authors' knowledge, this was the first time that the focusing schlieren technique was successfully applied to SSIs. It was also the first time that such technique was employed in our facilities, and it certainly proved to be robust at blurring out-of-focus elements for practical purposes. We thus envision the use of the focusing schlieren technique in future experiments where the spanwise organization of the

flow is of interest, such as in the case of STBLIs in presence of flexible components or shock-control elements.

8.2. Shock-wave/turbulent boundary-layer interactions

The second part of the thesis was fully focused on the physics of STBLIs with substantial flow separation. Understanding the mechanisms that drive the most energetic dynamics of STBLIs at high Reynolds numbers (chapters 5 and 6) and in presence of elastic structures (chapter 7) is essential for the development of effective flow control strategies that can effectively mitigate the risk of damage to the vehicle.

Reynolds number effects were quantified from a new wall-resolved LES database of a Mach 2.0 STBLI flow with strong boundary-layer separation at three different friction Reynolds numbers $Re_\tau = 355$, 1226 and 5118, and otherwise equal flow parameters. The high-Reynolds case significantly extends the available parameter range of strong STBLI covered with high-fidelity simulations and represents a leap towards the high-Reynolds conditions of experimental facilities. The LES database also includes simulations of the TBL flow in absence of the impinging shock, so as to properly characterize the undisturbed TBL, and of the moderate-Reynolds STBLI flow over a compliant thin-panel to investigate the resulting dynamic coupling. All STBLI cases exhibit substantial flow reversal and were integrated for a very long time to properly resolve low-frequency dynamics.

Effect of Reynolds number on the turbulent boundary layer

The discussion of Reynolds number effects was first centered around the undisturbed TBL, i.e., in absence of the incident shock, and was presented in a separate chapter (chapter 5). Considerable attention was dedicated to quantifying the size of the turbulent structures populating the TBL, with a specific focus on the outer layer at high Reynolds number.

Separation of the inner and outer scales in the high-Reynolds case was verified through examination of the pre-multiplied streamwise energy spectra of streamwise velocity fluctuations, which exhibited a bimodal configuration with an inner peak at $y^+ \approx 15$ and $\lambda_x^+ \approx 700$ and an outer peak at $y/\delta_0 \approx 0.1$ and $\lambda_x/\delta_0 \approx 6$. The significant elongation of the outer-layer structures at high Reynolds number was also highlighted via two-point autocorrelation maps of streamwise velocity fluctuations with the reference location at $y/\delta_0 \approx 0.2$. This data further revealed that outer-layer structures interact with the near-wall turbulence in all cases, at an oblique angle with respect to the free-stream flow. For the low- and moderate-Reynolds cases, the observed inclination angle closely matched the 14° angle reported by Marusic and Heuer [147] for incompressible TBLs, while the high-Reynolds case exhibited a slightly smaller inclination in the outer layer. All correlation maps were also found to conform to more shallow angles near the wall, between 8° and 11°, which suggests that a line fit of peak points in wall-normal direction is a poor representation of the structure inclination angle.

The average spanwise spacing of the dominant turbulent structures was also assessed from spanwise autocorrelation functions and related spectra. In all cases, the streamwise velocity correlation calculated at $y^+ \approx 15$ revealed a local minimum at $\Delta z^+ \approx 50$, thus providing an indication of the spanwise spacing between adjacent near-wall streaks. This minimum, however, was found at a positive correlation value for the high-Reynolds case, which highlights the organizing effect of the log-layer on the near-wall region. The global correlation minimum at $\Delta z^+ \approx 50$ could be recovered by removing the large-scale imprint with a high-pass filter, whereas correlations computed from low-pass filtered data at $y^+ \approx 15$ resembled the typical correlation function of the log-layer structures. These findings have very promising implications for flow control applications as well as for wall modelling in LES.

The inner-scaled spanwise spectra of the unfiltered data at $y^+ \approx 15$ also showed the imprint of log-layer structures for the high-Reynolds case, for which the location of the spectral peak was found at a much higher wavelengths than $\lambda_z^+ \approx 100$. The approximate spacing of the outer-layer motions was deduced from the outer-scaled spectra at $y/\delta_0 \approx 0.1$ where a peak is found at $\lambda_z \approx 0.7\delta_0$ in all cases. While the peak kinetic energy was found to increase with increasing Reynolds number, the fact that the corresponding wavelength remains unaltered indicates that the width of turbulent structures away from the wall is essentially independent of the Reynolds number. This observation is in very good agreement with the experimental results of Hutchins and Marusic [137] and Bross *et al.* [119].

Based on the aforementioned results, log-layer structures may (and do) contribute to the rippling appearance of the separation-shock foot in the corresponding STBLIs [159] but they are still too short in longitudinal direction to considerably modulate the low-frequency unsteadiness of the interaction in the considered Reynolds number range. As indicated by Ganapathisubramani *et al.* [37], only structures of order $\lambda_x = 50\delta_0$ can induce low-frequency scales of order $O(0.01u_\infty/\delta_0)$ on the STBLI flow, which are the values typically reported for the most energetic motions of the separation shock [30]. The observation that the largest structures in the present LES data were found to be one order of magnitude smaller in length is then compelling evidence to consider the low-frequency unsteadiness observed in the investigated STBLIs to be primarily induced by some other mechanism.

Effect of Reynolds number on the STBLI flow

After providing a detailed characterization of the undisturbed TBL in chapter 5, the ensuing dynamics and organization of the corresponding STBLI flow were discussed in chapter 6. The separation-shock foot appeared highly diffused at low Reynolds number, where flow separation at the leading edge of the interaction was found to be initially restricted to the wall. Conversely, at high Reynolds number, the detached shear layer was immediately lifted away from the wall, and the separation shock originated deep within the TBL, resulting in a distinct peak in wall-pressure fluctuation intensity. Furthermore, analysis of the instantaneous flow revealed noticeable spanwise variations of the separation-shock foot and local separation line at high-Reynolds number, associated with alternating regions of low- and high-momentum fluid in the incoming TBL. These fluctuations appeared to re-organize into larger

structures across the interaction, a phenomenon consistently observed across all cases.

In terms of the mean-flow, differences in upstream influence were assessed using a custom parameter defined for the impinging STBLI case, which revealed a decreasing upstream effect with increasing friction Reynolds number. Notably, the separation length L_{sep} and the post-shock flow deflection above the shear layer appeared largely unaffected by the Reynolds number, as did the incipient pressure plateau in the mean wall-pressure. However, the shape of the reverse-flow bubble showed more pronounced deviations from a triangular shape at low Reynolds number, alongside a curved leading edge with a large curvature radius.

Furthermore, inspection of velocity statistics showed that the peak value of the streamwise Reynolds stress τ_{11} moves from the separation-shock foot at low Reynolds number to the core of the shear layer at high Reynolds number. This finding motivated the analysis of τ_{11} transport budgets along mean-flow streamlines, as previous (low-Reynolds) studies have only identified the peak location at the separation-shock foot and attributed the maximum amplification to the influence of both the near-wall cycle of the TBL and the deceleration of the mean-flow. However, our results demonstrate a departure from this dominant amplification mechanisms at high Reynolds numbers. Instead, the emergence of the global stress peak is correlated with increased pressure transport in the separation-shock excursion domain, further away from the wall. This increase was attributed to the unsteadiness of the sharp separation shock at high Reynolds number, originating deep within the TBL.

The effect of Reynolds number on the STBLI dynamics was also quantified by means of temporal spectra of wall-pressure, separation-shock location and separation-bubble volume. While the wall-pressure spectra for the low-Reynolds case only exhibited moderate low-frequency content around the diffused separation-shock foot, broadband and very energetic low-frequency content was well-established in the other cases. Particularly at high Reynolds number, the wall-pressure signal underneath the separation-shock foot exhibited strong intermittency, characterized by a bimodal and highly right-skewed probability density function. The spectra of the separation-shock location, tracked above the shear layer, revealed broadband energetic low-frequency content in all cases at a separation-length-based Strouhal number $St_{L_{sep}} < 0.1$, thus confirming that the mechanisms driving the low-frequency dynamics of STBLIs are fundamentally independent of Reynolds number.

Notably, the low-frequency range also exhibited energy in the spectra for the reverse-flow bubble volume, but the dominant contributions to the signal variance were found at $St_{L_{sep}} \approx 0.1$–0.2 in all cases. This moderate frequency is similarly energetic in subsonic detached shear layers and supersonic backward-facing steps, where it is linked to the flapping motion of the shear layer. We hypothesized whether a comparable mechanism manifests in the investigated impinging STBLI flow.

The relationship between the reverse-flow bubble volume and the spanwise-averaged separation-shock was also examined by cross-correlating both signals, revealing that the separation-shock motion consistently lags behind bubble-volume variations in all cases. Interestingly, we found that the time lag between both signals is approximately the acoustic propagation time from reattachment to separation

in all cases. This provides compelling evidence for a downstream mechanism driving the motion of the separation shock.

Lastly, we performed sparsity-promoting dynamic mode decomposition (SPDMD) of the three-dimensional pressure, streamwise velocity and streamwise vorticity fields to relate energetic frequencies in the temporal spectra with global flow phenomena. We found that the subset of dynamically relevant modes exhibits an increased concentration at low-frequencies with increasing Reynolds number. Inspection of the corresponding low-frequency modes confirmed a consistent statistical link among large-amplitude excursions of the separation shock, large-scale velocity streaks and streamwise-aligned vortices across all cases.

While these findings seem to align with hypotheses in the literature suggesting that Görtler-like vortices drive the low-frequency unsteadiness of STBLIs, causality cannot be established with the present results. In fact, the relevance of the identified large-scale vortices is called into question by their presence also extending to higher frequencies, above $St_{L_{sep}} = 0.1$, and not being exclusively associated with low-frequency dynamics.

Reconsideration of the source of low-frequency unsteadiness

While a primary mechanism for mass exchange between the reversed-flow region and the free-shear layer appears around $St_{L_{sep}} \approx 0.1$ in both subsonic and supersonic detached shear layers, we note that only those configurations with unconstrained separation and reattachment points additionally exhibit energetic content at lower frequencies, i.e., at $St_{L_{sep}} < 0.1$. This is the case for impinging and compression-ramp STBLIs, where boundary-layer separation is induced by an adverse pressure gradient and is bound by two strong and unconstrained compressions. Forward-facing and backward-facing step flows, in contrast, do not exhibit such energetic low-frequency dynamics [193, 205], in our opinion, because either the separation or the reattachment points are geometrically constrained in streamwise direction by the step.

The significance of this observation should not be understated because most of the potential mechanisms hypothesized in literature as drivers of the low-frequency unsteadiness are present in step-induced STBLIs, yet their dynamic characteristics are evidently different. Our hypothesis is that the interaction does not require a particular low-frequency forcing, but rather energetic low frequencies simply emerge as a result of a dynamic feedback between the separation and reattachment points (very much like hysteresis) that appears in the higher-frequency oscillations of the recirculation bubble, i.e., at $St_{L_{sep}} \gtrsim 0.1$. This can only occur when both separation and reattachment points are unconstrained and can dynamically couple, which is not the case in step flows. If this hypothesis holds, it would imply that suppressing the undesirable low-frequency content of the interaction is achievable by breaking the dynamic coupling between separation and reattachment, without the need for reducing the size of the recirculation bubble and with most of the mechanisms considered as potential drivers of the low-frequency unsteadiness remaining active. Future efforts will be directed towards providing further insights into these observations.

A remark on the employed modal decomposition

The DMD algorithm and its sparsity-promoting variant were found to be effective at isolating tonal behavior (chapter 7). However, care must be taken with the physical interpretation of DMD modes when the system dynamics are broadband. The fact that the resulting modal basis is not energy-ranked (relative to the variance of the data sequence) is a disadvantage in this regard, specially when one is concerned with building a reduced-order model of the flow system. An alternative to DMD worth exploring is spectral POD or SPOD [222]. This method not only identifies frequency-ranked coherent structures but also optimally ranks them by energy. We are currently exploring the capabilities of this method in the context of STBLI flows, as well as the benefits of performing a Fourier decomposition in the homogeneous spanwise direction (prior to the modal analysis) to reduce memory requirements of the decomposition algorithm and better pinpoint the spanwise spacing of elongated structures statistically linked to the low-frequency unsteadiness of STBLIs.

Effect of static and dynamic surface deformations

In the last chapter of PART TWO of the thesis, which corresponds to chapter 7, the dynamic coupling between STBLI and a compliant thin-panel was investigated. Coupled FSI simulations involving wall-resolved LES were conducted in order to capture this phenomenon at the same flow conditions as the moderate-Reynolds interaction discussed in chapter 6 ($Re_\tau = 1226$). The different effects of mean and dynamic panel displacements on the STBLI dynamics were also assessed by employing the mean panel deflection as a rigid-wall geometry in a separate simulation, which was integrated for the same time interval as the coupled case.

Our simulation results showed that the flexible panel exhibited self-sustained oscillatory behavior with varying oscillation amplitude, confirming the strong and complex dynamic coupling with the flow over a broad frequency range. The first three bending modes of the panel oscillation were found to make up most of the unsteady panel response. The corresponding modal frequencies were in close agreement with natural oscillation frequencies of the pre-stressed panel, which were significantly higher than those for the flat (unloaded) configuration. This highlighted the importance of mean surface displacements and the corresponding stiffening of the structure in the investigated FSI, which need to be accurately captured for a reliable prediction of the panel dynamics.

Furthermore, we found that the mean panel deflection enlarged the reverse-flow region, while dynamic panel motion around the mean deflection had a negligible influence on the mean bubble volume. The separation-shock unsteadiness, however, was enhanced by the panel motion, leading to higher wall-pressure fluctuations at its foot. Spectral analysis of the separation-shock location and bubble volume showed that the FSI coupling was mainly established through the first bending mode of the panel oscillation. This was further confirmed by SPDMD of the flow and displacement data.

The analysis of the low-order modal reconstruction of the FSI revealed that variations in the reverse-flow region followed the panel bending motion and drove the separation-shock unsteadiness. Subsequently, the response of the STBLI flow to sur-

face displacements was found to alter the panel load, thereby affecting the panel motion and sustaining the dynamic coupling. Low-frequency modes that were not associated with the fluid-structure coupling, in turn, were very similar to those obtained for the rigid-wall interactions. This evidenced that the STBLI dynamics emerging from the unsteady FSI coexist with, rather than replace, the characteristic low-frequency (non-FSI) content of the interaction.

Based on the present results, it is clear that dynamic FSIs involving STBLIs and flexible panels can accentuate the undesirable features of STBLIs. Even though results may vary depending on impingement location, interaction strength or cavity pressure, the use of flexible structural components as passive flow control devices (as hypothesized in literature) is not supported by the present findings.

Afterword

Embarking on a PhD journey was a decision I made during my graduate studies, once I had discovered my personal interests and aspirations, which were not so apparent earlier in my life. And now that this journey is coming to an end, I can confidently say that it has been a success. And I say this not because I find the scientific findings summarized in these pages interesting or valuable, which I do, but because of the immense personal growth that I have achieved over the past years and the many experiences that I have shared with truly remarkable individuals. These are the most important accomplishments of this journey, and they extend far beyond the content of these pages.

In fact, given the profound impact that many people have had on me over the past years, it is only logical that I take a moment to express my gratitude and appreciation towards them. I want to begin by extending my sincerest thanks to my promotor and supervisor, Stefan Hickel. Stefan, thank you very much for believing in me and for your invaluable guidance and support. Your relentless dedication to your work, combined with your expertise across a wide variety of disciplines, is not only inspiring but also deeply contagious, motivating everyone around you to strive for excellence. Collaborating with you has been a privilege, and I am genuinely grateful for the opportunity to continue working together.

A heartfelt thank you also goes to my other two supervisors, Ferry Schrijer and Bas van Oudheusden. Ferry, I want to thank you for your guidance throughout the years and for the time spent together in gas dynamics, both in lectures and during the oral exams; it was undeniably a highlight of my PhD journey that made it unique and from which I learnt a lot. And Bas, your voice of experience and wisdom has been invaluable during our discussions and paper revisions - thank you. You will be genuinely missed once you embark on your well-deserved retirement.

I must also express my gratitude to all my colleagues in the HSL building, with whom I've had the privilege of sharing this journey. Firstly, to the scientific staff members whose brilliance creates an intellectually stimulating environment that is truly invigorating. Next, to the technicians, whose diligent work behind the scenes ensures that everything runs smoothly in the lab. And of course, to our indispensable and dear friend Colette Russo: without you, the lab would be in total disarray.

I haven't forgotten about all my PhD colleagues and friends that have shared the journey with me. It is hard to describe how profoundly you all have impacted my life and how inspiring it has been to be surrounded by such remarkable individuals. While some of you have left already, as is the nature of temporary endeavors, I'm convinced that our friendship will endure alongside the memories that have shaped

my life throughout these past years.

I want to start by expressing my gratitude to my senior colleagues, Tiago, Yi, Zeno, Martin, Varun, Koen, Wouter, for being such a reference and showing the younger generations how it's done. To my contemporaries, Jordi, Alessandro, Christoph, Beto, Mohamad, Garbiel, Edo, Constantin, Alex, Sven, Julia, Weibo, Xiaodong, Sagar, thank you for creating such a vibrant and stimulating atmosphere, both on and off work. You are exceptional individuals, and your presence has made every day in the office a joy. To the newer generation, Marina, Tyler, Haris, Ata, Jane, Kherlen, Wencan, Adrian, Thomas, Giulio, Parisa, Renzhi, Ilda, Andrea, Max, Luuk, your energy and talent have brought a new dimension to the lab. Thank you for shining bright. And lastly, thank you to all the other colleagues that were not PhDs in the HSL, like Inés, Oscar and Jaime, but who played equally important roles in this endeavor.

It is inevitable, however, to create even deeper connections with those whom one truly resonates with, whether in Delft or far away. These connections significantly influenced my perception and understanding of the world around us, so I would like to take a moment to acknowledge them.

To my good friends Jordi, Alessandro and Tiago. Jordi, company, you approach life and friendships with the same passion, commitment and elegance that you approach science, and that is truly remarkable and inspiring. I am deeply grateful for our friendship and the experiences we've shared. Alessandro, sir, the same sentiment applies to you. Thank you for being such a professional in this world, and thank you also to your partner Ella for all those memorable moments spent all together. And Tiago, my heartfelt gratitude also goes to you for our friendship and for being such a reference throughout the years, in science, life and even at the tennis court. Who would have imagined? We can just wonder.

To my dear friends Marc and Dani, or Rovira and Jarne as I call them, I am so grateful for our friendship. Rovira, you have been a very important figure in my life long before my PhD, and I sincerely hope it continues for many more years to come. I am delighted that you, Maria and lovely Rita are back in Delft, allowing us the opportunity to engage in more conversations about science and society, more board game nights, and share more runs together. And Jarne, these past years together have been truly special, and I sincerely hope that you are back in the Netherlands soon. Those nights spent out with beers, reflecting about life and the world, are unique and necessary for me.

To my Wiener Neustadt friends. Dima, Roger, Tim and Thomas, I'm so lucky that we coincided in 2015 and are friends ever since. You have had a profound impact on me, and are part of the reason why I decided to pursue a PhD. So thank you, amigos. And Dima, I must express once again my admiration for your father, who is defending freedom with his life. He is a true inspiration for the world.

A heartfelt thank you also goes out to Bać, Sara, Lenka, and Ben, spread between Vienna and Paris. You are all amazing, and I can't wait to have many more memories all together, *moja braćo*.

And to my dear friends in my hometown, Mataró, for always being there, no matter distance or time. I truly believe that I wouldn't be the person I am today

without each and every one of you. So, from the bottom of my heart, a big thank you to all of you. *Only plash can judge me.*

It is now time to say a few words to my family, to whom this thesis is dedicated. A la Triana, la filla del meu germà i el membre més jove de la família. Triana, tens el tresor més preuat que una persona pot tenir, i és una vida sencera al davant. Que aquest volum et serveixi d'inspiració per perseguir els teus somnis i inquietuds, i per mirar el món que et rodeja amb curiositat i actitud crítica. A la meva família, tant la queda més a prop geogràficament – el meu germà, les meves tietes i tiets, els meus cosins i la Iaia – como la que queda más lejos pero igual de cerca en el corazón – mis tíos y mis primos. També a aquells que ja han marxat, la Abuela i l'Avi, però que no oblidem. L'Avi va poder veure com vaig iniciar aquest viatge, i segur que estaria molt orgullós si pogués ser avui entre nosaltres. Una cosa personal i intransferible.

I com no podria ser d'una altra manera, als meus pares, que m'ho han donat tot en aquesta vida. Vosaltres m'heu ensenyat el significat de l'esforç i dels valors pels quals cal lluitar i que vull transmetre als meus fills. Mi mayor suerte es la de teneros como padres, y sin vosotros nada de esto hubiera sido posible. Muchísimas gracias de todo corazón, por todo. Us estimo molt.

And last but not least, to my dear Tijana, the person that made all of this possible. The biggest thank you goes to you. Without your smile and warming love, without your energy and curious mind, without your unwavering support during my darkest days, I wouldn't be where I am today, nor would I be the person that I have become. I simply cannot imagine a world without you, and while you may be closing this book, you have actually opened the most important book in my life, a book that we are writing together and that will be filled with love, adventures and joy. To the moon and back Tićo, *volim te.*

Lluís Laguarda Sánchez
Delft, May 7, 2024

Appendix

A

ALDM for compressible turbulence

The adaptive local deconvolution method (ALDM) is a non-linear discretization scheme designed for implicit LES of turbulent flows. Within this framework, the truncation error of the discretization of the convective terms serves as a subgrid-scale (SGS) model, which renders explicit computation of model terms (as in explicit LES) unnecessary. Initially developed by Hickel *et al.* [223] for incompressible turbulence, ALDM was subsequently extended in Hickel *et al.* [71] to compressible turbulence with shock waves.

Below is an outline of the key concepts behind the ALDM framework for compressible flows; for further details and validation results, the reader is referred to the original publications.

Finite-volume discretization

In essence, ALDM relies on conventional finite-volume discretization methods, but with modifications that convert the resulting truncation error into an implicit SGS model. The foundational elements of finite-volume methods involve reconstructing solutions at cell faces and approximating the physical flux function with a numerical counterpart that operates on the reconstructed solution; these same components form the core of ALDM.

The finite-volume discretization of the governing equations corresponds to convolving the integral form of (2.1) with a top-hat filter G, where the latter is associated with the numerical grid $x_N = \{x_j\}$ onto which the filtered continuous variables are projected. For a scalar quantity ϕ, this results in

$$\overline{\phi}_N = \{\overline{\phi}(x_j)\}, \quad j \in \mathbb{Z}, \tag{A.1}$$

where $\overline{\phi} = G \star \phi$. The filter kernel is

$$G(\boldsymbol{x}, V_j) = \begin{cases} 1/V_j & \boldsymbol{x} \in \Omega_j \\ 0, & \text{else} \end{cases}, \tag{A.2}$$

where the volume of the computational cell Ω_j is denoted as V_j.

A

Reconstruction

With ALDM, reconstruction of the unfiltered solution at the cell faces (i.e., simultaneous deconvolution and interpolation) is performed using a non-linear combination of Lagrange interpolation polynomials [96]. This step is as follows.

First, given a generic $k-$point stencil ranging from x_{i-r} to $x_{i-r+k-1}$, the resulting 1D ansatz at cell faces (denoted by half integers) is

$$\breve{g}^{\mp}_{k,r}(x_{j\pm1/2}) = \sum_{l=0}^{k-1} c^{\mp}_{k,r,l}(x_N)\overline{\phi}_N(x_{i-r+l}), \quad \text{with } r \in \{0,\dots,k\}, \tag{A.3}$$

where the check indicates the polynomial approximation of the solution. The coefficients $c^{\mp}_{k,r,l}(x_N)$ encapsulate the grid-dependent deconvolution and interpolation operator, which is independent of ϕ and can be computed as described in Shu [96].

Next, and drawing inspiration from the weighted essentially non-oscillatory (WENO) scheme of Shu [96], ALDM considers a non-linear combination of the above-described interpolation polynomials for the reconstruction of the solution at the cell faces. Instead of maximizing accuracy, however, the deconvolution is regularized by limiting the degree k of the local approximation polynomials to $k \leqslant K = 3$ and allowing all polynomials of degree $1 \leqslant k \leqslant K$ to contribute to the reconstructed solution. That is,

$$\breve{\phi}^{\mp}_{k}(x_{j\pm1/2}) = \sum_{k=1}^{K}\sum_{r=0}^{k-1} \omega^{\mp}_{k,r}(\gamma_{k,r},\overline{\phi}_N)\breve{g}^{\mp}_{k,r}(x_{j\pm1/2}), \tag{A.4}$$

where each contribution is dynamically weighted by $\omega^{\mp}_{k,r}(\gamma_{k,r},\overline{\phi}_N)$. Weights are defined as

$$\omega^{\mp}_{k,r}(\gamma_{k,r},\overline{\phi}_N) = \frac{\gamma_{k,r}\beta_{k,r}(\overline{\phi}_N)}{\sum_{s=0}^{k-1}\gamma_{k,s}\beta_{k,s}(\overline{\phi}_N)}, \tag{A.5}$$

with $\gamma_{k,r}$ representing free-model parameters that are exploited to control error cancellations. The functional $\beta_{k,r}$ is defined as

$$\beta_{k,r}(\overline{\phi}_N) = \left(\varepsilon_\beta + \sum_{l=-r}^{k-r-2}\left(\overline{\phi}_{i+m+l} - \overline{\phi}_{i+m}\right)^2\right)^{-2}, \tag{A.6}$$

where $\varepsilon_\beta = 10^{-151}$ and the summation term measures the smoothness of the grid function within the respective stencil. This provides a non-linear adaptation of the deconvolution [223].

The procedure outline above results in a hierarchy of reconstructions with increasing order of accuracy, see (A.4). These reconstructions are then combined to form the final reconstruction:

$$\breve{\phi}^{\mp}(x_{j\pm1/2}) = \sum_{k=1}^{K}\alpha_k\breve{\phi}^{\mp}_{k}(x_{j\pm1/2}), \quad \text{with } K = 3. \tag{A.7}$$

Note that the weights α_k introduce additional degrees of freedom for SGS modeling, a feature not exploited in the original ALDM formulation for incompressible flows [71].

For an efficient implementation of the described reconstruction step, which is here applied to the cell-averaged density $\overline{\rho}$, velocity $\overline{\boldsymbol{u}}$, pressure $\overline{p}$ and internal energy $\overline{\rho e}$, the reader is referred to Hickel and Adams [224].

Numerical flux function

The hyperbolic flux $\boldsymbol{C} + \boldsymbol{H}$ is considered for implicit SGS modeling in the ALDM framework, see (2.1), while the diffusive flux $\boldsymbol{D}$ is not exploited for modeling purposes [71]. The employed numerical flux function for the hyperbolic fluxes has the general form

$$\breve{F}_{j\pm1/2} = F\left(\frac{1}{2}\left(\breve{\phi}^{+} + \breve{\phi}^{-}\right)\right) - R \cdot \left(\breve{\phi}^{+} - \breve{\phi}^{-}\right). \tag{A.8}$$

The first term corresponds to the physical Navier-Stokes flux. For maximum order of consistency it is computed from the mean of both reconstructions of the unfiltered solution at the considered cell face, which differs from classic numerical flux functions, such as the Lax-Friedrichs scheme where the flux is averaged [225]. The difference between both interpolants is then exploited in the second term as an estimate of the local truncation error. Non-linear numerical dissipation is controlled by R, which can take the form of any non-negative, shift-invariant functional of $\overline{\phi}_N$ and $\breve{\phi}_N$, with appropriate units. For physical SGS modeling, the dissipation function R needs to be defined specifically for each individual differential equation.

The approximation of the numerical convective flux for the continuity, momentum and energy equations employed in ALDM is, respectively

$$\breve{C}_i^{\rho} = \breve{u}_i^{*}\frac{\breve{\rho}^{+} + \breve{\rho}^{-}}{2} - R_i^{\rho}(\breve{\rho}^{+} - \breve{\rho}^{-}), \tag{A.9}$$

$$\breve{C}_i^{\rho u_k} = \breve{C}_i^{\rho}\frac{\breve{u}_k^{+} + \breve{u}_k^{-}}{2} - R_i^{\rho u}\frac{\breve{\rho}^{+} + \breve{\rho}^{+}}{2}(\breve{u}_k^{+} - \breve{u}_k^{-}), \tag{A.10}$$

$$\breve{C}_i^{\rho e} = \breve{u}_i^{*}\frac{\widetilde{\rho e}^{+} - \widetilde{\rho e}^{-}}{2} + \frac{\breve{u}_k^{+} + \breve{u}_k^{-}}{2}\left(\breve{C}_i^{\rho u_k} - \frac{\breve{u}_k^{+} + \breve{u}_k^{-}}{4}\breve{C}_i^{\rho}\right) - R_i^{\rho e}(\breve{\rho e}^{+} - \breve{\rho e}^{-}), \tag{A.11}$$

where the transport velocity $\breve{u}_i^{*}$ is defined as

$$\breve{u}_i^{*} = \frac{\breve{u}_k^{+} + \breve{u}_k^{-}}{2} - \frac{\alpha_3}{\breve{c}}\frac{\breve{p}_3^{+} - \breve{p}_3^{-}}{\breve{\rho}_3^{+} + \breve{\rho}_3^{-}} \tag{A.12}$$

to ensure pressure-velocity coupling, see appendix B in Hickel *et al.* [71]. The subscript 3 in (A.12) refers to the third order reconstruction polynomial, and $\breve{c}$ is the maximum speed of sound in the adjacent cells.

A

Additionally, the pressure flux is straightforwardly defined as

$$\breve{\boldsymbol{H}}_i = \begin{bmatrix} 0 \\ \delta_{i1}(\breve{p}^+ + \breve{p}^-)/2 \\ \delta_{i2}(\breve{p}^+ + \breve{p}^-)/2 \\ \delta_{i3}(\breve{p}^+ + \breve{p}^-)/2 \\ \breve{u}_i^*(\breve{p}^+ + \breve{p}^-)/2 \end{bmatrix}. \tag{A.13}$$

The only remaining item is then the definition of the dissipation matrix, which in ALDM takes the form

$$\boldsymbol{R}_i = \begin{bmatrix} R_i^\rho \\ R_i^{\rho u} \\ R_i^{\rho u} \\ R_i^{\rho u} \\ R_i^{\rho e} \end{bmatrix} = \begin{bmatrix} \sigma^\rho \mid \breve{u}_i^+ - \breve{u}_i^- \mid \\ \sigma^{\rho u} \mid \breve{u}_1^+ - \breve{u}_1^- \mid \\ \sigma^{\rho u} \mid \breve{u}_2^+ - \breve{u}_2^- \mid \\ \sigma^{\rho u} \mid \breve{u}_3^+ - \breve{u}_3^- \mid \\ \sigma^{\rho e} \mid \breve{u}_i^+ - \breve{u}_i^- \mid \end{bmatrix}, \tag{A.14}$$

where the σ coefficients are case-independent model parameters of order 1. As discussed in Hickel *et al.* [226], this definition of the dissipation matrix ensures consistency of the numerical flux with ALDM for incompressible turbulence and passive scalar mixing in the limit of $M \to 0$.

The free parameters $\{\alpha, \gamma, \sigma\}$ contained in the reconstruction scheme and the employed numerical flux function are therefore utilized for modeling purposes, to ensure that the spatial truncation error of the discretization acts as a physically consistent model for SGS turbulence and discontinuities. As discussed in Hickel *et al.* [71], the values of α and γ are directly adopted from the incompressible ALDM framework on the grounds of Morkovin's hypothesis. These values were systematically obtained by Hickel *et al.* [223] using reinforcement learning with an evolutionary optimization algorithm that minimized the difference between the spectral numerical viscosity of ALDM and the eddy viscosity from eddy-damped quasi-normal Markovian theory for isotropic turbulence. The σ parameters in (A.14), on the other hand, are identical to those obtained for passive scalars [226], with the exception of $\sigma^{\rho u}$, which is recalibrated using a procedure outlined in Hickel and Larsson [227] to account for the difference between the incompressible and compressible flux functions. All model parameters are given in table I of Hickel *et al.* [71].

Finally, the present method is made shock-capturing by introducing an additional term into the dissipation matrix,

$$\boldsymbol{R}_i = \begin{bmatrix} \sigma^\rho \mid \breve{u}_i^+ - \breve{u}_i^- \mid \\ \sigma^{\rho u} \mid \breve{u}_1^+ - \breve{u}_1^- \mid \\ \sigma^{\rho u} \mid \breve{u}_2^+ - \breve{u}_2^- \mid \\ \sigma^{\rho u} \mid \breve{u}_3^+ - \breve{u}_3^- \mid \\ \sigma^{\rho e} \mid \breve{u}_i^+ - \breve{u}_i^- \mid \end{bmatrix} + f_s \frac{\mid \breve{u}_i^* \mid + \mid \breve{u}_i^+ - \breve{u}_i^- \mid}{2} \begin{bmatrix} 1 \\ 1 \\ 1 \\ 1 \\ 1 \end{bmatrix}, \tag{A.15}$$

which is only activated at strong discontinuities, providing additional dissipation.

Its activation is controlled by f_s, which corresponds to the following shock sensor[1]

$$f_s = \begin{cases} 1, & \dfrac{|\nabla \cdot \overline{\boldsymbol{u}}|}{0.01\|\nabla \times \overline{u}\|_1 + \|\mathbf{I} \odot \nabla \overline{u}\|_1 + 10^{-15}} \geqslant 0.98 \text{ and } \nabla \cdot \overline{\boldsymbol{u}} < 0 \\ 0, & \text{else} \end{cases} . \quad \text{(A.16)}$$

As outlined in Hickel *et al.* [71], the resulting ALDM flux maintains low Mach number consistency and yields essentially non-oscillatory solutions at strong discontinuities. The physical amplification of disturbances passing through shock waves is also addressed by incorporating f_s in the α parameters, as shown in their publication.

[1] S. Hickel, personal communication.

B

Analyisis of digital filter inflow generation methods

Several improvements of the accuracy and performance of the digital filter turbulent inflow generation technique are discussed in this chapter and evaluated for wall-resolved LES of a compressible turbulent boundary layer. This part of the PhD work is presented here in order to maintain the concise form of the main thesis.

B.1. The digital filter technique

Turbulence-resolving simulations provide the highest accuracy for the study of complex phenomena in wall-bounded turbulence and associated flow-control applications. However, quality and reliability of the resulting data strongly depends on the accuracy of the employed boundary conditions. Of particular relevance is the inflow boundary condition, which dictates the downstream flow evolution. Inappropriate inflow data can lead to excessively long spatial transients until the turbulent flow is fully developed. This naturally increases the computational domain size required for a given flow problem, which, in the worst case, can become intractable in combination with high spatio-temporal resolution requirements of LES and DNS.

For these reasons, a vast variety of turbulence generation methodologies have emerged in the past decades [228, 229]. Besides data-driven approaches, where the inflow condition stems from a detailed data base, a reduced-order model of the same flow [230] or, more recently, from deep learning models [231], turbulence generation techniques are classified into recycling methods and synthetic methods. Recycling methods extract the required inflow state from an auxiliary simulation or directly from a downstream plane with appropriate re-scaling [232, 233]. Synthetic inflow methods, on the other hand, are based on constraining random fluctuations to satisfy prescribed statistics and recover a target coherence or energy spectrum [234–236]. Comprehensive reviews of the available techniques within these two categories are provided by Tabor and Baba-Ahmadi [237], Wu [228] and Dhamankar *et al.* [229].

The content of this appendix chapter has been published as: L. Laguarda and S. Hickel. Assessment of Reynolds number effects in supersonic turbulent boundary layers, *Comput Fluids* **268**, 2024.

The digital filter technique used in the present work falls within the latter category [125, 235]. As already introduced in chapter 2, this technique is essentially based on imposing target spatial and temporal correlations on random fields via explicit filtering. The appropriately correlated and scaled random fields are then added to a given target mean fields to generate the instantaneous inflow data. The required knowledge of the target flow is therefore limited to mean flow quantities, auto and cross correlations of their fluctuations, and approximate integral spatio-temporal scales for a given autocorrelation function. Contrary to recycling/re-scaling methods, digital-filter techniques do not introduce any undesired low-frequency or long-wavelength structures. This is an attractive feature of the digital filter that combined with its straightforward integration in numerical solvers have made the technique a common choice for the simulation of several flows of practical interest [23, 34, 108, 238, 239].

Despite being widely adopted, the digital filter is far from being the ideal turbulence generator [229]. An important drawback is the lack of proper phase information of realistic turbulent eddies, which inevitably leads to a finite spatial transient during which physical flow structures develop [240]. The resulting adaptation or induction length, that is, the distance required for turbulence to recover from the modelling errors, depends also on the metric of interest, i.e., whether one is primarily interested in realistic mean profiles, or also in pressure fluctuations, Reynolds stresses, etc. [241]. In wall-bounded turbulence, this transient typically manifests as a significant dip in the skin-friction distribution [239], which extends over approximately 5 boundary layer thicknesses and is followed by a spatial transient of approximately 10-20 boundary layer thicknesses until agreement with most reference correlations is attained. As indicated by Wenzel *et al.* [108] and confirmed by Huang *et al.* [115], the induction length can be even longer when defined based on the compliance with the von Kármán integral equation. In compressible flows, the spatial transient additionally results in strong pressure disturbances that substantially contaminate the downstream acoustic field [239, 242].

In an attempt to mitigate some of the aforementioned deficiencies, different improvements of the digital filter technique have been considered [229]. For instance, Di Mare *et al.* [243] and Veloudis *et al.* [126] investigated the effect of spatially varying scales at the inflow plane, instead of constant scales throughout, which led to a better prediction of downstream turbulence profiles. Other strategies involve sponge zones located after the digital filter boundary as means to damp spurious acoustic noise from the non-equilibrium flow [239] or directly forcing the solution towards the expected developed state [244]. More recently, Ceci *et al.* [241] investigated the effect of suppressing streamwise velocity fluctuations at the inflow plane, which led to a faster relaxation of pressure fluctuations. Interestingly, this counter-intuitive approach did not incur additional penalties in the development of the Reynolds stresses, at least in the low supersonic regime.

Therefore, much potential exists for improving the capabilities of the digital filter method. However, proposed improvements have not been investigated systematically and they appear scattered over different studies (which involve different applications, flow conditions and numerical strategies). This makes it hard for re-

searchers to assess, based on an acceptable level of accuracy, whether any additional modifications of the digital filter technique are worth the extra effort. At the same time, few studies attempt to explain the observed deficiencies from a flow physics perspective, which, in our opinion, is key for further refinement of the method.

The purpose of this chapter is thus to systematically assess the efficacy of several methods that can improve the accuracy and performance of the digital filter technique based on a compressible turbulent boundary layer benchmark and to explain the observed differences upon inspection of the dominant terms in the transport equations for the Reynolds stresses. Improvements of accuracy motivated by flow physics include a novel filter kernel function for the transversal directions and varying target length scales with wall-distance. Following a recent suggestion of Ceci *et al.* [241], we also consider suppressing streamwise velocity fluctuations at the inflow plane. To further improve the latter method, we asses the potential benefits of preserving the inflow turbulence kinetic energy by amplifying one of the cross-stream Reynolds stresses. In addition, we present selected details of our implementation for massively parallel simulations that reduce the computational cost of the method.

B.1.1. Baseline method

The baseline digital filter method considered in this paper is based on the method proposed by Xie and Castro [125] for incompressible flows, which is an extension of the original work of Klein *et al.* [235] and proceeds as follows:

1. At every time step, three slices of uncorrelated Gaussian random numbers $\mathcal{S}_i$, with $i = \{1, 2, 3\}$, are generated. Each slice has zero mean and unit variance, and is uncorrelated from the others.

2. A two-dimensional spatial filter is then applied to each random slice in order to impose spatial coherence. The two-dimensional filter kernel is defined as the tensor product of two one-dimensional kernels that are based on the following exponential correlation function

$$R(r) = \exp\left(-\frac{\pi r}{2I_L}\right), \tag{B.1}$$

where I_L is the target integral length scale, which can have different values for each random field, direction, and wall distance. In discrete form, and for a constant grid spacing h with $I_L = nh$ and $r = kh$, equation (B.1) becomes

$$R(kh) = \exp\left(-\frac{\pi|k|}{2n}\right). \tag{B.2}$$

To approximate the discrete filter coefficients, namely b_k, Xie and Castro [125] propose the following relations

$$b_k = \widetilde{b}_k \left(\sum_{j=-N}^{N} \widetilde{b}_j^2\right)^{-1/2}, \quad \text{and} \quad \widetilde{b}_k \approx \exp\left(-\frac{\pi|k|}{n}\right), \tag{B.3}$$

where N is the filter support, taken as $N \geqslant 2n$. The filtered fields are denoted as $\tilde{\mathcal{S}}_i$.

3. Temporal coherence is also assumed of exponential form, and is achieved via

$$\mathcal{G}_i(t) = \mathcal{G}_i(t - \Delta t)\, \exp\left(\frac{-\pi \Delta t}{2 I_T}\right) + \tilde{\mathcal{S}}_i(t) \left[1 - \exp\left(\frac{-\pi \Delta t}{I_T}\right)\right]^{1/2}, \tag{B.4}$$

where I_T is the target time scale and $\mathcal{G}_i$ are the space-time correlated random fields.

4. The inflow data $\widetilde{u}_i(t) = \widetilde{U}_i + u_i''(t)$ is composed from target mean velocity $\widetilde{U}_i$ and instantaneous fluctuations $u_i''(t) = a_{ij}\mathcal{G}_j(t)$, where a_{ij} is the Cholesky decomposition of the target Reynolds stress tensor. This transformation, originally proposed by Lund *et al.* [232], scales the slice variance (originally unity) to provide the target second-order statistics.

We refer the reader to the original publications [125, 235] for additional details.

B.1.2. Implementation for compressible flows

For compressible simulations, thermodynamic fluctuations are also required at the inflow boundary. As commonly done in previous works [34], we use the strong Reynolds analogy (SRA) to relate velocity and temperature fluctuations of a perfect gas

$$T'' = -(\gamma - 1) M^2 \frac{\overline{T}}{\widetilde{U}_1} u_1'', \tag{B.5}$$

where u_1'' is the streamwise velocity fluctuation given by the digital filter. The mean streamwise velocity $\widetilde{U}_1$ and temperature $\overline{T}$ are inputs, and $M = \widetilde{U_1}/\sqrt{\gamma \mathcal{R} \overline{T}}$ is the local Mach number, γ the specific heat capacity ratio, and $\mathcal{R}$ the specific gas constant. Density and temperature fluctuations are related through the perfect gas law at constant pressure

$$\rho' = -\frac{\overline{\rho}}{\overline{T}} T'' \,. \tag{B.6}$$

The mean density $\overline{\rho}$ is also provided as input. Note that this method approximates an inflow state with zero pressure fluctuations.

All inflow conditions generated by the digital filter are then prescribed at the inflow plane via a characteristic-based method in order to minimize spurious noise [124].

B.1.3. Improvements of accuracy

Xie and Castro [125] propose the exponential form (B.1) for the velocity correlation function. However, an exponential function is a very poor approximation for the transversal velocity correlation functions [113], even when optimized length scales are employed. For this reason, we consider a correlation function of the form

$$R(r) = \left(1 - \frac{r}{I_L}\right) \exp\left(-\frac{r}{I_L}\right), \tag{B.7}$$

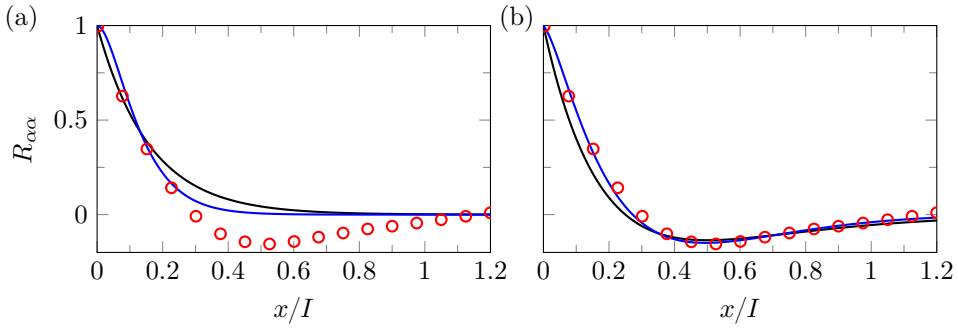

Figure B.1: (a) Exponential correlation suggested by Xie and Castro [125], and (b) proposed correlation function for transversal directions. Legend: (black line) target correlation; (blue line) correlation provided by the approximated digital filter kernel; (red markers) spanwise u' autocorrelation function computed from DNS data of a supersonic TBL at Mach 2.0 and $y/\delta = 0.5$ (from Pirozzoli and Bernardini [113]).

which includes negative values and thus much better resembles transversal correlation functions. We propose the following relation

$$\widetilde{b}_k \approx \left(1 - \left(\frac{|k|}{n}\right)^{0.3}\right) \exp\left(-\frac{|k|}{n}\right), \tag{B.8}$$

for the calculation of the discrete filter coefficients in the transversal directions (e.g. for the spanwise coherence of u''), which approximates the target correlation function (B.7) well. In normal directions (e.g., for the spanwise coherence of w''), the exponential correlation function proposed by Xie and Castro [125] is still employed since it is a good approximation of the target spatial coherence, see Pirozzoli and Bernardini [113].

Figure B.1 compares the exponential correlation suggested by Xie and Castro [125], in figure B.1(a), with the correlation function that we propose for the transversal directions, see figure B.1(b). Black lines denote the corresponding target correlation functions whereas the actual correlations provided by the digital filter with approximated filter coefficients is indicated with a blue line. The length scale is set to $I_z = 0.25\delta$, which is the value reported by Pirozzoli and Bernardini [113] for the autocorrelation of u' in spanwise direction at $y/\delta = 0.5$ (see figure 26(b) in their publication). The autocorrelation function that Pirozzoli and Bernardini [113] obtain is also included for reference. Figure B.1 shows that our model correlation (B.7) for tangential directions as well as the actual correlation provided by digital filter with the approximated filter kernels (B.8) are in much better agreement with the reference DNS data than the purely exponential relations suggested by Xie and Castro [125].

As means to further increase the accuracy of the inflow data, we employ the zonal approach proposed by Veloudis *et al.* [126] whereby the digital filter inflow plane is divided in multiple regions with different target scales. The considered regions and their corresponding scales are presented in section B.2.

In addition to modifications that are directly motivated by improving the physical realism of the imposed velocity fluctuations, we also analyse a modification recently proposed by Ceci *et al.* [241], who found that suppressing streamwise velocity fluctuations at the inflow plane effectively reduces spurious pressure perturbations. Since the inflow turbulence kinetic energy $k_{in} = \widetilde{u_i'' u_i''}/2$ would be highly reduced by setting $u_1'' = 0$, the potential benefits of preserving k_{in} by amplifying one of the cross-stream Reynolds stresses is also assessed; that is, we prescribe for the wall-normal stress $\widetilde{u_2''^2}(y) = 2k_{in}(y) - \widetilde{u_3''^2}(y)$ while the spanwise stress $\widetilde{u_3''^2}(y)$ remains unaltered, and vice-versa.

Lastly, since pressure fluctuations are an important element in turbulent flows [245, 246], we also considered generating both pressure and density fluctuations from the temperature field under the assumption of isentropic flow. For a calorically perfect gas, the isentropic condition implies that $\rho \propto T^{1/(\gamma-1)}$ which leads to

$$\frac{\rho'}{\overline{\rho}} = \left(1 + \frac{T''}{\overline{T}}\right)^{\dfrac{1}{\gamma - 1}} - 1, \tag{B.9}$$

and the corresponding pressure fluctuation then follows from the ideal gas law. Results for this approach, however, are not reported in this paper since no significant changes of the results were observed compared to the SRA-based method, where pressure fluctuations are neglected.

B.1.4. Improvements of performance

The generation of high-quality random fields can be a major contribution to the computational cost. We have therefore implemented a highly optimized, parallel version of the Mersenne Twister MT19937 of Matsumoto and Nishimura [247] for the generation of single-precision Gaussian random numbers. The compute load is equally distributed over all processes, and each process initializes its random stream at a different positions along the sequence. The very long period of the stream avoids unwanted correlations for all practical purposes. Particular attention was put on optimizing memory alignment and vectorization. All operations on the random fields and velocity fluctuations are performed in single precision and only the final inflow data is stored in double precision.

In order to further reduce the computational costs incurred by the method, we consider updating the inflow data at a prescribed time interval instead of every time step. We propose to choose the update interval as $1/20^{th}$ of the smallest time scale of the input dataset, which for the considered benchmark case corresponds to approximately 25 time-steps. At the intermediate time-steps, linear interpolation is used between the corresponding digital filter solutions. With these measures, the computational cost of the digital filter boundary condition amounts to about 1% of the total.

Table B.1: Details of the investigated digital filter modifications

Case	Zones	R_t	update interval	u''_{in} supressed	k_{in} preserved	Legend
R0	3	$\exp(-\pi r/(2I_L))$	1 step	No	Yes	
A1	3	$(1-r/I_L)\exp(-r/I_L)$	1 step	No	Yes	
A2	3	$(1-r/I_L)\exp(-r/I_L)$	25 steps	No	Yes	
A3	1	$(1-r/I_L)\exp(-r/I_L)$	1 step	No	Yes	
B1	3	$(1-r/I_L)\exp(-r/I_L)$	1 step	Yes	Yes, via $\overline{v''^2}$	
B2	3	$(1-r/I_L)\exp(-r/I_L)$	1 step	Yes	Yes, via $\overline{w''^2}$	
B3	3	$(1-r/I_L)\exp(-r/I_L)$	1 step	Yes	No	

Table B.2: Target length scales per region, velocity component and spatial direction.

Zone	Range	L_{ref}	I_x/L_{ref}			I_y/L_{ref}			I_z/L_{ref}		
			u	v	w	u	v	w	u	v	w
1	0 to $y^+ = 100$	l^+_{in}	400	100	60	75	100	50	100	50	100
2	$y^+ = 100$ to $0.2\delta_{0,in}$	$\delta_{0,in}$	1.2	0.2	0.3	0.2	0.2	0.15	0.2	0.15	0.3
3	above $0.2\delta_{0,in}$	$\delta_{0,in}$	0.9	0.3	0.3	0.3	0.3	0.25	0.35	0.25	0.35

B.2. Benchmark case and numerical setup

The benchmark case considered is a spatially developing turbulent boundary layer at Mach 2.0, and corresponds to case $\mathcal{T}_2$ in chapter 5 - for a complete description of the study case, see section 5.2. The employed computational domain is also the same as case $\mathcal{T}_2$; the only difference lies in the treatment of the digital filter boundary. Table B.1 includes a summary of the performed simulations with their corresponding digital filter settings. The reference case R0, which involves the standard digital filter implementation for compressible flows, considers exponential correlations in all directions. All cases except for A3 consider three different zones at the inflow plane, corresponding to the inner region, the overlap region, and the outer region of the boundary layer. The target length scales, which differ for each zone, are given in table B.2. Case A3, on the other hand, only includes one zone with target length scales corresponding to the largest values in table B.2 per direction and velocity component. Table B.1 also states the employed correlation function in tangential directions (R_t) and the time-step interval at which new inflow data is generated. For cases B1 to B3 streamwise velocity fluctuations are suppressed at the inflow plane, and additional information is provided regarding the treatment of the turbulence kinetic energy at the inflow k_{in}. For later reference, the employed line legend in the upcoming figures is also included in table B.1.

All simulations were performed with the numerical method described in section 2.1.2 and proceeded as follows. First, an initial transient of 10 FTT of the full

domain length was simulated to ensure a fully developed turbulent flow in statistical equilibrium. This solution interval was discarded from the analysis. After this transient, simulations were integrated for another 12 FTT of the full domain length. During this second interval, statistics samples were collected at a sampling interval of $\Delta t u_\infty/\delta_{0,in} \approx 0.013$ and averaged in spanwise direction and in time.

B

B.3. Results and discussion

In wall-bounded flows, a primary metric to assess the performance of inflow turbulence generators is the evolution of the skin-friction coefficient. This is shown in figure B.2(a) against the streamwise coordinate $(x - x_{in})/\delta_{0,in}$, where x_{in} is the location of the inflow plane. As observed, all cases exhibit a characteristic dip in $\langle C_f \rangle$ right after the inflow that is recovered within approximately $5\delta_{0,in}$. The strength of the dip clearly depends on the digital filter settings; for instance case B1 additionally exhibits an initial overshoot. See table B.1 for details on the employed digital filter settings per simulation as well as the line legend.

While an apparent equilibrium behavior is observed after the transient region of $5\delta_{0,in}$, differences between the skin-friction distributions remain visible for the investigated cases. For instance, the $\langle C_f \rangle$ distributions for cases A1 and A2 are very similar to that for the baseline case R0, while case A3 shows discrepancies that include larger skin-friction magnitudes. This suggests a non-negligible effect of the excessively large scales at the wall, which is retained throughout the computational domain. Suppressing streamwise velocity fluctuations at the inflow also influences the solution noticeably, with case B3 exhibiting the lowest $\langle C_f \rangle$ values. Note that k_{in} is not preserved for case B3.

The van Driest II transformation [128] is employed to remove Mach number effects and enable comparison with reference incompressible correlations. That is, skin-friction and momentum thickness Reynolds number Re_θ are reduced to their incompressible counterparts, $C_{f,inc}$ and $Re_{\theta,inc}$, by applying the compressible transformation outlined in equation (5.1). Resulting distributions are shown in figure B.2(b) together with the empirical correlation functions of Kármán-Schoenherr (denoted by KS) and of Smits *et al.* [132] (denoted by S). Combined, these correlations indicate a range of plausible solutions, which appears shaded in gray in the figure. In agreement with the previous discussion, cases A3 and B3 noticeably deviate from the expected behavior. The same can be said for case B2, which only recovers the expected skin-friction distribution at high values of $Re_{\theta,i}$, i.e., in the vicinity of the outflow plane. On the other hand, cases R0, A1, A2 and B1 seem to recover the modelling errors faster and exhibit quasi-equilibrium behavior from $Re_{\theta,i} \approx 3400$ onward. The fact that case B1 is in very good agreement with the reference correlations, while cases B2 and particularly B3 deviate substantially from them, highlights the beneficial effect of preserving the target k_{in} by amplifying $\widetilde{v''^2}$. This is expected since the wall-normal stress, as opposed to $\widetilde{w''^2}$, plays a key role in the turbulence generation cycle [248]. We also note that the marginal differences between cases A1 and A2 suggest that spurious interpolation errors do not seem to meaningfully alter the near-wall turbulence development.

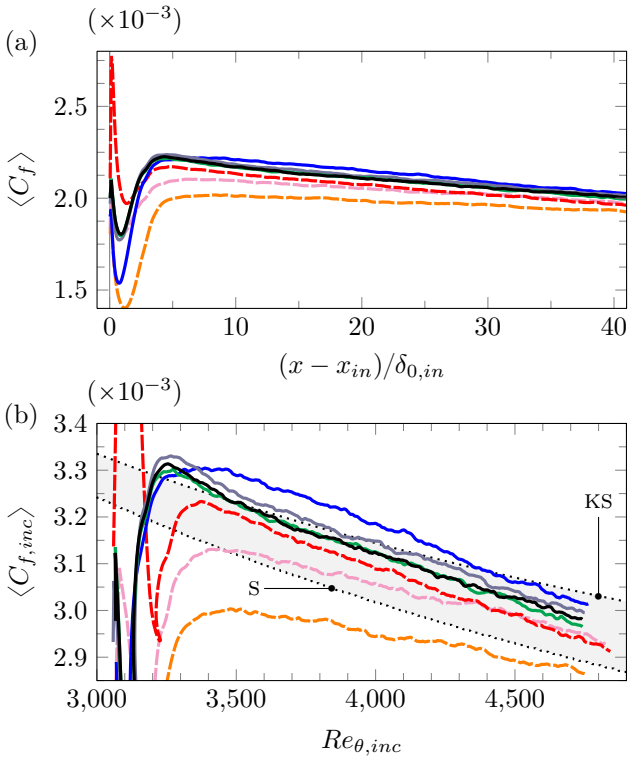

Figure B.2: (a) Streamwise evolution of the time- and spanwise-averaged skin-friction, and (b) equivalent incompressible skin-friction as a function of the transformed momentum-thickness Reynolds number. The grey area in (a) is bounded by the correlation of Kármán-Schoenherr (KS) and the correlation of Smits *et al.* [132] (S). See table B.1 for details on the employed digital filter settings per simulation as well as the line legend.

In order to better identify the fraction of the computational domain where turbulence is fully established, we also inspect the compliance with the von Kármán integral equation [108, 249], i.e.,

$$\langle C_f \rangle = 2\frac{d\theta}{dx} \tag{B.10}$$

which relates the growth of the momentum thickness to the local skin-friction coefficient. Note that the above formulation neglects the integral contribution of the Reynolds stresses, as their streamwise derivatives are supposed to contribute negligibly in a fully developed equilibrium boundary layer. This approximation naturally does not hold in the initial transient region, where turbulence is rapidly recovering from modelling errors. An effective compliance evaluator is thus the ratio $\langle C_f \rangle / (2d\theta/dx)$, which should approach unity as the boundary layer returns to an equilibrium state.

The streamwise evolution of this parameter is shown for all cases in figure B.3

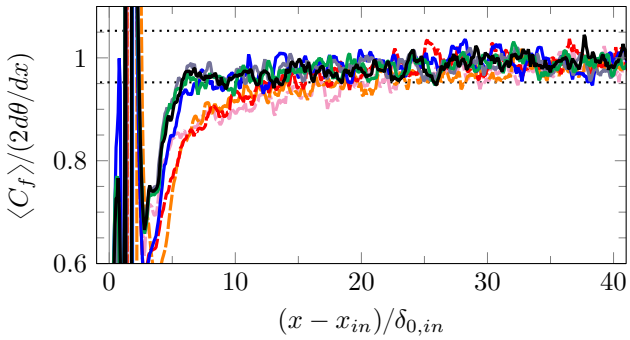

Figure B.3: Compliance with the von Kármán integral equation. Dotted lines indicate ±5% deviation.

together with a ±5% tolerance band. Despite the residual noise, two clear trends can be observed. On the one hand, the baseline case R0 and cases A1 to A3 satisfy equation (B.10) within 5% accuracy after a transient of about $5\delta_{0,in}$ from the inflow plane. On the other hand, cases B1 to B3 (in which u'' is suppressed at the inflow) reach the same level of accuracy only $\sim 10\delta_{0,in}$ from the inflow plane, which is effectively double the distance. Therefore, based on the compliance with the von Kármán integral equation, the nonphysical suppression of streamwise velocity fluctuations at the inflow plane results in a longer adaptation length.

Next, we assess the effect of the considered digital filter modifications on the wall-pressure fluctuations. As these fluctuations are influenced by inner and outer layer eddies [250], they provide a good indication of the overall boundary layer development. The spanwise evolution of the wall-pressure fluctuations is shown in figure B.4(a). It is evident that all cases systematically over-predict the pressure fluctuations near the inflow. Suppressing streamwise velocity fluctuations has a clear benefit according to this metric. Cases B1 to B3 exhibit the fastest relaxation of the wall-pressure fluctuations. The method proposed by Ceci *et al.* [241], case B3, predicts the lowest fluctuation intensities. The baseline case R0 and cases A1 to A3, on the other hand, show a slower recovery from the increased wall-pressure fluctuations at the inflow plane. Also note that case A3, the only case that considers exponential correlation functions in all directions and velocity components, results in the largest fluctuation intensities throughout the computational domain.

Empirical evidence suggests a logarithmic Re_τ-dependence of the wall-pressure fluctuations when normalized using inner variables, i.e., the wall shear stress τ_w [246, 250]. To verify whether that is also the case in our LES data, we compare the corresponding inner-scaled wall-pressure fluctuations against the empirical correlation of Farabee and Casarella [154]. This comparison is shown in figure B.4(b). In agreement with previous observations, cases B1 and B3 closely follow the expected behavior after the initial transient. This is not the case for the baseline case R0 and cases A1 to A3, which seem to asymptotically approach the reference correlation but exhibit larger fluctuations intensities throughout the computational domain. Nevertheless, cases A1 and A2 with our custom transversal correlation function

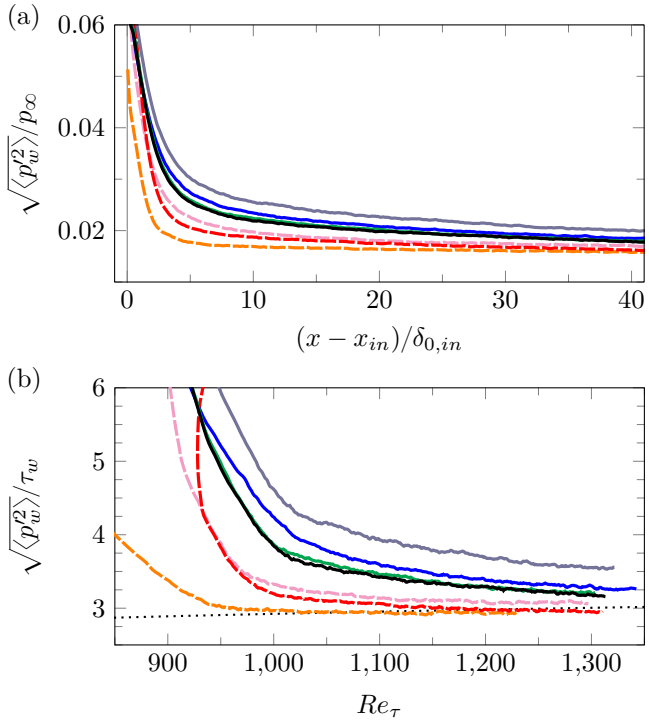

Figure B.4: (a) Streamwise evolution of the time- and spanwise-averaged wall-pressure fluctuations, and (b) inner-scaled wall-pressure fluctuations as a function of the friction Reynolds number. Dotted lines indicate the semi-empirical correlation of Farabee and Casarella [154]

perform better than the baseline case R0 and case A3. The very close agreement of the results for A1 and A2 further justifies updating inflow data at prescribed time intervals to reduce computational costs.

We now turn our attention to the evaluation of the Reynolds stresses. First, the evolution of the peak values for the streamwise and shear stresses are considered. The former is indicative of the near wall streaks, which make up the stress-producing cycle that sustains turbulence [248]. The peak shear stress, on the other hand, is associated with quasi-logarithmic behavior of the mean velocity profile and reflects a multi-scale momentum transfer [251, 252]. The streamwise evolution of the inner-scaled streamwise stress peak is shown in figure B.5(a) for all cases. As observed, the corresponding distributions for the baseline case R0 as well as cases A1, A2, B1 and B2 effectively yield identical values after $10\delta_{0,in}$ from the inflow plane. Furthermore, these distributions closely follow the empirical relation of Ceci *et al.* [241] derived from their DNS data, which relates the peak streamwise stress magnitude with the friction Reynolds number (not shown here). The peak streamwise stress for case B3, in turn, shows a much slower recovery as indicated by the dashed orange line in figure B.5(a). This further highlights the importance of preserving the turbulence kinetic energy at the inflow plane, which did not happen for this case. Therefore,

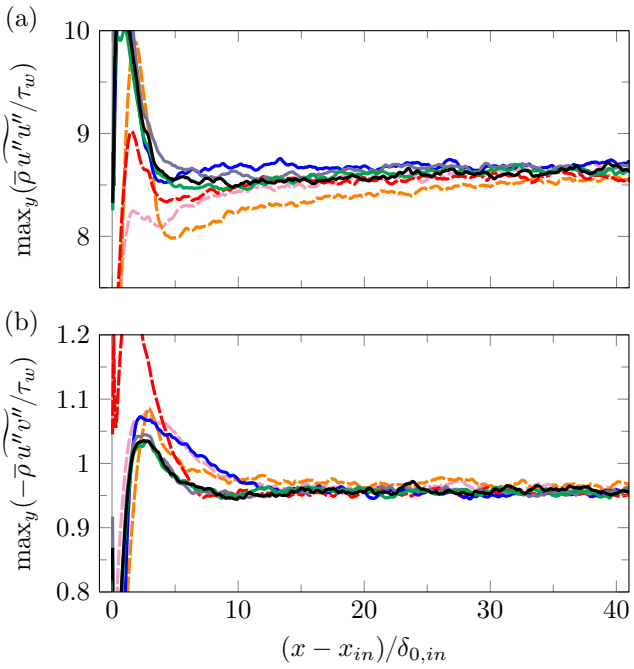

Figure B.5: Streamwise evolution of normalized Reynolds stresses: (a) streamwise stress, and (b) shear stress.

our results indicate that suppressing u'' can meaningfully hamper the near-wall turbulence development when the inflow turbulence is energy deficient. Figure B.5(b) shows that the evolution of its inner-scaled peak magnitude of the Reynolds shear stress is less affected by the inflow conditions than the streamwise component. As observed, all cases exhibit a constant peak value close to unity after approximately 10-15$\delta_{0,in}$ from the inflow plane. However, cases A1, A2 and B1 exhibit a faster development than the other cases, with an adaptation length of approximately $7\delta_{0,in}$ for this metric.

To this end, conclusions can be drawn about the analysis of the results so far. By comparing the data for cases A1 and A2, it is clear that updating the inflow data at a prescribed time interval does not incur additional penalties, and is therefore desired performance-wise. The addition of multiple inflow regions with varying length scales per region, as done for all cases except for case A3, is also recommended as it leads to a faster relaxation of the local skin-friction and peak magnitudes of the inner-scales Reynolds stresses, see figure B.2 and figure B.5 respectively. The alternative correlation function for the transversal directions defined in equation (B.7) leads to a substantial reduction of the spurious acoustic radiation of the non-equilibrium boundary layer and small improvements for the other metrics. However, if the downstream acoustic field is a priority, suppressing streamwise velocity fluctuations at the inflow plane becomes appealing as it leads to the fastest relaxation of the wall-pressure fluctuation intensity, see figure B.4. Provided that sufficient energy

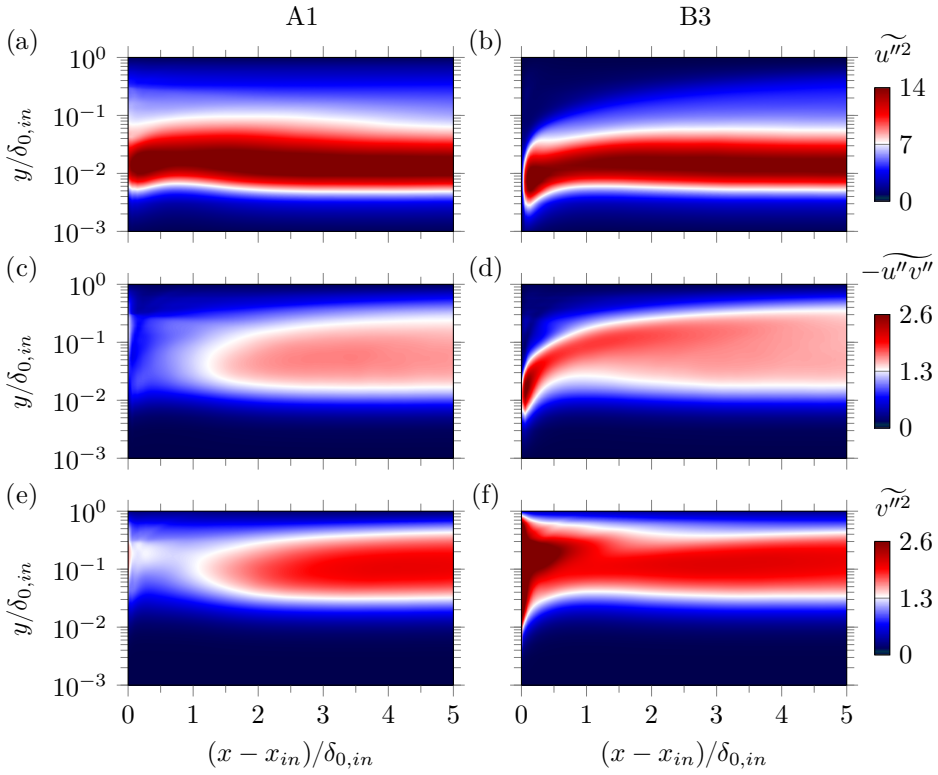

Figure B.6: Streamwise stress, shear stress and wall-normal stress distributions for (left) case A1, and (right) case B1. Stresses are shown normalized with $0.001u_\infty^2$.

is supplied by amplifying the wall-normal Reynolds stress $\widetilde{v''^2}$, our results indicate that the only deficiency of this approach, at least in a qualitative sense, is the poor compliance with the von Kármán integral equation within the first $10\delta_{0,in}$ from the inflow plane.

The question now remains as to what physical mechanisms contribute to a longer adaptation length, and why suppressing streamwise velocity fluctuations at the inflow plane leads to a rapid turbulence development and a quieter downstream flow. To shed some light on these matters, the two-dimensional distributions of the primary Reynolds stresses (i.e., streamwise, wall-normal and shear) and their transport budgets are examined. The former are shown in figure B.6 for cases A1 and B1 near the digital filter boundary to highlight the near-inflow behavior. The streamwise stress fields shown in figures B.6(a) and B.6(b) exhibit the expected differences, i.e., the stress is mostly convected downstream from the inflow plane for case A1 while it is rapidly generated for case B1. As indicated in figure B.5(a), both distributions converge to the same peak $\widetilde{u''^2}$ magnitude within $\sim 10\delta_{0,in}$ from the digital filter boundary. With respect to the other stresses, $-\widetilde{u''v''}$ and $\widetilde{v''^2}$, interesting observations can be made for case A1. As observed in figures B.6(c) and B.6(e), both

stresses initially fall noticeably below the target magnitude for this case, and they progressively recover within $\sim 3\delta_{0,in}$ from the inflow plane. The baseline case R0 as well as cases A2 and A3 also exhibit the exact same behavior near the inflow (not shown here), indicating that this is a characteristic drawback associated with the baseline digital filter implementation for compressible flows. The wall-normal stress for case B1, on the other hand, initially decays but does not significantly undershoot the target value, see figure B.6(f). Therefore, the deliberate amplification of this stress at the digital filter boundary gives superior results during the initial transient. In addition, and similarly to the streamwise stress, the shear stress for this case is also rapidly generated, see figure B.6(d).

The observed behavior near the inflow can be explained by inspecting the dominant terms in the transport equations for the $\widetilde{u''v''}$ and $\widetilde{v''^2}$ Reynolds stresses. The reader is referred to section 6.3.5 of chapter 6 (equation (6.1) in particular) for the definition of such equations and the expressions of the various budget terms mentioned in the following. For the sake of brevity, these are not repeated here.

Starting with the wall-normal stress, we find that the terms that contribute most to its initial decay are those involving the pressure, that is, the pressure transport and pressure-strain correlation terms. For the sake of simplicity, we consider their aggregate effect via the pressure-gradient/velocity correlation term $\Phi_{ij} = \mathcal{D}^p_{ij} + \Pi_{ij}$. The corresponding contribution to the balance of $\widetilde{v''^2}$, i.e., Φ_{22}, is thus shown for cases A1 and B1 in figures B.7(a) and B.7(b), respectively. As observed, Φ_{22} constitutes a sink near the inflow plane in both cases, whereas this term is supposed to be the major source of energy for $\widetilde{v''^2}$ in an equilibrium boundary layer (there is no direct contribution from production, [253]). This could be expected for case B1, since the pressure-strain correlation may be redistributing the energy from the deliberately amplified $\widetilde{v''^2}$ to the other stresses. However, Φ_{22} becoming a sink for case A1 represents an important weakness of the digital filter technique; it fails to realistically account for this term.

Since the production term for $-\widetilde{u''v''}$, namely $\mathcal{P}_{12}$, is directly proportional to $\widetilde{v''^2}$, variations in the latter directly impact the shear stress balance. The production term for the shear stress is shown in figures B.7(c) and B.7(d) for cases A1 and B1, and confirms this correspondence. For case A1, a decay in $-\mathcal{P}_{12}$ near the inflow is clearly visible. For case B1, on the other hand, the amplification of $\widetilde{v''^2}$ leads to a large $-\mathcal{P}_{12}$ close to the digital filter boundary that promotes the generation of $-\widetilde{u''v''}$ instead, see figure B.7(d). Since the main energy sink for the shear stress is $-\Phi_{12}$, we also show the contributions of this term in figures B.7(e) and B.7(f) for the two cases considered. As observed, $-\Phi_{12}$ is very strong in magnitude near the inflow in both cases, and this negative contribution extends throughout most of the boundary layer thickness for case A1. Since $-\Phi_{12}$ exceeds $-\mathcal{P}_{12}$ at the digital filter boundary for this case, $-\widetilde{u''v''}$ is effectively damped as shown in figure B.6(b). The same cannot be said for case B1, which exhibits a net production of shear stress near the wall.

It is also important to note that, while the production term for the streamwise stress is directly proportional to $-\widetilde{u''v''}$, this stress does not exhibit an initial decay

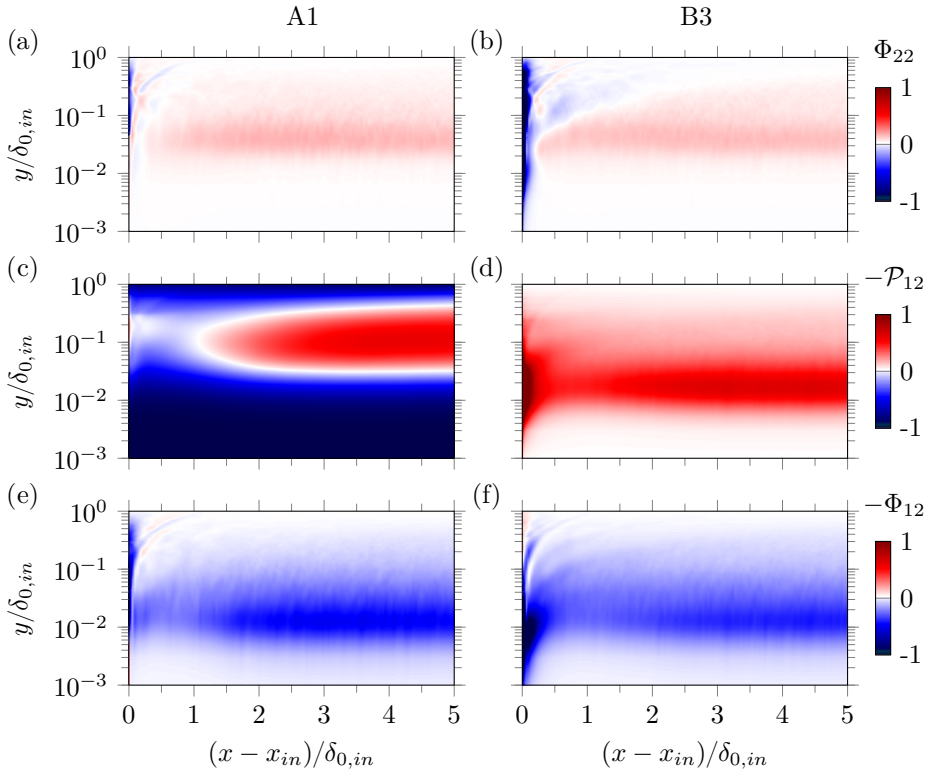

Figure B.7: Pressure-gradient/velocity correlation terms, Φ_{22} and $-\Phi_{12}$, and shear stress production $-\mathcal{P}_{12}$ for (left) case A1, and (right) case B1. Budget terms are normalized with $u_\infty^3/\delta_{0,in}$

at the inflow plane for case A1. In fact, as shown in figure B.5(a), it is initially amplified and then decays towards the expected value. The reason is that the dissipation and pressure-gradient/velocity correlation terms, which are important in balancing production in the buffer and quasi-logarithmic region [175], also exhibit reduced values near the inflow. For instance, Φ_{11}, which is not shown here, is positive near the wall.

Therefore, it is clear that the inability of the digital filter to realistically account for different terms in the Reynolds-stress transport, and in particular those involving the pressure, contributes greatly to the spatial transient. By considering zero pressure fluctuations and the SRA in the digital filter implementation for compressible flows, nonphysical pressure fluctuations are only generated inside the computational domain, and fluctuations observed directly at the inflow are due to the non-reflecting nature of the boundary scheme. These spurious fluctuations disrupt the pressure-related mechanisms in the Reynolds stress transport equation, and consequently, the turbulence regeneration cycle. A further confirmation of this is the fact that employing the above mentioned isentropic assumption to impose non-zero p' at the inflow does not improve the results, since the fluctuations are still non-

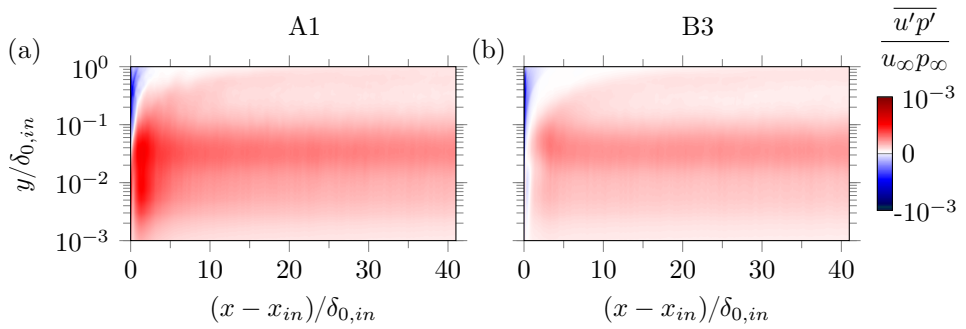

Figure B.8: Normalized pressure-velocity correlation $\overline{u'p'}$ for (a) case A1, and (b) case B3.

physical. Additionally, we find that the pressure fluctuations that develop near the inflow are directly correlated with u'', which generally exhibits very large integral scales in streamwise direction. As a consequence, increased fluctuation intensities are retained for a long distance within the computational domain as illustrated in figure B.4(a) for the baseline case R0 and cases A1-A3. The suppression of the streamwise velocity fluctuations, in turn, effectively eliminates the correlation between u'' and the thermodynamic fluctuations, which leads to a faster relaxation of the latter. The pressure velocity correlation $\overline{u'p'}$ is shown in figure B.8 for cases A1 and B3 to illustrate the above-mentioned.

B.4. Final remarks

The digital filter implementation employed in all simulations presented in PART TWO of this thesis, i.e., that of case A1, has proven effective at introducing appropriate turbulent boundary conditions in a cost-effective fashion. Combined with the fact that the technique does not introduce any spurious low-frequency tone in the computational domain, we find it particularly suitable for the simulation of STBLI flows. However, like any other synthetic turbulence generator, the method is certainly not perfect and still has room for improvement. For instance, we have shown the inability of the current digital filter implementation to realistically account for different terms in the Reynolds-stress transport, and in particular those involving the pressure, which contributes to the spatial transient. A potential improvement in this regard would be to generate additional random slices for the thermodynamic variables and introduce physical auto- and cross-correlations of their fluctuations, since these play a key role in compressible turbulence. Cross-correlations between thermodynamic variables and velocity components can also be controlled with this approach, which could effectively eliminate the spurious $p-u$ correlation that emerges with the standard digital filter methodology without the need to artificially suppress streamwise velocity fluctuations. The additional computational costs incurred by the aforementioned improvements would still be negligible considering that the update of the inflow data at a prescribed time interval rather than every time step does not incur additional penalties in accuracy (as we have shown). The correlation

data reported in chapter 5 can thus be used as a starting point to produce more realistic turbulence in future implementations of the method, which we are currently exploring.

Another aspect that cannot be properly modeled with the current implementation of the digital filter method is the influence of outer-layer motions on the near-wall turbulence (see chapter 5). While the target Reynolds stresses may be physical, the prescribed two-point correlations near the wall still disregard such influence, which should be accounted for in order to increase the accuracy of synthetic turbulence generation methods. Consider again figure 5.10 which shows spanwise autocorrelation functions of streamwise velocity fluctuations at $Re_\tau = 382$ and $Re_\tau = 5371$. In the former case, the corresponding velocity streaks at a given distance from the wall are characterized by a single spanwise length scale, that is, their spanwise spacing, which results in a correlation function that goes to negative values near the axis, see figure 5.10(a). This correlation is well represented by the transversal correlation function that we propose (see equation (B.7)), which only requires one target length scale. Figure 5.10(b), on the other hand, shows that a single spanwise length scale is not sufficient to properly model the coherence of the near-wall turbulence at high Reynolds number. By spatially low-pass and high-pass filtering the flowfield, we have shown the separate and important contribution of both the small scales and the large scales to the total correlation. The observed correspondence between the log-layer region and the near-wall turbulence at high Reynolds number thus highlights the need for a second set of target scales near the wall that correctly accounts for inter-scale interactions at the digital filter boundary.

In the context of the zonal approach employed, instead of attempting to model the influence of outer-layer motions on the near-wall turbulence with a complex filter kernel, one could simply re-filter the zone corresponding to the inner-layer of the TBL (where adequate correlations according to the near-wall turbulence have already been prescribed) with the filter kernel applied in the log-layer region. This strategy would effectively incorporate the corresponding large-scale effects on the small-scale behavior and thus result in more realistic inflow turbulence.

C

Sensitivity of LES results to grid resolution and domain size

Tables C.1 and C.2 provide a summary of the grid and domain sensitivity study conducted for case $\mathcal{B}_2$, which is inspired by a similar investigation conducted by Pasquariello *et al.* [23]. In the present study, four different grid resolutions and domain sizes are considered. The former include the coarsest grid level $\mathcal{G}^1$, characterized by $\Delta x^+_{min} = 78$ and $\Delta z^+_{min} = 19.6$. The second grid $\mathcal{G}^1_x$ doubles the number of grid cells in the streamwise direction compared to $\mathcal{G}^1$. The reference grid level $\mathcal{G}^2$ then doubles the number of cells in spanwise direction, and finally, the finest grid $\mathcal{G}^2_x$ doubles the number of cells of $\mathcal{G}^2$ in streamwise direction. The domain size study considers the narrow domain $\mathcal{D}^1$, extending $2\delta_{0,i}$ in span, the reference domain $\mathcal{D}^2$, which spans $4\delta_{0,i}$, and the wide domain $\mathcal{D}^3$, with a width of $8\delta_{0,i}$. The impact of the domain length on the results is also assessed by considering the long domain $\mathcal{D}^4$, which has the same width as $\mathcal{D}^2$ but is 50% longer in the streamwise direction, i.e., $67.5\delta_{0,i}$ compared to $45\delta_{0,i}$.

All cases were integrated for a time period of $2050\delta_{0,i}/u_\infty$, which corresponds to 45 FTT of the reference domain length. However, the reference configuration involving $\mathcal{G}^2$ and $\mathcal{D}^2$ was integrated for an additional $2050\delta_{0,i}/u_\infty$ (totaling 90 FTT) to produce the results presented in the paper. Statistical samples were collected at a sampling interval of $\Delta t \approx 0.02\delta_{0,i}/u_\infty$ in all simulations.

Figures C.1 show the distinct impact of the grid resolution and domain size on selected wall-properties. Starting with the effect of grid resolution in the left panels, it becomes evident that the under-resolved grid $\mathcal{G}^1$ delays separation and under-predicts the extent of the recirculation bubble compared to the other grid levels. The peak in $\langle C_f \rangle$ within the recirculation bubble is also slightly under-predicted on this coarse grid, see figure C.1(a), while the plateau level is well captured in all cases. Moreover, figures C.1(b,c) indicate that the interaction region predicted by $\mathcal{G}^1$ exhibits increased wall-pressure levels at reattachment and lower wall-pressure fluctuation intensities throughout the interaction. The fluctuating wall-pressure

Table C.1: Numerical parameters of the grid-sensitivity study for case $\mathcal{B}_2$. Percentage deviations from the reference grid resolution $\mathcal{G}^2$ are reported in brackets, and TBL statistics are measured at $Re_\tau = 1100$ in all cases.

Grid	$\mathcal{G}^1$	$\mathcal{G}^1_x$	$\mathcal{G}^2$	$\mathcal{G}^2_x$
Line legend	– – –	– – – –	———	– · – · –
Domain size				
$L_x/\delta_{0,in}$	45	45	45	45
$L_y/\delta_{0,in}$	16.5	16.5	16.5	16.5
$L_z/\delta_{0,in}$	4	4	4	4
Grid resolution				
Δx^+_{min}	78	39	39	19.5
Δy^+_{min}	0.94	0.94	0.94	0.94
Δz^+_{min}	19.6	19.6	9.8	9.8
Runtime				
$\Delta t u_\infty/\delta_{0,in}$	2050	2050	4100	2050
TBL statistics				
$\max_y(\tau^+_{11})$	11.44 (+33.6%)	9.94 (+16.2%)	8.56	8.35 (−2.5%)
$\max_y(-\tau^+_{12})$	0.99 (+3.1%)	0.96 (+0.0%)	0.96	0.96 (+0.0%)
STBLI statistics				
$L_{sep}/\delta_{0,in}$	8.42 (−9.1%)	8.59 (−7.3%)	9.26	9.44 (+2.0%)
$H_{sep}/\delta_{0,in}$	0.38 (−26.0%)	0.48 (−6.8%)	0.52	0.53 (+2.0%)

distribution in the first half of the interaction is also qualitatively different compared to the higher grid resolutions.

Table C.1 reports selected upstream TBL and STBLI statistics to highlight the convergence of the solution as the grid is refined. Percentage deviations from the reference grid resolution $\mathcal{G}^2$ are provided in brackets for clarity. In the upstream TBL flow, the coarser grid levels $\mathcal{G}^1$ and $\mathcal{G}^1_x$ over-predict the peak value of the streamwise stress by 33.6% and 16.2%, respectively, whereas the difference between the finest grids $\mathcal{G}^2$ and $\mathcal{G}^2_x$ is only 2.5%. The peak shear stress, in turn, shows minimal sensitivity to the grid resolution. In terms of STBLI statistics, $\mathcal{G}^1$ under-predicts the bubble extent as mentioned earlier, specifically by 9.1% in length and 26% in height compared to the reference. As the grid resolution increases, however, the percentage difference reduces to about $\sim 7\%$ for both metrics at $\mathcal{G}^1_x$ and to only 2% at the finest grid resolution $\mathcal{G}^2_x$, see table C.1. This confirms the convergence of the results at the reference grid level $\mathcal{G}^2$ for practical purposes.

The effect of domain size is shown in the right panels of figure C.1. It is evident that both skin-friction and wall-pressure distributions show little sensitivity to the investigated domain dimensions. Statistics reported in table C.2 confirm

Table C.2: Numerical parameters of the domain-sensitivity study for case $\mathcal{B}_2$. Percentage deviations from the reference domain size $\mathcal{D}^2$ are reported in brackets, and TBL statistics are measured at $Re_\tau = 1100$ in all cases.

Domain	$\mathcal{D}^1$	$\mathcal{D}^2$	$\mathcal{D}^3$	$\mathcal{D}^4$
Line legend	– – –	———	- - - - -	-·-·-·-
Domain size				
$L_x/\delta_{0,in}$	45	45	45	67.5
$L_y/\delta_{0,in}$	16.5	16.5	16.5	16.5
$L_z/\delta_{0,in}$	2	4	8	4
Grid resolution				
Δx^+_{min}	39	39	39	39
Δy^+_{min}	0.94	0.94	0.94	0.94
Δz^+_{min}	9.8	9.8	9.8	9.8
Runtime				
$\Delta t u_\infty/\delta_{0,in}$	2050	4100	2050	2050
TBL statistics				
$\max_y(\tau^+_{11})$	8.60 (+0.4%)	8.56	8.59 (+0.4%)	8.55 (−0.1%)
$\max_y(-\tau^+_{12})$	0.96 (+0.0%)	0.96	0.96 (+0.0%)	0.96 (+0.0%)
STBLI statistics				
$L_{sep}/\delta_{0,in}$	9.87 (+6.6%)	9.26	9.10 (−1.7%)	9.28 (+0.2%)
$H_{sep}/\delta_{0,in}$	0.56 (+7.0%)	0.52	0.51 (−2.0%)	0.52 (+0.0%)

that incoming turbulence does not exhibit small-span effects in any domain configuration, while the extent of the recirculation region is only slightly over-predicted by $\mathcal{D}^1$ (around $\sim 7\%$ in both length and height). Moreover, figure C.1(c) shows that the STBLI dynamics, as opposed to the mean-flow, are notably influenced by a narrow domain width of $2\delta_{0,i}$, leading to much higher wall-pressure fluctuations beneath the separation-shock foot and around the reattachment location. However, such confinement effects are only observed for $\mathcal{D}^1$; the other domain configurations lead to almost identical wall-pressure fluctuations throughout the interaction, which confirms the adequacy of the selected domain configuration $\mathcal{D}^2$ for the simulation of STBLI flows.

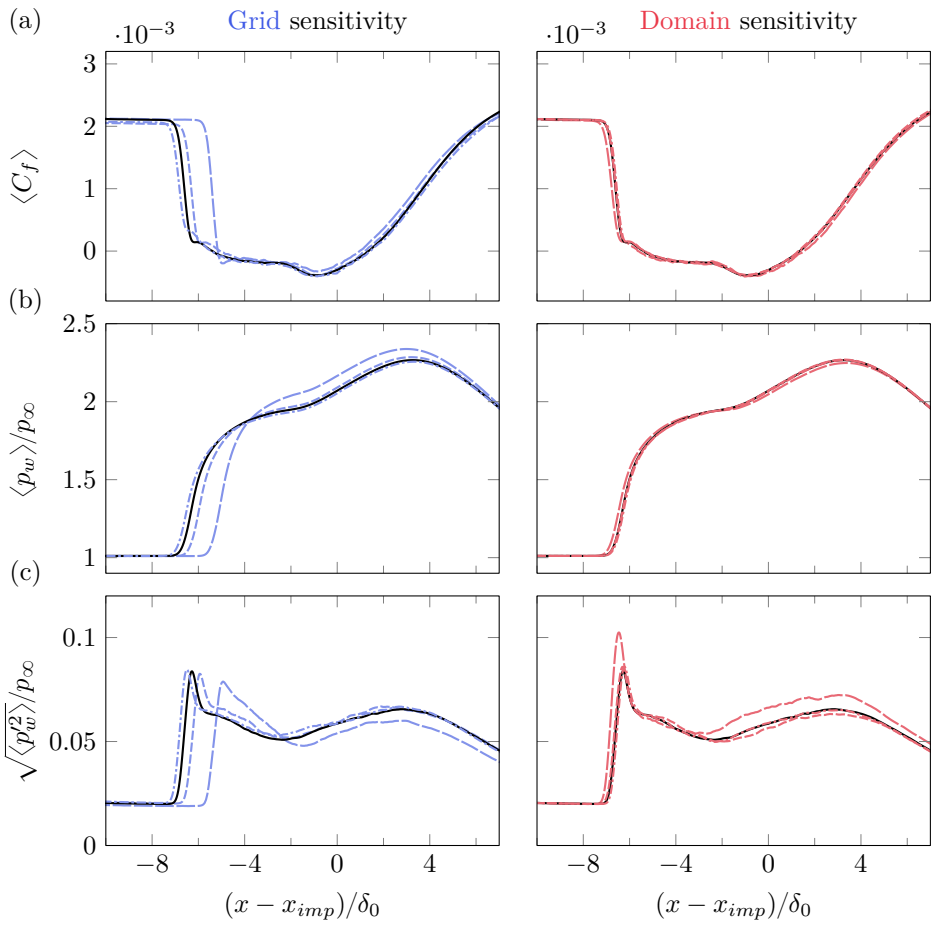

Figure C.1: Sensitivity of time- and spanwise-averaged wall-properties for case $\mathcal{B}_2$ to grid resolution and domain size: (a) skin-friction, (b) wall-pressure, (c) wall-pressure fluctuations. For the line legend, see tables C.1 and C.2.

D

DMD formulation and its sparsity-promoting variant

Dynamic mode decomposition (DMD [61]) is a purely data-driven technique that seeks to extract coherent spatio-temporal structures from a snapshot sequence. The snapshot matrix $\boldsymbol{X}_1^n = \{\boldsymbol{x}(t_1), \boldsymbol{x}(t_2), \ldots, \boldsymbol{x}(t_n)\} \in \mathbb{R}^{m \times n}$ is built from instantaneous snapshots $\boldsymbol{x}(t_k)$ arranged as column vectors and sampled at a constant time interval, i.e., $t_k = k\Delta t$ (irregular sampling is also possible, [254]). For fluid flows, as in the present work, the snapshot matrix $\boldsymbol{X}_1^n$ tends to be very tall and skinny, i.e., $m >> n$. The (presumably non-linear) physical process described by the snapshot matrix is then assumed to be a linear, time-invariant dynamical system obeying $\partial_t \boldsymbol{x}(t) = \boldsymbol{A}\boldsymbol{x}(t)$. In discrete form, the snapshot $\boldsymbol{x}(t_k)$ is connected with $\boldsymbol{x}(t_{k+1})$ via the linear mapping $\boldsymbol{A}$

$$\boldsymbol{x}(t_{k+1}) \approx \boldsymbol{A}\boldsymbol{x}(t_k), \tag{D.1}$$

which remains constant over the sampling interval $[0, (n-1)\Delta t]$. Often, this mapping is also interpreted as the Koopman operator evolving linear measurements of the state [255]. Taking the full snapshot sequence, (D.1) can be equivalently written as

$$\boldsymbol{X}_2^n \approx \boldsymbol{A}\boldsymbol{X}_1^{n-1}, \tag{D.2}$$

where $\boldsymbol{X}_1^{n-1} = \{\boldsymbol{x}(t_1), \boldsymbol{x}(t_2), \ldots, \boldsymbol{x}(t_{n-1})\}$ and $\boldsymbol{X}_2^n = \{\boldsymbol{x}(t_2), \boldsymbol{x}(t_3), \ldots, \boldsymbol{x}(t_n)\}$. The advantage of this approximation is that the spectral decomposition of $\boldsymbol{A}$ provides a basis that can be used to expand each snapshot $\boldsymbol{x}(t_k)$, i.e.,

$$\boldsymbol{x}(t_k) \approx \sum_{j=1}^{n} \boldsymbol{\phi}_j \mu_j^{k-1} \alpha_j, \tag{D.3}$$

where $\boldsymbol{\phi}_j$ are the eigenvectors of $\boldsymbol{A}$ (DMD modes), μ_j are the corresponding eigenvalues (time dynamics) and α_j the modal amplitudes. Valuable insights into the underlying physical process can then be gained by close examination of the dominant modes and their time evolution (growth/decay rate and frequency of oscillation).

If the snapshot matrices $\boldsymbol{X}_1^{n-1}$ and $\boldsymbol{X}_1^{n-1}$ are not too large, the best-fit operator $\boldsymbol{A}$ is obtained from the pseudo-inverse of $\boldsymbol{X}_1^{n-1}$, i.e., $\boldsymbol{A} = \boldsymbol{X}_2^n \, \boldsymbol{X}_1^{n-1^\dagger}$ [254].

However, representing the full matrix $\boldsymbol{A} \in \mathbb{R}^{(m-1)\times(m-1)}$, let alone finding its spectral decomposition, is very often intractable. An alternative to this approach is to realize that, for a constant mapping between snapshots, the columns of $\boldsymbol{X}_1^n$ can be rewritten as a Krylov sequence generated by the propagator $\boldsymbol{A}$ and $\boldsymbol{x}(t_1)$, i.e., $\boldsymbol{X}_1^n \approx \{\boldsymbol{x}(t_1), \boldsymbol{A}\boldsymbol{x}(t_1), \boldsymbol{A}^2\boldsymbol{x}(t_1), \ldots, \boldsymbol{A}^{N-1}\boldsymbol{x}(t_1)\}$. In this case, the $\boldsymbol{X}_1^{n-1}$ and $\boldsymbol{X}_2^n$ may be related via $\boldsymbol{X}_2^n \approx \boldsymbol{X}_1^{n-1}\boldsymbol{S}$, where $\boldsymbol{S} \in \mathbb{R}^{(n-1)\times(n-1)}$ is of companion type and reflects the fact that the snapshots in $\boldsymbol{X}_1^{n-1}$ appear shifted one column to the left in $\boldsymbol{X}_2^n$. The only unknowns in $\boldsymbol{S}$ are thus the elements of the last column, which can be obtained as a best-fit combination of the $n-1$ columns of $\boldsymbol{X}_1^{n-1}$. Note that $\boldsymbol{S}$ is a lower-dimensional representation of $\boldsymbol{A}$ so it may be used to extract modal structures [255].

D

Computations based on $\boldsymbol{S}$, however, are often numerically unstable and noise-sensitive. To overcome these issues, [61] proposed a different and more robust approach by which the DMD modes are approximated from the "full" matrix $\tilde{\boldsymbol{A}}$, which is related to $\boldsymbol{A}$ via a similarity transformation. That is, $\tilde{\boldsymbol{A}}$ results from the projection of $\boldsymbol{A}$ onto the subspace spanned by the singular vectors, i.e., POD modes, of the snapshot matrix $\boldsymbol{X}_1^{n-1}$. A pre-processing step is then required to compute the economy-size singular-value decomposition (SVD) of $\boldsymbol{X}_1^{n-1}$, i.e., $\boldsymbol{X}_1^{n-1} \approx \boldsymbol{U}\boldsymbol{\Sigma}\boldsymbol{V}^{\boldsymbol{H}}$ where $\boldsymbol{U} \in \mathbb{C}^{(m-1)\times r}$, $\boldsymbol{V} \in \mathbb{C}^{r\times r}$ and $\boldsymbol{\Sigma} \in \mathbb{C}^{(m-1)\times r}$ ($r \leqslant (n-1)$ indicates optional truncation). Rearranging the resulting expression yields

$$\boldsymbol{U}^H\boldsymbol{A}\boldsymbol{U} = \boldsymbol{U}^H\boldsymbol{X}_2^n\boldsymbol{V}\,\boldsymbol{\Sigma}^{-1} \equiv \tilde{\boldsymbol{A}}. \tag{D.4}$$

Modal structures may now be extracted from $\tilde{\boldsymbol{A}}$, i.e., $\tilde{\boldsymbol{A}}\tilde{\boldsymbol{\phi}}_j = \mu_j\tilde{\boldsymbol{\phi}}_j$ where $\tilde{\boldsymbol{\phi}}_j$ and μ_j are the corresponding eigenvectors and eigenvalues of $\tilde{\boldsymbol{A}}$, the latter corresponding to eigenvalues of the full matrix $\boldsymbol{A}$. The following transformation can finally be used to map the eigenvectors in the subspace back into physical space

$$\boldsymbol{\phi}_j = \boldsymbol{X}_2^n\boldsymbol{V}\,\boldsymbol{\Sigma}^{-1}\tilde{\boldsymbol{\phi}}_j. \tag{D.5}$$

Alternatively, the matrix of POD modes $\boldsymbol{U}$ can also be used to recover the high-dimensional DMD modes, i.e., $\boldsymbol{\phi}_j = \boldsymbol{U}\tilde{\boldsymbol{\phi}}_j$. However, these are known as *projected modes* and they are not guaranteed to be exact eigenvectors of $\boldsymbol{A}$ [254]. The growth rate β_j and angular frequency ω_j of each individual mode can be directly extracted from the corresponding eigenvalue μ_j, e.g.,

$$\mu_j = |\mu_j|e^{i\theta} \equiv e^{(\beta_j + i\omega_j)\Delta t}, \tag{D.6}$$

where $\theta = \arg(\mu_j)$. Thus, $\beta_j = \ln|\mu_j|/\Delta t$ and $\omega_j = \theta\Delta t$.

With the above procedure, it is therefore possible to approximate snapshots using a linear combination of DMD modes, see (D.3). As indicated by [201], this can

be equivalently written in matrix form as

$$\boldsymbol{X}_1^{n-1} \approx \underbrace{\begin{bmatrix}\boldsymbol{\phi}_1 & \boldsymbol{\phi}_2 & \dots & \boldsymbol{\phi}_{n-1}\end{bmatrix}}_{\boldsymbol{\Phi}} \underbrace{\begin{bmatrix}\alpha_1 & & & \\ & \alpha_2 & & \\ & & \ddots & \\ & & & \alpha_{n-1}\end{bmatrix}}_{\boldsymbol{D}_\alpha := diag\{\alpha\}} \underbrace{\begin{bmatrix}1 & \mu_1 & \dots & \mu^1 \\ 1 & \mu_2 & \dots & \mu^2 \\ \vdots & \vdots & \ddots & \vdots \\ 1 & \mu_{n-1} & \dots & \mu_{n-1}^{n-1}\end{bmatrix}}_{\boldsymbol{V}_{and}}, \tag{D.7}$$

where the temporal evolution of the dynamic modes is governed by the Vandermonde matrix $\boldsymbol{V}_{and} \in \mathbb{C}^{(n-1)\times(n-1)}$. The vector of unknown amplitudes $\boldsymbol{\alpha} := [\alpha_1 \dots \alpha_{n-1}]$, on the other hand, results from the following optimization problem

$$\underset{\alpha}{\text{minimize}} \quad \|\boldsymbol{X}_1^{n-1} - \boldsymbol{\Phi}\boldsymbol{D}_\alpha\boldsymbol{V}_{and}\|_F^2, \tag{D.8}$$

which leads to the optimal representation of the entire data sequence. Note that $\|\cdot\|_F$ denotes the Frobenius norm.

In many situations, it is of interest to seek further dimensionality reduction and identify the subset of DMD modes that have the strongest influence on the data sequence. Using the modal amplitudes for this purpose, however, is sometimes misleading since the largest amplitudes may correspond to spurious modes that are strongly damped. A more robust approach, that focuses on identifying the strongest influence over the entire time history of available snapshots, was proposed by [201], the so-called sparsity-promoting DMD (SPDMD). This approach is based on regularizing the least-squares deviation in (D.8) with an additional term that penalizes the ℓ_1-norm of the vector of amplitudes $\boldsymbol{\alpha} \in \mathbb{C}^{n-1}$, i.e.,

$$\underset{\alpha}{\text{minimize}} \quad \|\boldsymbol{X}_1^{n-1} - \boldsymbol{\Phi}\boldsymbol{D}_\alpha\boldsymbol{V}_{and}\|_F^2 \; + \; \gamma_r \sum_{j=0}^{n-1} |\alpha_j|, \tag{D.9}$$

where γ_r is a positive regularization parameter that reflects the emphasis on sparsity: large values of γ_r enforce a sparse $\boldsymbol{\alpha}$ while $\gamma_r = 0$ recovers the original optimization problem (D.8). To solve the resulting convex optimization problem (D.9), we use the method employed in [201] which is the alternating direction method of multipliers. For algorithmic details, we refer the reader to their publication.

Finally, the performance loss of a given sparse structure is defined as

$$\%\Pi_{loss} := 100\frac{\|\boldsymbol{X}_1^{n-1} - \boldsymbol{\Phi}\boldsymbol{D}_\alpha\boldsymbol{V}_{and}\|_F^2}{\|\boldsymbol{X}_1^{n-1}\|_F^2}, \tag{D.10}$$

with the (now known) vector of amplitudes $\boldsymbol{D}_\alpha$ provided by the solution of the convex optimization problem in equation D.9.

Bibliography

[1] T. A. Weaver, *The structure of supernova shock waves,* Astrophysical Journal Supplement Series **32**, 233 (1976).

[2] M. Dryer, *Interplanetary shock waves generated by solar flares,* Space Science Reviews **15**, 403 (1974).

[3] F. J. Regan, *Dynamics of atmospheric re-entry* (AIAA, 1993).

[4] J. Délery and J.-P. Dussauge, *Some physical aspects of shock wave/boundary layer interactions,* Shock Waves **19**, 453 (2009).

[5] H. Babinsky and J. K. Harvey, *Shock wave-boundary-layer interactions*, Vol. 32 (Cambridge University Press, 2011).

[6] V. F. Dippold III, *High Speed Inlet Distortion Test for the X-59 Low Boom Flight Demonstrator in the NASA Glenn 8-by 6-Foot Supersonic Wind Tunnel*, Tech. Rep. (2022).

[7] J. D. Anderson, *Fundamentals of Aerodynamics (SI units)* (McGraw-Hill, 2011).

[8] J. Seddon and E. Goldsmith, *Intake aerodynamics* (American Institute of Aeronautics and Astronautics, Inc., 1999).

[9] S. Das and J. K. Prasad, *Cowl deflection angle in a supersonic air intake.* Defence Science Journal **59** (2009).

[10] J. C. Esterhuyse, *Aerodynamic drag of a two-dimensional external compression inlet at supersonic speed*, Ph.D. thesis, Cape Technikon (1997).

[11] S. Farokhi, *Aircraft Propulsion* (Wiley, 2014).

[12] J. Colville, R. Starkey, and M. Lewis, *Extending the flight Mach number of the SR-71 inlet,* AIAA Paper 2005-3284 (2005).

[13] T. R. Conners, *Predicted performance of a thrust-enhanced SR-71 aircraft with an external payload,* **78798** (1995).

[14] K. G. Bowcutt, *Flying at the edge of space and beyond: The opportunities and challenges of hypersonic flight,* The Bridge **50** (2020).

[15] C. J. Weit, J. Wen, T. A. Zaidi, and D. N. Mavris, *Estimating supersonic commercial aircraft market and resulting CO2 emissions using public movement data,* CEAS Aeronautical Journal **12**, 191 (2021).

[16] L. Miraux, A. R. Wilson, and G. J. D. Calabuig, *Environmental sustainability of future proposed space activities,* Acta Astronautica **200**, 329 (2022).

[17] D. A. Durston, J. D. Wolter, P. Shea, C. S. Winski, A. A. Elmiligui, M. B. Carter, S. Langston, and M. D. Bozeman, *X-59 sonic boom test results from the NASA Glenn 8-by 6-foot supersonic wind tunnel,* AIAA Paper 2023-4317 (2023).

[18] T. T. Takahashi, J. A. Griffin, and R. V. Grandhi, *A review of high-speed aircraft stability and control challenges,* AIAA Paper 2023-3231 (2023).

[19] H. Welge, C. Nelson, and J. Bonet, *Supersonic vehicle systems for the 2020 to 2035 timeframe,* AIAA Paper 2010-4930 (2010).

[20] J. Slater, *Design and analysis tool for external-compression supersonic inlets,* AIAA Paper 2012-0016 (2012).

[21] B. Willis, D. Davis, and W. Hingst, *Flow coefficient behavior for boundary layer bleed holes and slots,* AIAA Paper 1995-0031 (1995).

[22] G. Ben-Dor, *Shock wave reflection phenomena*, Vol. 2 (Springer, 2007).

[23] V. Pasquariello, S. Hickel, and N. A. Adams, *Unsteady effects of strong shock-wave/boundary-layer interaction at high Reynolds number,* Journal of Fluid Mechanics **823**, 617 (2017).

[24] V. J. Shinde and D. V. Gaitonde, *Features of oblique shock wave turbulent boundary layer interaction,* AIAA Paper 2022-1975 (2022).

[25] S. Trapier, P. Duveau, and S. Deck, *Experimental study of supersonic inlet buzz,* AIAA Journal **44**, 2354 (2006).

[26] E. Touber, *Unsteadiness in shock-wave/boundary layer interactions*, Ph.D. thesis, University of Southampton (2010).

[27] E. Schülein, *Skin friction and heat flux measurements in shock/boundary layer interaction flows,* AIAA Journal **44**, 1732 (2006).

[28] M. Bernardini, I. Asproulias, J. Larsson, S. Pirozzoli, and F. Grasso, *Heat transfer and wall temperature effects in shock wave turbulent boundary layer interactions,* Physical Review Fluids **1**, 084403 (2016).

[29] D. Daub, S. Willems, and A. Gülhan, *Experimental results on unsteady shock-wave/boundary-layer interaction induced by an impinging shock,* CEAS Space Journal **8**, 3 (2016).

[30] N. T. Clemens and V. Narayanaswamy, *Low-frequency unsteadiness of shock wave/turbulent boundary layer interactions,* Annual Review of Fluid Mechanics **46**, 469 (2014).

[31] J.-P. Dussauge, P. Dupont, and J.-F. Debiève, *Unsteadiness in shock wave boundary layer interactions with separation,* Aerospace Science and Technology **10**, 85 (2006).

[32] J. J. McNamara and P. P. Friedmann, *Aeroelastic and aerothermoelastic analysis in hypersonic flow: past, present, and future,* AIAA Journal **49**, 1089 (2011).

[33] S. M. Spottswood, T. J. Beberniss, T. G. Eason, R. A. Perez, J. M. Donbar, D. A. Ehrhardt, and Z. B. Riley, *Exploring the response of a thin, flexible panel to shock-turbulent boundary-layer interactions,* Journal of Sound and Vibration **443**, 74 (2019).

[34] E. Touber and N. D. Sandham, *Large-eddy simulation of low-frequency unsteadiness in a turbulent shock-induced separation bubble,* Theoretical and Computational Fluid Dynamics **23**, 79 (2009).

[35] M. Grilli, P. J. Schmid, S. Hickel, and N. A. Adams, *Analysis of unsteady behaviour in shockwave turbulent boundary layer interaction,* Journal of Fluid Mechanics **700**, 16 (2012).

[36] B. Morgan, K. Duraisamy, N. Nguyen, S. Kawai, and S. K. Lele, *Flow physics and RANS modelling of oblique shock/turbulent boundary layer interaction,* Journal of Fluid Mechanics **729**, 231 (2013).

[37] B. Ganapathisubramani, N. T. Clemens, and D. S. Dolling, *Low-frequency dynamics of shock-induced separation in a compression ramp interaction,* Journal of Fluid Mechanics **636**, 397 (2009).

[38] R. A. Humble, G. E. Elsinga, F. Scarano, and B. W. Van Oudheusden, *Three-dimensional instantaneous structure of a shock wave/turbulent boundary layer interaction,* Journal of Fluid Mechanics **622**, 33 (2009).

[39] L. Agostini, L. Larchevêque, and P. Dupont, *Mechanism of shock unsteadiness in separated shock/boundary-layer interactions,* Physics of Fluids **27**, 126103 (2015).

[40] S. Pirozzoli and F. Grasso, *Direct numerical simulation of impinging shock wave/turbulent boundary layer interaction at M=2.25,* Physics of Fluids **18**, 065113 (2006).

[41] M. Wu and M. P. Martin, *Analysis of shock motion in shockwave and turbulent boundary layer interaction using direct numerical simulation data,* Journal of Fluid Mechanics **594**, 71 (2008).

[42] S. Piponniau, J.-P. Dussauge, J.-F. Debieve, and P. Dupont, *A simple model for low-frequency unsteadiness in shock-induced separation,* Journal of Fluid Mechanics **629**, 87 (2009).

[43] S. Priebe, J. H. Tu, C. W. Rowley, and M. P. Martín, *Low-frequency dynamics in a shock-induced separated flow,* Journal of Fluid Mechanics **807**, 441 (2016).

[44] D. V. Gaitonde, *Progress in shock wave/boundary layer interactions,* Progress in Aerospace Sciences **72**, 80 (2015).

[45] R. D. Blevins, I. Holehouse, and K. R. Wentz, *Thermoacoustic loads and fatigue of hypersonic vehicle skin panels,* Journal of Aircraft **30**, 971 (1993).

[46] J. Matheis and S. Hickel, *On the transition between regular and irregular shock patterns of shock-wave/boundary-layer interactions,* Journal of Fluid Mechanics **776**, 200 (2015).

[47] M. S. Ivanov, G. N. Markelov, A. N. Kudryavtsev, and S. F. Gimelshein, *Numerical analysis of shock wave reflection transition in steady flows,* AIAA Journal **36**, 2079 (1998).

[48] A. N. Kudryavtsev, D. V. Khotyanovsky, M. S. Ivanov, A. Hadjadj, and D. Vandromme, *Numerical investigations of transition between regular and Mach reflections caused by free-stream disturbances,* Shock Waves **12**, 157 (2002).

[49] D. V. Khotyanovsky, A. N. Kudryavtsev, and M. S. Ivanov, *Effects of a single-pulse energy deposition on steady shock wave reflection,* Shock Waves **15**, 353 (2006).

[50] C. A. Mouton and H. G. Hornung, *Experiments on the mechanism of inducing transition between regular and Mach reflection,* Physics of Fluids **20**, 126103 (2008).

[51] N. Sudani, M. Sato, T. Karasawa, J. Noda, A. Tate, and M. Watanabe, *Irregular effects on the transition from regular to Mach reflection of shock waves in wind tunnel flows,* Journal of Fluid Mechanics **459**, 167 (2002).

[52] G. N. Markelov, I. V. Pivkin, and M. Ivanov, *Impulsive wedge rotation effects on the transition from regular to Mach reflection,* in *Proc. of 22nd Int. Sympos. on Shock Waves* (1999) pp. 1243–1248.

[53] L. T. Felthun and B. W. Skews, *Dynamic shock wave reflection,* AIAA Journal **42**, 1633 (2004).

[54] K. Naidoo and B. W. Skews, *Dynamic effects on the transition between two-dimensional regular and Mach reflection of shock waves in an ideal, steady supersonic free stream,* Journal of Fluid Mechanics **676**, 432 (2011).

[55] A. Durand, B. Chanetz, R. Benay, and A. Chpoun, *Investigation of shock waves interference and associated hysteresis effect at variable-Mach-number upstream flow,* Shock Waves **12**, 469 (2003).

[56] D. S. Dolling, *Fifty years of shock-wave/boundary-layer interaction research: what next?* AIAA Journal **39**, 1517 (2001).

[57] A. J. Smits and J.-P. Dussauge, *Turbulent shear layers in supersonic flow* (Springer Science & Business Media, 2006).

[58] R. A. Humble, F. Scarano, and B. W. Van Oudheusden, *Particle image velocimetry measurements of a shock wave/turbulent boundary layer interaction,* Experiments in Fluids **43**, 173 (2007).

[59] G. S. Settles, S. M. Bogdonoff, and I. E. Vas, *Incipient separation of a supersonic turbulent boundary layer at high Reynolds numbers,* AIAA Journal **14**, 50 (1976).

[60] D. S. Dolling and M. T. Murphy, *Unsteadiness of the separation shock wave structure in a supersonic compression ramp flowfield,* AIAA Journal **21**, 1628 (1983).

[61] P. J. Schmid, *Dynamic mode decomposition of numerical and experimental data,* Journal of Fluid Mechanics **656**, 5 (2010).

[62] J. W. Nichols, J. Larsson, M. Bernardini, and S. Pirozzoli, *Stability and modal analysis of shock/boundary layer interactions,* Theoretical and Computational Fluid Dynamics **31**, 33 (2017).

[63] T. G. Eason and S. Spottswood, *A structures perspective on the challenges associated with analyzing a reusable hypersonic platform,* AIAA Paper 2013-1747 (2013).

[64] S. M. Spottswood, T. Eason, and T. Beberniss, *Influence of shock-boundary layer interactions on the dynamic response of a flexible panel,* in *Proceedings of the International Conference on Noise and Vibration Engineering ISMA*, Vol. 2012 (2012) pp. 603–616.

[65] V. Shinde, J. McNamara, and D. Gaitonde, *Dynamic interaction between shock wave turbulent boundary layer and flexible panel,* Journal of Fluids and Structures **113**, 103660 (2022).

[66] A. D'Aguanno, P. Quesada Allerhand, F. F. J. Schrijer, and B. W. van Oudheusden, *Characterization of shock-induced panel flutter with simultaneous use of DIC and PIV,* Experiments in Fluids **64**, 15 (2023).

[67] M. C. Neet and J. M. Austin, *Effects of surface compliance on shock boundary layer interaction in the caltech Mach 4 ludwieg tube,* AIAA Paper 2020-0816 (2020).

[68] R. Ravichandran, M. Gramola, and P. J. Bruce, *Simultaneous pressure and displacement measurements on a 3D flexible surface in a supersonic flow,* AIAA Paper 2020-0315 (2020).

[69] K. R. Brouwer, A. Gogulapati, and J. J. McNamara, *Interplay of surface deformation and shock-induced separation in shock/boundary-layer interactions,* AIAA Journal **55**, 4258 (2017).

[70] A. Thari, V. Pasquariello, N. Aage, and S. Hickel, *Adaptive reduced-order modeling for non-linear fluid–structure interaction,* Computers & Fluids **229**, 105099 (2021).

[71] S. Hickel, C. P. Egerer, and J. Larsson, *Subgrid-scale modeling for implicit large eddy simulation of compressible flows and shock-turbulence interaction,* Physics of Fluids **26**, 106101 (2014).

[72] S. Gottlieb and C.-W. Shu, *Total variation diminishing runge-kutta schemes,* Mathematics of Computation **67**, 73 (1998).

[73] F. Örley, V. Pasquariello, S. Hickel, and N. A. Adams, *Cut-element based immersed boundary method for moving geometries in compressible liquid flows with cavitation,* Journal of Computational Physics **283**, 1 (2015).

[74] V. Pasquariello, G. Hammerl, F. Örley, S. Hickel, C. Danowski, A. Popp, W. A. Wall, and N. A. Adams, *A cut-cell finite volume–finite element coupling approach for fluid–structure interaction in compressible flow,* Journal of Computational Physics **307**, 670 (2016).

[75] H. M. Hilber, T. J. R. Hughes, and R. L. Taylor, *Improved numerical dissipation for time integration algorithms in structural dynamics,* Earthquake Engineering & Structural Dynamics **5**, 283 (1977).

[76] N. M. Newmark, *A method of computation for structural dynamics,* Journal of the Engineering Mechanics Division **85**, 67 (1959).

[77] E. H. Dowell and K. C. Hall, *Modeling of fluid-structure interaction,* Annual Review of Fluid Mechanics **33**, 445 (2001).

[78] J. M. Dickens, J. M. Nakagawa, and M. J. Wittbrodt, *A critique of mode acceleration and modal truncation augmentation methods for modal response analysis,* Computers & Structures **62**, 985 (1997).

[79] J. Santiago Patterson, *Experimental Study of Shock-Shock Interactions with Variable Inflow Mach Number*, Ph.D. thesis, TU Delft (2019).

[80] L. M. Weinstein, *Large-field high-brightness focusing schlieren system,* AIAA Journal **31**, 1250 (1993).

[81] B. Edney, *Anomalous heat transfer and pressure distributions on blunt bodies at hypersonic speeds in the presence of an impinging shock.*, Tech. Rep. FFA Report 115, Stockholm (1968).

[82] H. G. Hornung and M. L. Robinson, *Transition from regular to Mach reflection of shock waves Part 2. The steady-flow criterion,* Journal of Fluid Mechanics **123**, 155 (1982).

[83] H. Li and G. Ben-Dor, *A parametric study of Mach reflection in steady flows,* Journal of Fluid Mechanics **341**, 101 (1997).

[84] C. A. Mouton and H. G. Hornung, *Mach stem height and growth rate predictions,* AIAA Journal **45**, 1977 (2007).

[85] Y. Tao, W. Liu, X. Fan, B. Xiong, J. Yu, and M. Sun, *A study of the asymmetric shock reflection configurations in steady flows,* Journal of Fluid Mechanics **825**, 1 (2017).

[86] H. Li, A. Chpoun, and G. Ben-Dor, *Analytical and experimental investigations of the reflection of asymmetric shock waves in steady flows,* Journal of Fluid Mechanics **390**, 25 (1999).

[87] H. G. Hornung, H. Oertel, and R. J. Sandeman, *Transition to Mach reflexion of shock waves in steady and pseudosteady flow with and without relaxation,* Journal of Fluid Mechanics **90**, 541 (1979).

[88] A. Chpoun, D. Passerel, H. Li, and G. Ben-Dor, *Reconsideration of oblique shock wave reflections in steady flows. Part 1. Experimental investigation,* Journal of Fluid Mechanics **301**, 19 (1995).

[89] M. S. Ivanov, D. V. Khotyanovsky, K. A. N., and S. Nikiforov, *Experimental study of 3D shock wave configurations during RR↔MR transition,* in *Proc. of 23rd Int. Sympos. on Shock Waves* (2001).

[90] M. S. Ivanov, A. N. Kudryavtsev, S. B. Nikiforov, D. V. Khotyanovsky, and A. A. Pavlov, *Experiments on shock wave reflection transition and hysteresis in low-noise wind tunnel,* Physics of Fluids **15**, 1807 (2003).

[91] M. S. Ivanov, S. F. Gimelshein, and A. E. Beylich, *Hysteresis effect in stationary reflection of shock waves,* Physics of Fluids **7**, 685 (1995).

[92] J. Vuillon, D. Zeitoun, and G. Ben-Dor, *Reconsideration of oblique shock wave reflections in steady flows. Part 2. Numerical investigation,* Journal of Fluid Mechanics **301**, 37 (1995).

[93] A. Chpoun and G. Ben-Dor, *Numerical confirmation of the hysteresis phenomenon in the regular to the Mach reflection transition in steady flows,* Shock Waves **5**, 199 (1995).

[94] M. S. Ivanov, G. Ben-Dor, T. Elperin, A. N. Kudryavtsev, and D. V. Khotyanovsky, *The reflection of asymmetric shock waves in steady flows: a numerical investigation,* Journal of Fluid Mechanics **469**, 71 (2002).

[95] E. Touber and N. D. Sandham, *Low-order stochastic modelling of low-frequency motions in reflected shock-wave/boundary-layer interactions,* Journal of Fluid Mechanics **671**, 417 (2011).

[96] C. W. Shu, *Essentially non-oscillatory and weighted essentially non-oscillatory schemes for hyperbolic conservation laws,* in *Advanced numerical approximation of nonlinear hyperbolic equations* (Springer, 1998) pp. 325–432.

[97] I. J. Grossman and P. J. K. Bruce, *Confinement effects on regular–irregular transition in shock-wave–boundary-layer interactions,* Journal of Fluid Mechanics **853**, 171 (2018).

[98] L. Laguarda, S. Hickel, F. F. J. Schrijer, and B. W. Van Oudheusden, *Dynamics of unsteady asymmetric shock interactions,* Journal of Fluid Mechanics **888**, A18 (2020).

[99] M. Ivanov, G. Markelov, A. Kudryavtsev, S. Gimelshein, M. Ivanov, G. Markelov, A. Kudryavtsev, and S. Gimelshein, *Transition between regular and Mach reflections of shock waves in steady flows,* in *32nd Thermophysics conference* (1997) p. 2511.

[100] M. S. Ivanov, G. P. Klemenkov, A. N. Kudryavtsev, S. B. Nikiforov, A. A. Pavlov, V. M. Fomin, A. M. Kharitonov, D. V. Khotyanovsky, and H. G. Hornung, *Experimental and numerical study of the transition between regular and Mach reflections of shock waves in steady flows,* in *The 21st International Symposium on Shock Waves* (1997).

[101] V. M. Fomin, H. G. Hornung, M. S. Ivanov, A. M. Kharitonov, G. P. Klemenkov, A. N. Kudryavtsev, and A. A. Pavlov, *The study of transition between regular and Mach reflection of shock waves in different wind tunnels,* in *Proc. 12th Int. Mach Reflection Symposium* (1996) pp. 137–151.

[102] B. W. Skews, *Three-dimensional effects in wind tunnel studies of shock wave reflection,* Journal of Fluid Mechanics **407**, 85 (2000).

[103] L. Laguarda, F. F. J. Schrijer, B. W. van Oudheusden, and S. Hickel, *Supplementary material to the publication 'Experimental investigation of shock-shock interactions with variable inflow Mach number'.* (2020).

[104] M. Yu, C.-X. Xu, and S. Pirozzoli, *Genuine compressibility effects in wall-bounded turbulence,* Physical Review Fluids **4**, 123402 (2019).

[105] M. V. Morkovin, *Effects of compressibility on turbulent flows,* Mécanique de la Turbulence **367**, 26 (1962).

[106] L. Duan, I. Beekman, and M. P. Martin, *Direct numerical simulation of hypersonic turbulent boundary layers. Part 3. Effect of Mach number,* Journal of Fluid Mechanics **672**, 245 (2011).

[107] M. F. Shahab, G. Lehnasch, T. B. Gatski, and P. Comte, *Statistical characteristics of an isothermal, supersonic developing boundary layer flow from DNS data,* Flow, Turbulence and Combustion **86**, 369 (2011).

[108] C. Wenzel, B. Selent, M. Kloker, and U. Rist, *DNS of compressible turbulent boundary layers and assessment of data/scaling-law quality,* Journal of Fluid Mechanics **842**, 428 (2018).

[109] J. Gaviglio, *Reynolds analogies and experimental study of heat transfer in the supersonic boundary layer,* International Journal of Heat and Mass Transfer **30**, 911 (1987).

[110] P. G. Huang, G. N. Coleman, and P. Bradshaw, *Compressible turbulent channel flows: DNS results and modelling,* Journal of Fluid Mechanics **305**, 185 (1995).

[111] S. E. Guarini, R. D. Moser, K. Shariff, and A. Wray, *Direct numerical simulation of a supersonic turbulent boundary layer at Mach 2.5,* Journal of Fluid Mechanics **414**, 1 (2000).

[112] H. Choi and P. Moin, *Grid-point requirements for large eddy simulation: Chapman's estimates revisited,* Physics of Fluids **24**, 011702 (2012).

[113] S. Pirozzoli and M. Bernardini, *Turbulence in supersonic boundary layers at moderate Reynolds number,* Journal of Fluid Mechanics **688**, 120 (2011).

[114] S. Pirozzoli and M. Bernardini, *Probing high-Reynolds-number effects in numerical boundary layers,* Physics of Fluids **25**, 021704 (2013).

[115] J. Huang, L. Duan, and M. M. Choudhari, *Direct numerical simulation of hypersonic turbulent boundary layers: effect of spatial evolution and Reynolds number,* Journal of Fluid Mechanics **937** (2022).

[116] M. Cogo, F. Salvadore, F. Picano, and M. Bernardini, *Direct numerical simulation of supersonic and hypersonic turbulent boundary layers at moderate-high Reynolds numbers and isothermal wall condition,* Journal of Fluid Mechanics **945**, A30 (2022).

[117] B. Ganapathisubramani, N. T. Clemens, and D. S. Dolling, *Large-scale motions in a supersonic turbulent boundary layer,* Journal of Fluid Mechanics **556**, 271 (2006).

[118] G. E. Elsinga, R. J. Adrian, B. W. Van Oudheusden, and F. Scarano, *Three-dimensional vortex organization in a high-Reynolds-number supersonic turbulent boundary layer,* Journal of Fluid Mechanics **644**, 35 (2010).

[119] M. Bross, S. Scharnowski, and C. J. Kähler, *Large-scale coherent structures in compressible turbulent boundary layers,* Journal of Fluid Mechanics **911** (2021).

[120] P. Schlatter, Q. Li, G. Brethouwer, A. V. Johansson, and D. S. Henningson, *Simulations of spatially evolving turbulent boundary layers up to Reθ= 4300,* International Journal of Heat and Fluid Flow **31**, 251 (2010).

[121] R. J. Adrian, C. D. Meinhart, and C. D. Tomkins, *Vortex organization in the outer region of the turbulent boundary layer,* Journal of Fluid Mechanics **422**, 1 (2000).

[122] C. M. de Silva, N. Hutchins, and I. Marusic, *Uniform momentum zones in turbulent boundary layers,* Journal of Fluid Mechanics **786**, 309 (2016).

[123] A. Laskari, R. de Kat, R. J. Hearst, and B. Ganapathisubramani, *Time evolution of uniform momentum zones in a turbulent boundary layer,* Journal of Fluid Mechanics **842**, 554 (2018).

[124] T. J. Poinsot and S. K. Lele, *Boundary conditions for direct simulations of compressible viscous flows,* Journal of Computational Physics **101**, 104 (1992).

[125] Z.-T. Xie and I. P. Castro, *Efficient generation of inflow conditions for large eddy simulation of street-scale flows,* Flow, Turbulence and Combustion **81**, 449 (2008).

[126] I. Veloudis, Z. Yang, J. J. McGuirk, G. J. Page, and A. Spencer, *Novel implementation and assessment of a digital filter based approach for the generation of LES inlet conditions,* Flow, Turbulence and Combustion **79**, 1 (2007).

[127] L. Laguarda and S. Hickel, *Analysis of improved digital filter inflow generation methods for compressible turbulent boundary layers,* Computers & Fluids **268** (2024).

[128] E. R. Van Driest, *The problem of aerodynamic heating* (Institute of the Aeronautical Sciences, 1956).

[129] A. Hadjadj, O. Ben-Nasr, M. S. Shadloo, and A. Chaudhuri, *Effect of wall temperature in supersonic turbulent boundary layers: A numerical study,* International Journal of Heat and Mass Transfer **81**, 426 (2015).

[130] P. Schlatter and R. Örlü, *Assessment of direct numerical simulation data of turbulent boundary layers,* Journal of Fluid Mechanics **659**, 116 (2010).

[131] K. E. Schoenherr, *Resistance of flat surfaces moving through a fluid,* Trans. Soc. Nav. Archit. Mar. Eng. **40**, 279 (1932).

[132] A. J. Smits, N. Matheson, and P. N. Joubert, *Low-Reynolds-number turbulent boundary layers in zero and favorable pressure gradients,* Journal of Ship Research **27**, 147 (1983).

[133] M. P. Simens, J. Jiménez, S. Hoyas, and Y. Mizuno, *A high-resolution code for turbulent boundary layers,* Journal of Computational Physics **228**, 4218 (2009).

[134] J. Sillero, J. Jiménez, R. D. Moser, and N. P. Malaya, *Direct simulation of a zero-pressure-gradient turbulent boundary layer up to $Re\theta = 6650$,* in *Journal of Physics: Conference Series*, Vol. 318 (IOP Publishing, 2011) p. 022023.

[135] M. Lagha, J. Kim, J. D. Eldredge, and X. Zhong, *A numerical study of compressible turbulent boundary layers,* Physics of Fluids **23**, 015106 (2011).

[136] T. B. Gatski and J.-P. Bonnet, *Compressibility, turbulence and high speed flow* (Academic Press, 2013).

[137] N. Hutchins and I. Marusic, *Evidence of very long meandering features in the logarithmic region of turbulent boundary layers,* Journal of Fluid Mechanics **579**, 1 (2007).

[138] N. Hutchins and I. Marusic, *Large-scale influences in near-wall turbulence,* Philosophical Transactions of the Royal Society A: Mathematical, Physical and Engineering Sciences **365**, 647 (2007).

[139] J. Jiménez and A. Pinelli, *The autonomous cycle of near-wall turbulence,* Journal of Fluid Mechanics **389**, 335 (1999).

[140] M. Lagha, J. Kim, J. D. Eldredge, and X. Zhong, *Near-wall dynamics of compressible boundary layers,* Physics of Fluids **23**, 065109 (2011).

[141] S. Hoyas and J. Jimenez, *Scaling of the velocity fluctuations in turbulent channels up to $Re_\tau = 2003$,* Physics of Fluids **18**, 011702 (2006).

[142] A. A. Townsend, *Equilibrium layers and wall turbulence,* Journal of Fluid Mechanics **11**, 97 (1961).

[143] A. Trettel and J. Larsson, *Mean velocity scaling for compressible wall turbulence with heat transfer,* Physics of Fluids **28**, 026102 (2016).

[144] A. Patel, J. W. R. Peeters, B. J. Boersma, and R. Pecnik, *Semi-local scaling and turbulence modulation in variable property turbulent channel flows,* Physics of Fluids **27**, 095101 (2015).

[145] K. P. Griffin, L. Fu, and P. Moin, *Velocity transformation for compressible wall-bounded turbulent flows with and without heat transfer,* Proceedings of the National Academy of Sciences **118**, e2111144118 (2021).

[146] S. Pirozzoli, M. Bernardini, and F. Grasso, *Characterization of coherent vortical structures in a supersonic turbulent boundary layer,* Journal of Fluid Mechanics **613**, 205 (2008).

[147] I. Marusic and W. D. C. Heuer, *Reynolds number invariance of the structure inclination angle in wall turbulence,* Physical Review Letters **99**, 114504 (2007).

[148] M. J. Ringuette, M. Wu, and M. P. Martin, *Coherent structures in direct numerical simulation of turbulent boundary layers at Mach 3,* Journal of Fluid Mechanics **594**, 59 (2008).

[149] S. Pirozzoli, F. Grasso, and T. B. Gatski, *Direct numerical simulation and analysis of a spatially evolving supersonic turbulent boundary layer at M= 2.25,* Physics of Fluids **16**, 530 (2004).

[150] R. J. Adrian, *Hairpin vortex organization in wall turbulence,* Physics of Fluids **19**, 041301 (2007).

[151] B. Ganapathisubramani, *Statistical properties of streamwise velocity in a supersonic turbulent boundary layer,* Physics of Fluids **19**, 098108 (2007).

[152] O. J. H. Williams, D. Sahoo, M. L. Baumgartner, and A. J. Smits, *Experiments on the structure and scaling of hypersonic turbulent boundary layers,* Journal of Fluid Mechanics **834**, 237 (2018).

[153] J. Zhou, R. J. Adrian, S. Balachandar, and T. M. Kendall, *Mechanisms for generating coherent packets of hairpin vortices in channel flow,* Journal of Fluid Mechanics **387**, 353 (1999).

[154] T. M. Farabee and M. J. Casarella, *Spectral features of wall pressure fluctuations beneath turbulent boundary layers,* Physics of Fluids A: Fluid Dynamics **3**, 2410 (1991).

[155] G. A. Gerolymos and I. Vallet, *Pressure, density, temperature and entropy fluctuations in compressible turbulent plane channel flow,* Journal of Fluid Mechanics **757**, 701 (2014).

[156] B. Kulfan, *Reynolds numbers considerations for supersonic flight,* AIAA Paper 2002-2839 (2002).

[157] M. J. Ringuette, P. Bookey, C. Wyckham, and A. J. Smits, *Experimental study of a Mach 3 compression ramp interaction at Re_θ= 2400,* AIAA Journal **47**, 373 (2009).

[158] M. Ringuette, M. Wu, and M. P. Martin, *Low Reynolds number effects in a Mach 3 shock/turbulent-boundary-layer interaction,* AIAA Journal **46**, 1883 (2008).

[159] K.-C. Muck, J. Andreopoulos, and J.-P. Dussauge, *Unsteady nature of shock-wave/turbulent boundary-layer interaction,* AIAA Journal **26**, 179 (1988).

[160] J. Andreopoulos and K. Muck, *Some new aspects of the shock-wave/boundary-layer interaction in compression-ramp flows,* Journal of Fluid Mechanics **180**, 405 (1987).

[161] M. E. Erengil and D. S. Dolling, *Correlation of separation shock motion with pressure fluctuations inthe incoming boundary layer,* AIAA Journal **29**, 1868 (1991).

[162] B. Ganapathisubramani, N. T. Clemens, and D. S. Dolling, *Effects of upstream boundary layer on the unsteadiness of shock-induced separation,* Journal of Fluid Mechanics **585**, 369 (2007).

[163] S. Priebe, M. Wu, and M. P. Martin, *Direct numerical simulation of a reflected-shock-wave/turbulent-boundary-layer interaction,* AIAA Journal **47**, 1173 (2009).

[164] E. Touber and N. D. Sandham, *Comparison of three large-eddy simulations of shock-induced turbulent separation bubbles,* Shock Waves **19**, 469 (2009).

[165] B. Morgan, S. Kawai, and S. Lele, *Large-eddy simulation of an oblique shock impinging on a turbulent boundary layer,* AIAA Paper 2010-4467 (2010).

[166] S. Pirozzoli, J. Larsson, J. W. Nichols, M. Bernardini, B. E. Morgan, and S. K. Lele, *Analysis of unsteady effects in shock/boundary layer interactions,* in *Proceedings of the Summer Program* (2010) pp. 153–164.

[167] S. Pirozzoli and M. Bernardini, *Direct numerical simulation database for impinging shock wave/turbulent boundary-layer interaction,* AIAA Journal **49**, 1307 (2011).

[168] L. Agostini, L. Larchevêque, P. Dupont, J.-F. Debiève, and J.-P. Dussauge, *Zones of influence and shock motion in a shock/boundary-layer interaction,* AIAA Journal **50**, 1377 (2012).

[169] A. Hadjadj, *Large-eddy simulation of shock/boundary-layer interaction,* AIAA Journal **50**, 2919 (2012).

[170] G. Aubard, X. Gloerfelt, and J.-C. Robinet, *Large-eddy simulation of broadband unsteadiness in a shock/boundary-layer interaction,* AIAA Journal **51**, 2395 (2013).

[171] N. Mullenix and D. Gaitonde, *Analysis of unsteady behavior in shock/turbulent boundary layer interactions with large-eddy simulations,* AIAA Paper 2013-0404 (2013).

[172] V. Pasquariello, M. Grilli, S. Hickel, and N. A. Adams, *Large-eddy simulation of passive shock-wave/boundary-layer interaction control,* International Journal of Heat and Fluid Flow **49**, 116 (2014).

[173] B. Wang, N. D. Sandham, Z. Hu, and W. Liu, *Numerical study of oblique shock-wave/boundary-layer interaction considering sidewall effects,* Journal of Fluid Mechanics **767**, 526 (2015).

[174] T. Jiang, A.-M. Schreyer, L. Larchevêque, S. Piponniau, and P. Dupont, *Velocity spectrum estimation in shock-wave/turbulent boundary-layer interaction,* AIAA Journal **55**, 3486 (2017).

[175] M. A. Vyas, D. A. Yoder, and D. V. Gaitonde, *Reynolds-stress budgets in an impinging shock-wave/boundary-layer interaction,* AIAA Journal **57**, 4698 (2019).

[176] J. Fang, A. A. Zheltovodov, Y. Yao, C. Moulinec, and D. R. Emerson, *On the turbulence amplification in shock-wave/turbulent boundary layer interaction,* Journal of Fluid Mechanics **897** (2020).

[177] M. Gao, T. Kuhn, and C.-D. Munz, *On the investigation of oblique shock-wave/turbulent boundary-layer interactions with a high-order discontinuous Galerkin method,* International Journal for Numerical Methods in Fluids **94**, 1331 (2022).

[178] A. Gross, J. Little, and H. F. Fasel, *Numerical investigation of unswept and swept turbulent shock-wave boundary layer interactions,* Aerospace Science and Technology **123**, 107455 (2022).

[179] M. Bernardini, G. Della Posta, F. Salvadore, and E. Martelli, *Unsteadiness characterisation of shock wave/turbulent boundary-layer interaction at moderate reynolds number,* Journal of Fluid Mechanics **954**, A43 (2023).

[180] P. Bookey, C. Wyckham, A. Smits, and P. Martin, *New experimental data of STBLI at DNS/LES accessible Reynolds numbers,* AIAA Paper 2005-0309 (2005).

[181] P. Dupont, C. Haddad, and J. F. Debieve, *Space and time organization in a shock-induced separated boundary layer,* Journal of Fluid Mechanics **559**, 255 (2006).

[182] L. J. Souverein, P. Dupont, J.-F. Debieve, J.-P. Dussauge, B. W. Van Oudheusden, and F. Scarano, *Effect of interaction strength on unsteadiness in shock-wave-induced separations,* AIAA Journal **48**, 1480 (2010).

[183] B. W. Van Oudheusden, A. J. P. Jöbsis, F. Scarano, and L. J. Souverein, *Investigation of the unsteadiness of a shock-reflection interaction with time-resolved particle image velocimetry,* Shock Waves **21**, 397 (2011).

[184] N. Webb, C. Clifford, and M. Samimy, *Preliminary results on shock wave/boundary layer interaction control using localized arc filament plasma actuators,* AIAA Paper 2011-3426 (2011).

[185] N. Webb, C. Clifford, and M. Samimy, *Control of oblique shock wave/boundary layer interactions using plasma actuators,* Experiments in Fluids **54**, 1 (2013).

[186] R. H. M. Giepman, F. F. J. Schrijer, and B. W. Van Oudheusden, *Flow control of an oblique shock wave reflection with micro-ramp vortex generators: Effects of location and size,* Physics of Fluids **26**, 066101 (2014).

[187] A.-M. Schreyer, J. J. Lasserre, and P. Dupont, *Development of a dual-PIV system for high-speed flow applications,* Experiments in Fluids **56**, 187 (2015).

[188] J. A. Threadgill and P. J. K. Bruce, *Shock wave boundary layer interaction unsteadiness: the effects of configuration and strength,* AIAA Paper 2016-0077 (2016).

[189] P. K. Rabey and P. J. Bruce, *Experimental study exploring unsteadiness length scales in a reflected shock-boundary layer interaction,* AIAA Paper 2017-0983 (2017).

[190] P. Dupont, S. Piponniau, and J. P. Dussauge, *Compressible mixing layer in shock-induced separation,* Journal of Fluid Mechanics **863**, 620 (2019).

[191] P. K. Rabey, S. P. Jammy, P. J. K. Bruce, and N. D. Sandham, *Two-dimensional unsteadiness map of oblique shock wave/boundary layer interaction with sidewalls,* Journal of Fluid Mechanics **871**, R4 (2019).

[192] D. V. Gaitonde and M. C. Adler, *Dynamics of three-dimensional shock-wave/boundary-layer interactions,* Annual Review of Fluid Mechanics **55** (2023).

[193] W. Hu, S. Hickel, and B. W. Van Oudheusden, *Low-frequency unsteadiness mechanisms in shock wave/turbulent boundary layer interactions over a backward-facing step,* Journal of Fluid Mechanics **915** (2021).

[194] R. H. M. Giepman, *Flow control for oblique shock wave reflections*, Ph.D. thesis, TU Delft (2016).

[195] R. L. Simpson, *Turbulent boundary-layer separation,* Annual Review of Fluid Mechanics **21**, 205 (1989).

[196] E. E. Zukoski, *Turbulent boundary-layer separation in front of a forward-facing step.* AIAA Journal **5**, 1746 (1967).

[197] J. Délery, J. G. Marvin, and E. Reshotko, *Shock-wave boundary layer interactions*, AGARD-AG *Tech. Rep.* 280 (1986).

[198] P. Dupont, S. Piponniau, A. Sidorenko, and J. F. Debiève, *Investigation of an oblique shock reflection with separation by PIV measurements,* AIAA Paper 2007-0119 (2007).

[199] N. D. Sandham, *Effects of compressibility and shock-wave interactions on turbulent shear flows,* Flow, Turbulence and Combustion **97**, 1 (2016).

[200] Y. Kang and S. Lee, *Direct numerical simulation of turbulence amplification in a strong shock-wave/turbulent boundary layer interaction,* Physics of Fluids **36** (2024).

[201] M. R. Jovanović, P. J. Schmid, and J. W. Nichols, *Sparsity-promoting dynamic mode decomposition,* Physics of Fluids **26**, 024103 (2014).

[202] D. S. Dolling and C. T. Or, *Unsteadiness of the shock wave structure in attached and separated compression ramp flows,* Experiments in Fluids **3**, 24 (1985).

[203] M. C. Adler and D. V. Gaitonde, *Dynamic linear response of a shock/turbulent-boundary-layer interaction using constrained perturbations,* Journal of Fluid Mechanics **840**, 291 (2018).

[204] N. J. Cherry, R. Hillier, and M. Latour, *Unsteady measurements in a separated and reattaching flow,* Journal of Fluid Mechanics **144**, 13 (1984).

[205] F. F. J. Schrijer, A. Sciacchitano, and F. Scarano, *Spatio-temporal and modal analysis of unsteady fluctuations in a high-subsonic base flow,* Physics of Fluids **26**, 086101 (2014).

[206] T. Sayadi and P. J. Schmid, *Parallel data-driven decomposition algorithm for large-scale datasets: with application to transitional boundary layers,* Theoretical and Computational Fluid Dynamics **30**, 415 (2016).

[207] L. Laguarda, S. Hickel, F. F. J. Schrijer, and B. W. van Oudheusden, *Supplementary material to the publication 'Reynolds number effects in shock-wave/turbulent boundary-layer interactions'. (Version 1) [Dataset]. 4TU.researchdata.* https://doi.org/10.4121/7f9d8b26-0f1d-4bc0-895c-e36394891c62 (2023).

[208] A. Gogulapati, R. Deshmukh, A. R. Crowell, J. J. McNamara, V. Vyas, X. Q. Wang, M. Mignolet, T. Beberniss, S. M. Spottswood, and T. G. Eason, *Response of a panel to shock impingement: modeling and comparison with experiments,* AIAA Paper 2014-0148 (2014).

[209] Y.-J. Ahn, M. A. Eitner, M. N. Musta, J. Sirohi, N. T. Clemens, and S. Rafati, *Experimental investigation of flow-structure interaction for a compliant panel under a Mach 2 compression-ramp,* AIAA Paper 2022-0293 (2022).

[210] M. N. Musta, Y.-J. Ahn, M. A. Eitner, J. Sirohi, and N. Clemens, *Unsteadiness in shock/boundary-layer interaction over a compliant panel at mach 2,* AIAA Paper 2022-4136 (2022).

[211] K. R. Brouwer, R. A. Perez, T. J. Beberniss, S. M. Spottswood, and D. A. Ehrhardt, *Experiments on a thin panel excited by turbulent flow and shock/boundary-layer interactions,* AIAA Journal **59**, 2737 (2021).

[212] A. Tripathi, L. Mears, K. Shoele, and R. Kumar, *Oblique shockwave boundary layer interactions on a flexible panel at Mach 2,* (), aIAA Paper 2020-0568 (2020).

[213] A. Tripathi, J. Gustavsson, K. Shoele, and R. Kumar, *Fluid structure interaction on a compliant panel subject to shock boundary layer interaction,* (), aIAA Paper 2021-2806 (2021).

[214] M. A. Eitner, Y.-J. Ahn, M. N. Musta, J. Sirohi, and N. Clemens, *Effect of ramp-induced shock/boundary layer interaction on the vibration of a compliant panel at Mach 5,* AIAA Paper 2023-0081 (2023).

[215] Y. Bazilevs, K. Takizawa, and T. E. Tezduyar, *Computational fluid-structure interaction: methods and applications* (John Wiley & Sons, 2013).

[216] A. de Boer, A. H. van Zuijlen, and H. Bijl, *Review of coupling methods for non-matching meshes,* Computer methods in Applied Mechanics and Engineering **196**, 1515 (2007).

[217] V. Pasquariello, S. Hickel, N. A. Adams, G. Hammerl, W. A. Wall, D. Daub, S. Willems, and A. Gülhan, *Coupled simulation of shock-wave/turbulent boundary-layer interaction over a flexible panel,* in *6th European Conference for Aerospace Sciences* (2015).

[218] D. Daub, S. Willems, and A. Gülhan, *Experiments on the interaction of a fast-moving shock with an elastic panel,* AIAA Journal **54**, 670 (2016).

[219] J. F. Hoy and I. Bermejo-Moreno, *Numerical study of STBLI on flexible panels with wall-modeled LES,* AIAA Paper 2021-0250 (2021).

[220] L. Laguarda, S. Hickel, F. F. J. Schrijer, and B. W. van Oudheusden, *Supplementary material to the publication 'Shock-wave/turbulent boundary-layer interaction with a flexible panel'. (Version 1) [Dataset]. 4TU.researchdata.* https://doi.org/10.4121/01bb5a10-aa50-4ac9-b638-ec57937e27a9 (2023).

[221] S. Priebe and M. P. Martín, *Low-frequency unsteadiness in shock wave–turbulent boundary layer interaction,* Journal of Fluid Mechanics **699**, 1 (2012).

[222] O. T. Schmidt and T. Colonius, *Guide to spectral proper orthogonal decomposition,* AIAA Journal **58**, 1023 (2020).

[223] S. Hickel, N. A. Adams, and J. A. Domaradzki, *An adaptive local deconvolution method for implicit LES,* Journal of Computational Physics **213**, 413 (2006).

[224] S. Hickel and N. A. Adams, *Efficient implementation of nonlinear deconvolution methods for implicit large-eddy simulation,* in *High Performance Computing in Science and Engineering'06: Transactions of the High Performance Computing Center Stuttgart (HLRS) 2006* (Springer, 2007) pp. 293–306.

[225] R. J. LeVeque, *Numerical methods for conservation laws*, Vol. 214 (Springer, 1992).

[226] S. Hickel, N. A. Adams, and N. N. Mansour, *Implicit subgrid-scale modeling for large-eddy simulation of passive-scalar mixing,* Physics of Fluids **19** (2007).

[227] S. Hickel and J. Larsson, *An adaptive local deconvolution model for compressible turbulence,* in *Proceedings of the Summer Program* (2008) p. 85.

[228] X. Wu, *Inflow turbulence generation methods,* Annual Review of Fluid Mechanics **49**, 23 (2017).

[229] N. S. Dhamankar, G. A. Blaisdell, and A. S. Lyrintzis, *Overview of turbulent inflow boundary conditions for large-eddy simulations,* AIAA Journal **56**, 1317 (2018).

[230] P. S. Johansson and H. I. Andersson, *Generation of inflow data for inhomogeneous turbulence,* Theoretical and Computational Fluid Dynamics **18**, 371 (2004).

[231] J. Kim and C. Lee, *Deep unsupervised learning of turbulence for inflow generation at various Reynolds numbers,* Journal of Computational Physics **406**, 109216 (2020).

[232] T. S. Lund, X. Wu, and K. D. Squires, *Generation of turbulent inflow data for spatially-developing boundary layer simulations,* Journal of Computational Physics **140**, 233 (1998).

[233] S. Xu and M. P. Martin, *Assessment of inflow boundary conditions for compressible turbulent boundary layers,* Physics of Fluids **16**, 2623 (2004).

[234] H. Le, P. Moin, and J. Kim, *Direct numerical simulation of turbulent flow over a backward-facing step,* Journal of Fluid Mechanics **330**, 349 (1997).

[235] M. Klein, A. Sadiki, and J. Janicka, *A digital filter based generation of inflow data for spatially developing direct numerical or large eddy simulations,* Journal of Computational Physics **186**, 652 (2003).

[236] N. Jarrin, S. Benhamadouche, D. Laurence, and R. Prosser, *A synthetic-eddy-method for generating inflow conditions for large-eddy simulations,* International Journal of Heat and Fluid Flow **27**, 585 (2006).

[237] G. R. Tabor and M. H. Baba-Ahmadi, *Inlet conditions for large eddy simulation: A review,* Computers & Fluids **39**, 553 (2010).

[238] M. Grilli, S. Hickel, and N. A. Adams, *Large-eddy simulation of a supersonic turbulent boundary layer over a compression–expansion ramp,* International Journal of Heat and Fluid Flow **42**, 79 (2013).

[239] M. C. Adler, D. R. Gonzalez, C. M. Stack, and D. V. Gaitonde, *Synthetic generation of equilibrium boundary layer turbulence from modeled statistics,* Computers & Fluids **165**, 127 (2018).

[240] A. Keating, U. Piomelli, E. Balaras, and H.-J. Kaltenbach, *A priori and a posteriori tests of inflow conditions for large-eddy simulation,* Physics of Fluids **16**, 4696 (2004).

[241] A. Ceci, A. Palumbo, J. Larsson, and S. Pirozzoli, *Numerical tripping of high-speed turbulent boundary layers,* Theoretical and Computational Fluid Dynamics **36**, 865 (2022).

[242] N. S. Dhamankar, C. S. Martha, Y. Situ, K. M. Aikens, G. A. Blaisdell, A. S. Lyrintzis, and Z. Li, *Digital filter-based turbulent inflow generation for jet aeroacoustics on non-uniform structured grids,* AIAA Paper 2014-1401 (2014).

[243] L. Di Mare, M. Klein, W. P. Jones, and J. Janicka, *Synthetic turbulence inflow conditions for large-eddy simulation,* Physics of Fluids **18** (2006).

[244] J. Larsson, *Simple inflow sponge for faster turbulent boundary-layer development,* AIAA Journal **59**, 4271 (2021).

[245] Y. Tsuji, J. H. M. Fransson, P. H. Alfredsson, and A. V. Johansson, *Pressure statistics and their scaling in high-Reynolds-number turbulent boundary layers,* Journal of Fluid Mechanics **585**, 1 (2007).

[246] M. Bernardini and S. Pirozzoli, *Wall pressure fluctuations beneath supersonic turbulent boundary layers,* Physics of Fluids **23**, 085102 (2011).

[247] M. Matsumoto and T. Nishimura, *Mersenne twister: a 623-dimensionally equidistributed uniform pseudo-random number generator,* ACM Transactions on Modeling and Computer Simulation (TOMACS) **8**, 3 (1998).

[248] R. L. Panton, *Overview of the self-sustaining mechanisms of wall turbulence,* Progress in Aerospace Sciences **37**, 341 (2001).

[249] P. Schlatter, R. Örlü, Q. Li, G. Brethouwer, J. H. M. Fransson, A. V. Johansson, P. H. Alfredsson, and D. S. Henningson, *Turbulent boundary layers up to Re θ= 2500 studied through simulation and experiment,* Physics of Fluids **21**, 051702 (2009).

[250] M. K. Bull, *Wall-pressure fluctuations beneath turbulent boundary layers: some reflections on forty years of research,* Journal of Sound and Vibration **190**, 299 (1996).

[251] J. Jiménez, *Cascades in wall-bounded turbulence,* Annual Review of Fluid Mechanics **44**, 27 (2012).

[252] X. Chen, F. Hussain, and Z.-S. She, *Non-universal scaling transition of momentum cascade in wall turbulence,* Journal of Fluid Mechanics **871** (2019).

[253] F. Hatay and S. Biringen, *Direct numerical simulation of low-Reynolds number supersonic turbulent boundary layers,* in *33rd Aerospace Sciences Meeting and Exhibit* (1995) p. 581.

[254] S. L. Brunton and J. N. Kutz, *Data-driven science and engineering: Machine learning, dynamical systems, and control* (Cambridge University Press, 2022).

[255] C. W. Rowley, I. Mezić, S. Bagheri, P. Schlatter, and D. S. Henningson, *Spectral analysis of nonlinear flows,* Journal of Fluid Mechanics **641**, 115 (2009).

Scientific contributions

6. **L. Laguarda**, S. Hickel, F. F. J. Schrijer and B. W. van Oudheusden. Reynolds number effects in shock-wave/turbulent boundary-layer interactions. Accepted for publication in *J. Fluid Mech.*, 2024.

5. **L. Laguarda**, S. Hickel, F. F. J. Schrijer and B. W. van Oudheusden. Shock-wave/turbulent boundary-layer interaction with a flexible panel, *Phys. Fluids* **36** (1), 2024. doi: https://doi.org/10.1063/5.0179082

4. **L. Laguarda**, L. and Hickel, S. Analysis of improved digital filter inflow generation methods for compressible turbulent boundary layers. Comput Fluids **268**, 2024. doi: https://doi.org/10.1016/j.compfluid.2023.106105

3. **L. Laguarda**, S. Hickel, F. F. J. Schrijer and B. W. van Oudheusden. Assessment of Reynolds number effects in supersonic turbulent boundary layers, *Int J Heat Fluid Flow* **105**, 2024. doi: https://doi.org/10.1016/j.ijheatfluidflow.2023.109234

2. **L. Laguarda**, J. Santiago Patterson, S. Hickel, F. F. J. Schrijer and B. W. van Oudheusden. Experimental investigation of shock–shock interactions with variable inflow Mach number, *Shock Waves* **31** (5), 2021. doi: https://doi.org/10.1007/s00193-021-01029-3

1. **L. Laguarda**, S. Hickel, F. F. J. Schrijer and B. W. van Oudheusden. Dynamics of unsteady asymmetric shock interactions, *J. Fluid Mech.* **888**, 2020. doi: https://doi.org/10.1017/jfm.2020.28

About the author

by Tijana Davidović

Luis was born on a sunny May day in a Barcelona hospital, but the place he truly calls home is a nearby city Mataró where he was living until he turned 23.

Luis obtained his Bachelor's degree from Universitat Politècnica de Catalunya in the field of Aerospace Engineering, having also spent 6 months at the University of California, Irvine working on his thesis. But there is so much more about Luis that led to this first notable academic achievement. His most important quality is the relentless passion towards things he finds important. Growing up, you could see it not only in his studies and relationship with close friends but also on a basketball court, while painting figures and canvases, or in the way he'd dance to Michael Jackson songs. Luis also had very strong support at home while growing up, and if someone deserves credit for all his success and the kind of person he became, it is his parents Encarna and Albert.

After these formative years, in 2015 Luis continued his professional journey at the University of Applied Sciences Wiener Neustadt, Austria pursuing his Master's degree. And again, his relentless passion resulted in him graduating first of class and receiving an Outstanding Performance award. Coincidentally, 2015 was also the year in which I met Luis. This was on a basketball court, and without exchanging a single word I could immediately feel how big his passion was – not just for basketball, but all-things-life. And looking back, I was so right.

Next step in his professional journey led us to where we are today. Luis came to the Netherlands in 2017 for his master's thesis at TU Delft, and in 2018 he started his PhD journey while working as a researcher for the past year. Today, after more than 7 years, we call this country our home. While Luis really loves what he does and enjoys his time at work, it is all the days spent with Jordi, Alessandro, Maria, Marc and many more, that make us call this country our home.

Subject index